



City Research Online

City, University of London Institutional Repository

Citation: Haxha, S. (2004). Optimization of ultra-high speed electrooptic modulators using the finite element method. (Unpublished Doctoral thesis, City, University of London)

This is the accepted version of the paper.

This version of the publication may differ from the final published version.

Permanent repository link: <https://openaccess.city.ac.uk/id/eprint/30506/>

Link to published version:

Copyright: City Research Online aims to make research outputs of City, University of London available to a wider audience. Copyright and Moral Rights remain with the author(s) and/or copyright holders. URLs from City Research Online may be freely distributed and linked to.

Reuse: Copies of full items can be used for personal research or study, educational, or not-for-profit purposes without prior permission or charge. Provided that the authors, title and full bibliographic details are credited, a hyperlink and/or URL is given for the original metadata page and the content is not changed in any way.

Optimization of Ultra-High Speed Electrooptic Modulators using the Finite Element Method

by

Shyqyri Haxha

A thesis submitted to City University in fulfillment of the requirement
for the Degree of Doctor of Philosophy in
Electrical and Electronic Engineering

City University

School of Engineering and Mathematical Sciences
Northampton Square London EC1V 0HB

January 2004

*This work is lovingly dedicated to my brother Bahri Hasha
my parents my niece my children my wife and my family*

Table of Contents

Table of Contents.....	ii
List of Tables.....	vii
List of Figures.....	viii
Acknowledgements.....	xviii
Declaration.....	xix
Abstract.....	xx
Symbols and Abbreviations.....	xxii
1. Introduction.....	1
1.1. Historical Introduction of Lightwave Technology.....	1
1.2. Optical Communication Systems.....	4
1.3. Integrated Optics and Photonic Devices.....	8
1.4. Optical Fiber Waveguides.....	10
1.5. Planar Optical Waveguides.....	16
1.6. Photonic Devices (Modulators).....	22
1.7. Aims and Objectives of the Thesis.....	23
1.8. Structure of the Thesis.....	26
2. Numerical Techniques.....	29
2.1. Introduction.....	29
2.2. Analytical solution techniques of optical waveguides.....	30
2.2.1. Marcatili Method.....	30

2.2.2. The effective index method.....	31
2.3. Numerical solution techniques of optical waveguides.....	32
2.3.1. Finite difference method	33
2.3.2. Finite element method	34
2.3.3. Beam propagation method.....	35
2.3.4. The method of lines.....	36
2.3.5. Point matching method.....	37
2.3.6. The boundary element method.....	38
2.3.7. The mode-matching method (MMM) or the equivalent network method (ENM).....	39
2.3.8. The spectral index method.....	40
2.4. The Least-Square Boundary Residual (LSBR) Method.....	41
2.4.1. Analysis of optical waveguide discontinuities by (LSBR) method.....	42
2.4.2. Numerical analysis of waveguide discontinuity (LSBR) using FE modal solution output.....	45
3. The Finite Element Method.....	48
3.1. Introduction.....	48
3.2. Maxwell's Equations.....	50
3.3. Finite Element Formulations.....	53
3.4. Scalar Finite Element Formulations.....	54
3.5. Vectorial Finite Element Formulations.....	55
3.6. Boundary Conditions.....	56
3.7. Natural Boundary Conditions.....	60
3.8 Formulation of the Finite Element Method.....	61
3.8.1. Finite Element Discretization.....	61
3.8.2. Shape Functions.....	62
3.8.3. Element and Global Matrices.....	67
3.8.4. Infinite Elements Analysis.....	70
3.9. Spurious Solutions in Finite Element Method.....	72
3.10. Matrix Solution Techniques in Finite Element Method.....	74

4. Optical Modulators.....	75
4.1. Introduction.....	75
4.2. Various Optical Modulators.....	80
4.3. Modulator Characteristics.....	84
4.4. Electrooptic Effect.....	88
4.5. Electrooptic Effect of LiNbO ₃ Modulators (Transverse Electrooptic Modulation).....	91
4.6. Electrooptic Effect of the GaAs (Modulators) Crystal Orientation.....	97
4.7. Calculation of Half-Wave Length Product $V_{\pi}L$	102
4.8. Driving Power Calculation of the Electrooptic Modulators.....	106
5. Microwave Properties of the Electrooptic Modulators.....	107
5.1. Introduction.....	107
5.2. Quasi-TEM Analysis of Electrooptic Modulators by the Finite Element Method.....	109
5.3. Electric Field Calculation.....	113
5.4. Capacitance Calculations of the Electrooptic Modulators.....	114
5.5. Microwave Index Calculations of the Electrooptic Modulators.....	117
5.6. Characteristic Impedance Calculation of the Electrooptic Modulators.....	118
5.7. Conductor Loss Calculation.....	121
5.8. Dielectric Loss Calculation.....	123
5.9. Bandwidth Calculation.....	125
5.10. Velocity Matching Techniques.....	128
6. Unetched Lithium Niobate Electrooptic Modulator.....	135
6.1. Introduction.....	135
6.2. Modulator Fabrication.....	137
6.3. Titanium Diffused Waveguide Fabrication.....	137
6.4. Fabrication of the Buffer Layer SiO ₂	143

6.5. Fabrication of the Gold Electrodes.....	144
6.6. Dicing, Polishing, Pigtailling, Packaging, and Testing of Electrooptic Modulators.....	145
6.7. Simulated Results for Unetched Lithium Niobate Waveguide Electrooptic Modulators.....	146
7. Ultra-Broad-Band LiNbO₃ Optical Modulator with Ridge Structure.....	169
7.1. Introduction.....	169
7.2. Etching Substrate Fabrication.....	171
7.3. Simulated Results for Ridge Electrooptic Modulator and its advantage over Conventional Planar Structure.....	172
8. Deeply-Etched Semiconductor Electrooptic Modulator.....	208
8.1. Introduction.....	208
8.2. Design and Fabrication of Deeply-Etched Semiconductor Waveguide Electrooptic Modulator.....	209
8.3. Velocity Matching Techniques for the Semiconductor Electrooptic Modulator.....	212
8.4. Simulated Results for the Deeply-Etched Semiconductor Electrooptic Modulators.....	215
9. Polarization Conversion Phenomenon in deeply-Etched Semiconductor Electrooptic Waveguide Modulators.....	236
9.1 Introduction.....	236
9.2 Unexpected Polarization Conversion.....	237
9.3 Simulated Results for the Characterization of Polarization Conversion in Semiconductor Electrooptic Modulators.....	238
10. Conclusions and Suggestions for the Future Work.....	257
10.1. General Conclusions.....	257
10.2. Future Work.....	260

Appendix 1 Electro-optic Effect.....	262
Appendix 2 Divergence theorem.....	270
Appendix 3 Flow chart of FEM.....	273
Appendix 4 List of Publications by the author	
Relevant to the thesis.....	276
References.....	279

List of Tables

Table 1.1: The electromagnetic spectrum.

Table 4.1: Development and performance of optical modulators.

Table 8.1 Al mole concentration on the %GaAs composition.

List of Figures

- Figure 1.1:** Capacity per fiber (Gb/s) from 1980-2005.
- Figure 1.2:** DWDM Capacity and Interface Speeds.
- Figure 1.3:** An optical communication system.
- Figure 1.4:** Block diagram of an optoelectronic phase array antenna system.
- Figure 1.5:** Direction of light propagation perpendicular to the electromagnetic waves (a), and (b) electric field of an electromagnetic wave as function of the time t .
- Figure 1.6:** Plane wave with its propagation vector k in the (x, y) plane.
- Figure 1.7:** Reflection and transmission, Snell's law (a) and total internal reflected ray (b).
- Figure 1.8:** Schematic diagram of an optical fiber and the acceptance angle, when launching light in an optical fiber.
- Figure 1.9:** Slab Optical waveguide.
- Figure 1.10:** Refractive index profile of the slab waveguide (a) and Field distribution for TE_m modes, where $m = 0, 1, 2, \dots$ (First and higher order modes) (b).
- Figure 1.11:** Various types of waveguides.
- Figure 2.1:** Two dimensional buried rectangular waveguide for Marcatili method.
- Figure 2.2:** The model representation of effective index method.
- Figure 2.3:** Typical two-dimensional finite different mesh.
- Figure 2.4:** Typical three-dimensional finite element subdivision analysis.
- Figure 2.5:** Schematic illustration of BPM analysis (light propagating in z -direction).
- Figure 2.6:** One half of the cross section of a microstrip line analyzed by MOL.
- Figure 2.7:** Schematic dielectric layers structure with several electrodes on top analyzed by PMM (Marcuse, 1989).
- Figure 2.8:** Two-dimensional region Ω surrounded by boundary Γ .

- Figure 2.9:** Waveguide discontinuities analyzed by (MMM).
- Figure 2.10:** Cross section of rib-waveguide illustrating use of spectral index method.
- Figure 2.11:** Discontinuity at the junction of two dielectric waveguide. (a) Vertical section, (b) Transverse section.
- Figure 3.1:** An arbitrary shape of the optical waveguide geometry divided into finite number of subregions or elements, where each subregion is consisted from different materials.
- Figure 3.2:** Various waveguide shapes with transverse distribution of permittivity, (a). planar, (b). axial symmetric (c) and arbitrary.
- Figure 3.3:** The interface between medium 1 and medium 2.
- Figure 3.4:** Cartesian coordinate system.
- Figure 3.5:** Properties of the *unity vectors*, i , j , and k in vectorial and scalar formulation.
- Figure 3.6:** (a) The solution region by FEM, and (b) Finite element discretization.
- Figure 3.7:** The typical elements for one-, two-, and three-dimensional problems.
- Figure 3.8:** Pattern of nodes on a single element compared with Pascal's triangle.
- Figure 3.9:** Coordinates and node numbers of a typical first-order triangular elements.
- Figure 3.10:** Rectangular (1/4 symmetry) dielectric waveguide cross section discretized into orthodox and infinite elements.
- Figure 4.1:** Mach-Zehnder modulator (a), Mach-Zender Interferometric (MZI) modulator (b).
- Figure 4.2:** Directional coupler based modulator.
- Figure 4.3:** Deeply-etched waveguide electrooptic GaAs modulator, Mach-Zehnder part.
- Figure 4.4:** Schematic structure of an semiconductor modulator (GaAs).
- Figure 4.5:** Schematic structure of an InGaAsP/InGaAsP MQW electroabsorption modulator.
- Figure 4.6:** Application of the optical modulators for high-capacity transmission systems.
- Figure 4.7:** The principle of the modulator and its interacting with the light.

- Figure 4.8:** Electrooptic amplitude modulation.
- Figure 4.9:** CPW Z-cut electrooptic modulator with vertical field ($E \perp$) TM mode.
- Figure 4.10:** CPW X-cut electrooptic modulator with horizontal field ($E \parallel$) TE mode.
- Figure 4.11:** Intersection of index ellipsoid with x - y plane.
- Figure 4.12:** Deeply-etched semiconductor electrooptic modulator.
- Figure 4.13:** Miller Indices.
- Figure 4.14:** The process of the modulation of an optical signal.
- Figure 5.1:** Coplanar waveguide (CPW) LiNbO₃ electrooptic modulator.
- Figure 5.2:** Microstrip type Semiconductor electrooptic modulator.
- Figure 5.3:** Electrooptic LiNbO₃ CPW modulator fields distributions.
- Figure 5.4:** a) Triangle elements over an L-shape region b).Typical triangle element in x - y plane.
- Figure 5.5:** Potential distribution for the LiNbO₃ electrooptic modulator considered at voltage applied, $V = 5$ volt.
- Figure 5.6:** Cross-section geometry of three parallel strip lines, equipotential lines (potential lines) with integration path.
- Figure 5.7:** Traveling-wave electrooptic modulator with coupled electrode (V_1 and V_2).
- Figure 5.8:** Recession of conducting walls of LiNbO₃ modulator structure.
- Figure 5.9:** Recession of conducting walls of GaAs modulator structure.
- Figure 5.10:** General principal work of the traveling wave phase LiNbO₃ electrooptic modulator.
- Figure 5.11:** Cross-section of the LiNbO₃ (a) un-etched and (b) etched Mach-Zehnder modulator.
- Figure 5.12:** Schematic diagrams of a deep-etched GaAs/AlGaAs of the semiconductor electrooptic modulators for two types of the Ta₂O₅ overlayers arrangements, A and B .
- Figure 6.1:** Cross section of Z-cut unetched lithium niobate electrooptic modulator.
- Figure 6.2:** Step one expose waveguide pattern.
- Figure 6.3:** Step two deposit titanium dopant.
- Figure 6.4:** Step three liftoff process.

- Figure 6.5:** Step four diffused waveguide.
- Figure 6.6:** Fabrication steps of the gold electrodes for LiNbO₃ electrooptic modulator.
- Figure 6.7:** Schematic illustration of unetched LiNbO₃ electrooptic modulator.
- Figure 6.8:** 3D potential distribution for unetched LN electrooptic modulator for $V = 5$ volts.
- Figure 6.9:** 2-D illustration of potential distribution for unetched LN electrooptic modulator.
- Figure 6.10:** 3D illustration of the electric field concentration in x direction (E_x).
- Figure 6.11:** Two dimensional presentation of $E_x(x, y)$ component.
- Figure 6.12:** 3D plot of the modulating electric field $E_y(x, y)$ for unetched LN modulator.
- Figure 6.13:** 2D plot of the $E_y(x, y)$ electric field for unetched LN electrooptic modulator.
- Figure 6.14:** Variation of magnetic field component along x -direction, H_x .
- Figure 6.15:** 3D plot of the change in refractive index due to an applied electric field, for an applied voltage of 5 V for unetched LiNbO₃ electrooptic modulator.
- Figure 6.16:** 2D plot for refractive index change due to the electric field, for an applied voltage of 5 V for unetched LiNbO₃ electrooptic modulator.
- Figure 6.17:** The optical field H_x contours of the quasi-TM mode for unetched LiNbO₃ electrooptic modulator.
- Figure 6.18:** Variation of microwave index, N_m and characteristic impedance, Z_C with the buffer layer thickness, B .
- Figure 6.19:** Variation of conductor and dielectric losses, α_C and α_d , normalized at 1 GHz, with buffer layer thickness, B for unetched LN structure.
- Figure 6.20:** Variation of microwave effective index, N_m and characteristic impedance, Z_C with central electrode width, S .
- Figure 6.21:** Required electrode thickness, T , and buffer layer thickness, B , values for simultaneous matching of N_m and Z_C with the electrode width, S .

- Figure 6.22:** Variation of the α_C and α_d with S when both N_m and Z_C are simultaneously matched.
- Figure 6.23:** Variation of the modulator bandwidth, Δf and half-wave length product $V\pi L$ with buffer layer thickness, B .
- Figure 6.24:** Variation of the modulator bandwidth with the buffer layer thickness, B , and Variation of the product $V\pi L$ with buffer layer thickness, B , under velocity and impedance matching conditions.
- Figure 6.25:** Variation of the modulator bandwidth with the electrode width, S under velocity and impedance matching conditions.
- Figure 7.1:** 3-D and 2-D cross sections of ridged structure LiNbO₃ electrooptic modulator.
- Figure 7.2:** Picture of a LiNbO₃ electrooptic modulator.
- Figure 7.3:** Ridged LiNbO₃ electrooptic modulator.
- Figure 7.4:** 3-D potential distribution for ridge LN electrooptic modulator at $V=5$ voltage.
- Figure 7.5:** 2-D and 3-D (small scale) illustration of the electric field concentration in x direction (E_x).
- Figure 7.6:** 2-D and 3-D (small scale) plot of the $E_y(x, y)$ electric field for ridge electrooptic modulator.
- Figure 7.7:** The change of refractive index due to an applied electric field for ridge structure, $H=3 \mu\text{m}$, 3-D plot a) and 2-D plot b).
- Figure 7.8:** The optical field H_x contours of the quasi-TM mode for an etched structure with ridge height, $H=3 \mu\text{m}$.
- Figure 7.9:** The optical field H_x contours of quasi-TM modes for left and right waveguides.
- Figure 7.10:** Variation of the microwave index, N_m and the Characteristic Z_C with the buffer layer thickness, B .
- Figure 7.11:** Variation of the microwave parameters N_m and Z_C with ridge depth, H .
- Figure 7.12:** Variation of microwave parameters N_m and Z_C with the central electrode.
- Figure 7.13:** Variation of the microwave index, N_m , the characteristic impedance, Z_C as a function of the buffer layer, B , for an electrode gap, $G=20 \mu\text{m}$ and $G=25$

μm and for the ridge depth, $H=0\ \mu\text{m}$ and $H=3\ \mu\text{m}$ when the electrode thickness, $T=5\ \mu\text{m}$.

- Figure 7.14:** Variation of the conductor loss and dielectric loss with buffer layer thickness normalized at 1 GHz, for ridge height, $H=3\ \mu\text{m}$.
- Figure 7.15:** Variation of the conductor loss and dielectric losses with the ridge depth.
- Figure 7.16:** Variation of conductor loss and dielectric loss with the buffer layer thickness, normalized at 1 GHz, for an electrode gap, $G=20\ \mu\text{m}$ and $G=25\ \mu\text{m}$ and for the ridge depth, $H=0\ \mu\text{m}$ and $H=3\ \mu\text{m}$ when the electrode thickness, $T=5\ \mu\text{m}$.
- Figure 7.17:** Variation of conductor loss, α_C dielectric loss, α_d and total dielectric, α_T loss with the operating frequency f .
- Figure 7.18:** Required electrode thickness to achieve the phase matching and the corresponding characteristic impedance, Z_C for certain buffer layer thickness, B .
- Figure 7.19:** Required electrode thickness, T , to achieve velocity matching, $N_m=2.15$ and the variation of the characteristic impedance, Z_C , under this condition as a function of the buffer layer, B .
- Figure 7.20:** Variation of conductor loss, dielectric loss in LN and SiO_2 with buffer layer thickness, under velocity matching condition.
- Figure 7.21:** Variation of the conductor loss and the dielectric loss with the buffer layer thickness, B , normalized at 1 GHz for an electrode gap, $20\ \mu\text{m}$ and $25\ \mu\text{m}$ and ridge depth $0\ \mu\text{m}$ and $3\ \mu\text{m}$ under the velocity matching condition.
- Figure 7.22:** Variation of the electrode thickness T and electrode width S with the buffer layer thickness B under the simultaneous matching condition of N_m and Z_C .
- Figure 7.23:** Variation of the conductor loss and dielectric loss with buffer layer thickness under simultaneous matching condition of N_m and Z_C .
- Figure 7.24:** Variation of the product $V_\pi L$ as a function of the ridge depth, H for two different buffer layer thicknesses, B and the structure of modulator.

- Figure 7.25:** Variation of $V_{\pi}L$ as a function of the buffer layer, for an electrode gap, $G=15 \mu\text{m}$ and $G=25 \mu\text{m}$ for etched, ($H=3 \mu\text{m}$, $H=4 \mu\text{m}$) and unetched, ($H=0 \mu\text{m}$) structures.
- Figure 7.26:** Variation of the product $V_{\pi}L$ with the electrode gap, G , for values of ridge depth, $H=0 \mu\text{m}$, $H=3 \mu\text{m}$ and $H=4 \mu\text{m}$.
- Figure 7.27:** Variation of the product $V_{\pi}L$ with the width of center electrode, S , for a waveguide width, $W=8 \mu\text{m}$, $W=9 \mu\text{m}$ and $W=10 \mu\text{m}$.
- Figure 7.28:** Variation of the 3dB optical bandwidth, with buffer layer thickness, B , for different values of electrode thickness, T .
- Figure 7.29:** Variation of the 3dB optical bandwidth for etched and unetched structures, with the buffer layer thickness, B , at a fixed voltage $V=5 \text{ V}$ under the velocity matching condition.
- Figure 7.30:** Variation of the 3dB optical bandwidth and the product $V_{\pi}L$ with buffer layer thickness, B , under velocity and impedance matching conditions.
- Figure 7.31:** Variation of the driving power with buffer layer thickness under velocity and impedance matching condition for etched and unetched structure.
- Figure 7.32:** Variation of the optical loss with buffer layer thickness for different electrode thickness and gap between electrodes.
- Figure 8.1:** Deeply-etched AlGaAs/GaAs semiconductor electrooptic modulator.
- Figure 8.2:** a) Cross section (Nees, 1989) of the GaAs electrooptic modulator and b) variation of the effective index, N_m and characteristic impedance, Z_C , with electrode thickness, T , with and without GaAs substrate placed in top of the structure.
- Figure 8.3:** Variation of the characteristic impedance a) and microwave index b) with electrode thickness for different value of gap between electrodes, G , and electrode width, S , when GaAs substrate is placed in top of the structure.
- Figure 8.4:** Schematic illustration of cross section of the deeply-etched semiconductor electrooptic modulator.
- Figure 8.5:** Horizontal or x component of the electric field profile $E_x(x, y)$.
- Figure 8.6:** Vertical or y component of the electric field $E_y(x, y)$.

- Figure 8.7:** Variation of the $V_{\pi}L$ product with buffer layer thickness for different values of Al mole concentration of the buffer layer, X_I .
- Figure 8.8:** Variation of microwave index N_m and characteristic impedance Z_C with buffer layer thickness B for two different values of the core height H .
- Figure 8.9:** Schematic diagrams of a deep-etched GaAs/AlGaAs of the semiconductor electrooptic modulators for two types of the Ta₂O₅ over layers arrangements, A and B .
- Figure 8.10:** Variation of microwave index, N_m with Ta₂O₅ for the structures A and B .
- Figure 8.11:** Variation of characteristic impedance, Z_C with coating thickness, Ta₂O₅ for the structures A and B .
- Figure 8.12:** Variation of the conductor loss, α_C for two structures A and B .
- Figure 8.13:** Variation of the dielectric losses, α_d , α_{dg} , and α_{dt} , with the coating thickness, Ta₂O₅ for the structures, A and B .
- Figure 8.14:** Variation of the product $V_{\pi}L$ with buffer layer thickness, D , for coating thickness, $T=2.5 \mu\text{m}$, $T=0.75 \mu\text{m}$ and $T=0.0 \mu\text{m}$ for the structures, A and B .
- Figure 8.15:** Variation of the microwave effective index, N_m and characteristic impedance, Z_C with buffer layer thickness, D for the coating thickness, $T=2.5 \mu\text{m}$, $T=0.75 \mu\text{m}$ and $T=0.0 \mu\text{m}$ for both structures A and B .
- Figure 8.16:** Variation of the conductor loss, α_C , and dielectric losses, α_d , α_{dg} , and α_{dt} , with buffer layer thickness D for the coating thickness, $T=2.5 \mu\text{m}$, $T=0.75 \mu\text{m}$ and $T=0.0 \mu\text{m}$ for both structures A and B .
- Figure 8.17:** Variation of the microwave effective index, N_m and characteristic impedance, Z_C with electrode thickness, E for the coating thickness, $T=2.5 \mu\text{m}$, $T=2.0 \mu\text{m}$, $T=1.5 \mu\text{m}$, $T=1.0 \mu\text{m}$ and $T=0.75 \mu\text{m}$ for the structure A .
- Figure 8.18:** Variation of the conductor loss, α_C and dielectric losses, α_d , α_{dg} , and α_{dt} , with electrode thickness, E for the coating thickness, $T=2.5 \mu\text{m}$, $T=1.5 \mu\text{m}$ and $T=0.75 \mu\text{m}$ for the structure A .

- Figure 8.19:** Variation of the 3dB optical bandwidth for the structure *A*, with the electrode thickness, *E*, for coating thickness, $T=3.0\ \mu\text{m}$, $T=2.5\ \mu\text{m}$, $T=2.0\ \mu\text{m}$, $T=1.5\ \mu\text{m}$, $T=1.0\ \mu\text{m}$ and $T=0.75\ \mu\text{m}$.
- Figure 8.20:** Variation of the 3dB optical bandwidth for both structures *A* and *B*, with the electrode thickness, *E*, for coating thickness, $T=4.0\ \mu\text{m}$, $T=3.0\ \mu\text{m}$.
- Figure 9.1:** Schematic diagram of a deeply-etched AlGaAs/GaAs semiconductor electrooptic modulator with slanted sidewalls.
- Figure 9.2:** Variation of the propagation constants of the fundamental TE and TM modes with the modulating voltage for different values of the slant angle.
- Figure 9.3:** Horizontal electric field or *x* component, $E_x(x, y)$ for slant sidewall.
- Figure 9.4:** Vertical or *y* component of the electric field $E_y(x, y)$ with slanted walls.
- Figure 9.5:** Refractive change due to *y* component of electric field $E_y(x, y)$.
- Figure 9.6:** Refractive change due to *x* component of electric field $E_x(x, y)$.
- Figure 9.7:** Contour plot of the major (a) H_x and minor (b) H_y field components of the fundamental TM mode for zero modulating voltage.
- Figure 9.8:** Contour plot of the minor H_y field component of the fundamental TM mode when the modulating voltage is (a) $-10\ \text{V}$ and (b) $-24.2\ \text{V}$.
- Figure 9.9:** Various field plots for $V=0$, $V=-24$, $\theta=0$, $\theta=10^\circ$ and $X_1=30\%$, for dominant and nondominant modes.
- Figure 9.10:** Variation of the beat length with the modulating voltage for different values of the slant angle.
- Figure 9.11:** Variation of modal transmission coefficients of both the fundamental TE and TM modes with the modulating voltage for different values of the slant angle.
- Figure 9.12:** Variation of the TM power with the propagation distance, *Z*, for different values of the modulating voltage.
- Figure 9.13:** Variation of the maximum polarization conversion ratio with the modulating voltage for different values of the slant angle.
- Figure 9.14:** Variation of the polarization conversion ratio with the modulating voltage for different values of the slant angle at 2 cm device length.

Figure 9.15: Variation of the polarization conversion ratio with the modulating voltage for different values of the slant angle at 4 cm device length.

Figure 9.16: Variation of the beat length with the modulating voltage for different values of the Al concentration of the buffer layer, x_1 .

Figure 9.17: Variation of the polarization conversion ratio with the modulating voltage for different values of the Al concentration of the buffer layer, x_1 , at 2 cm device length.

Acknowledgements

I wish to express deep gratitude to **Prof. B. M. A. Rahman** for his excellent supervision of this work and for providing his useful suggestions and devoting his time to discuss problems of all sorts.

I am deeply indebted to **Prof. K. T. V. Grattan** for his advice and guidance throughout this research work.

I wish to acknowledge Dr John Heaton, QinetiQ, Marvern, UK for his support and his useful comments throughout this work.

I also would like to thank other Photonic Devices Modelling group members, at City University Dr. S. Salah Obayya, Dr Fathi Abdelmalek, Ms Niranthi Somasiri, for their help and the friendly, joyful atmosphere surrounding me in the course of this work.

I would like to take this opportunity to thank the staff of School of Engineering and Mathematical Science at City University for their assistance.

Finally, my deepest gratitude is devoted to my father, mother, niece, children, wife, brothers and sisters. It is only their loves, encouragements and patience that my research is made possible.

Declaration

I grant power of discretion to the University Library to allow this thesis to be copied in whole or in part without further reference to the author. This permission covers only single copies made for study purposes, subject to normal conditions of the acknowledgements.

Abstract

Ultra-high-speed optical modulators are amongst the most promising and useful components in optical communications systems. External ultra-high-speed optical modulators of multi-gigahertz bandwidth with a high optical power handling capacity are key components in current optical communications systems and valuable for future optical signal processing technology. In recent years, optical fiber communication networks have been experiencing a very rapid development, driven by the explosive growth of internet technology, mobile phones, video phones, video conferencing, video-on-demand, and e-commerce. Therefore, it is essential to create advanced tools to design new ultra-high-speed optical modulators which fulfill the requirements of such high capacity transmission systems.

The recent advances in lightwave technology indicate a crucial need for the accurate design, characterization and optimization of modern optoelectronic devices such as electrooptical modulators, using rigorous and efficient computational modeling methods. The finite element method is the most versatile and popular numerical approach for the solution of various engineering problems. The vector H -field finite element method provides the most accurate and efficient computational numerical technique for the analysis of different uniform optical waveguide problems involving isotropic, anisotropic, and nonlinear waveguide materials.

A numerical approach using quasi-TEM analysis based on the efficient finite element method is developed to investigate the microwave properties of the electrooptic modulators, LiNbO₃ and GaAs, respectively. The combination of the vector H -field finite element method and the Least Square Boundary Residual (LSBR) has been employed successfully to investigate the polarization conversion phenomenon in a

deeply-etched GaAs/AlGaAs semiconductor electrooptic modulator has been investigated and physically justified.

The potential distribution, capacitance calculation, electric and magnetic field distribution, microwave index, characteristic impedance, optical field confinement, conductor loss and the dielectric loss for different regions of the substrate, half-wave voltage length, bandwidth, driving power and optical loss are investigated thoroughly. Simultaneous matching between the microwave effective index and the optical and the characteristic impedance are achieved. The work shows for the first time, that conductor loss, dielectric loss and the mismatch between optical and microwave carrier and characteristic impedance for both LN and GaAs electrooptic modulators operating beyond 40 GHz, will play a significant role in the determination of the overall speed of these modulators.

The effect of various imperfect fabrication parameters of GaAs electrooptic modulators has been thoroughly investigated. It is confirmed that the use of full vectorial simulation techniques such as the FEM (Finite Element Method) and LSBR (Least-Square Boundary Residual) are very important in order to account for, and to avoid problems arising as a result of such unexpected and also unwanted polarization conversion effects in electrooptic semiconductor modulators. It has been confirmed for the first time that for the new semiconductor electrooptic modulator designs and fabrication methods, it is essential to take in account these parameters in order to avoid unwanted polarization conversion, which can negatively impact the performance of the device.

Symbols and Abbreviations

FEM- Finite Element Method	α_d - Dielectric Loss
TEM- Transverse Electromagnetic Mode	E - Electric Field
TE- Transverse Electric	B - Magnetic Flux Density
TM- Transverse Magnetic	H - Magnetic Field Intensity
CPW- Coplanar Waveguide	J - Current Density
CPS- Coplanar Strip	D - Electric Flux Density
ACPS- Asymmetric Coplanar Strip	ρ - Electric Charge Density
CMM- Conformal Mapping Method	μ - Permeability
VMFD- Vectorial Method in Fourier Transformed Domain	ϵ - Permittivity
SIM- Spectral Index Method	α_C - Conductor Loss
MM- Marcatili Method	P_0 - Total Power
EIM- Effective Index Method	C – Capacitance
FDM- Finite Difference Method	C_0 . Free Space Capacitance
FFT- Fast Fourier Transform	μ_d - Velocity Mismatch Factor
MMM- Mode Matching Method	λ - Wavelength
BPM- Beam Propagation Mode	c - Velocity of Light
MQW- Multiple Quantum Well	k - Wave number
ENM- Equivalent Network Method	L_c - Coupling length
ECR- Electron Cyclotron Resonance	β - Propagation Constant
EO- Electro Optic	n - Refractive Index
ER- Extinction Ratio	P - Electric Polarization
OEIC- Optoelectronic Integrated Circuits	M - Magnetic Polarization
LSBR- Least Square Boundary Residual Conductor	χ - Susceptibility
VFEM- Vectorial Finite Element Method	R_S - Surface Resistance of the
BW- Bandwidth	N_m – Microwave Effective Index
APE- Annealed Proton Exchanges	$V_{\pi}L$ - Half-Wave Length Product
	T (%) - Transmission of Light
	ϕ - Potential

Symbols and Abbreviations

CVD- Chemical Vapour Deposition	P_{in} - Driving Power
MZI- Mach-Zender-Interferometric	Δn - Refractive Index Change
DC- Directional Coupler	L_{π} - Beat Length
IMDD- Intensity Modulation Direct Detection	τ - Transmissions Coefficient
TDM- Time Division Multiplexing	X_I - Aluminium Concentration
WDM- Wavelength Division Multiplexing	P_d - Time-averaged Power
PANDA- Polarization-Maintaining Fiber	r_{ij} - Electrooptic Coefficient
KDP- KH_2PO_4 Ferroelectric Crystal	$d_{x,y}$ - Diffusion Length
ADP- $NH_4H_2PO_4$ Antiferroelectric Crystal	$C(x, y)$ - Titanium Concentration
KTP- Potassium Titanyl Phosphate Crystal	$D_{x,y}$ - Diffusion Coefficient
PMMA- Polymethylmethacrylate (Polymer organic Modulator)	σ - Conductivity
TAT-8 Trans-Atlantic	η - Intrinsic Impedance of Medium
FEBPM- Finite Element Beam Propagation Method	BEM- Boundary Element Method
MOL- Method of Lines	MBE- Molecular Beam Epitaxy
PMM- Point Matching Method	MOVPE- Metallorganic Vapour Phase Epitaxy

Introduction

1.1 Historical introduction of lightwave technology

Lightwave technology is not a new science as the use of a visible carrier wave or light for communications has been common for many years. In the 1790s the French engineer Claude Chappe invented the optical telegraph. In the military environment sunlight powered devices (optical telegraph) had been used to send telegraph information from mountain top to mountain top in the early 1800. Later, in 1880 Alexander Graham Bell reported the transmission of speech using a light beam in the so-called “photophone”. The photophone proposed by Bell, after four years of innovation involved a telephone modulating sunlight with a diaphragm giving speech transmission over a distance of 200 m. Although, some further innovation in optical communications continued in to the early part of the 20th century, however its use was limited to mobile, low capacity communications links. This was due to both the lack of suitable light sources and the fact that light transmission in the atmosphere is restricted to line of sight affected by disturbances such as, dust, rain, fog, snow and other atmospheric turbulence. Nevertheless, lower frequency and hence longer wavelengths of electromagnetic waves such as radio and microwave proved to suitable carriers for information in the atmosphere, being far less affected by much atmospheric conditions. The electromagnetic carrier waves can be transmitted over considerable distance but are limited in the amount of information they can convey at these frequencies. The information-carrier capacity is directly related to the *bandwidth* (band or of the range of frequencies within the spectrum occupied by a signal and used by the signal for conveying information) or frequency extent of the modulated carrier, which is generally limited to a fixed fraction of the carrier frequency. The greater the carrier frequency, the larger the available transmission bandwidth and thus the information-carrying capacity of the communications systems. This is one of the reasons why the radio communication was developed to higher frequencies much as the VHF and UHF bands, leading to the introduction of the even higher frequencies microwave and, latterly,

millimeter wave transmission. The relative frequencies and wavelengths of the electromagnetic waves that may be used are illustrated in Table 1.1 (Ishii, 1986). It can be noted that communications at optical frequencies offer an increase in the potential usable bandwidth by a factor of around 10^4 over high frequency microwave transmission. An additional benefit of the use of a high carrier frequency is the ability of the communication systems to concentrate the available power within the transmitted electromagnetic wave, thus giving an improved system performance.

Electromagnetic	Frequency ν	Wavelength λ
Long Wave	30-300kHz	10km-1km
Medium waves	300-3000kHz	1000m-100m
Short waves	3-300MHz	100m-10m
Ultra short waves (meter waves)	30-300MHz	10m-1m
Microwave (centimeter wave)	300-30000MHz	100cm-1 cm
Ultra microwave (millimeter waves) (submillimeter waves)	30-3000GHz	10mm-0.1mm
Infrared rays (Optical fiber communications)	3000-416000GHz 10^5 - 10^6 GHz	0.1mm-0.00072mm 1.7 μm-0.8μm
Red-Violet (Visible spectrum)	10^5 - 10^6 GHz	0.7μm-0.4μm
Ultraviolet	10^5 - 10^7 GHz	3 μm-30nm
X-rays	10^7 - 10^{11} GHz	30nm-3pm
Gamma rays	10^9-10^{13}GHz	0.3nm-0.3pm
Cosmic rays	10^{13}GHz-continue	0.3pm- and bellow

Table 1.1 The electromagnetic spectrum

A renewed interest in optical communication was stimulated in the early 1960s with the invention of laser. This device has provided a powerful coherent light source with the possibility of light modulation at high frequency. There has also been interest in optical communications between satellites in outer space using similar techniques with lasers.

The use of the laser for the free space optical communication occurs over a limited range: however the invention of the laser has enabled a significant research effort to be developed in the study of optical components needed to achieve reliable information transfer using light as a carrier. In the early 1960s Kao and Hockham (Kao and Hockham, 1966) proposed an optical communication system using dielectric waveguides or optical fibers fabricated from glass. Later, (1966), Werts has considered ways to avoid the degradation of the optical signal. Initially the optical fibers that were available exhibited very high attenuation (i.e. 1000 dB km^{-1}) and this were not comparable in performance with the coaxial cables (i.e. showing $5\text{-}10 \text{ dB km}^{-1}$ loss). Nevertheless, within ten years optical fiber losses were reduced below 5 dB km^{-1} and suitable loss jointing techniques were perfected. Corning, UK achieved a reduction to 20 dB/cm recently.

The development of the fiber waveguides has played a significant role in the development of other optical components which would constitute an optical fiber communication system. Based on the optical operating frequency, this new technology of optical component has used extremely small wavelengths. Thus semiconductor optical sources (i.e. injection lasers and light emitting diodes), as well as matched detectors (i.e. photodiodes and transistors) compatible in size with optical fibers were designed and fabricated to enable successful implementation of the optical fiber communication systems proposed. Which were originally fabricated in 1977 from alloys of gallium arsenide (AlGaAs) which emitted in the near infrared between 0.8 and $0.9 \mu\text{m}$. More recently, suitable semiconductor laser sources such as these in InGaAsP and Ge detectors for the $1.3 \mu\text{m}$ wavelength have been developed. In 1980 Bell Labs published a commitment to using single mode $1.3 \mu\text{m}$ technology and for the first time a transatlantic fiber-optic cable, TAT-8 began service in December 1988. This technology has spread into wider telecommunication applications, and remains the standard for the most fiber communications systems.

1.2 Optical communication systems

Progress in optical communications has been very rapid over the last three decades. Research sponsored by telecommunication authorities soon led to breakthroughs in telecommunication systems, so that now optical systems are carrying almost all proportion of the short haul telecommunication traffic. In many developed countries, UK, USA, Germany and Japan, optical fibre is the dominant transmission medium for the long distance network. In the United Kingdom in 1984, 64% of the traffic was on optical fibres, with 13% on microwave radio and 23% on coaxial or pair cable, compare to 1995, where 90% of the traffic is over the optical network.

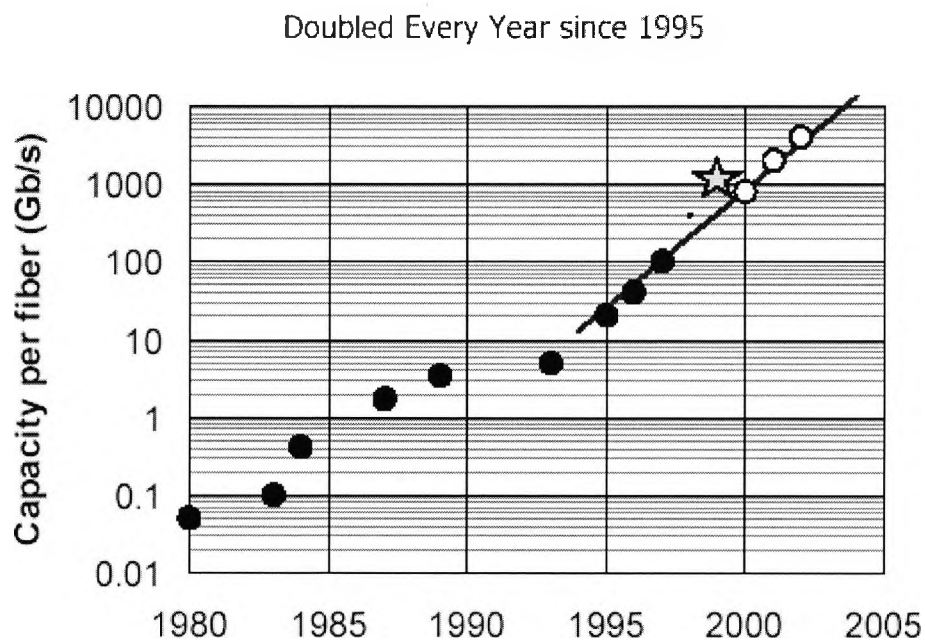


Fig. 1.1 Capacity per fiber (Gb/s) from 1980-2005. (Livescu, 2002)

The world market for optical communications systems and components is currently estimated to be about \$40 billion. This is forecast to grow at over 10% a year over the next five years, driven by the rapid increase in data traffic arising from internet company intranets and telecommunications generally, as illustrated in the Table.1.1. Also last 3-4 years this increase has not developed as was predicted in the late 1990s, it is expected

that the market will grow again, although the pace is likely to slow. The optimism for this growth remains the fundamental benefits of optical fibre communications:

- ◆ The system offers vastly increased carrying capacity, more than one thousand times greater than comparable copper wire
- ◆ Optical signals are unaffected by electromagnetic interference, no crosstalk between fibres, meaning communication is clearer and can be used in hostile environments
- ◆ Optical fibres do not radiate electromagnetic energy, so do not interfere with radio and television broadcast signals
- ◆ Low attenuation, low cost and high bandwidth.
- ◆ Waveguides can be integrated with other components
- ◆ High capacity data storage
- ◆ The costs of an optical system are partly controlled by the sources, detectors, and couplers at the end of the transmission lines.

One of the important recent innovations is the dense wavelength division multiplexing (DWDM), a technique by which a large number of different 'colours' of light signals are simultaneously transmitted. This has the effect of increasing the capacity of the fibre to carry information. Dense Wavelength Division Multiplexing (DWDM) system data speeds have risen to 40 Gbit/s and beyond. The developments through recent years of (DWDM) system capacity in optical networks is illustrated in Fig.1.2

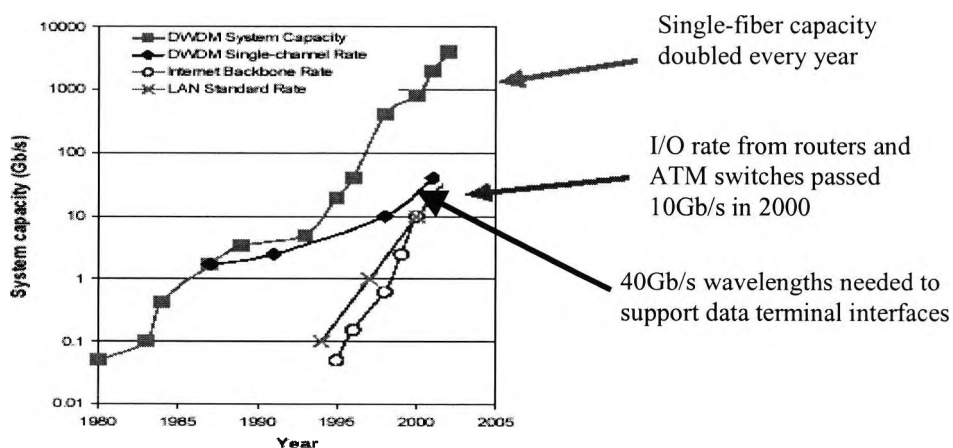


Fig. 1.2 DWDM Capacity and Interface Speeds (Livescu, 2002).

A schematic of a simple optical communications system is shown in Fig. 1.3. The block diagram includes a repeater, although the fibre loss is so low that can be spaced many tens of kilometres apart. The repeater is actually a receiver and transmitter “back-to-back”. The amplifiers are used every 50 to 100km to boost the light signal. All the present generation of systems use power transmission and detection where a source generates a wide band of energy which is modulated by turning it on and off. Detection is by using diode detection and heterodyne, or coherent achieved (the longer the fiber length, the more severe the pulse spreading will become, therefore the photons produced by simulated emission will have a defined phase relations) detection using a local oscillator are not used. This may come in the next generation of systems.

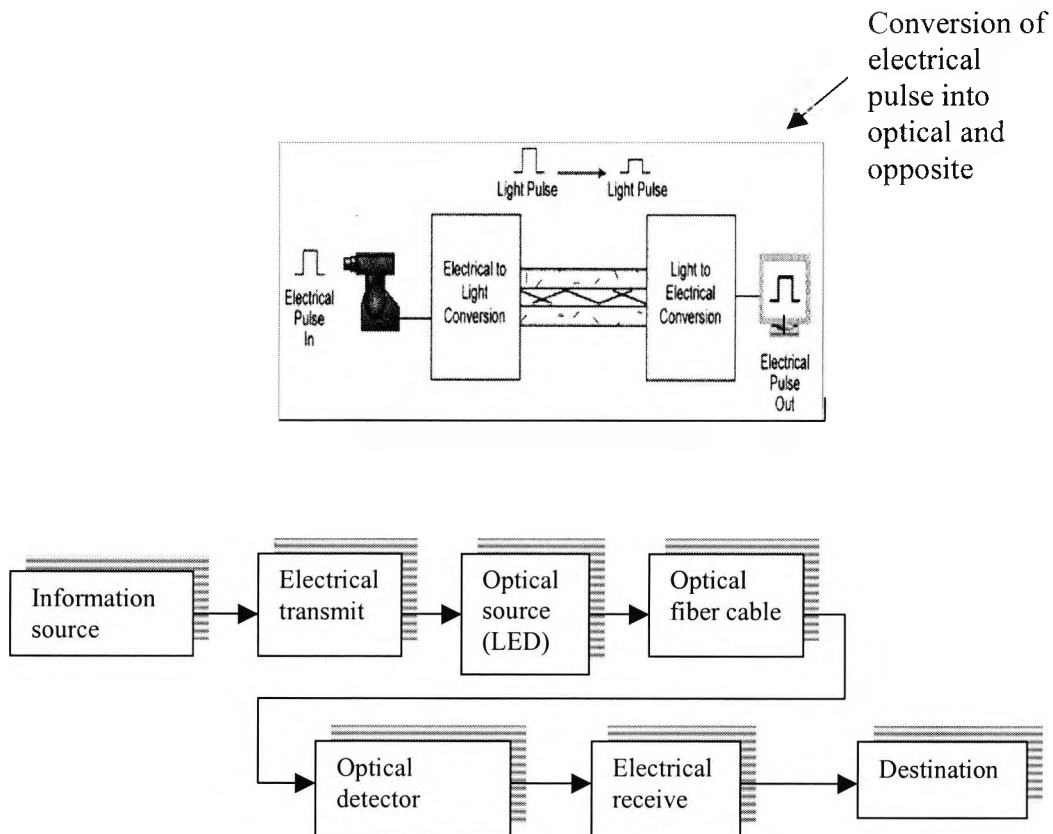


Fig. 1.3 An optical communication system.

The transmitter in such a system consists of a light source and a modulator of the base band digital or analogue signals onto the optical waves. The light source will be either

an LED for a low cost, low capacity, system or a semiconductor laser for a higher capacity system. The modulation is often done by modulating the signal through the current feeding the LED or the laser. The alternative is to use an optical modulator, and this can be done in many ways using integrated optics. One method is based on using a directional coupler or a Mach-Zehnder section in LiNbO_3 using the electro-optic effect or in a GaAs or InP based system.

In an LED the generation of photons occurs via a spontaneous process whereas in the lasers stimulated emission dominates. An LED is a relatively broadband source, with a bandwidth of typically 20 THz (centre frequency about 450 THz) and the injection laser is much narrower with a bandwidth between a few GHz and 500 GHz. Lasers using feedback and cavities to stabilise the signal may have bandwidths of a few MHz.

The connection between the source, receiver and the optical fibre is a significant part of an optical system because of the need to align the fibre core to a high precision over the very small distances involved in alignment. Misalignment gives rise to coupling losses and can only be overcome by using a very accurate system geometry to enable systems to be analysed accurately. An optical fibre connector must terminate and protect the end of the fibre, act as an alignment guide and protect the cable from the environment.

New technology and systems are still being developed for ultra high-speed long-haul systems operating at channel bit rates in excess of 40 Gbit/s with an aggregate throughputs in excess of around 1 Tb/s. Fibre optic communication system technology offers greater efficiency in vital growth areas such as to meet the rising demands for wireless data transfer, networking, graphics, communications using the internet World Wide Web, sensors and the possibility of improvements in fields from medicine to civil engineering and aerospace that would not be possible otherwise.

1.3 Integrated Optics and Photonic Devices

Optical systems in communications provides the inherent advantage of large bandwidth, parallelism, and reconfigurable configuration. However, such systems do not provide input-output isolation, as electronic devices do and it can be very difficult to focus multiple beams in a parallel system. Therefore it is logical to *couple* electronic and photonic devices, resulting in optoelectronic integration.

The aim of integrated optics is to do signal processing as much as possible directly on the optical chip itself. The basic concept of the integration was proposed by Anderson in 1965 (Anderson, 1965) and considerable progress has been made, although not a great deal of integration has been achieved.

An attractive form of define integration is the interconnection of the optical devices which can take a form of free space, integrated optical waveguides, or optical fiber. An illustration via a simple schematic block diagram of an optoelectronic phase integration array antenna system is illustrated in the Fig. 1.4. With optical interconnects and transmission, immunity to manual interference and crosstalk and freedom from capacitive loading effects. The large bandwidth of the optical device contributes to system size reduction, reduced system power, and increased fanout capabilities of the device.

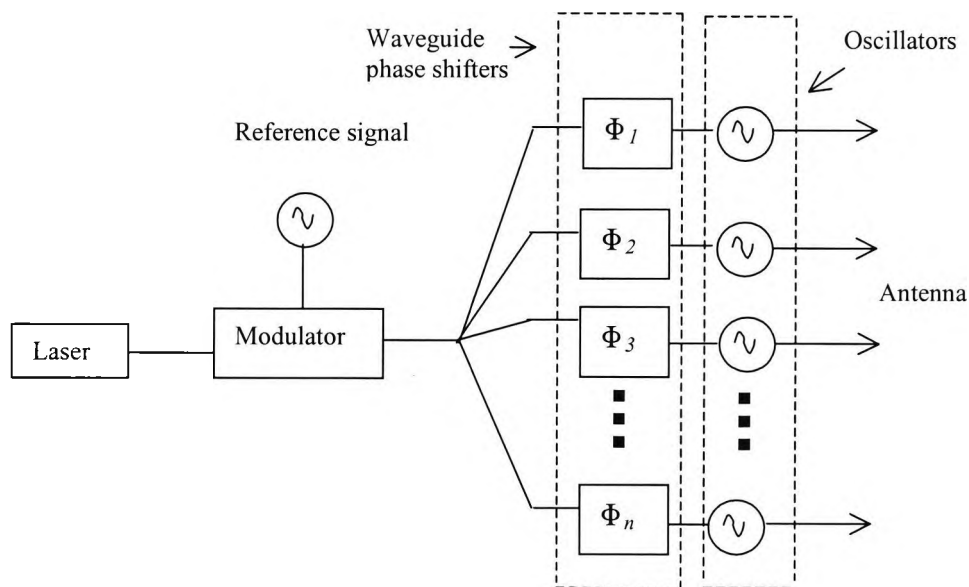


Fig. 1.4 Block diagram of an optoelectronic phase array antenna system

Optoelectronic integrated circuits (OEIC) involve the integration of electronic and optic components and optical interconnects. The monolithic integration of electronic and optical devices on the same chip will contribute to high-speed, high-sensitivity,

compactness, reliability and low cost. In order to achieve an integration of these devices, first the optical devices which may have different layer structures must be very high quality and secondly there is a major issue of compability and impedance matching between the devices and, last but not least, the cost in designing and realization of OEIC is a relevant factor.

There are two major ways of integration in OEIC hybrid integration and monolithic. Hybrid integration involves the connection of discrete devices, blocks or chips using electronic (leads) or optic (fibre) interconnects. Alternatively monolithic integration involves the building of all the active and passive components on the same chip, which makes this type of integration a real challenge, because of heterostructures (some components are made of different materials, layers).

Practical integrated optics also can be classified as active and passive. Passive components are used for transmission, splitting, beam splitting, polarization converters, polarization controllers, switches, and wavelength division multiplexer. Active components are usually (electronically controlled) and have both optical and electrical properties, such as lasers, detectors, modulators (LiNbO_3), transceivers, and amplifiers. Modulators can be also directly integrated with the laser, like GaAs or as an external modulator, like in LiNbO_3 .

The two most common semiconductor materials used in optoelectronics are based on the ternary alloy gallium aluminium arsenide (GaAlAs) and the quaternary alloy indium gallium arsenide phosphate (InGaAsP). The variation of the alloy content between the layers then yields the refractive index difference necessary for a waveguide. Although several types of devices of the kind that will undoubtedly be needed have been successfully demonstrated, they require a wide range of different substrates. These follows some discussion of possible structure for these devices.

1.4 Optical fiber waveguides

Light transmission via a dielectric waveguide structure was first proposed and investigated by Hondros and Derbe (Hondros and Derbe, 1910).

An optical waveguide that is uniform in the direction of propagation is considered the most basic type of waveguide. In order to understand the basic principal of photonic

devices of this type it is important to utilize the ray theory model to take account of the refractive index of the dielectric medium.

Light as an electromagnetic wave is characterized by a combination of time varying electric (\mathbf{E}) and magnetic (\mathbf{H}) fields propagating through space (c speed of light) obtained from the Maxwell equations, known as the *wave equation*, which satisfies the partial equation:

$$\nabla^2(\mathbf{E}, \mathbf{H}) = \frac{1}{c^2} \frac{\partial^2}{\partial t^2}(\mathbf{E}, \mathbf{H}) \quad (1.1)$$

The frequency of oscillation of these fields and their wavelength in vacuum is given as:

$$c = v\lambda = \frac{1}{\sqrt{\epsilon\mu}} \quad (1.2)$$

where ϵ and μ are the permittivity and the permeability, respectively, and λ is the wavelength of the electromagnetic wave

In any other media the speed of propagation is given by:

$$v = \frac{c}{n} = v\lambda \quad (1.3)$$

where v is the frequency, and n is the refraction index of the medium given as:

$$n = \sqrt{\mu_r \epsilon_r} \quad (1.4)$$

where μ_r and ϵ_r are relative permeability and relative permittivity of the medium, respectively.

The simplest waves are in sinusoidal form and can be expressed as:

$$\mathbf{E}(z, t) = \mathbf{E}_0 \cos(\omega t - kz + \phi) \quad (1.5)$$

where E_0 is the amplitude of the wave illustrated in Fig. 1.5 (b), ω is the angular frequency ($\omega = 2\pi\nu$), k is the wavenumber ($k = 2\pi/\lambda$), ϕ is the phase constant, whereas the term $(\omega t - kz + \phi)$ is the phase of the wave described by equation (1.5). As time elapses in plane waves the wavefronts (constant phase or wavesurfaces) propagate through space with a velocity given as:

$$\nu = \frac{\omega}{k} = \nu\lambda \quad (1.6)$$

The electric and magnetic vectors vibrate in orthogonal planes and perpendicularly to the direction of the propagation as illustrated in the Fig. 1.5 (a). This explains the nature of the light, consisting of the combination of the electric wave vector and the magnetic wave vector.

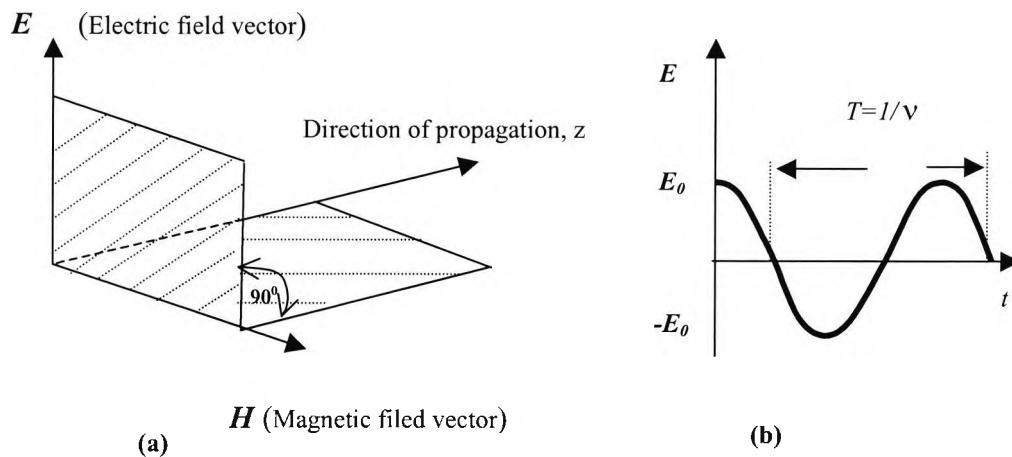


Fig 1.5 Direction of light propagation perpendicular to the electromagnetic waves (a), and (b) electric field of an electromagnetic wave as function of the time t .

Equation (1.5) represents a plane wave propagating along z axis, and if this equation is modified for a general wave propagating in an arbitrary direction, including the plane wave, then this equation becomes:

$$E(x, y, z, t) = E_0 \cos(\omega t - \mathbf{k} \cdot \mathbf{r} + \phi) \quad (1.7)$$

This wave equation is characterized by the wavevector \mathbf{k} where $|\mathbf{k}| = \frac{2\pi}{\lambda}$ and \mathbf{r} is the vector origin of the point (x, y, z) . These vectors, \mathbf{k} and \mathbf{r} can be expressed as:

$$\mathbf{k} \cdot \mathbf{r} = (ik_x + jk_y) \cdot (ix + jy) = xk_x + yk_y = xk \cos \theta + yk \sin \theta \quad (1.8)$$

Hence we can write equation (1.7) in this form:

$$E(x, y, t) = E_0 \cos(\omega t - xk \cos \theta - yk \sin \theta + \phi) \quad (1.9)$$

The general form of the wave (nature of the light) propagation equation is illustrated schematically in Fig. 1.6.

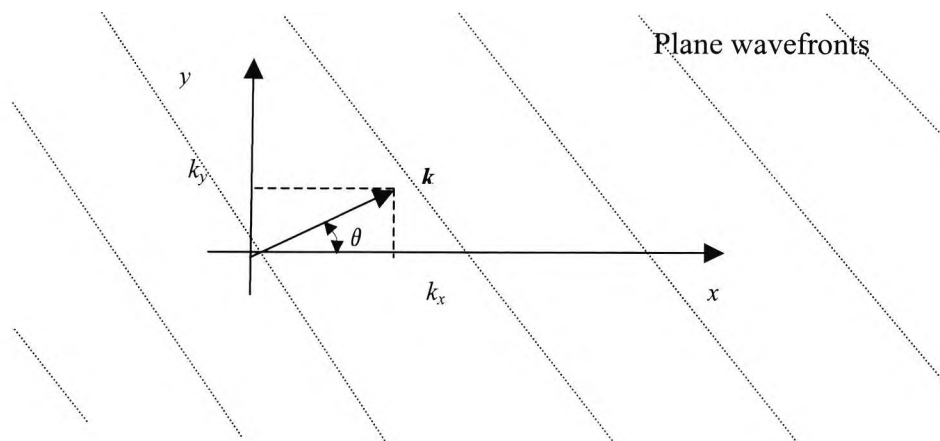


Fig. 1.6 Plane wave with its propagation vector \mathbf{k} in the (x, y) plane.

The refractive index of a medium (dielectric) is defined above in equation(1.4). When a ray is incident on the interface between two dielectrics of different refractive indices refraction occurs, as is illustrated in Fig. 1.7. The angles of incidence ϕ_1 and refraction

ϕ_2 are related to each other and to the refractive indices n_1 and n_2 of the dielectrics by Snell's law of refraction (Born, 1980), given as:

$$n_1 \sin \phi_1 = n_2 \sin \phi_2 \quad \text{or} \quad \frac{\sin \phi_1}{\sin \phi_2} = \frac{n_2}{n_1} \quad (1.10)$$

It can be noted from the Fig. 1.7 (a) that a small amount of light is reflected back into the dielectric (internal reflection) and some light is transmitted. In the case when the refraction angle ϕ_2 is 90° , the angle of incidence is known as the critical angle ϕ_c .

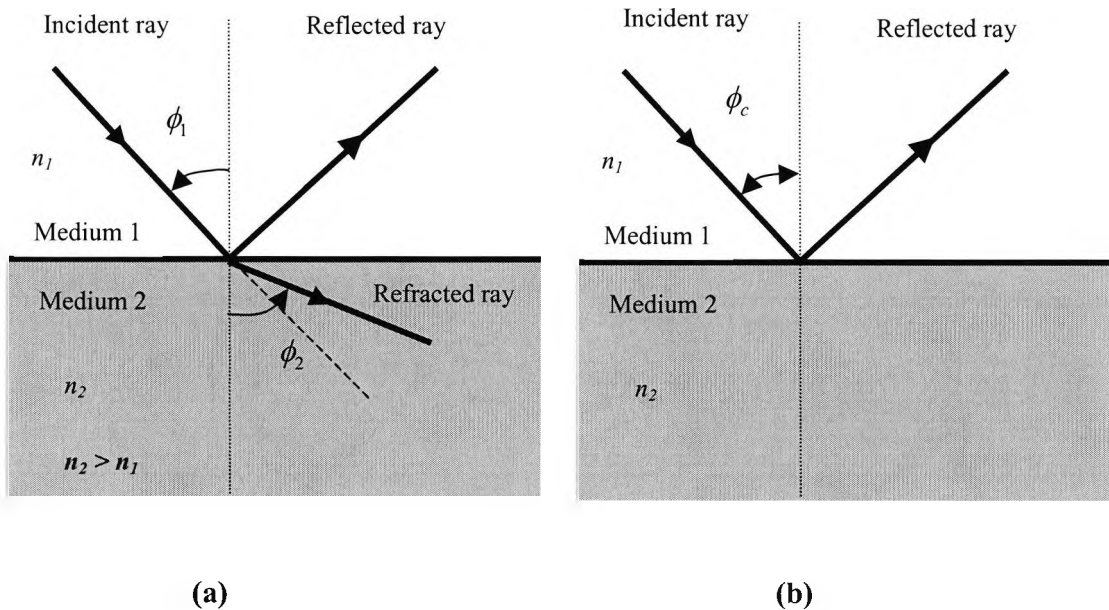


Fig. 1.7 Reflection and transmission, Snell's law (a) and total internal reflected ray (b).

The critical angle is given as:

$$\sin \phi_c = \frac{n_2}{n_1} \quad (1.11)$$

The critical angle (acceptance angle) is very important in light propagation through the optical fiber. Having considered the propagation in an optical fiber through total internal

reflection at the core-cladding interface, it is useful to take into account the light ray entering the fiber.

The principle of the total internal reflection as it elementary for the understanding of a optical light beam penetrating a second medium will slow down and change its direction at the interface between the two media. Hence, the so-called refracted beam bends towards the normal. It is this basic principle, where two different media with slightly different refractive indices are necessary to create the conditions for an optical waveguide. The more dense medium will form the core and the other medium will be the cladding of the optical waveguide. Any discontinuity or imperfections at the core-cladding interface would result in refraction rather than total internal reflection, with the subsequent loss of the light into the cladding, as illustrated in Fig. 1.8.

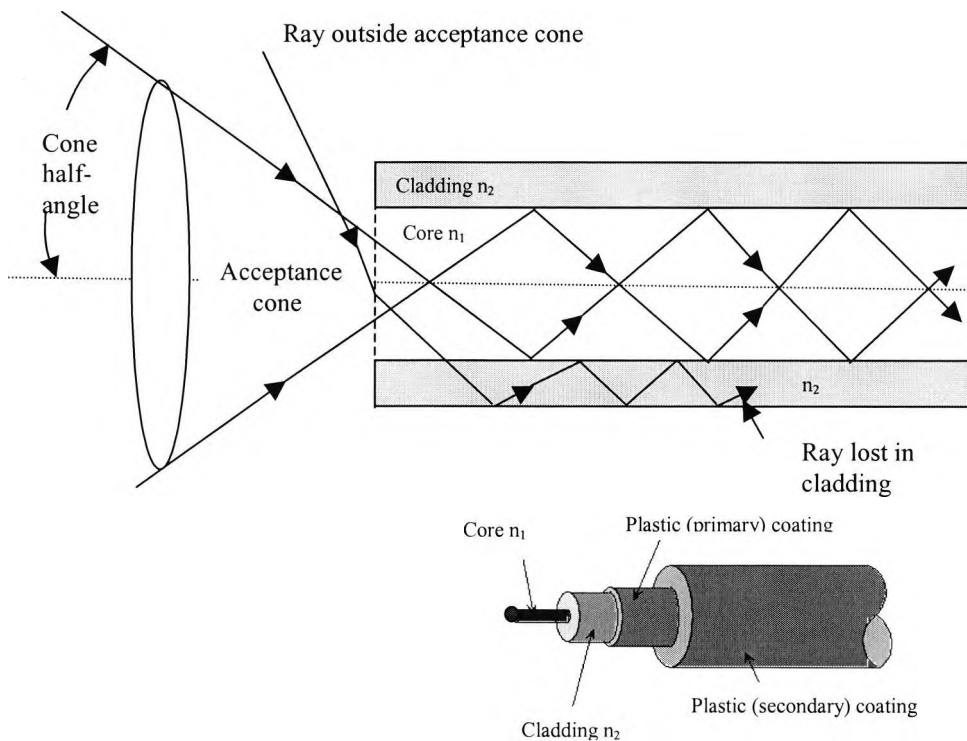


Fig. 1.8 Schematic diagram of an optical fiber and the acceptance angle, when launching light in an optical fiber.

The optical fiber considered in this section has a core of constant refractive index and cladding of slightly lower index known as step index fiber, which can be multi-mode (allow more than one mode to propagate). A schematic of step index fiber is shown in

Fig. 1.8 and single mode step index fiber can be controlled. On the other hand, when the refractive index of the core is not constant, but shows a decreasing core index $n(r)$ with the radial distance from the maximum value at the axis to a constant value n_2 beyond the core radius a in the cladding graded index fibre may be made. Also, this type of fiber can be multi-mode graded index (showing substantial bandwidth improvement) or single-mode graded index fiber, (Dean P. J. 1985).

1.5 Planar optical waveguides

Planar optical waveguides are the key devices used to construct integrated optical circuits. In most applications of optoelectronics, the optical beams are confined laterally to a finite region of space. Special optical elements are used to confine and then allow the propagation of such optical modes. An important structure used in optical systems is the layered structure or waveguide structure. As the name *waveguide* implies, these structures are used to confine the optical waves in a well-defined region and to guide their propagation. The layered structure can be made from both non-crystalline or crystalline materials. The mechanism of optical confinement in symmetrical planar waveguides is discussed above (under the optical fiber section), prior to an investigation of circular structures. The simplest waveguide is the slab waveguide shown in the Fig. 1.9. Generally, rectangular waveguides consist of a square or rectangular core surrounded by a cladding with a lower refractive index than that of the core.

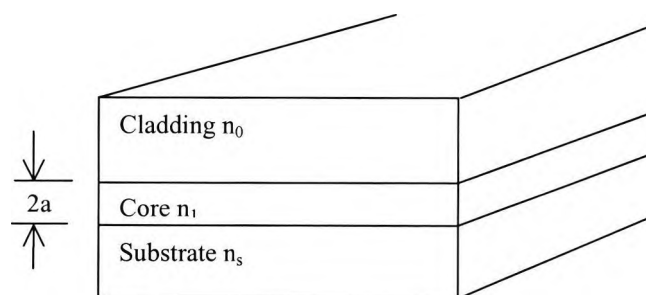


Fig. 1.9 Slab Optical waveguide.

In the slab waveguide as illustrated in the Fig. 1.9, electromagnetic fields E and H do not have y -axis dependency (i.e. $\partial/\partial y = 0$). Based on Maxwell's equation and the wave equations, assuming a lossless medium with a scalar dielectric constant $\epsilon = \epsilon_0 n^2$ and magnetic permeability μ , the electromagnetic fields are:

$$\nabla \times \mathbf{E} = -\mu_0 \frac{\partial \mathbf{H}}{\partial t} \quad \text{and} \quad \nabla \times \mathbf{H} = \epsilon_0 n^2 \frac{\partial \mathbf{E}}{\partial t} \quad (1.12)$$

For the planar-wave propagation the wave equations have the form:

$$\mathbf{E} = \mathbf{E}(x, y) e^{j(\omega t - \beta z)} \quad (1.13)$$

$$\mathbf{H} = \mathbf{H}(x, y) e^{j(\omega t - \beta z)} \quad (1.14)$$

After derivation with $\partial \mathbf{E} / \partial y = 0$ and $\partial \mathbf{H} / \partial y = 0$, two independent electromagnetic modes are obtained, which are denoted as the TE mode and the TM mode, respectively. A planar waveguide supports transverse electric (TE) modes with zero longitudinal electric field ($E_z = 0$) and the transverse magnetic modes (TM) with zero longitudinal magnetic field ($H_z = 0$). The slab waveguide is considered to have a uniform refractive profile in the core as illustrated in Fig. 1.10 (a). Also, it can be shown that only certain values of β can satisfy it, so this guide will also only support a discrete set of guided modes, Fig. 1.10 (b). Considering the fact also that the guided electromagnetic fields are confined in the core and exponentially decay in the cladding, the field distribution may be expressed as (Okamoto, 2000).

For TE-modes $E_x = E_z = H_y = 0$

$$E_y = \begin{cases} A \cos(\kappa a - \phi) e^{-\sigma(x-a)} & (x > a) \\ A \cos(\kappa x - \phi) & (-a \leq x \leq a) \\ A \cos(\kappa a + \phi) e^{\xi(x+a)} & (x < -a) \end{cases} \quad (1.15)$$

For TM-modes $E_y = H_x = H_z = 0$

$$H_y = \begin{cases} A \cos(\kappa a - \phi) e^{-\sigma(x-a)} & (x > a) \\ A \cos(\kappa x - \phi) & (-a \leq x \leq a) \\ A \cos(\kappa a + \phi) e^{\xi(x+a)} & (x < -a) \end{cases} \quad (1.16)$$

The electromagnetic field components are continuous at the boundaries of core-cladding interface ($x = \pm a$), where the wavenumbers in core (n_1) and cladding (n_0 and n_s) region are given as:

$$\begin{cases} \kappa = \sqrt{k^2 n_1^2 - \beta^2} \\ \sigma = \sqrt{\beta^2 - k^2 n_0^2} \\ \xi = \sqrt{\beta^2 - k^2 n_s^2} \end{cases} \quad (1.17)$$

$$k = \omega \sqrt{\epsilon \mu} = \frac{\omega}{\lambda} \quad (1.18)$$

After eliminating the constant A , the eigenvalue equation for the \mathbf{TE}_m mode is obtained:

$$\tan(u + \phi) = \frac{w}{u} \quad (1.19)$$

$$\tan(u - \phi) = \frac{w^*}{u} \quad (1.20)$$

where

$$\begin{cases} u = \kappa a \\ w = \xi a \\ w^* = \sigma a \end{cases} \quad (1.21)$$

The eigenvalue equation can be obtained as:

$$u = \frac{m\pi}{2} + \frac{1}{2} \tan^{-1}\left(\frac{w}{u}\right) + \frac{1}{2} \tan^{-1}\left(\frac{w^*}{u}\right) \quad (m = 0, 1, 2, 3, \dots) \quad (1.22)$$

$$\phi = \frac{m\pi}{2} + \frac{1}{2} \tan^{-1}\left(\frac{w}{u}\right) - \frac{1}{2} \tan^{-1}\left(\frac{w^*}{u}\right) \quad (1.23)$$

$$v^2 \equiv w^2 + u^2 = k^2 a^2 (n_1^2 - n_s^2) \quad (1.24)$$

$$\gamma = \frac{n_s^2 - n_0^2}{n_1^2 - n_s^2} \quad (1.25)$$

When the wavelength of the light signal and the geometrical parameters are determined, in other words, the normalized frequency v and the asymmetric parameter γ then the propagation constant can be easily determined from the above equations. In order for the transverse wave number to be real for the core region, the following condition should be satisfied:

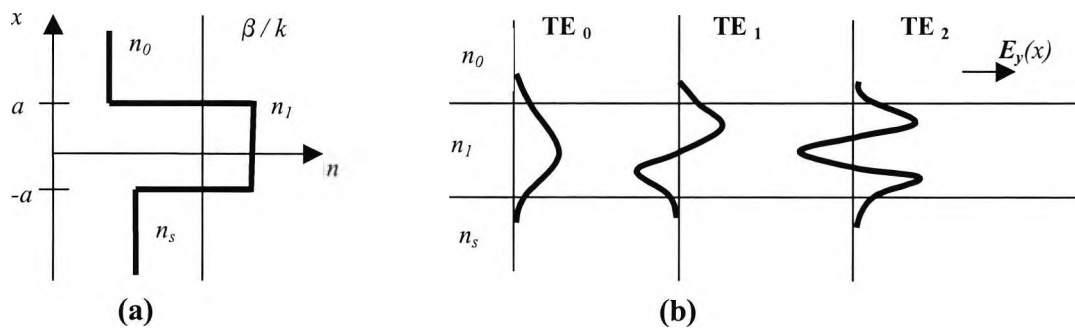


Fig. 1.10 Refractive index profile of the slab waveguide (a) and Field distribution for TE_m modes, where $m = 0, 1, 2, \dots$ (First and higher order modes) (b).

$$n_s \leq \frac{\beta}{k} \leq n_1 \quad (1.26)$$

where β/k is the refractive index itself for the plane wave

The effective index may be expressed as:

$$n_e = \frac{\beta}{k} \quad (1.27)$$

When $n_e < n_s$ the electromagnetic field in the cladding region is oscillatory along the transverse direction, this dissipation of the field is called the *radiation mode* (non-guided mode). This critical condition where the field is cut off and becomes a *radiation mode* is called the “cutoff condition” and is expressed by:

$$\beta = kn_s \text{ and } b = 0 \quad (1.28)$$

The condition for the guided mode is

$$0 \leq b \leq 1 \quad (1.29)$$

where, b is termed the *normalized propagation* constant and it can be expressed as:

$$b = \frac{n_e^2 - n_s^2}{n_1^2 - n_s^2} \quad (1.30)$$

The eigenvalue equation can be rewritten by using the normalized frequency and the normalized propagation constant as:

$$\begin{cases} u = v\sqrt{1-b} \\ w = v\sqrt{b} \\ w^* = v\sqrt{b+\gamma} \end{cases} \quad (1.31)$$

When the waveguide is symmetric with $n_0 = n_s$, $\gamma = 0$ and the dispersion equations (1.22) and (1.23) will be reduced to:

$$u = \frac{m\pi}{2} + \tan^{-1}\left(\frac{w}{u}\right) \quad (1.32)$$

$$\phi = \frac{m\pi}{2} \quad (1.33)$$

or in general form:

$$v\sqrt{1-b} = \frac{m\pi}{2} + \tan^{-1}\sqrt{\frac{b}{1-b}} \quad (1.34)$$

Since the parameters κ and γ are all functions of the propagation constant β , the eigenvalue equation is obviously a function of β as well. However, it is a transcendental equation (which means the solution cannot be written in closed form), so the β -values must be found numerically.

There are various types of practical waveguide structures, for example with two-dimensional optical confinement, including rib waveguides, ridge waveguides, strip loaded waveguides, buried waveguides and deep etched waveguide, as illustrated in Fig. 1.11. Techniques such as ion implantation, etching, epitaxial growth and regrowth techniques are used to create a spatial variation in the material composition needed for waveguide.

Also the channel waveguide is special of interest. It may be fabricated by diffusing another chemical element or material into the bulk material to increase the refractive

index in this region slightly. This waveguide can be reached by diffusing titanium into the LiNbO_3 . The result then will be a Ti:LiNbO_3 waveguide. The core will then be represented by the Ti diffused channel, as can be seen in LiNbO_3 electrooptic modulator described later.

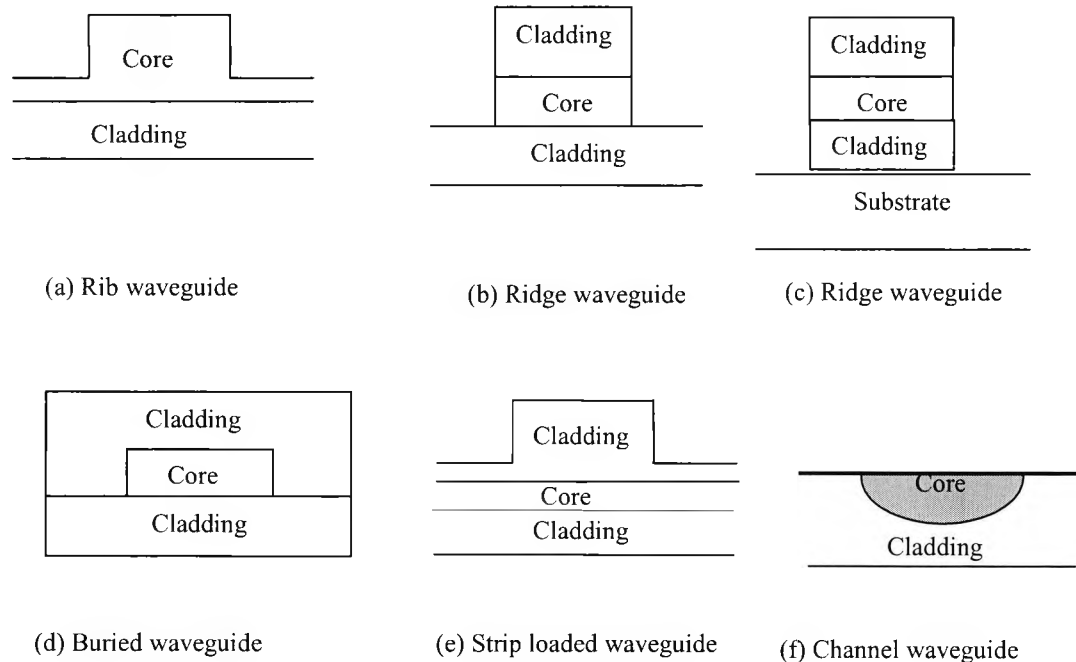


Fig. 1.11 Various types of waveguides.

In this introductory part, the nonlinearity effects of the optical waveguide devices, waveguide dispersions, leaky modes, quasimodes, bending loss, nonlinear scattering loss, and geometric non-uniformities have not been taken into consideration.

1.6 Photonic Devices (Modulators)

When two waveguides are brought sufficiently close to each other, laterally, so that their modal fields overlap, then the modes of the two fibres become coupled, and power can be transferred between two waveguides. This power transfer efficiency can be controlled by an applied modulating field for optical modulators, depending on the type of the modulator structure.

The modulator is photonic device which modulates the lightwave signals. There are three different types of light modulation: direct, internal and external modulation. The direct modulation is represented straight from the laser diode, where the injection current for the laser diode is changed by external signals. The internal modulation is applied to change the current in the cavity of solid state lasers by inserting the modulator (internal). Internal modulation is highly efficient, but it is difficult to obtain stable lightwave signals due to the relaxation oscillations of the laser associated with modulation. The structure of an internal modulator is similar to that of an external modulator.

External modulators are very popular and widely used in optoelectronics. Various types of external modulator have been described in literature. Based on the various types of materials used, electrooptic modulators can be classified as: ceramics (crystals), semiconductors and polymer electrooptic modulators. Ceramic (crystal) modulators are further classified as: LiNbO_3 , LiTaO_3 and KTP modulators. Semiconductor modulators may be categorized as: GaAs, InP and InGaAsP modulators, respectively and the polymer (organic polymer) modulators are typically PMMA modulators. Also, these modulators (ceramics, semiconductors and polymer) can be classified as: phase, amplitude and polarization modulators for the particular applications.

The major characteristics of a modulator are the bias voltage (current), the bandwidth, the insertion loss, the stability, the chirp, the distortion, the integration, the maximum power, the extinction ratio, the temperature sensitivity and the fibre device input/output. A good design of a modulator should be based on the optimization of these parameters.

Some other optical components (including modulators) that today make optical communication systems work include: III-V semiconductors (lasers, receivers), LiNbO_3 (switches...), magneto-optic materials (isolators, circulators, attenuators...), dielectric thin film (couplers, filters, WAD, interleavers...), fibre (OA, dispersion compensators, filters, interleavers, couplers...), fiber grating (WAD, gain equalizers, optical monitors, dispersion compensators...), planar waveguide (MUX, DMUX, WAD, interleavers, switches, attenuators, gain equalizers....), liquid crystal (switches, attenuators, WAD, gain equalizers...) and many other IO components.

A more detailed description, optimization and application of LiNbO₃ and semiconductor modulators based upon the finite element method, will be considered separately in the subsequent chapters.

1.7 Aims and Objectives of the thesis

The basic introduction with regard to applications in optical communications systems, involving a range of optical components provides the background to the research work undertaken in this thesis. The primary aims and objectives of this research work are to investigate and the develop alternative designs and configurations that can lead to improvement of the performance of electrooptic modulators. The major aims and objectives of this thesis can be summarized as follows:

1. Microwave properties of the LiNbO₃ Electro-Optic Modulator.

a). By applying the FEM with quasi static -TEM analysis, using scalar potential functions, to find the (capacitance C and C_0) microwave index N_m , and characteristic impedance Z_C . Also to determine the conductor losses due to imperfect conductors (metal electrode), α_C and the dielectric losses of the different dielectric layers, α_d for coplanar waveguide structures with an anisotropic LiNbO₃ substrate and a SiO₂ buffer layer thickness for unetched and etched Z-cut structures.

b). To find the 3dB optical bandwidth of a LiNbO₃ modulator for structures, both etched and unetched. The effect of the dielectric loss (for the first time) and the conductor loss on the reduction of the overall bandwidth of the device will be investigated. To create design which lead the increasing of the bandwidth of the device is a major objective of this research work.

c). To investigate the effect of the different parameters in the design and optimization of the modulator. The effect of each parameter such as buffer thickness, electrode thickness, electrode width, a gap between the electrode, and ridge depth have an important impact on the device performance, new design optimization of these parameters will lead to the improvement of the performance of the modulator.

d). To achieve the velocity and impedance matching between optical and microwave signals. Simultaneous matching of velocity and impedance between optical and microwave signals has a significant role to play in the determination of the overall speed of the modulator.

e). To find the advantage of the use of the *Z*-cut crystal orientation over the *X*-cut and *Y*-cut, by comparing data with experimental results from the different research groups around the world. To investigate the effect of etched over unetched structures.

2. To develop and accurately implement the rigorous and effective FEM based on the **H**-field variation formulation for the analysis of the optical properties of the LiNbO_3 modulator.

a). To study the effect of applying an external **E**-Field to a length of Pockels material while an optical signal is passed through it will result in an optical phase shift. The electro-optic effect is the change in the refractive index caused by an applied electric field. The Pockels effect refers to a material that changes its index of refraction linearly with the applied electric field (**E**-Field).

b). To find the key parameter for an optical modulator $V_\pi L$ half-voltage product calculated by using the FEM-based modal solution approach. Graded refractive index profiles due to diffused titanium ions have been considered for the modal simulations. An important parameter for optical modulators is the half-wave voltage (V_π); this is the applied voltage that results in an optical phase shift of π and device length L . To find the effect of etched the structure in order to reduce the half-wave voltage length $V_\pi L$.

3. Design and optimization of the deep-etched semiconductor electrooptic modulator.

a). New designs for the velocity matching of a deep-etched semiconductor electrooptic modulator are presented. Tantalum pentoxide (Ta_2O_5) coating is considered, to aim to achieve velocity matching between microwave and optical signals. The effects of the velocity mismatch, the conductor loss, the dielectric loss and the impedance mismatch are studied on the optical bandwidth of high-speed semiconductor modulator

- b).** To find the 3dB optical bandwidth of the GaAs modulator for different Ta₂O₅ coating thickness structures. The effect of the dielectric loss (for the first time) and conductor loss on the reduction of the overall bandwidth of the device will be investigated. Increasing the bandwidth of the device by varying core height, buffer layer thickness, electrode thickness is an objective of this research work.
- c).** To show that both the dielectric loss and impedance matching play a key role for velocity matched high-speed modulators with low conductor loss. To find the effects of Tantalum pentoxide thickness on the overall bandwidth and on the half-wave voltage length product, $V_{\pi}L$.
- 4.** To implement the least squares boundary residual (LSBR) method with the exploration of the accurate modal solution obtained from the finite element method for studding of unexpected polarization conversion of the deeply-etched GaAs modulator.
- a).** To calculate the power conversion between the two orthogonally polarized modes, when a pure TE or TM mode is incident from the input waveguide (with no modulating voltage), a rigorous and full vectorial approach is used to obtain the scattering coefficients.
- b).** To avoid unwanted and unexpected polarization conversion effects. Based on a powerful and versatile finite element package, the effect of various imperfect fabrication conditions on the unwanted and unexpected polarization conversions in electrooptic semiconductor modulators is, for the first time, reported and physically explained.

1.8 Structure of the thesis

The work presented in this thesis is based on research carried out by the author in the use of the finite element method, the least square boundary residual approach and using simple quasi-TEM analysis using the scalar field to design, analyse and optimize various electrooptic modulator structures. The research work presented here is devoted to the study of optical properties, microwave properties, optimization and polarization issues in the LN and GaAs electrooptic modulators.

Chapter 1 gives a brief historical overview of the lightwave technology followed by the development of the integrated optics and photonic devices and their applications to today's optical communications systems. A theoretical explanation based on the ray theory model and light as an electromagnetic wave, in particular for optical fibre waveguides and planar optical waveguides is carried out.

Chapter 2 provides a brief description of some representative and important numerical techniques useful for waveguide and millimeter-wave structures such as analytical and numerical solution techniques for optical waveguides, to achieve. In particular, Chapter 2 presents a discussion of the LSBR method and the role of the FE program in utilizing the LSBR technique.

In chapter 3 the finite element method (FEM) history and its application is presented. Variational principles in the modal solution of the microwave and optical waveguides are discussed. Various aspects of the finite element method are illustrated, including different scalar and vector formulations, boundary conditions, natural boundary conditions, shape functions, global matrices and infinite elements. The penalty term approach in order to reduce the non-physical solutions or spurious mode is also discussed in the Chapter 3.

Chapter 4 deals with most of the commonly used optical modulators, their characteristics and performance, through many years on the market. Various types of modulators are investigated in this Chapter, in particular LiNbO₃ electrooptic modulator and deeply-etched waveguide GaAs electrooptic modulators and their electrooptic effects.

Arrangements of different crystal orientation involving Z-cut and X-cut LN crystal orientations used in LiNbO₃ electrooptic modulators are examined. In Chapter 4 the optical properties, such as $V_{\pi}L$ and its relation to the driving power of both LN and GaAs modulators, are presented.

Chapter 5 presents the microwave properties of electrooptic modulators, in particular LiNbO₃ and semiconductor modulators. Analytical analysis using quasi-TEM and the FEM is presented with respect to microwave parameters calculations. The potential distribution for both structures, the electric field, the magnetic field, the capacitance calculation through the line integral, the microwave index, the characteristic impedance,

the conductor loss, the dielectric loss and the bandwidth calculation are examined also in Chapter 5.

Chapter 6 deals with unetched LiNbO₃. In particular result of simulations and fabrication procedures for the Ti-diffusion technique for obtaining low-loss waveguides and high-quality buffer layer SiO₂ thin film fabrication and electrode fabrication techniques are reported. Simulation results of potential distributions, electromagnetic fields, the microwave effective index, the characteristic impedance, the conductor loss, the dielectric loss, bandwidth calculation and the product of half-wave voltage length are also reported. The effects of various key device parameters are presented in this Chapter. The effect of conductor, loss impedance mismatch and the dielectric loss in the bandwidth determination for unetched LN electrooptic modulators are also presented in Chapter 6.

Chapter 7 is devoted to etched LN electrooptic modulators. As in Chapter 6, simulated results for all microwave and optical parameters are presented, showing the advantage of etched over unetched electrooptic modulators. The effect of the ridge height and the fabrication procedure are discussed in Chapter 7 also.

In Chapter 8 a numerical approach based on the efficient finite element method is presented to study some of the key semiconductor electrooptic modulator parameters. The effect of coating thickness of tantalum pentoxide to achieve velocity matching is reported. Simulated results are presented where the coating thickness plays an important role in increasing the optical bandwidth. The numerical simulations presented in this Chapter indicate that for GaAs modulators, velocity matching is possible by using Ta₂O₅ coating instead of slow-wave structures with segmented electrodes, to increase the optical bandwidth. The $V_{\pi}L$ product and the bandwidth are presented in Chapter 8 for a specific design requirement, by adjusting various device parameters such as the core height, width, electrode width, and the aluminium concentration of the AlGaAs buffer layer.

Chapter 9 deals with polarization conversion issues of deeply-etched GaAs electrooptic modulators. The effects of various imperfect fabrication parameters such as the slant angle, the electrode offset, the Al concentration of the buffer layer and the modulating voltage on the polarization conversion ratio, the modal hybridism, the beat length,

unexpected and also unwanted polarization conversion effects in electrooptic semiconductor modulators are presented.

Finally in Chapter 10 general conclusions and other contributions gained from this research work are discussed. Further, the advantages and disadvantages of LN and GaAs electrooptic modulators are reported in this Chapter. Future work for LN and GaAs electrooptic modulators is suggested in order to improve the LN and GaAs electrooptic modulator performance. The thesis concludes with Appendices, a list of publications by the author, followed by a list of references cited in alphabetical order.

Numerical techniques

2.1 Introduction

In the design, analysis and optimization of electromagnetic devices and systems, scientists and engineers use a range of techniques. These techniques for solving field problems can be classified as experimental, analytical, or numerical. In this chapter concentration is on numerical techniques involved in microwave and optical waveguide analysis. Every numerical method involves an analytical simplification to the point, these are major benefits to apply this numerical method. Examples of these methods include:

A. Analytical methods (Exact solutions)

1. Conformal mapping
2. Integral solutions, e.g., Laplace and Fourier transforms
3. Perturbation methods
4. Series expansion
5. Separation of variables

B. Numerical methods (approximate solutions)

1. Finite difference method
2. Method of weight residuals
3. Method of lines
4. Finite element method
5. Beam propagation method
6. Point matching method

Numerical techniques and modeling itself of guided-wave elements as passive components have been very much studied in the past two decades. Today these methods need a high level of accuracy to model various structures in millimeter-wave.

2.2 Analytical solution techniques for optical waveguides

These methods are used to determine the solution of propagation constant for optical waveguides with relatively simple geometries. Such solutions are based on the Marcatili method, the Effective Index method, and the equivalent network method. In this section some of these methods and their applications are discussed briefly.

2.2.1 Marcatili Method

The Marcatili method (MM) (Marcatili, 1969) is one of the first methods (semi-analytical approximation methods) to be developed for the analysis of simple dielectric waveguides. The dielectric rod with rectangular cross section is surrounded by four different layers with lower refractive indices, as shown in Fig. 2.1. The field is assumed to exist in the core and four other cladding regions and is assumed to vary in sinusoidal form in the core region, whereas in the cladding regions this variation of the field is of exponential form.

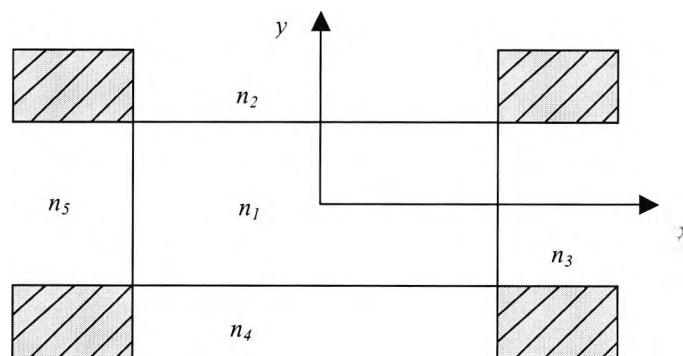


Fig. 2.1 Two dimensional buried rectangular waveguide for Marcatili method.

The field is approximated to the field in two slab waveguides, one of which is vertical and the other one is horizontal. When the optical field is confined and transmitted sufficiently, the electromagnetic field abruptly decreases as it goes away from the boundary. Subsequently the intensity of the optical energy in the parts of the shaded regions is negligible and we can solve the electromagnetic field components by separating the variables. When the refractive index changes to a step index, the E_x mode (with $H_x = 0$) and E_y mode (with $H_y = 0$) are obtained. This involves the solution of the transcendental eigenvalue for each slab waveguide simultaneously to give the axial

propagation constant. This method works well as long as the field is well confined to the core regions, far from cut-off, but this method gives poor results near the cut-off regions, reported by Chiang *et al.* (1994).

2.2.2 The effective index method

The effective index method (EIM) is proposed by Knox and Toullos (1970). The approach effective index method (EIM) is an improvement on Marcatili's method, where the core of a rectangular waveguide structure is replaced by an equivalent slab with the effective index solution, already obtained from another slab waveguide. The rectangular dielectric waveguide is decoupled into two slab waveguides in each transverse direction as illustrated in Fig. 2.2. In this approach two equivalent slabs are used to replace the core of the rectangular structure. Each of these 2-D structures can then be considered homogeneous in either the x or the y directions.

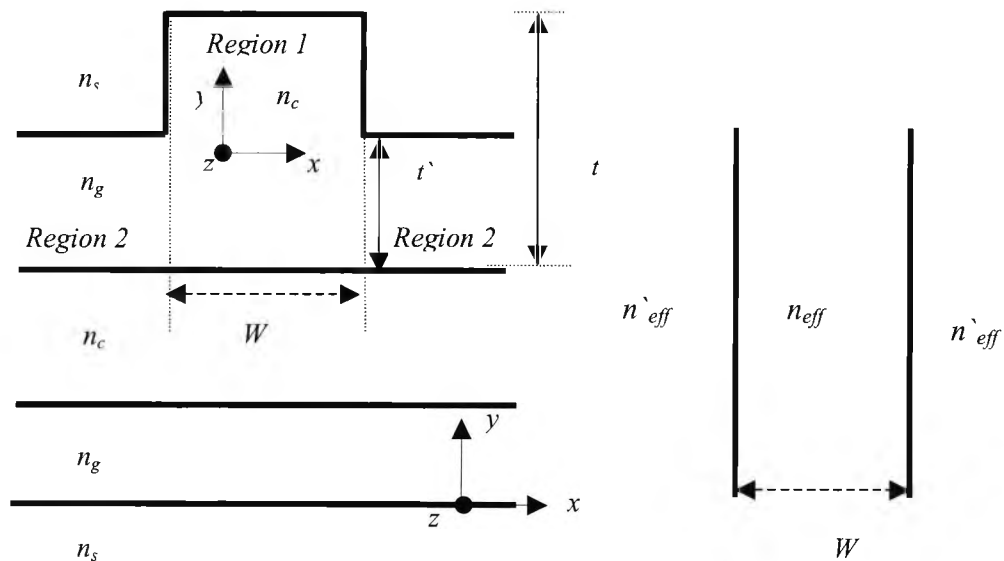


Fig. 2.2 The model representation of effective index method.

This method was significantly efficient compared to other methods that solved the rectangular waveguide structures. Also this method is not accurate near the cut-off regions; therefore several techniques have been proposed to improve this accuracy. Zhou and Itoh (1982) proposed an EIM for a trapped image guide, where they replaced the original waveguide by an equivalent structure. Chiang *et al.* (1994) proposed a dual

effective approach. By combining two solutions of two different EIMs to the waveguides, they managed to reduce the error by applying each solution separately.

2.3 Numerical solution techniques of optical waveguides

Numerical methods and modeling of waveguides is very important in optical design. This is due to increased research and development in millimeter-wave integrated circuits and monolithic integrated circuits. Numerical methods usually are developed in terms of their generality, efficiency, accuracy and complexity.

The selection of an appropriate numerical technique for analysis of the waveguide structures may be based upon several factors which should be taken in account, as reviewed by Davies *et al.* (1972), Chiang *at al.* (1994) and Vassalo *et al.* (1997). These factors are as follows:

1. the cross section shape of the waveguide structure, whether it is curved or polygonal or whether it is convex or non-convex;
2. whether the numerical method should be capable and programmable in order to solve a wide waveguide structure automatically, or programmed specifically for each region of the structure separately;
3. whether a computer program requires human intervention;
4. whether the dominant mode or the other higher order modes are required.
5. whether the field distribution or cut-off frequency is needed, or both;
6. the accuracy of the method modeling the dielectric boundaries and other regions;
7. the requirement of the methods needed for solving eigenvalues and eigen functions;
8. whether method is sufficiently accurate to distinguish optical modes which are very close together;
9. the ability of the method to eliminate spurious solutions;
10. the limitations and assumptions of the method for specific analysis;
11. the degree of understanding and involvement required from the user;
12. the efficiency and economy in both time and storage requirements;

A brief discussion of some numerical techniques is introduced in the following sections.

2.3.1 Finite difference method

The finite difference method (FDM) is considered to be one of the oldest and perhaps the most commonly used numerical techniques in analysis of dielectric waveguide and microwave problems (Wexler, 1969, Mur, 1974 and Davies, 1989).

The (FDM) is one of the simplest methods that employs the discretization procedure. The waveguide structure analyzed by this method is enclosed by a rectangular box, with side walls either electric or magnetic. The region of interest then is divided into mesh points separated by a certain distance as shown in Fig. 2.3. The nodes are placed on mesh points so that each node can be associated to four different refractive indices. Considering any interior node and using five-point finite difference formula, based on Taylor's series expansion, the differential operators can be expressed in terms of field nodal values at the neighboring nodes in two transverse conditions. Imposing boundary conditions at the interfaces between different dielectric media leads to an eigenvalue matrix equation which can be solved for the modal propagation constants associated with the field profile.

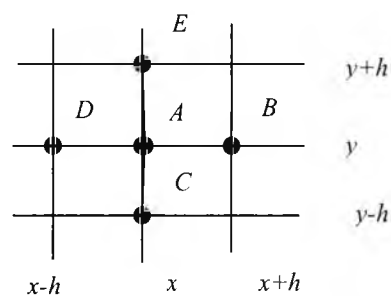


Fig. 2.3 Typical two-dimensional finite different mesh

The (FDM) is considered to be the least analytical. It can be applied to a wide range of complex shapes. However, a rectangular grid (FDM) as considered is not suitable for curved boundaries or interfaces, because they intersect gridlines obliquely at points other than the nodes. The accuracy of this method lies on the mesh size, because is node wise approximation. Disadvantage include that it is time consuming and requires a high memory space and also the mesh points lie on the boundary.

2.3.2 Finite element method

The finite element method (FEM) is the most powerful and versatile numerical technique for solving problems involving complex geometries and non-homogeneous waveguide structures. The finite element method is suitable for the modal analysis of the waveguides with arbitrary refractive-index profiles and complex waveguide structures. This method is based upon dividing the considered waveguide region into non-overlapping patchwork of polygons, usually triangular elements as shown in Fig. 2.4. The field is solved at each element in terms of polynomials, and then the total value of the field is found by linear summations of the fields over each element.

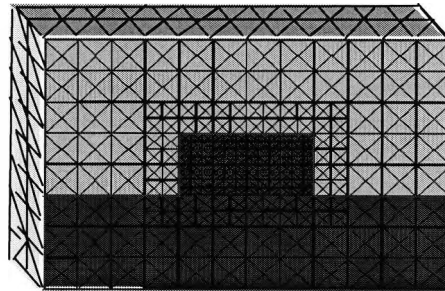


Fig. 2.4 Typical three-dimensional finite element subdivision analysis.

In the FEM, a simple form of function is adopted to approximate the field in each element. By applying the variational principles to the system functional, the problem reduces to an eigenvalue equation which can be solved by using iteration technique to obtain the propagation constant and their associated field profiles (Rahman and Davies, 1984). The accuracy of this method can be increased simply by increasing the mesh division. The finite element method can handle accurately open type waveguide problems close to cut-off regions. The introduction of infinite elements by Rahman and Davies has increased the accuracy of the FEM and its application. The spurious solutions has also been reduced by the introduction of penalty function method (Rahman and Davies, 1984), or in some cases totally eliminated. A more detailed study of this method and its application will be discussed explicitly in Chapter 2 of this thesis, also the flow chart of FEM implementation is presented in the Appendix 3.

2.3.3 Beam propagation method

The beam propagation mode (BPM) is one of the most powerful techniques to investigate linear and nonlinear longitudinal light propagation. The schematic illustration of BPM analysis is shown in Fig. 2.5. Curvilinear waveguide, branches, Y-junctions, S-shaped, bend waveguides and tapered waveguides are indispensable components in constructing optical integrated circuits (OIC). Therefore, a new numerical technique is needed in order to take into account the arbitrary index variations in all required directions.

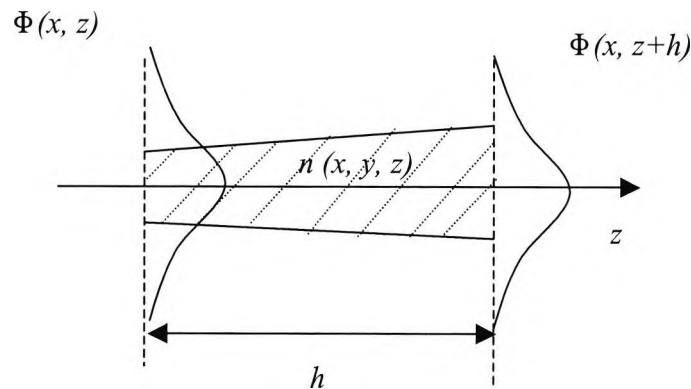


Fig. 2.5 Schematic illustration of BPM analysis (light propagating in z-direction).

Different kinds of BPM procedures can be evaluated based on the fast Fourier transform (FFT) or based on finite element method (FEM) or based on finite difference method (FDM). A first algorithm of BPM was formulated based on the FFT by Feit and Fleck in 1980, which could solve simple scalar wave equations. Since then this method has been developed to semivectorial and full-vectorial based on FDM from Chung *et al.*, (1990), and Huang and Xu *et al.*, (1992).

Recently, the finite element method (FEM) has been utilized in developing BPM. The unified finite element beam propagation method (FEPBM) approaches based on scalar and full-vector formulations have been reported by Hayata *et al.* 1990 and Montanari *et al.* 1998 for TE and TM waves propagating in longitudinally varying optical

waveguides. The BPM has been developed by Danielsen *et al.* 1984 to analyze electrooptic modulators. The scalar BPM approaches are numerically more efficient because they solve only one field component; however it cannot accurately model three-dimensional waveguides with hybrid fields where polarization effect is clear and polarization coupling is possible. The full vectorial finite element-based beam propagation method (VFEBPM) reported from Obayya *et al.*, (2000) is based on the use of the two transverse magnetic field components and the polarization effects and conversion terms are transverse accounted for by using line integral terms around the part of the element boundary which lies between different materials. This numerical formulation is very efficient and, yet sufficiently accurate for solving semiconductor laser waveguide with gain, leaky mode optical waveguide, curved waveguide and nonlinear optical waveguide with and without bistabilities.

2.3.4 The method of lines

The method of lines (MOL) was first suggested by Schulz and Pregla (1981) for analysis of dispersion characteristics of planar isotropic waveguides and microstrips. Recently, Berini and Wu (1996) have applied the MOL in modeling of optical waveguides with lossy inhomogeneous anisotropic media. In this method the waveguide is considered to be enclosed inside a rectangular box with magnetic or electric walls on the sides in order to satisfy the boundary conditions for the required polarization. The region considered is divided into equidistant lines along the x -direction parallel to the y -axis separated by distance h as shown in Fig.2.6.

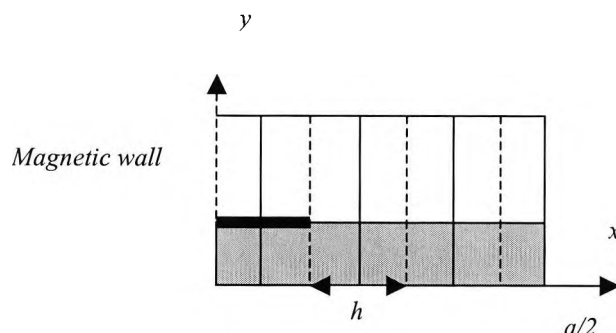


Fig.2.6 One half of the cross section of a microstrip line analyzed by MOL

The essential feature of the methods of lines in the diagonalisation of the matrix form is that the equation for the field can be solved independently for each discretization i . This feature makes this method very accurate. However the MOL is very difficult to apply for waveguides with curved boundaries and the accuracy close to the cut-off is limited.

2.3.5 Point matching method

The point matching method (PMM) is considered to be one of the oldest ‘boundary solution’ methods for solving of isotropic homogenous dielectric waveguides. This numerical method is mainly concerned with solving scattering waveguide problems. This approach for the first time was established by Goell (1969) for solving rectangular dielectric waveguides. In this method the electromagnetic fields inside the core are expressed by the sum of Bessel functions and their derivatives, with the fields outside the core represented by the sum of modified Bessel functions and their derivatives, both of them multiplied by trigonometric functions. A system of linear equations is obtained, by matching the tangential fields at optimally selected points around the boundary and is called ‘Matching points’. By applying the boundary conditions of nontrivial solution the propagation constant and its characteristic equation arranged into a matrix equation whose solution gives the eigenvalue and eigenvectors.

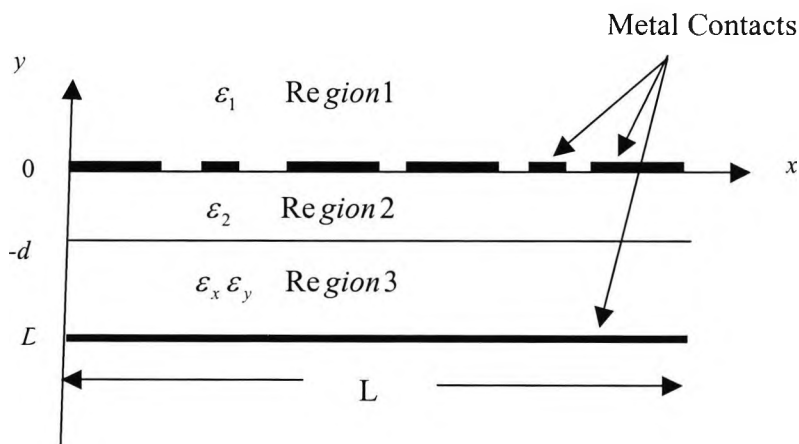


Fig. 2.7 Schematic dielectric layers structure with several electrodes on top analyzed by PMM (Marcuse, 1989).

The above approach can be applied to solve the dielectric waveguides with arbitrary cross sections, coupled dielectric waveguides and also computing coupling coefficients between rectangular rods. An example (Marcuse, 1989) of a capacitance calculation from the Laplace equation by the PMM analysis of an electrostatic field of coplanar lines is illustrated in Fig.2.7. In these situations this method is very simple formulation of the problem and well suited for the computer solution with relatively little programming effort. The PMM is computational efficient compared with other numerical methods, because the matching points are needed only at the boundaries rather than the whole computational region. However, the PMM is difficult to be applied to the three-dimensional waveguide structures with inhomogeneous index distribution such as graded index fibres.

2.3.6 The boundary element method

The boundary element method (BEM) is a numerical technique where basic equations are boundary integral equations (Morita, 1990). The boundary element method is one of the boundary-type methods based on the integral equation method and therefore, if the region to be considered is homogenous, as illustrated in Fig. 2.8, then it required nodes, necessary for calculation, on its boundary only (Koshiya, 1987). This method shows some similar features with FEM, but instead of taking unknown at nodal field values throughout the waveguide region, the unknown are taken only along the boundary, often performed using two-dimensional Helmholtz equation and the formulation of Green's functions.

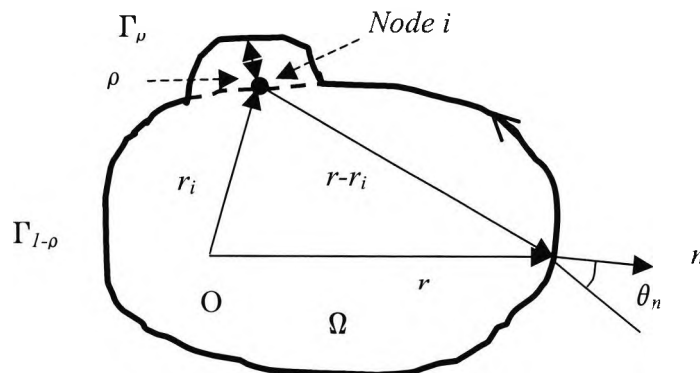


Fig. 2.8 Two-dimensional region Ω surrounded by boundary Γ .

Integral representations play a key role throughout the process in the evaluation of the physical quantities.

The BEM is capable of dealing with arbitrary shape discontinuities as FEM, by using a far smaller number of nodes than FEM. Also unlike the FEM, the BEM can automatically incorporate boundary conditions at infinity, so that no infinity element is needed.

The disadvantage of the BEM lies in that it is applicable only for homogenous structures and also some nonphysical solutions, known as resonant solutions, may not be avoided. Also, The BEM formulation leads to dense matrices unlike those in FEM which are sparse. Therefore the FEM can be considered as more computationally efficient.

2.3.7 The mode-matching method (MMM) or the equivalent network method (ENM)

This method is typically a numerical approximation applied to determine the propagation characteristics of an open dielectric waveguide (Pen and Oliner, 1981). The open waveguide structure is artificially bounded and waveguide cross section is considered in terms of building blocks, which usually consist of uniform dielectric layered structures interfaced by dielectric step discontinuity such as the one in Fig.2.9 (Davies, 1989).

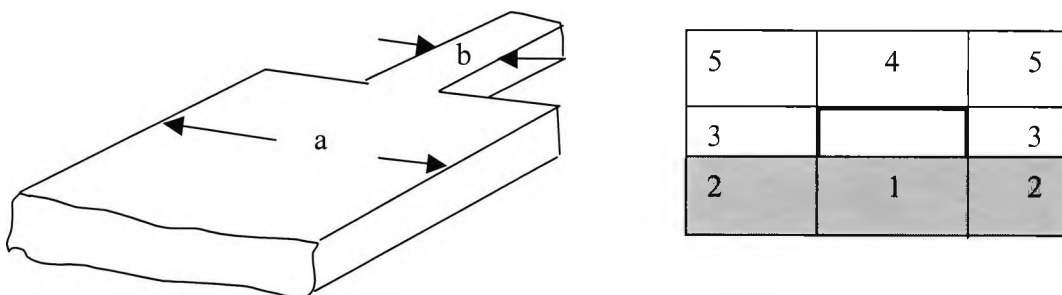


Fig. 2.9 Waveguide discontinuities analyzed by (MMM).

The field on both sides of the discontinuity is expanded in terms of the modes with unknown coefficients (Shin and Gray, 1983). The fields in the dielectric subdivided

regions are expanded in terms of appropriate orthogonal sets with a common but unknown propagation constant. By applying the orthogonal of expansion functions and boundary conditions to each region we obtain the determinant of this system. The value of the propagation constant can be obtained after the determinant of these systems is equalized to zero.

In the similar way the ENM is suitable where the dielectric regions are represented by uniform transmission lines with their characteristic impedance and the various step discontinuities are characterized by transforms. Where equivalent network admittance takes into consideration the effect of region outside, the total admittance seen at any ports is equalized to zero from where the propagation constant can be obtained.

Koshiba and Suzuki (1985) have reported a full-vectorial analysis of optical waveguides with rectangular structures by the ENM, where the TE-TM coupling and the discretization of the continuous modal spectrum is taken into account.

2.3.8 The spectral index method

The spectral index method (SIM) is a relatively fast and accurate approach where the wave equations are expressed in the version integral form of Fourier transforms and Fourier series. This method has been applied to solve a simple semiconductor rib waveguide structure (Kendall *et al.*, 1989) and strip loaded directional coupler (Burke, 1990).

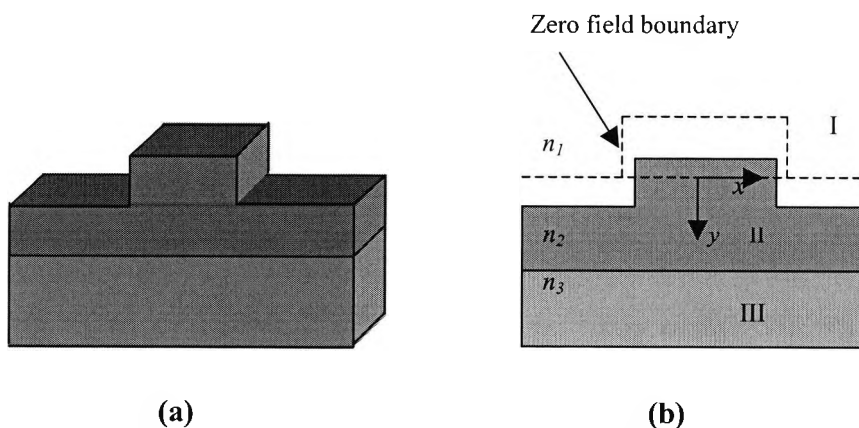


Fig. 2.10 Cross section of rib-waveguide illustrating use of spectral index method.

According to the principles of SIM analysis, a rib waveguide structure (a) as illustrated in Fig. 2.10, can be replaced with an effective structure (b), displacing the actual physical dimensions to the new one on which the optical field is equalized to zero, in order to model the penetration of this field into the cladding. The field in each region is expressed as a superposition of local solutions of the wave equation, these regions being I the rib, II the multi-layered medium below the rib III, continuity of the field, enforced at the boundary of regions I and II, with a variational boundary condition being used to match the gradient. The result is a simple transcendental equation that can be solved, yielding the propagation constants of the guided modes of the structure and subsequently the field profiles of the guided modes. The electric or the magnetic field, dependent on the polarization, is expressed in terms of cosine and sine Fourier series which represent the symmetric and asymmetric modes, respectively. In the region below the rib the waveguide equation is expressed in terms of its Fourier transform and the problem is reduced to a one dimension slab, where the refractive indices are represented by their corresponding spectral indices. These equations for two regions are linked in order to obtain a transcendental equation, which is solved for the propagation constant of the rib structure. The evanescent regions are expressed by imaginary spectral indices.

The SIM requires less computational time than other methods. However, in the presence of dielectric corners, where electric field exhibits singularities produced by its transverse components, such behaviour leads to complicated field distribution.

2.4 The Least-Square Boundary Residual (LSBR) Method

The LSBR method is an alternative point-matching method of numerically solving scattering problems. Discontinuity problems in optical waveguide devices are very important issues to be studied for theoretical and practical interest. They play an important role in designing practical devices such as an isolated abrupt step discontinuity as in butt joints of two waveguides with different core dimension widths, or waveguide structures when electrooptic effect is considered (side I when $V = 0$, and side II when $V \neq 0$), or as finite cascade sections such as gratings, tapers, bendings, or y-junctions, branches.

The LSBR method is a very powerful tool for the calculation of discontinuity problems; it is widely used in several modern simulation packages for the analysis of photonic devices. It is a rigorous convergent and highly accurate way of solving those problems. In contrast to other methods for junction analysis like point matching method the LSBR method is a rigorously convergence procedure free from the phenomenon of relative convergence. Also in comparison with the overlap integral method (OI), where the boundary conditions are satisfied automatically, LSBR has big advantages. Nevertheless, the OI method is also widely used, because it is simple to use. However, the disadvantage of OI is restricted to certain types of discontinuities.

The problem considered here in this study is an abrupt discontinuity, in the transverse plane $z = 0$ between two arbitrary shaped uniform waveguides (guides with cross sections independent of z). Each guide can have permittivity (isotropic or anisotropic) that varies arbitrarily in the two transverse directions and an incident wave is assumed to be one mode.

The least squares boundary residual method was introduced (Davies, 1973) as an alternative to point-matching (and Galerkin) methods, satisfying the boundary conditions in the usual least-square sense over the interface between different dielectric materials. This method is rigorously convergent, the error minimization being global rather than sampled, and has the flexibility of introducing an electric/magnetic weighting factor.

2.4.1 Analysis of optical waveguide discontinuities by (LSBR) method.

In this section, LSBR method is used as a powerful numerical tool to analyse an abrupt junction of two slab dielectric waveguides as shown in Fig. 2.11. The incoming wave incident is on the discontinuity junction between waveguide **I** (side **I**) and waveguide **II** (side **II**). Part of the incident wave is reflected, part transmitted and the rest radiated. Consider E_t^i and H_t^i to be the transverse components of the electric and magnetic fields of the incident wave, respectively. Some of the incident wave is reflected into side **I**, noted as, (ρ) . Also, from the mode definition and boundary conditions, with the wave

incident on the discontinuity junction, many modes will be generated at the discontinuity plane in order to satisfy the boundary condition. These can be guided or radiated modes on both sides **I** and **II** of the discontinuity.

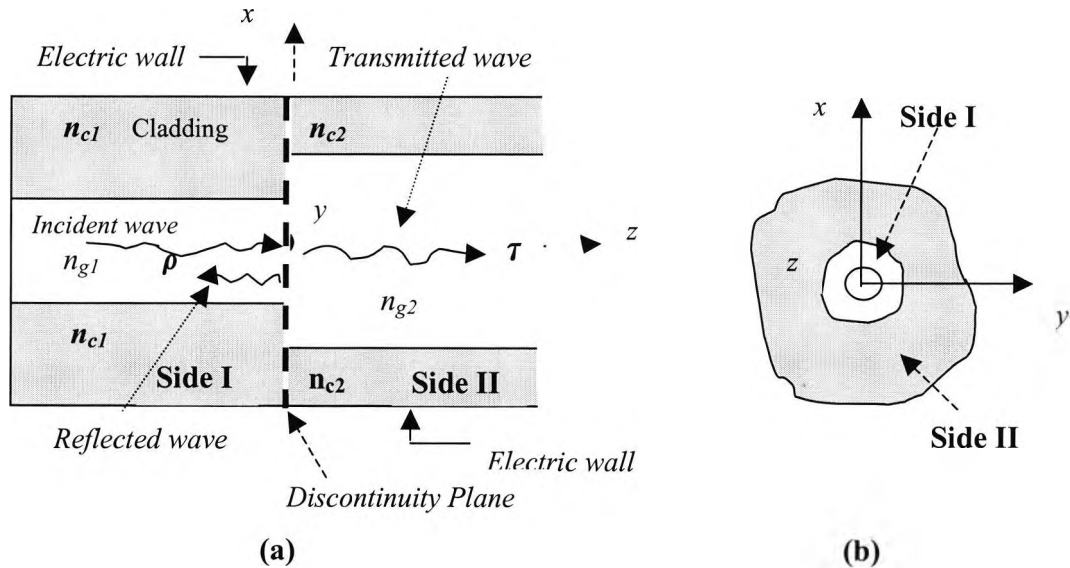


Fig. 2.11 Discontinuity at the junction of two dielectric waveguide. **(a)** Vertical section, **(b)** Transverse section

The transverse components of the total electromagnetic fields E_t^I and H_t^I in side **I** and E_t^{II} and H_t^{II} in side **II** at the discontinuity plane can be expressed in terms of eigenmodes in side **I** and side **II**, respectively, as follows:

$$E_t^I = E_t^i + \sum_{i=1}^{\infty} a_i E_{ii}^I \quad (2.1)$$

$$H_t^I = H_t^i - \sum_{i=1}^{\infty} a_i H_{ii}^I \quad (2.2)$$

$$\mathbf{E}_t'' = \sum_{i=1}^{\infty} b_i \mathbf{E}_{ti}'' \quad (2.3)$$

$$\mathbf{H}_t'' = \sum_{i=1}^{\infty} b_i \mathbf{H}_{ti}'' \quad (2.4)$$

As mentioned above, at the discontinuity plane, many modes are generated to satisfy the boundary conditions; some of them may be propagating, radiating or evanescent. Therefore \mathbf{E}_t^I and \mathbf{H}_t^I are transverse field components of the i^{th} mode reflected from the discontinuity plane (junction) in side I and a_i are the corresponding modal amplitudes of these reflected modes. Similarly, \mathbf{E}_{ti}'' and \mathbf{H}_{ti}'' represent the transverse field components of the i^{th} mode transmitted in side II, and b_i are the modal amplitudes of those transmitted modes.

The LSBR method for a stationary solution in order to satisfy the continuity conditions of the tangential fields in a least square sense will be evaluated by minimising J , given as:

$$J = \int |\mathbf{E}_t^I - \mathbf{E}_t''|^2 + \alpha \cdot Z_0^2 |\mathbf{H}_t^I - \mathbf{H}_t''|^2 d\Omega \quad (2.5)$$

where $Z_0 = \sqrt{\epsilon_0 \mu_0} = 376.7(\Omega)$ is the free-space wave impedance and α is a dimensionless weighting factor. To get the approximate numerical solution of the problem, the infinite expansions of equations (2.1)-(2.4) are truncated, including all relevant propagating modes plus as many radiating and/or evanescent modes as is convenient. The minimum criterion of equation (2.5) reduces to the following linear equation:

$$\frac{\partial J}{\partial a_i} = 0 \quad \frac{\partial J}{\partial b_i} = 0 \quad i = 1, 2, 3, \dots, \infty \quad (2.6)$$

$$\mathbf{C}x = v \quad (2.7)$$

The solution of this equation gives $\{x\}$ the required approximation coefficients of a_i and b_i . Where \mathbf{C} is square matrix generated from the eigenvectors and v is an array due to incident modes. The elements of \mathbf{C} -matrix and v are given as:

$$C_{ij} = \langle \mathbf{E}_{ii}, \mathbf{E}_{ij} \rangle + \alpha Z^2 \langle \mathbf{H}_{ii}, \mathbf{H}_{ij} \rangle \quad (2.8)$$

$$v_i = \langle \mathbf{E}_t^i, \mathbf{E}_{ii} \rangle + \alpha Z^2 \langle \mathbf{H}_t^i, \mathbf{H}_{ii} \rangle \quad (2.9)$$

where $i, j=1, 2, \dots, N$ and N is the total number of modes in side **I** and side **II** and vectors \mathbf{E}_t and \mathbf{H}_t are made up of all the corresponding fields in both sides. The inner product involved in the above equations is as follows:

$$\langle x_1, x_2 \rangle = \int x_1 \cdot x_2^* ds \quad (2.10)$$

where x_1 and x_2 are field vectors, x_2^* is the complex conjugate of x_2 and the integration is carried over the cross section of the waveguide. This concludes the LSBR method applied to the numerical solving scattering problems. This approach will be applied in the later chapters in order to analyse the unwanted polarization crosstalk in the semiconductor electrooptic modulator and power transfer between waveguides.

2.4.2 Numerical analysis of waveguide discontinuity (LSBR) using FE modal solution output.

By employing the FE program we obtain two guides, nodal values of the complete \mathbf{H} field for each considered mode. The electric field \mathbf{E} of each element can be calculated by the relations between electric and magnetic fields using Maxwell's equation. Many modal eigenvalues and eigenvectors for both sides **I** and side **II** of the discontinuity plane are used as an input to the LSBR program. These eigenvalues and eigenvectors of

both sides are calculated by using FEM program. The LSBR program calculates the integral J and minimizes the error criteria given by equation (2.5) with respect to each value of a_i and b_i for any given incidence by solving a homogeneous linear equation (2.7). The solution of this equation gives the unknown column vector $\{x\}$ values, consisting of unknown reflected and transmitted coefficients (in our case $\tau_{TE}, \tau_{TM}, \dots$) of all the considered modes in the analysis. For numerical efficiency, the FE nodal points in side **I** are matched with nodal points of side **II** across the transverse plane at the interface. There is no need of exploration to find J as these points can be computed over each triangle element and summed over all the elements over $\sum_A \int J_e$. Also, it does not

require generating nodal E fields, because they can be directly taken from the nodal H fields to calculate field part of the integral J .

The LSBR method can be applied to all types of discontinuity problem involving an abrupt change at a transverse plane, between arbitrary guiding structures of uniform cross sections, vertical shifts, and horizontal misalignments, sudden change of width or height, change in guide dimensions of material, electrooptic effect, and combination of all these varieties. On other hand the LSBR can be used as powerful tool to find the optimum matching of the two waveguides by controlling the geometries and material properties of the guides. Also, by choosing the optimum guide parameters, the radiation loss resulting from random fluctuations in waveguide geometry and refractive index can be minimized. The resulting reflecting matrix and the transmission matrix give a complete understanding of the discontinuity problem which improves better design of optical and microwave devices.

The LSBR method can be applied to analyze the optical losses in the waveguide devices. The source of losses in these devices can be coupling loss, propagation loss, electrode loading loss and bending loss. Radiation loss becomes significant when the waveguides are bent through a curve, where photons can be scattered, absorbed or radiated which leads to the reduction of the total power transmission. The power per area at any point along the length of the waveguide is given as:

$$I(z) = I_0 e^{-\alpha z} \quad (2.11)$$

where I_0 is the initial intensity at $z = 0$ and α is the power attenuation coefficient. The LSBR method analyzes the waveguide junction in order to calculate the power transfer from the input guide to the another guide. If there is a guide TE or TM mode incident on the discontinuity plane between two waveguides (Side I and Side II) some of the incident wave (light) energy is lost, the so called the *insertion loss*. This method can also be used to calculate the power loss suffered by TE or TM mode, by utilizing the scattering coefficients; therefore the *insertion loss* expressed in decibel (dB) is given as:

$$L = 10 \cdot \log_{10} \left(\sum_{i=1}^N |b_i|^2 \right) \quad (2.12)$$

The attenuation of an optical beam is measured in decibel (dB). If an input power P_1 results in an output power P_2 , then the loss in decibel is given as:

$$\alpha = 10 \cdot \log_{10} \frac{P_1}{P_2} \quad (2.13)$$

Summary

This chapter has provided a brief description of some representative numerical techniques which are useful for the analysis of waveguide and millimeter-wave structures. As illustrated here, each method has its own specific advantages and disadvantages. In particular, in this Chapter more effort has been spent on the discussion of the LSBR method and the role of the FE program in utilizing the LSBR technique. The FEM and LSBR technique and their applications are discussed in greater detail in the subsequent Chapters of this thesis, also the flow chart of interaction between FEM (modal solution) and LSBR implementation are presented in the Appendix 3.

The Finite Element Method

3.1 Introduction

The finite element method (FEM) has become the most popular numerical technique, widely accepted for a wide range of structural engineering applications in aerospace, electromagnetics, aeronautics naval architecture and electromagnetics both low and high frequency. The earlier mathematical treatment of the method was provided by Courant in 1943, and in the early 1950s, computers made it possible to solve structural problems very effectively, but the method was accepted slowly by industry. Turner, Clough, Martin, and Topp introduced the finite element concept in 1956 at the Boeing Aircraft Company and used this method as a useful tool to calculate the stress-strain relations for complex aircraft structures. The finite element method was not applied to electromagnetic problems until 1968. Since then the approach has been employed in diverse areas such as waveguide problems, electrical machines, semiconductor devices and microstrip millimeter wave structures. Today many modern engineering projects have become extremely complex, costly and subject to several important reliability and safety constraints. For a proper understanding, analysts need mathematical models that can be used to simulate the behavior of complex physical systems. In the finite element method, instead of using differential equations for the system which is under investigation, the corresponding functions to which a variable principle is applied are set up, where the region of interest is divided into the so-called elements, an equivalent discretized model for each element is constructed and then all the elements of the system are assembled.

This method can be considered as a subclass of the Rayleigh-Ritz method, (Zienkiewicz, 1977). The Rayleigh-Ritz method is associated with some difficulties which prevent its use in a wider class of the physics and engineering problems. The difficulty of this method is the choice of the trial (basis) functions used in the approximation with very high degree polynomials being used to give an accurate description of the unknown function. Also the procedure becomes more complicated, especially if the domain includes abrupt changes of the material properties.

The finite element method is the most powerful and versatile numerical technique for handling problems involving complex geometries and inhomogeneous media. The systematic generality of the method makes it possible to construct general-purpose computer programs for solving a wide range engineering problems.

The piecewise-defined polynomial functions are used for trial functions and an infinite degree of freedom of the system and are discretized or replaced by a finite number of unknown parameters (Koshiba, 1992). In the finite element method, elements can have various shapes, such as triangles and rectangles which allowing the use of an irregular grid. Based on this advantage this method is suitable for problems with steep variations of fields. This method may also be applicable to problems where a variational principle does not exist or cannot be identified.

This chapter is concerned with the use of the finite element technique for general electromagnetic field computation with the use of one and two-dimensional optical and microwave guided-wave problems. An arbitrary shape of optical waveguide shown in Fig. 3.1, is discussed below. The waveguide is considered to be uniform along the axis of the propagation, the z -axis. This waveguide may be considered to composed of several different materials described by arbitrary magnetic permeability, μ and electric permittivity, ϵ . Assuming the time (t) and z variation are given by $e^{(j\omega t)}$ and $e^{(-j\beta z)}$ functions of the magnetic $H(x, y, z, t)$ and electric $E(x,y,z,t)$ fields respectively, at the angular frequency, ω , they can be expressed as:

$$\mathbf{E}(x, y, z, t) = \mathbf{E}(x, y) e^{[j(\omega t - \beta z)]} \quad (3.1)$$

$$\mathbf{H}(x, y, z, t) = \mathbf{H}(x, y) e^{[j(\omega t - \beta z)]} \quad (3.2)$$

where β is the propagation constant in the z -direction and $\mathbf{E}(x, y)$ and $\mathbf{H}(x, y)$ are the spatial time-independent electric and magnetic fields, respectively.

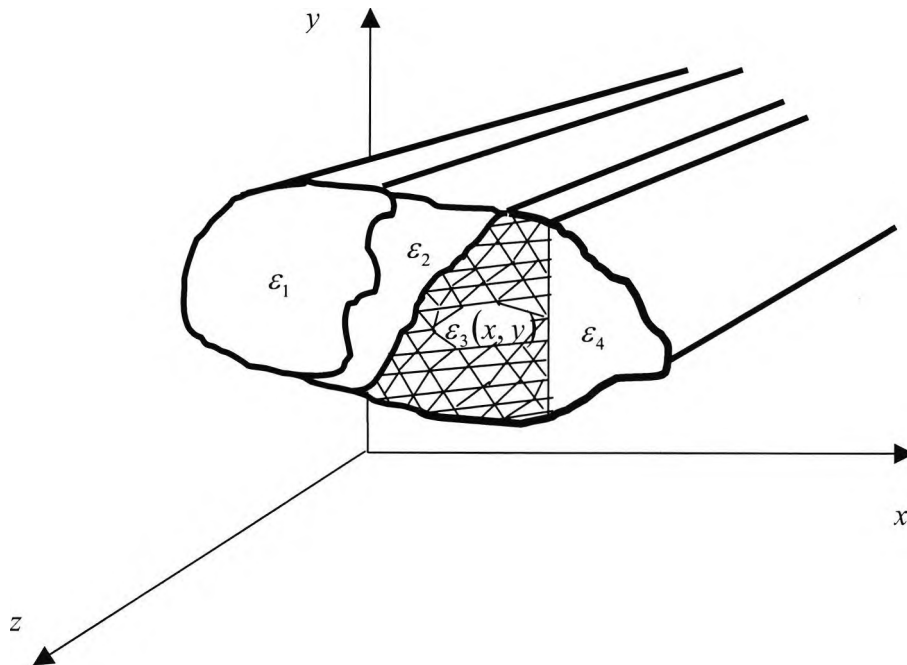


Fig. 3.1. An arbitrary shape of the optical waveguide geometry divided into finite number of subregions or elements, where each subregion is consisted from different materials.

The geometry of the waveguide can be very complicated, with an electric permittivity profile $\varepsilon(x, y)$ change in x - y directions, such as in LiNbO_3 dielectric waveguides with tensor permittivity, such as different constants $\varepsilon_x = 28$ and $\varepsilon_y = 43$.

3.2 Maxwell's Equations

In this chapter the concept of the FEM and its fundamentals are discussed. This includes a listing of the relevant forms of Maxwell's equations for optical waveguide analysis. Maxwell's equations are a set of the fundamental equations governing all macroscopic electromagnetic phenomena. They can be written in both differential and integral forms.

Since differential equations are more convenient to deal with using the finite element method, Maxwell's equations here are presented for time-varying fields in differential form as:

$$\nabla \times \mathbf{E} = - \partial \mathbf{B} / \partial t \quad (\text{Faraday's law}) \quad (3.3)$$

$$\nabla \times \mathbf{H} = - \partial \mathbf{D} / \partial t + \mathbf{J} \quad (\text{Ampere's law}) \quad (3.4)$$

$$\nabla \cdot \mathbf{D} = \rho \quad (\text{Gauss's law creation of electric flux}) \quad (3.5)$$

$$\nabla \cdot \mathbf{B} = 0 \quad (\text{Gauss's law continuity of magnetic flux}) \quad (3.6)$$

where \mathbf{E} is the electric field intensity (Volt/meter), \mathbf{B} is the magnetic flux density (Weber/meter²), t is the time (sec), \mathbf{H} is magnetic field intensity (Ampere/meter), \mathbf{J} is current density (Ampere/ meter²), \mathbf{D} is electric flux density (Coulomb/ meter²), and ρ is electric charge density (Coulomb/ meter³).

For the electromagnetic waves under consideration, \mathbf{E} and \mathbf{H} can be assumed to vary harmonically in time as

$$\mathbf{E} = \mathbf{E}_0 e^{(j\omega t)} \quad (3.7)$$

$$\mathbf{H} = \mathbf{H}_0 e^{(j\omega t)} \quad (3.8)$$

where \mathbf{E}_0 and \mathbf{H}_0 are the amplitude of the field and ω is the operating angular frequency of the wave. Substituting these equations into (3.3) and (3.4) the following is obtained

$$\nabla \times \mathbf{E} = - j\omega \mu \mathbf{H} \quad (3.9)$$

$$\nabla \times \mathbf{H} = (\sigma + j\omega \epsilon) \mathbf{E} \quad (3.10)$$

$$\mathbf{B} = \mu \mathbf{H} = \mu_0 \mu_r \mathbf{H} \quad (3.11)$$

$$\mathbf{J} = \sigma \mathbf{E} + \partial \mathbf{D} / \partial t = \sigma \mathbf{E} + \epsilon \partial \mathbf{E} / \partial t \quad (3.12)$$

$$\mathbf{D} = \epsilon \mathbf{E} = \epsilon_0 \epsilon_r \mathbf{E} \quad (3.13)$$

where, μ_0 and ϵ_0 are permeability and permittivity of free space respectively, σ is the conductivity of the medium (Siemens/meter), μ_r is the relative permeability of the medium and ϵ_r is the relative permittivity of the medium.

These symbolic equations are frequently displayed in component form by means of a matrix representation, with the field described by the column matrix

$$\mathbf{E} = \begin{bmatrix} E_x \\ E_y \\ E_z \end{bmatrix} \quad (3.14)$$

and the curl and divergence operators described by the matrix-differential operators.

$$\nabla \times = \begin{bmatrix} 0 & -\frac{\partial}{\partial z} & \frac{\partial}{\partial y} \\ \frac{\partial}{\partial z} & 0 & -\frac{\partial}{\partial x} \\ \frac{\partial}{\partial y} & \frac{\partial}{\partial x} & 0 \end{bmatrix} \quad (3.15)$$

$$\nabla \cdot = \begin{bmatrix} \frac{\partial}{\partial x} & \frac{\partial}{\partial y} & \frac{\partial}{\partial z} \end{bmatrix} \quad (3.16)$$

In Cartesian coordinates, these operators have the matrix forms

3.3 Finite element formulations

Electromagnetic waveguides can be classified into various categories according to their cross-section shapes. Often these can be treated as one dimensional problem, illustrated in Fig. 3.2 (a) as a planar waveguide and Fig. 3.2 (b) as an axial symmetric waveguide. Alternatively there are arbitrarily-shaped waveguides with an arbitrary transverse distribution of the permittivity or refractive index as shown in Fig. 3.2 (c) for a waveguide with an arbitrarily shaped cross-section, which can only be treated as a two-dimensional problem (Fernandez and Lu, 1996).

Finite element formulations may be obtained in a different ways direct from the differential or integral equations or so called weighted residual methods or variational method or using so-called Galerkin's approach (Harrington, 1968). In this chapter their formulation through the variation approach will be considered. When applying the standard finite element method to waveguide problems for propagation characteristics analysis, it is usual to arrive at a matrix eigenvalue equation of the form (Rahman and Davies, 1984)

$$[A]\{x\} = \lambda[B]\{x\} \quad (3.17)$$

where x is the vector of the nodal field values, λ is an eigenvalue which can be chosen as β^2 or k_0^2 (free space wave number depending on the formulation). A and B are symmetric sparse matrices.

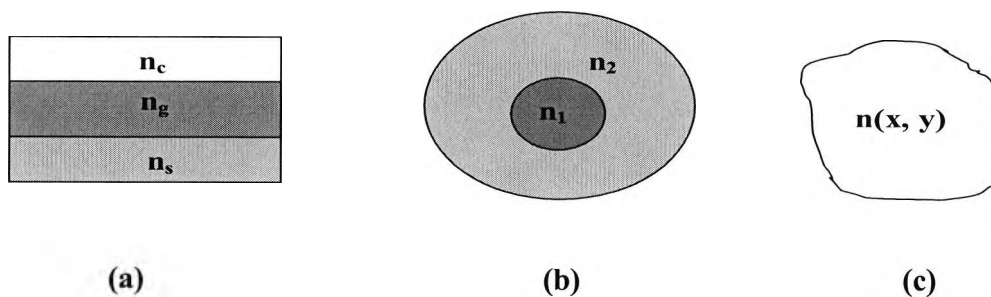


Fig. 3.2 Various waveguide shapes with transverse distribution of permittivity, (a). planar, (b). axial symmetric (c) and arbitrary.

3.4 Scalar finite element formulations

The scalar formulation of the finite element method can be adopted in terms of the longitudinal field of the TE or TM modes and is applicable to cases where the fields can be described with sufficient accuracy as predominantly TE or TM. It has been used for the solution of anisotropic waveguides and to approximate the analysis of lossy guide problems (Koshaiba, 1982), or open boundary problems (Wu and Chen, 1986). This formulation for TE can be written as (Mayaba, 1981).

$$J(\phi) = \iint_{\Omega} \left[\left(\frac{\partial \phi}{\partial x} \right)^2 + \left(\frac{\partial \phi}{\partial y} \right)^2 + (\beta^2 - k_0^2 n(x, y)^2) \phi^2 \right] dx dy \quad (3.18)$$

where β is the propagation constant, $n(x, y)$ is the refractive index profile in the x and y directions, k_0 is the free-space wave number, and the integration is carried out over the domain Ω . Based on this formulation, the finite element program can will consider β^2 as the eigenvalue of the matrix equation for a given free-space wave number, k_0 and the eigenvector $\phi(x, y)$ is the transverse field distribution, i.e. E_x component for the quasi-TE modes. The scalar formulation for the quasi-TM can be expressed as (Mabaya *et al.*, 1981).

$$J(\psi) = \iint_{\Omega} \left[\left(\frac{\partial \psi}{\partial x} \right)^2 + \left(\frac{\partial \psi}{\partial y} \right)^2 + (\beta^2 - k_0^2 n^2(x, y)) \psi^2 \right] dx dy \quad (3.19)$$

where $\psi(x, y)$ is the transverse field distribution, i.e. the H_x field component for the quasi-TM modes. The finite element program based on this formulation yields k_0^2 as the eigenvalue for the given propagation constant, β . These approximations can be sufficiently accurate for use in many practical cases. The scalar finite element formulation has a significantly lower computational cost where the number of the matrix elements is reduced, compared to vector formulation, and hence they can be suitable for the design procedures where the full vectorial finite element approximation can be too time-consuming. The scalar finite element formulation does not suffer from the

appearance of the spurious or non-physical solutions (Cesender and Silvester, 1970), which are often encountered in some vectorial formulations.

3.5 Vectorial finite element formulations

For the structure of inhomogeneous waveguide problems, the scalar formulation of the finite element method is not applicable; therefore it is essential for the accurate characterization of these optical waveguides to use the vectorial formulation. Earliest the vector finite element method formulation was based in terms of both the longitudinal electric and magnetic components (E_z , H_z). These field components have been used for analyzing microwave, optical waveguides, (Corr and Davies, 1972) and lossy waveguides. The use of the longitudinal electric and magnetic component (E_z , H_z) formulation (Mabaya *et al.*, 1981) for general anisotropic waveguides is not possible without destroying the canonical form of the matrix equation (3.17). Also for a waveguide with an arbitrary dielectric distribution, the enforcement of the boundary condition can be quite difficult. Another fundamental disadvantage of the vector formulation is that it is based on the longitudinal components which are usually the least important of the six components of the vector fields E and H . This type of formulation is also affected by non-physical spurious solutions and the techniques used to reduce them greatly increase the complexity of the computer programs required.

There are different types of vector finite element formulations depending on which electromagnetic field components are used for the formulations:

- Finite element method using transverse electromagnetic field components
- Finite element using longitudinal electromagnetic field components
- Finite element method using transverse electric field components
- Finite element method using transverse magnetic field components
- Finite element method using transverse three electric field components
- Finite element method using transverse three magnetic field components
- Finite element method using the six electromagnetic field components

Berk, in 1956, had presented a number of vector variational formulations in the form of the Rayleigh quotients for the lossless anisotropic microwave waveguides in terms of the H field the E field or combinations of both. The full vector H formulation has become

the most common choice and has been used extensively in the solution of microwave and optical waveguides (Konrad, 1976), where its clearest advantage over the \mathbf{E} formulation is apparent in the analysis of optical waveguides where the permeability is homogeneous and the magnetic field is continuous everywhere. Its natural boundary conditions corresponding to electric walls ($\mathbf{n} \times \mathbf{E} = 0$), and magnetic walls ($\mathbf{n} \times \mathbf{H} = 0$) are simple to force. This formulation can be written as (Berk, 1956; Rahman and Davies, 1984).

$$\omega^2 = \frac{\int (\nabla \times \mathbf{H})^* \cdot \hat{\epsilon}^{-1} \cdot (\nabla \times \mathbf{H}) \, d\Omega}{\int \mathbf{H}^* \cdot \hat{\mu} \cdot \mathbf{H} \, d\Omega} \quad (3.20)$$

The integration is carried out over the waveguide section, Ω , and $\hat{\epsilon}$ and $\hat{\mu}$ are general anisotropic permittivity and permeability tensors of the loss-free medium, respectively. The application of the Rayleigh-Ritz procedure to (3.20) leads to a similar eigenvalue problem to that in (3.17), where the matrix \mathbf{A} is in general complex Hermitian matrix which can be reduced to the real symmetric and positive case by using a suitable transformation (Rahman and Davies, 1984) and \mathbf{B} is real symmetric and positive defined. The vector \mathbf{x} now corresponds to the unknown values of all three components of the field in all nodal points with λ as their corresponding eigenvalues and also λ is proportional to ω^2 . To get the right solution of β at a certain wave length, it has to be changed iteratively until the output eigenvalue corresponds to the correct wavelength. Unfortunately, non-physical spurious solutions can appear (as in the \mathbf{E} -field formulation): however it will be discussed later how these spurious solutions can be avoided.

3.6 Boundary conditions

The boundary conditions are the conditions that have to be met at the boundary surface between two different media in contact with two different parameters. Figure 3.3 represent two different media with the unity normal vector, \mathbf{n} , directed from medium 1 to medium 2.

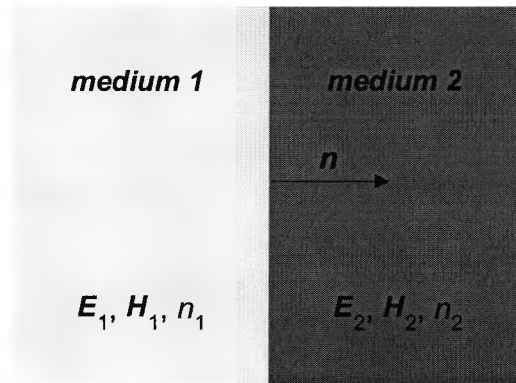


Fig. 3.3 The interface between medium 1 and medium 2.

The boundary condition will be applied in the absence of surface charges ($\rho = 0$) and surface currents ($J = 0$) as follows:

1. The tangential components of the electric field must be continuous, expressed as the vectorial product between n and $(E_1 - E_2)$ as follows:

$$n \times (E_1 - E_2) = 0 \quad (3.21)$$

2. The tangential components of the magnetic field must be continuous, expressed as vectorial product between n and $(H_1 - H_2)$ as follows:

$$n \times (H_1 - H_2) = 0 \quad (3.22)$$

3. The normal components of the electric flux density must be continuous, expressed as scalar product between n and $(D_1 - D_2)$ as follows:

$$n \cdot (D_1 - D_2) = 0 \quad (3.23)$$

4. The normal components of the magnetic flux density must be continuous, expressed as scalar product between n and $(B_1 - B_2)$ as follows:

$$\mathbf{n} \cdot (\mathbf{B}_1 - \mathbf{B}_2) = 0 \quad (3.24)$$

If one of two media becomes a perfect electric conductor then this condition, is called an '*electric wall*' boundary condition imposed as:

$$\mathbf{n} \times \mathbf{E} = 0 \quad \text{or} \quad \mathbf{n} \cdot \mathbf{H} = 0 \quad (3.25)$$

Condition (3.25) causes the magnetic field vector, \mathbf{H} , to vanish and ensures the continuity of the electric vector, \mathbf{E} at the boundary. On the other hand, if one of the two media becomes a perfect magnetic conductor, then this condition is called '*magnetic wall*' boundary condition, imposed as:

$$\mathbf{n} \times \mathbf{H} = 0 \quad \text{or} \quad \mathbf{n} \cdot \mathbf{E} = 0 \quad (3.26)$$

Condition (3.26) causes the electric field vector, \mathbf{E} , to vanish and ensures the continuity of the magnetic vector, \mathbf{H} at the boundary.

A vector can be specified by its components along any three mutual by perpendicular axes, as shown in Fig. 3.4. The vector \mathbf{A} can be uniquely expressed in terms of its components through the use of *unit vectors* \mathbf{i} , \mathbf{j} , \mathbf{k} which are defined as vectors of unit magnitude in the positive x , y , z directions, respectively. The scalar or dot product is the scalar quantity obtained of the multiplying the magnitude of the first vector by the magnitude of second and by cosine angle between them.

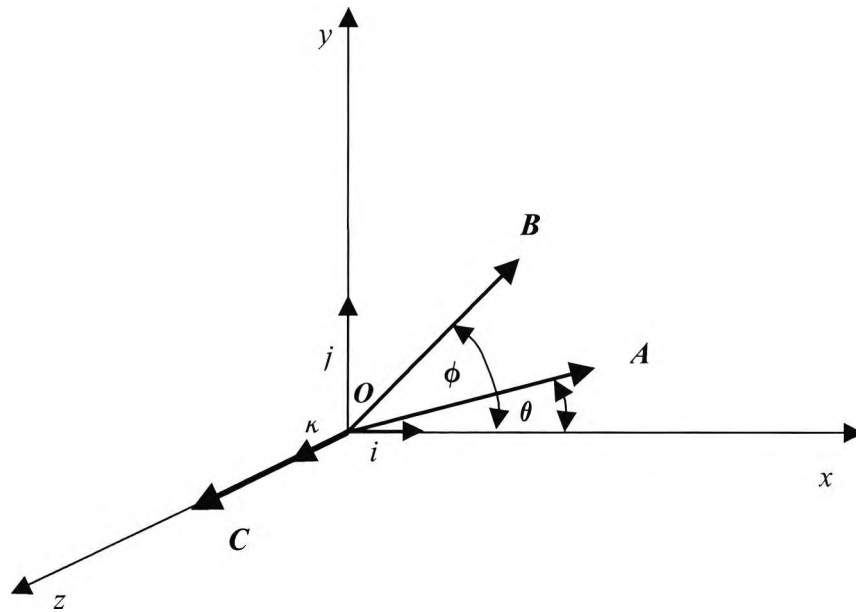


Fig. 3.4 Cartesian coordinate system.

The vectorial or cross product given by $C = A \times B = \begin{vmatrix} i & j & k \\ A_x & A_y & A_z \\ B_x & B_y & B_z \end{vmatrix}$ (3.27)

$$C = |AB \sin(\varphi - \theta)| \quad (3.28)$$

where C is the magnitude, and the scalar or dot product is:

$$A \cdot B = B \cdot A = AB \cos(\varphi - \theta) = A_x B_x + A_y B_y \quad (3.29)$$

From the definition of the coordinates systems such as that in Fig. 3.5, the following is given

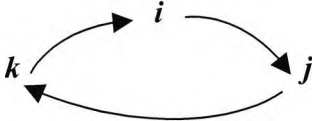
	Vectorial (cross) product	Scalar (dot) product
	$i \times i = 0$	$i \cdot i = 1$
	$j \times j = 0$	$j \cdot j = 1$
	$k \times k = 0$	$k \cdot k = 1$
	$i \times j = k$	$j \cdot k = 0$
	$j \times k = i$	$k \cdot i = 0$
	$k \times i = j$	$i \cdot j = 0$
	$j \times i = -k$	
	$i \times k = -j$	
	$k \times j = -i$	

Fig. 3.5 Properties of the *unity vectors*, i , j , and k in vectorial and scalar formulation.

3.7 Natural boundary conditions

The natural boundary condition is the condition which is automatically satisfied in the variational formulation (Davies, 1989). The advantage of the variational formulation is that the natural boundary condition is satisfied automatically, if left free. The scalar formulation of the finite element method, given by equation (3.18), has the continuity of $p(\partial\phi/\partial\hat{n})$ (where, $p = 1$ corresponds to the scalar formulation of quasi-TE and for $p = 1/n^2$ corresponds to the scalar formulation of quasi-TM) as the natural boundary condition. By contrast, the vector formulation H -field formulation described in equation (3.18) has the electric wall ($\mathbf{n} \cdot \mathbf{H} = 0$) as the natural boundary condition.

The importance of the natural boundary conditions is that it is often difficult, indeed sometimes impossible, to arrange for the essential conditions to be satisfied. At times these natural boundary conditions are not those that are required, as simply they do not correspond to the physical problem under consideration. In some cases if necessary the boundary conditions may be enforced in order to reduce the matrix size, but even in these situations they are automatically satisfied if left free. Sometimes it may be necessary to change and unsuitable natural boundary condition by introducing additional surface integral around the desired boundary. In the case where the symmetry of the waveguide exists, then we can easily impose the waveguide symmetry. However, it may

be necessary to analyze the structure with complementary symmetry conditions to obtain all the modes, although the exploration of the symmetry greatly reduces the computational cost.

3.8 Formulation of the finite element method.

The finite element analysis of any problem involves basically three steps (Sadiku, 1989) discretizing the solution region into finite number of subregions or elements as follows:

1. deriving governing equations for a typical elements
2. assembling of all elements in the solution region
3. solving the system of equations obtained.

Elements are classified as having one, two and three dimension, respectively. Within each element, the trial function is approximated by a suitable chosen polynomial. The transverse plane is covered with a grid of discrete nodes.

3.8.1 Finite element discretization

To find the solution for the two-dimension region shown in Fig. 3.6 (a) the region is divided into a number of element as shown in Fig. 3.6 (b) and then the solution region is subdivided into a number of nonoverlapping finite elements with three-node triangles. Problems with curved boundaries or surfaces have lead to elements with curved edges or faces (Koshiha and Inoue, 1992).

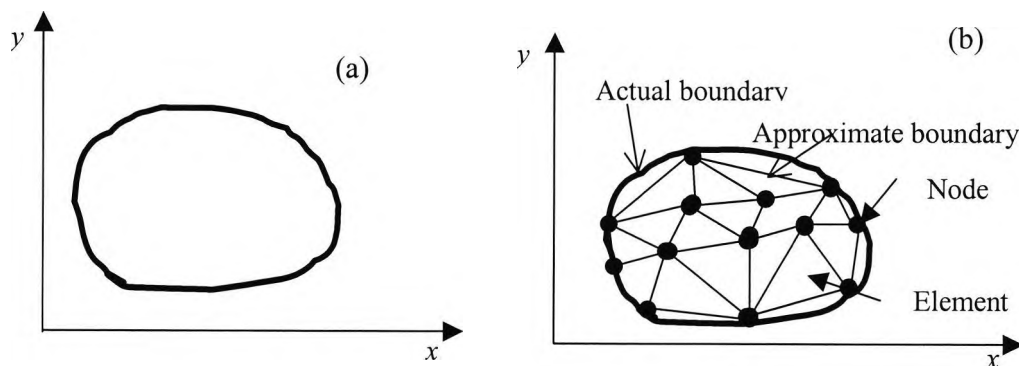


Fig. 3.6 (a) The solution region by FEM, and (b) Finite element discretization.

The unknown, H , is also considered to be discretised into corresponding subregions.

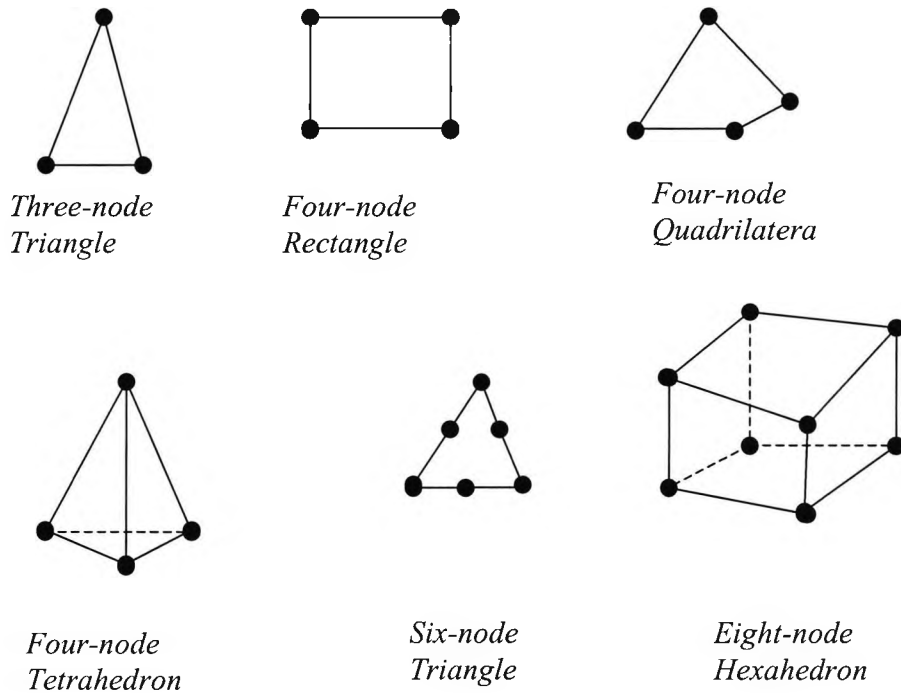


Fig. 3.7 The typical elements for one-, two-, and three-dimensional problems.

Problems with curved boundaries or surfaces have lead to elements with curved edges or faces (Koshiha and Inoue, 1992). Other type of elements in use include rectangular elements – two dimensional element, tetrahedral elements – three dimensional element, ring elements – axisymmetric two dimensional elements, triangular ring elements – axisymmetric three dimensional element and special element – edge, isoparametric or boundary elements. All these elements could either be of linear, second or higher order.

3.8.2 Shape functions

The unknown field, H , within each element is approximated by means of a suitable choice of the set of polynomials. These functions are called “shape functions” due to the fact that polynomials are relatively easy to manipulate. The choice of the functions should have continuity within each element and across the element boundaries. The

actual field over the entire domain should be approximated by trial sets of algebraic functions which can be uniquely defined, differentiated and integrated.

In the simplest case the elements are triangular and first degree polynomials are used. The total number of the terms involved in the polynomial is equal to the number of nodal degrees of freedom of the element. If the highest order term is x^N and y^N , it must also contain all possible terms $x^m y^n$, where $0 < m + n < N$, excluding other terms. The polynomial will be $M = (N+1)(N+2)/2$ terms or as we can see through the Pascal triangle in given in Fig. 3.8. The continuous field $\phi(x, y)$ of the domain may be replaced by a set of discrete values ($\phi_i, i = 1, 2, 3 \dots m$) where m is the total number of nodes.

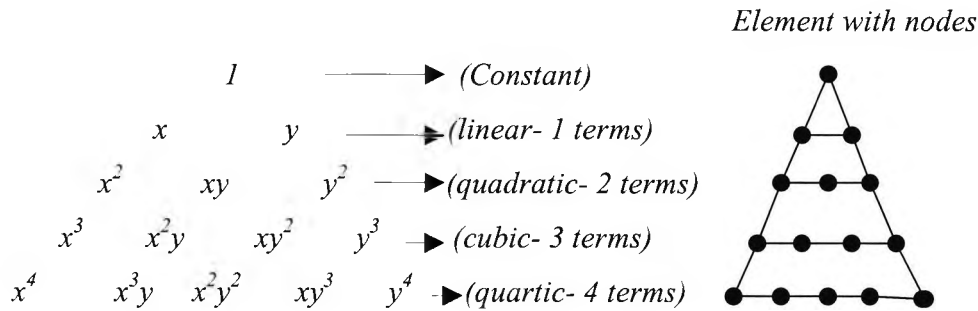


Fig. 3.8 Pattern of nodes on a single element compared with Pascal's triangle.

Our assumption of a linear variation of nodal values, ϕ_i within the triangular elements is the same as assuming that the $\phi_e(x, y)$ is uniform within the element. This continuity can be achieved by introducing the interpolation function, or so called "shape function" $N_i(x, y)$. The field inside the element $\phi_e(x, y)$ can be written as:

$$\phi_e(x, y) = \sum_i^3 N_i(x, y) \cdot \phi_i \quad (3.30)$$

and in matrix form can be written as follows:

$$\phi_e(x, y) = [N_1 \quad N_2 \quad N_3] \cdot \begin{Bmatrix} \phi_1 \\ \phi_2 \\ \phi_3 \end{Bmatrix} = [N] \cdot \{\phi_e\} \quad (3.31)$$

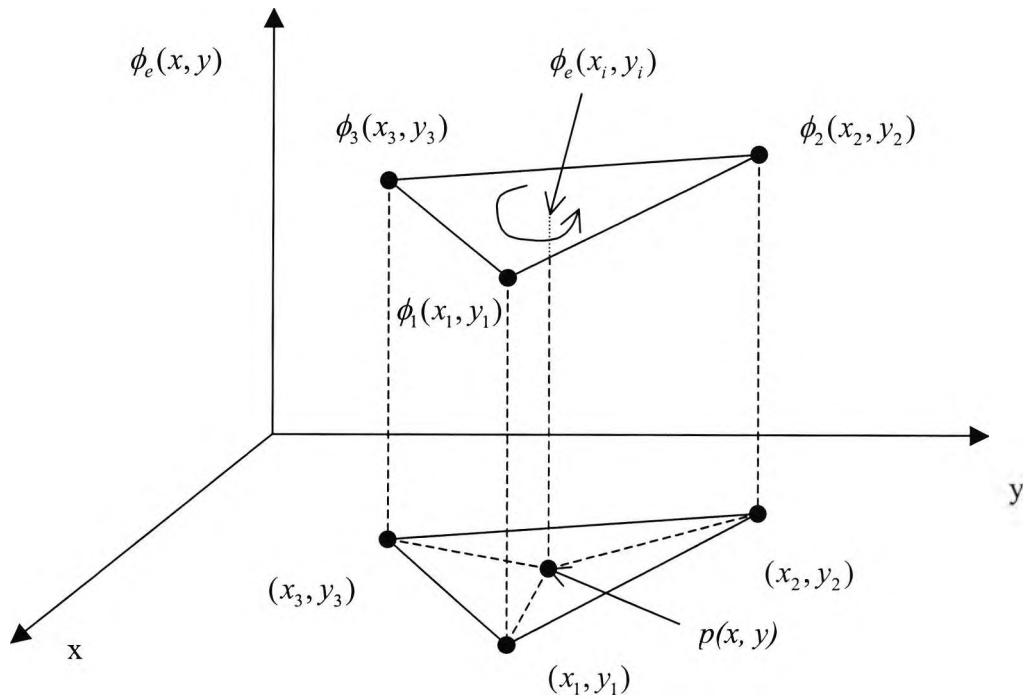


Fig. 3.9 Coordinates and node numbers of a typical first-order triangular elements.

A linear approximation of first element is:

$$\left. \begin{aligned} \phi_e(x_1, y_1) &= \alpha_1 + \alpha_2 x_1 + \alpha_3 y_1 \\ \phi_e(x_2, y_2) &= \alpha_1 + \alpha_2 x_2 + \alpha_3 y_2 \\ \phi_e(x_3, y_3) &= \alpha_1 + \alpha_2 x_3 + \alpha_3 y_3 \end{aligned} \right\} \quad (3.32)$$

in matrix form;

$$\begin{Bmatrix} \phi_e(x_1, y_1) \\ \phi_e(x_2, y_2) \\ \phi_e(x_3, y_3) \end{Bmatrix} = \begin{bmatrix} 1 & x_1 & y_1 \\ 1 & x_2 & y_2 \\ 1 & x_3 & y_3 \end{bmatrix} \begin{Bmatrix} \alpha_1 \\ \alpha_2 \\ \alpha_3 \end{Bmatrix} \quad (3.33)$$

After solving the matrix equation, the constants, α_1 , α_2 , and α_3 are as follows:

$$\left. \begin{aligned} \alpha_1 &= \frac{1}{2A_e} (\phi_e(x_2y_3 - x_3y_2) + \phi_e(x_3y_1 - x_1y_3) + \phi_e(x_1y_2 - x_2y_1)) \\ \alpha_2 &= \frac{1}{2A_e} (\phi_e(y_2 - y_3) + \phi_e(y_2 - y_1) + \phi_e(y_1 - y_2)) \\ \alpha_3 &= \frac{1}{2A_e} (\phi_e(x_3 - x_2) + \phi_e(x_1 - x_3) + \phi_e(x_2 - x_1)) \end{aligned} \right\} \quad (3.34)$$

where A_e is the area of the triangle given by

$$A_e = \frac{1}{2} \begin{vmatrix} 1 & x_1 & y_1 \\ 1 & x_2 & y_2 \\ 1 & x_3 & y_3 \end{vmatrix} = (x_2y_3 - x_3y_2) + (x_3y_1 - x_1y_3) + (x_1y_2 - x_2y_1) \quad (3.35)$$

This is similar to the equation given in (3.30). The corresponding polynomial of first-degree is $(a + bx + cy)$ applied over each element. The shape function can be written as (Davies, 1989).

$$[N]^T = \begin{bmatrix} N_1 \\ N_2 \\ N_3 \end{bmatrix} = \frac{1}{2A_e} \begin{bmatrix} x_2y_3 - x_3y_2 & y_2 - y_3 & x_3 - x_2 \\ x_3y_1 - x_1y_3 & y_3 - y_1 & x_1 - x_3 \\ x_1y_2 - x_2y_1 & y_1 - y_2 & x_2 - x_1 \end{bmatrix} \begin{bmatrix} 1 \\ x \\ y \end{bmatrix} \quad (3.36)$$

where T denotes the transpose of the existing matrix. The shape function matrix can be written in more convenient form.

$$[N]^T = \begin{bmatrix} N_1 \\ N_2 \\ N_3 \end{bmatrix} = \begin{bmatrix} a_1 + b_1x + c_1y \\ a_2 + b_2x + c_2y \\ a_3 + b_3x + c_3y \end{bmatrix} \quad (3.37)$$

By comparing equations (3.36) and (3.37), the coefficients a_i , b_i and c_i ($i=1, 2, 3$) may be calculated as

$$a_1 = \frac{x_2 y_3 - x_3 y_2}{2A_e} \quad (3.38)$$

$$b_1 = \frac{y_2 - y_3}{2A_e} \quad (3.39)$$

$$c_1 = \frac{x_3 - x_2}{2A_e} \quad (3.40)$$

In the same way the other coefficients, a_2 , b_2 , c_2 , a_3 , b_3 , c_3 can be calculated by the exchange of $1 \rightarrow 2 \rightarrow 3$ in equations (3.38), (3.39) and (3.40).

Consider a typical point $p(x, y)$ inside the triangular element shown in Fig. 3.9. The local coordinate L_1 can be written as:

$$L_1 = \frac{\text{area of the triangle p-2-3}}{\text{area of the triangle 1-2-3}} \quad (3.41)$$

It can be also be defined as:

$$N_1 = \frac{\begin{vmatrix} 1 & x & y \\ 1 & x_2 & y_2 \\ 1 & x_3 & y_3 \end{vmatrix}}{\begin{vmatrix} 1 & x_1 & y_1 \\ 1 & x_2 & y_2 \\ 1 & x_3 & y_3 \end{vmatrix}} = \frac{\begin{vmatrix} x_2 & y_2 \\ x_3 & y_3 \end{vmatrix} + (y_2 - y_3)x + (x_3 - x_2)y}{2A_e} = a_1 + b_1 x + c_1 y \quad (3.42)$$

in the same way we can define N_2 , and N_3 where

$$\sum_{i=1}^3 N_i = 1 \quad (3.43)$$

It is obvious that when the shape function N_1 is evaluated at node 1 (x_1, y_1) it gives the value 1, and the value 0 at nodes 2 and 3 and all other points on the line passing through the nodes, and therefore it is unique interpolation first degree polynomial for node 1. Similarly the shape functions N_2 and N_3 give the value of 1 at node 2 and 3 respectively and 0 at the other nodes.

3.8.3 Element and global matrices

The solution of the optical waveguide problems using the finite element method can be reduced to a standard eigenvalue problem as in equation (3.17). In this section, the element matrices are derived, based on the full \mathbf{H} -field variational expression of equation (3.18).

Within each element, the nodal magnetic field vectors can be written as

$$\mathbf{H}_x(x, y) = [N_1 \quad N_2 \quad N_3] \begin{Bmatrix} H_{x1} \\ H_{x2} \\ H_{x3} \end{Bmatrix} \quad (3.44)$$

$$\mathbf{H}_y(x, y) = [N_1 \quad N_2 \quad N_3] \begin{Bmatrix} H_{y1} \\ H_{y2} \\ H_{y3} \end{Bmatrix} \quad (3.45)$$

$$\mathbf{H}_z(x, y) = [N_1 \quad N_2 \quad N_3] \begin{Bmatrix} H_{z1} \\ H_{z2} \\ H_{z3} \end{Bmatrix} \quad (3.46)$$

The nodal magnetic field vector $[\mathbf{H}]_e$ can be expressed according to eq. (3.44)-(3.46).

$$[\mathbf{H}]_e = \begin{bmatrix} \mathbf{H}_x(x,y) \\ \mathbf{H}_y(x,y) \\ \mathbf{H}_z(x,y) \end{bmatrix} = \begin{bmatrix} N_1 & N_2 & N_3 & 0 & 0 & 0 & 0 & 0 & 0 \\ 0 & 0 & 0 & N_1 & N_2 & N_3 & 0 & 0 & 0 \\ 0 & 0 & 0 & 0 & 0 & 0 & N_1 & N_2 & N_3 \end{bmatrix} \begin{Bmatrix} \mathbf{H}_{x1} \\ \mathbf{H}_{x2} \\ \mathbf{H}_{x3} \\ \mathbf{H}_{y1} \\ \mathbf{H}_{y2} \\ \mathbf{H}_{y3} \\ \mathbf{H}_{z1} \\ \mathbf{H}_{z2} \\ \mathbf{H}_{z3} \end{Bmatrix} \quad (3.47)$$

Equation (3.10.4) can also be written as:

$$[\mathbf{H}]_e = [N]\{\mathbf{H}\}_e \quad (3.48)$$

where $\{\mathbf{H}\}_e$ represents the column vector of the nodal values of the three field components, and $[N]$ is the shape function matrix. Similarly, the eq. $(\nabla \times \mathbf{H})_e$ can be written as:

$$(\nabla \times \mathbf{H})_e = \nabla \times [N]\{\mathbf{H}\}_e = \begin{bmatrix} 0 & -\frac{\partial}{\partial z} & \frac{\partial}{\partial y} \\ \frac{\partial}{\partial z} & 0 & -\frac{\partial}{\partial x} \\ -\frac{\partial}{\partial y} & \frac{\partial}{\partial x} & 0 \end{bmatrix} [N]\{\mathbf{H}\}_e = [\mathbf{Q}]\{\mathbf{H}\}_e \quad (3.49)$$

where the matrix $[\mathbf{Q}]$ can be defined as:

$$[\mathbf{Q}] = \begin{bmatrix} [0] & -\frac{\partial[N]}{\partial z} & \frac{\partial[N]}{\partial y} \\ \frac{\partial[N]}{\partial z} & [0] & -\frac{\partial[N]}{\partial x} \\ -\frac{\partial[N]}{\partial y} & \frac{\partial[N]}{\partial x} & [0] \end{bmatrix} = \begin{bmatrix} 0 & j\beta[N] & \frac{\partial[N]}{\partial y} \\ -j\beta[N] & [0] & -\frac{\partial[N]}{\partial x} \\ -\frac{\partial[N]}{\partial y} & \frac{\partial[N]}{\partial x} & 0 \end{bmatrix} \quad (3.50)$$

$$\left. \begin{aligned} [0] &= [0 \quad 0 \quad 0] \\ [N] &= [N_1 \quad N_2 \quad N_3] \\ \frac{\partial[N]}{\partial x} &= [b_1 \quad b_2 \quad b_3] \\ \frac{\partial[N]}{\partial y} &= [c_1 \quad c_2 \quad c_3] \end{aligned} \right\} \quad (3.51)$$

Substituting equations (3.48) and (3.49) into equation (3.18) the vector \mathbf{H} -field formulation gives

$$\int_{\Omega} \epsilon^{-1} \{\mathbf{H}\}_e^T [\mathbf{Q}]^* [\mathbf{Q}] \{\mathbf{H}\}_e d\Omega - \omega^2 \int_{\Omega} \mu \{\mathbf{H}\}_e^T [N]^T [N] \{\mathbf{H}\}_e d\Omega = 0 \quad (3.52)$$

where the integration is carried out over the element domain, Ω , T denotes the transpose, and $*$ denotes the complex conjugate transpose. By applying the Rayleigh-Ritz procedure (differentiating with respect to the field nodal values and equalizing to zero) the following are obtained:

$$[\mathbf{A}]\{\mathbf{H}\} - \omega^2 [\mathbf{B}]\{\mathbf{H}\} = 0 \quad (3.53)$$

$$[\mathbf{A}] = \sum_e [\mathbf{A}]_e = \sum_e \int_{\Omega} \epsilon^{-1} [\mathbf{Q}]^T [\mathbf{Q}] d\Omega \quad (3.54)$$

$$[\mathbf{B}] = \sum_e [\mathbf{B}]_e = \sum_e \int_{\Omega} \mu [N]^T [N] d\Omega \quad (3.55)$$

where $\{H\}$ contains all H -field nodal values of the waveguide cross section, $[A]$ and $[B]$ are global matrices of the eigenvalue and $[A]_e$ and $[B]_e$ can be evaluated as:

$$[\mathbf{A}]_e = \varepsilon^{-1} \int_{\Omega} \begin{bmatrix} \beta^2 [N]^T [N] + \frac{\partial [N]^T}{\partial y} \frac{\partial [N]}{\partial y} & -\frac{\partial [N]^T}{\partial y} \frac{\partial [N]}{\partial x} & \beta [N]^T \frac{\partial [N]}{\partial x} \\ -\frac{\partial [N]^T}{\partial y} \frac{\partial [N]}{\partial x} & \beta^2 [N]^T [N] + \frac{\partial [N]^T}{\partial x} \frac{\partial [N]}{\partial x} & \beta [N]^T \frac{\partial [N]}{\partial y} \\ \beta [N]^T \frac{\partial [N]}{\partial x} & \beta [N]^T \frac{\partial [N]}{\partial y} & \frac{\partial [N]^T}{\partial y} \frac{\partial [N]}{\partial y} + \frac{\partial [N]^T}{\partial x} \frac{\partial [N]}{\partial x} \end{bmatrix} d\Omega \quad (3.56)$$

$$[\mathbf{B}]_e = \mu \int_{\Omega} \begin{bmatrix} [N]^T [N] & [0]^T [0] & [0]^T [0] \\ [0]^T [0] & [N]^T [N] & [0]^T [0] \\ [0]^T [0] & [N]^T [N] & [0]^T [0] \end{bmatrix} d\Omega \quad (3.57)$$

The shape functions given in (3.56) and (3.57) can be evaluated using (Davies J. B, 1989) as:

$$\int_{\Omega} N_1^i N_2^j N_3^k d\Omega = \frac{(i! j! k! 2!)}{(i+j+k+2)!} \cdot A_e \quad (3.58)$$

3.8.4 Infinite elements analysis

As mentioned in previous sections, the dielectric waveguides, in particular the optical waveguides, can have open boundaries. For this type of structure a finite field exists in the region outside the guide core and the field decays slowly (in an exponential manner). This extension is important for the solution close to cut off. In the orthodox finite element discretization, the region considered cannot extend to infinity, yet in many

waveguides the problem domain extends to infinity. Rahman and Davies (Rahman, 1984) have developed the infinite element approach which takes into consideration the effective region extending to infinity, as shown in Fig. 3.10 by also keeping the same matrix order.

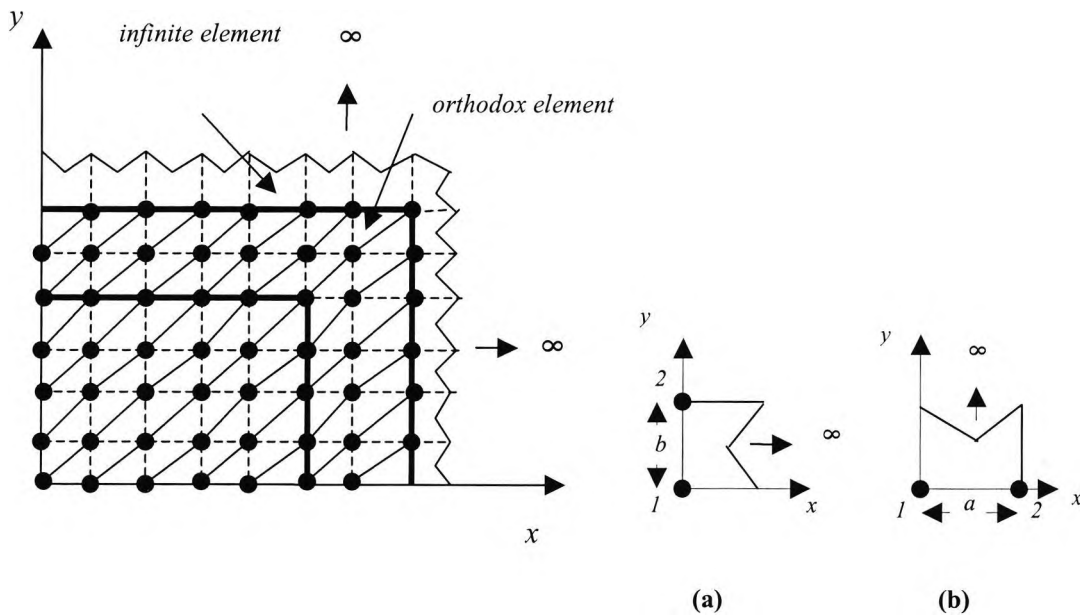


Fig. 3.10 Rectangular (1/4 symmetry) dielectric waveguide cross section discretized into orthodox and infinite elements.

In Cartesian coordinates, if an element extends to infinity in the positive x -direction, as shown in the Fig. 3.10 (a), the exponential decay is assumed to be in x -direction whereas the convenient shape function dependence as in the y -direction. Based on these conditions, the field components such as H_x can be written as follows:

$$H_x = f(x, y)H_{xi} = \sum_{i=1}^2 N_i(x, y)H_{xi} \quad (3.59)$$

where $N_i(x, y)$ is shape function in the y -direction, and at L , decay length can be written as:

$$N_i(x, y) = f_i(y) \cdot e^{(-x/L)} \quad (3.60)$$

At nodes 1 and 2, as shown in Fig. 3.10 (a), the field values, H_{x1} and H_{x2} and also the shape functions N_1 and N_2 can be defined as:

$$H_x = f_1(y) \cdot e^{(-x/L)} \cdot H_{x1} + f_2(y) \cdot e^{(-x/L)} \cdot H_{x2} = [N_1 \quad N_2] \begin{Bmatrix} H_{x1} \\ H_{x2} \end{Bmatrix} \quad (3.61)$$

$$N_1 = \frac{y}{b} \cdot e^{(-x/L)} \quad (3.62)$$

$$N_2 = \left(1 - \frac{y}{b}\right) \cdot e^{(-x/L)} \quad (3.63)$$

where b is the width of the infinite element in the y -direction and similarly other field components, H_y and H_z can be expressed in this way. The same approach can be used to analyze the infinite elements extending in the y -direction, as shown in Fig. 3.10 (b) and also for corners.

3.9 Spurious Solutions in finite element method

The most serious and difficult problem in finite element analysis is the appearance of spurious, or non-physical solutions interspersed with real solutions. Analysis of the optical waveguide is also associated with spurious modes. Many reasons could lie behind the spurious modes, such as the enforcement of the boundary conditions, or due to the nonzero divergence of the trial fields (Rahman and Davies, 1984). The spurious solution appears also in the finite element analysis using the full vector \mathbf{H} field. Maxwell's equations (3.9) and (3.10) do not satisfy the condition where $\nabla \cdot \mathbf{B} = 0$ which could be a one of the causes of spurious modes. In order to eliminate these spurious

modes Rahman and Davies, (1984) have utilized the penalty function which defines the solution if it is a real or spurious solution, and this can be achieved when the eigenvector of the physical mode satisfies the zero divergence condition $\text{div } \mathbf{H} = 0$. After each solution is obtained from the divergence condition, $\text{div } \mathbf{H}$ has to be calculated over the waveguide cross section. The value of $\text{div } \mathbf{H}$ has to be examined for different solutions, and only solution with a low value of $\text{div } \mathbf{H}$ will be considered as a real mode. The value of $\text{div } \mathbf{H}$ may be calculated from the discrete nodal field obtained after the solution of the eigenvalue equation, (3.17).

Rahman and Davies (1984), have used the penalty function approach, where an integral is added to the functional equation (3.20) in order to satisfy the zero divergence condition, $\text{div } \mathbf{H} = 0$. Thus the functional penalty term can be written as:

$$\omega^2 = \frac{\int (\nabla \times \mathbf{H})^* \cdot \hat{\epsilon}^{-1} \cdot (\nabla \times \mathbf{H}) d\Omega + \left(\frac{\alpha}{\epsilon_0} \right) \int (\nabla \cdot \mathbf{H})^* \cdot (\nabla \cdot \mathbf{H}) d\Omega}{\int \mathbf{H}^* \cdot \hat{\mu} \cdot \mathbf{H} d\Omega} \quad (3.64)$$

where α is the dimensionless penalty coefficient which can be estimated around $(1/\epsilon_g)$, where ϵ_g is the dielectric of the waveguide core. It has been confirmed that the higher value of the penalty coefficient leads to a reduction of the spurious modes, but it is possible that propagation constant of the real mode can deteriorate slightly.

Various approaches have been proposed by different research groups in order to reduce the spurious solutions. Mabaya, Lagasse and Vandebulcke proposed an scalar finite element formulation, but spurious modes does not appear at all with a scalar formulation. One of the formulations, in terms of the transverse \mathbf{H} -field, has been advanced by Hayata *et al.* and completely eliminates the spurious solution, and the penalty coefficient is not included. The component fields H_x and H_y are represented in the way that the shape functions have been eliminated, but the H_z component involves a stage involving differentials and is more an approximation representation. Davies and Rahman have established a successful new scheme (Davies, 1993), for avoiding the spurious modes. The first method involves a new formulation of the transverse magnetic

field with no special new finite elements, while the second method uses equation (3.20) but with a new vector finite element application.

3.10 Matrix solution techniques in finite element method

The choice of the algorithm in solving the eigenvalue matrix equations is very important in computer power and time consumption in the use of the FEM. The global matrices $[A]$ and $[B]$ given in (3.54) and (3.55) are highly sparse. Both matrices can be complex and asymmetric and this can cause difficulty in solving the problem due to the lack of efficient computer library routines. There is a large number of different methods available to solve the matrix eigenvalue problems involving sparse matrices. In this work the sparse matrix eigenvalue problem has been solved by an iteration process applied simultaneously to a subspace of eigenvectors, using the so-called method of subspace iterations (Rahman and Davies, 1984) and (Bathe and Wilson, 1976)

Summary

In this chapter the finite element method and its application has been presented. The variational principles in the modal solutions for microwave and optical waveguides have been studied. Various aspects of the finite element method have been examined, including, different scalar and vector formulations, boundary conditions, natural boundary conditions, shape functions, global matrices and infinite elements. Finally the use of the penalty term approach to reduce the non-physical solutions or spurious mode has been discussed. This chapter, in conjunction with the least squares boundary residual method presented in Chapter 2 represents a solid mathematical basis for the work involved in the analysis of optical waveguide and microwave problems in the subsequent chapters of this thesis. Flow chart of FEM, LSBR and Quasi-TEM analysis and their interaction are illustrated in the Appendix 3.

Optical Modulators

4.1 Introduction

Optic modulators are among the most promising and useful components in optical communications systems. In recent years, optical fibre communication networks have been experiencing a rapid growth, driven by the explosive growth of internet data traffic and voice traffic. In order best to utilize the enormous capacity of the optical fibre, intensity modulation direct detection (IMDD) systems with time division multiplexing (TDM) and/or wavelength division multiplexing (WDM) are widely used. In TDM systems, the low bit-rate baseband signals are multiplexed in time to a single-wavelength high bit-rate signal while in WDM systems, the signals are multiplexed in the wavelength domain such that more than one wavelength is guided in a single optical fibre. Therefore, the development of high-speed TDM systems will be the basis for future WDM systems.

Optical modulators have been developed for many years. During the first ten years external modulators were necessarily used with a light source (laser light), including ferroelectrics and anti-ferroelectrics, such as KDP and ADP. Over the last three decades, modulators were developed using both lithium niobate (LiNbO_3) or LN and GaAs or semiconductor modulators. With numerous refinements, such as single-mode waveguide creation by Ti-doped diffusion and travelling-wave electrode configuration, the technology has progressed to produce directional couplers and Mach-Zehnder interferometers with high bandwidth.

In the record, remaining until 1992, in long distance transmission experiments at AT&T Bell Labs (Mollenauer 1991), LiNbO_3 travelling wave modulators (Jungerman 1990) were used. These devices represented the state of the art in high bandwidth of that time, external light modulators, but guided wave quantum well modulators (Wakita 1990), traveling wave modulators based on electro-optic, organic materials (Girton 1991) and

multi-quantum well Fabry-Perot modulators (Simes, 1991), have all demonstrated similar or better performance in research laboratories.

Later the 3-dB bandwidth of a directly modulated laser has been reported to be 48 GHz (Zhang, 1997) at a wavelength of 0.98 μm . A 30 GHz bandwidth of a 1.55- μm laser has been reported from Masuni, 1997. These bandwidths are large enough for a system with channel speed as high as 40 Gbit/s; however, the biggest problem for a directly modulated laser is its frequency chirping, which represents itself as a wavelength (frequency) variation between on and off states (Henry 1982, Koch 1984, Koch 1986, Osinski 1987, Koyama 1988). Due to this wavelength variation, the optical pulse will have an extra broadening effect when transmitting through a dispersive fibre, and hence degrade the system performance.

Frequency chirping also exists in light modulated with external modulators (Koyama 1988) due to the Kramers-Kronig relations (Hutchings 1992) between the real and the imaginary parts of the dielectric constant, which is also the reason for frequency chirping in lasers.

External modulators made typically from titanium diffused lithium niobate (Ti: LN), in a Mach-Zehnder type structure with a travelling-wave electrode (Wooten, 2000) are the most promising due to their large electrooptic coefficients, low bias drift, zero or adjustable frequency chirp and their better coupling efficiency when directly butt-coupled to single mode fibres. Today 2.5 Gb/s and 10 Gb/s modulators are standard commercial products and 40 Gb/s modulators are also emerging on to the market after successful prototype demonstrations (Dagli, 1999). However, the continuous demand for further increases in data rate has the effect of pushing their operating frequency well into the millimeter wave range. To design more efficient ultra-high-speed modulators, ridge-type Z-cut LN modulators have been reported (Noguchi, 1995, Mitomi, 1995, Noguchi, 1998, Minakata, 2001), which show higher optical bandwidth than conventional planar or backslot-type (Minakata, 2001) LN modulators. LiNbO_3 modulators are, among the available kinds of modulators, the most widely commercialized. An optical 3-dB bandwidth as high as 75 GHz has been demonstrated (Noguchi 1994); however, the highest electrical 3-dB bandwidth is 40 GHz (Noguchi 1998, Mitomi 1998). The lowest drive voltage is 2.9 V (Noguchi 1998). The drawback of this type of modulator is the

bias point sensitivity to temperature and it is not suitable to be integrated with driving circuitry or lasers. The drive voltage of LiNbO₃ modulator (2.9 ~ 5 V) is generally higher than that of the electroabsorption modulator (1.2 ~ 3.3 V).

However, there is a continued demand for the design of more efficient ultra-high-speed semiconductor electrooptic modulators, (Wang, 1988, Walker, 1991 and Khan 1993) and GaAs/Al_xGa_{1-x}As travelling-wave electrooptic modulators offer the obvious advantage of monolithic integration of active/passive photonic and electronic devices to form opto-electronic integrated circuits (OEIC) and/or laser sources. GaAs/AlGaAs modulators have the advantage of possible integration with driving circuitry or a laser source, with a better opportunity to obtain an optical and electrical wave velocity match. These modulators usually use bulk materials and have a thick intrinsic layer (Spickermann 1996). However, due to the small electro-optic coefficient, these modulators usually require long interaction region and the drive voltages for these modulators are very high, making it hard to use them in communications. GaAs is the material of choice for many optoelectronic components such as lasers and detectors. Although GaAs electrooptic modulators suffer from a relatively small electrooptic coefficient, compared to the traditional materials like LiNbO₃ this is however, partly compensated by their higher refractive indices. Often travelling-wave designs are employed to increase the interaction length between the optical signal and the electrical signal and thus reduce the modulator half-wave voltage (V_{π}). These designs will increase the interaction length up to a point, but they are still limited by the velocity mismatch between the optical signal and the microwave signal.

Multiple quantum well (MQW) modulators InGaAsP/InP and InGaAlAs/InAlAs MQW Mach-Zehnder electrooptic modulators have bandgap energies close to the photon energy. These modulators use multiple quantum well structures, have thin intrinsic layers, and therefore have a larger electric field. Due to Kramers-Kronig relations (Hutchings, 1992), the electric field-induced index change is enhanced when close to bandgap. Also, quantum confined Stark effect will further reduce the drive voltage. These devices can be made with an order of magnitude shorter than the GaAs/AlGaAs devices, and have been demonstrated with reasonably low drive voltages. InGaAsP/InP MQW EO modulators have been integrated with long-wavelength lasers and transmission

experiments have also shown promising performance (Rolland, 1998). Table 4.1 represents the development and performance characteristics of four main traveling-electrooptic modulators, where ER_{max} is maximum extinction ratio.

LiNbO₃	V_{π} (V)	f3dB _(electrical) (GHz)	ER_{max} (dB)	Device Length & λ
Kawano, 1989	4.7	10		$\lambda=1.5 \mu\text{m}$
Gopalakrishnan, 1992	5.0	15		$\lambda=1.5 \mu\text{m}$
Dolfi, 1992	12.3	44		$\lambda=1.5 \mu\text{m}$
Rangaraj, 1992	5.0	10		$\lambda=1.5 \mu\text{m}$
Noguchi, 1994	5.0	40	22	$\lambda=1.5 \mu\text{m}$
Noguchi, 1998	2.9	30		L=2.7 cm, $\lambda=1.5 \mu\text{m}$
Mitomi, 1998	3	40		L=2.7 cm, $\lambda=1.5 \mu\text{m}$
This work(Haxha &Rahma, 2002)	5.0	>40		L=2 cm, $\lambda=1.5 \mu\text{m}$
GaAs/AlGaAs	V_{π} (V)	f3dB _{elec} (GHz)	ER_{max} (dB)	Device Length & λ
Wang, 1988		16	13	L=1.3 μm
Nees, 1989 (TW Buried coplanar)	288	110		$\lambda=1300 \text{ nm}$
Walker, 1991		22.5		(8 GHz* $\mu\text{m}/\text{V}$) $\lambda=1.5 \mu\text{m}$
Spickermann, 1996	14	>40		$\lambda=1.5 \mu\text{m}$
Khazaei, 1998	20.5	22	9.5	$\lambda=1.5 \mu\text{m}$
This work(Haxha &Rahma, 2002)	10	>40		$\lambda=1.5 \mu\text{m}$
InGaAsP/InP (MQW)	V_{π} (V)	f3dB _{Be} (GHz)	ER_{max} (dB)	Device Length & λ
Agrawal, 1995	6.8	14	19	$\lambda=1.5 \mu\text{m}$
Fetterman, 1996	6.0			L=300 μm $\lambda=1.5 \mu\text{m}$
Rolland, 1998	~4.0	~10	16 at (10 Gb/s)	L=500 μm , $\lambda=1.5 \mu\text{m}$
Rolland, 1998	2.6	~2.5		$\lambda=1.3 \mu\text{m}$, L=1200 μm
InGaAsP/InAlAs(MQW)	V_{π} (V)	f3dB _{Be} (GHz)	ER_{max} (dB)	Device Length & λ
Wakita, 1992	3.8	20	20	L=300 μm , $\lambda=1.5 \mu\text{m}$
Polymer	V_{π} (V)	f3dB _{Be} (GHz)	ER_{max} (dB)	Device Length
Van Schooti, 1996	7.5	20	20	L=2 cm, $\lambda=1.5 \mu\text{m}$
Lee, 1997	4.85			L=1.5 cm, $\lambda=1.5 \mu\text{m}$
Ermer, 1997	3.5			L=2.6 cm, $\lambda=1.5 \mu\text{m}$
Chen, 1997				$\lambda=1.3 \mu\text{m}$
Chen, 1999	<10	40		$\lambda=1.5 \mu\text{m}$

Table 4.1 Development and performance of optical modulators.

Polymer modulators have demonstrated less than 3-dB (optical) drop within the whole W band (75 ~ 110 GHz). However, these modulators usually require large drive voltage. Therefore, this restriction of large drive voltage has made them far from practical for use for ultra-high speed fiber optic communications.

Also, most of the (MQW) modulators reported (as illustrated in the Table. 4. 1) are lumped devices, which means that these devices are shorter than 200 μm . However, it is difficult to fabricate such a short device and the cleaving length restricts the minimum device length and hence the modulation speed. Another disadvantage of these modulators is that such a short device is hard to package because microwave strip lines, as well as the optical components, must be assembled close to the device. In order to achieve this ultra-short length, passive waveguides were grown to make the whole device long enough to handle (Ido, 1996). This therefore complicates the fabrication process. Also, the maximum extinction ratio of these modulators is lower and the drive voltage is higher compared to longer electrooptic modulators, like LiNbO_3 and GaAs modulators.

External modulators made from titanium diffused lithium niobate (Ti: LN), in a Mach-Zehnder type structure with a travelling-wave electrode (Wooten, 2000) and GaAs/AlGaAs are the most promising modulators.

The bandwidth of a high-speed optical modulator with a travelling-wave electrode is primarily limited by the velocity mismatch between the optical carrier wave and the modulating microwave signal. For high-speed modulators, when phase velocity matching is achieved, the limiting factor is then the overall microwave propagation losses. At lower operating frequencies, the electrode conduction loss, α_C , dominates; however, as the operating frequency is extended beyond 40 GHz, the dielectric loss, α_d , is expected to play an increasingly important role in the bandwidth determination. In practical applications, the characteristic impedance, Z_C , of the electrode also affects the performance of a high-speed modulator, which is typically matched to an external circuit of impedance 50 Ω .

To date, most of the work reported has focused only on obtaining the velocity matching condition as one of the essential aims of the design process. For the next generation of ultra-high-speed modulators, it is necessary to optimize the electrode structures to

achieve simultaneous matching of velocity and impedance along with a reduced overall microwave loss.

4.2 Various optical modulators

External modulators are very popular and widely used in optoelectronics. Various types of external modulator have been developed. Based on the type of the material used electrooptic modulators can be classified as: Ceramics (crystals), semiconductors and polymer electrooptic modulators. Ceramic (crystal) modulators, as illustrated in the Fig. 4.1 are classified as: LiNbO_3 , LiTaO_3 and KTP modulators. Semiconductor modulators are categorized as: GaAs, InP and InGaAsP modulators, illustrated in Fig.4.4 and Fig. 4.5, and the polymer (organic polymer) modulators are PMMA modulators. Also, these modulators (Ceramics, semiconductors and polymer) can be classified as: phase, amplitude and polarization modulators.

The most commonly used materials for external modulators are LiNbO_3 , GaAs (III-V) compound semiconductors, and electrooptic polymers. There are three different types of commercially available LiNbO_3 modulators.

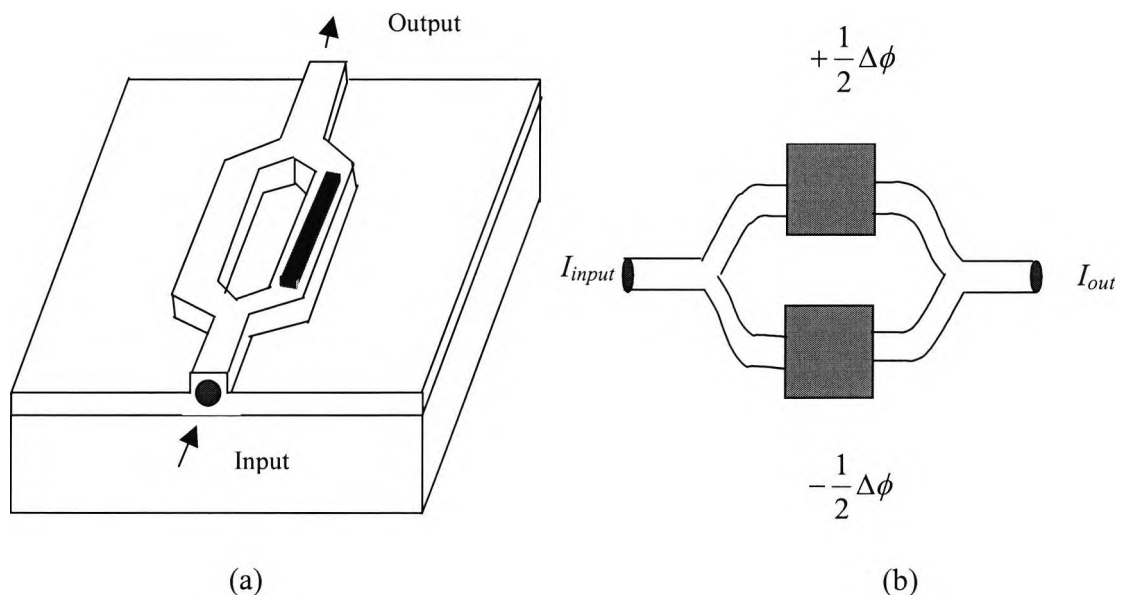


Fig. 4.1 Mach-Zehnder modulator (a), Mach-Zehnder Interferometric (MZI) modulator (b).

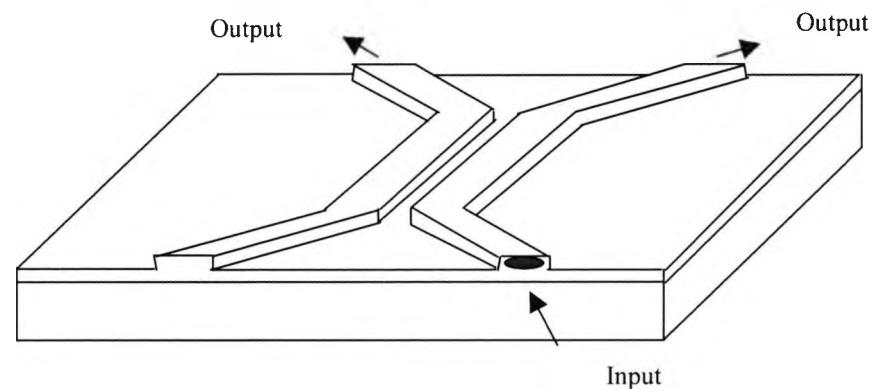


Fig. 4.2 Directional coupler based modulator.



Fig. 4.3 Deeply-etched waveguide electrooptic GaAs modulator, Mach-Zehnder part.

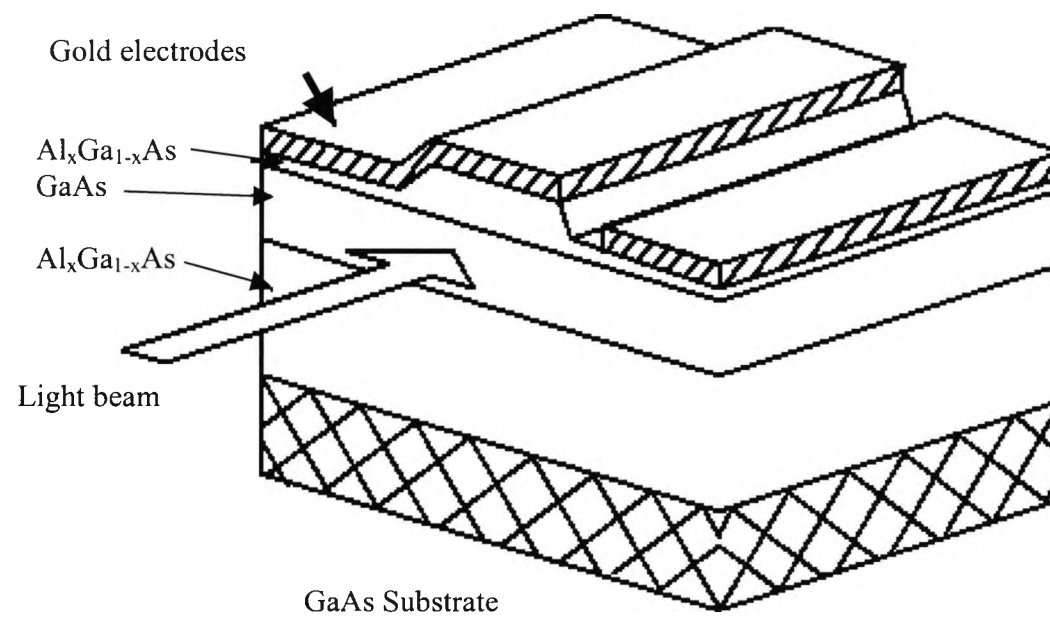


Fig. 4.4 Schematic structure of a semiconductor modulator (GaAs).

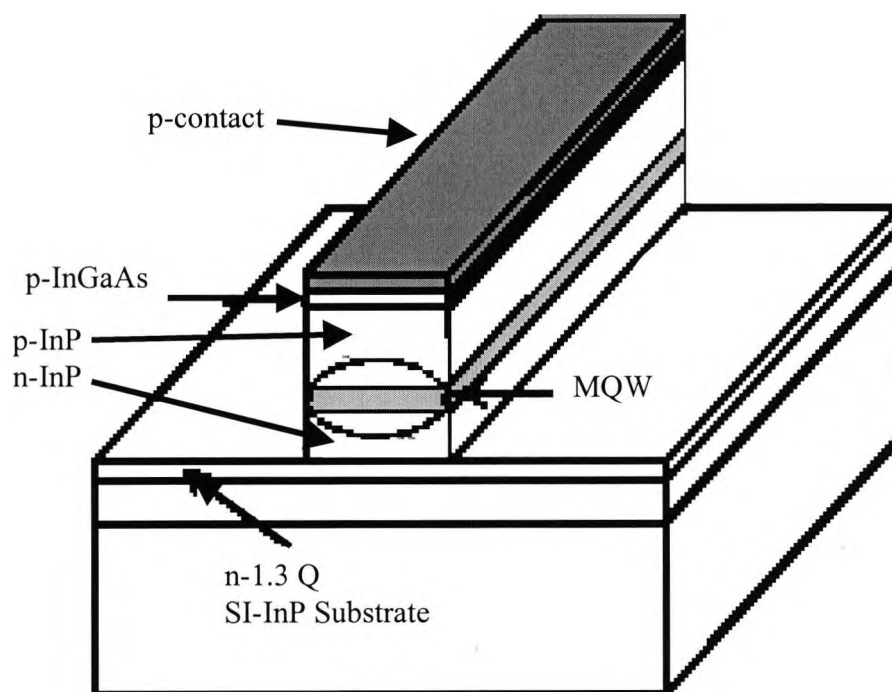


Fig. 4.5 Schematic structure of an InGaAsP/InGaAsP MQW electroabsorption modulator.

The differences depend on the orientation (or cut) of the crystal, and the method of waveguide fabrication. The crystals (LiNbO_3) themselves are available in wafers of X-cut, Z-cut, and Y-cut orientations, with the axis of the cut being perpendicular to substrate surface. Z-cut modulators typically use titanium ions for waveguide fabrication, while X-cut modulators can use either titanium ions or hydrogen ions (protons). The Y-cut orientation does not yield high enough electro-optic coefficients for an effectively functioning modulator. Modulators that are X-cut proton waveguides typically do not require much (if any) DC bias voltage. These types of modulators can be CPW (Coplanar waveguide) and asymmetric coplanar strip A-CPS. Furthermore, they can be etched and unetched electrooptic modulators. Usually these types of modulators are built from LiNbO_3 .

Different configuration types of the modulators are illustrated in Fig. 4.1-Fig. 4.5. The design of electrooptic modulators usually relies on the use of either directional coupler (DC) or Mach-Zehnder arrangements. The principal of operation of Mach-Zehnder inter

ferromagnetic modulators is when the incoming optical beam is separated equally in a “waveguide Y” and then recombined. If the phase shift in both arms is identical, the optical waveguide modes interfere constructively and all the power reappears in the output (minus losses). When the net phase-shift difference between the arms is 180° , the modes in the waveguides are 180° out of phase and excite an asymmetric mode in the output waveguide. If the output waveguide is a single-mode guide, there will be no power emerging from it; the power will be radiated out into substrate and is lost. Thus the power can be controlled by a voltage applied to the waveguides. A net phase-shift difference of 180° produces an asymmetric higher-order mode in the output waveguide as illustrated in Fig. 4.1. In the directional coupler based electrooptic modulator the light is split into two or more coupled (interacting) modes, the coupling length, the phase matching and hence the power coupling transfer between them as illustrated in Fig. 4.2. The principle of how the directional coupler works is that when two fibre cores are brought sufficiently close to each other laterally so that their modal fields overlap, then the modes of the two fibres become coupled and the power can transfer periodically between the two fibres. When the propagation constants of the modes of individual fibres are equal, then this power exchange is complete. On the other hand, if their propagation constants are different, then there is still a periodic, but incomplete, exchange of power between the fibres. When no voltage is applied, the two guides are phase-matched and light input into guide 1 is nearly 100% coupled into guide 2 (cross-state). When a voltage is applied, there is a change in the refractive index due to the applied electric field which can be made unequal in the two guides by implementing an appropriate design. This leads to a mismatch in the phase velocities in both guides and leads to a reduction of the interaction length ($L_c = \pi / (\beta_{\text{even}} - \beta_{\text{odd}})$). Sometimes DC is considered for the power controller; the application is in power splitting wavelength division multiplexing/demultiplexing, polarization splitting and optical switching networks. The deeply etched waveguide electrooptic modulator is presented in Fig. 4.3. This type of modulator is a desirable model with very good performances, which is a subject of this research presented in the next chapter. Semiconductor modulator and electroabsorption modulator (MQW) are illustrated in these figures also. Fig. 4.1 illustrates a LiNbO_3 Mach-Zehnder modulator in comparison to a Mach-Zehnder

Interferometric (MZI) modulator where the light is split into two isolated (non-interacting) waveguides and the phase shifts between two branches (left and right waveguides) from 180° due to an external electric field applied. The electrode structure has to be considered as an electrical waveguide structure for RF signals, and discontinuities in the electrode structure will give reflections inside the devices. To avoid reflections the electrical waveguide structure should have a characteristic impedance Z_0 , matched with the signal source at the input and the load at the output of the coplanar waveguide (CPW), which is $Z_0 = 50 \Omega$. This type of modulator will be discussed in more detail in the following chapters.

4.3 Modulator characteristics

External high-speed optical modulators of multi-gigahertz bandwidth and high optical power handling capacity are key components in current optical communications systems and valuable for future optical signal processing technology. The role of the optical modulators in the high-capacity transmission systems is illustrated in the Fig. 4.6.

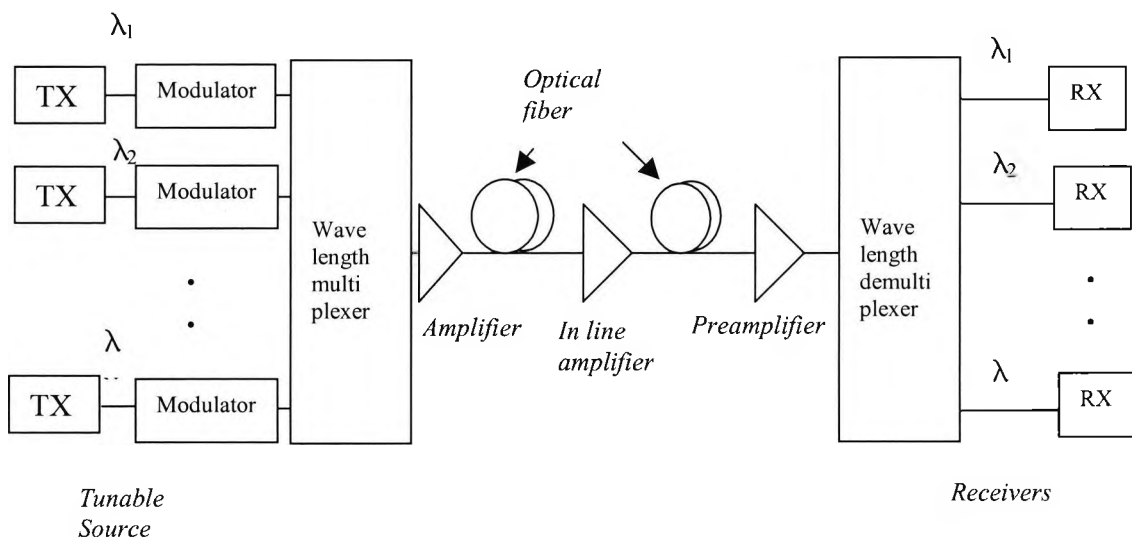


Fig. 4.6 Application of the optical modulators for high-capacity transmission systems.

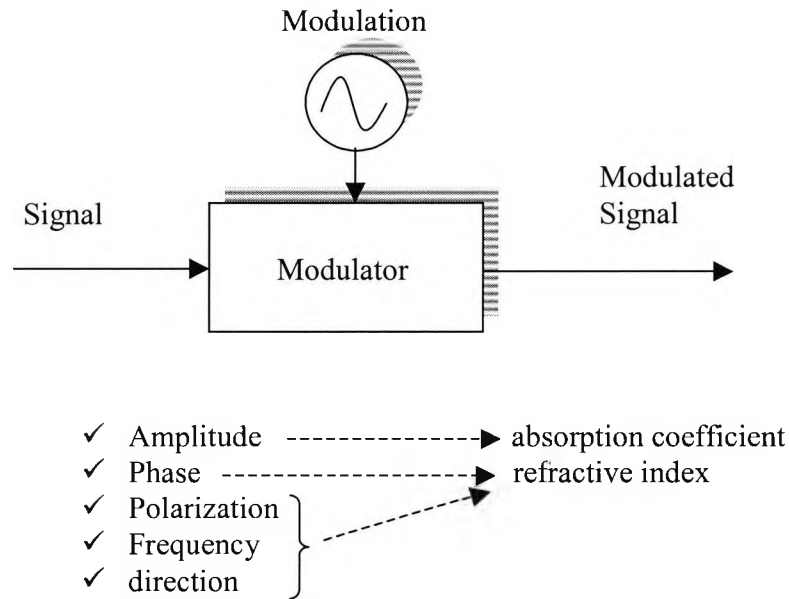


Fig. 4.7 The principle of the modulator and its interacting with the light.

As illustrated, it is very important to design an optical modulator which fulfills the requirements of such high capacity transmission systems. The most important aspects and characteristics of the design of the high-speed optical modulator are: bias voltage (current), bandwidth, insertion loss, stability, chirp, distortion, integration, maximum power, extinction ratio, temperature sensitivity, fiber device input/output and packaging.

- a) Extinction Ratio (on/off):** The extinction ratio or on/off ratio is defined as the ratio of the incident light intensity P_{in} and the transmitted intensity P_{out} given as:

$$[on/off] = -10 \cdot \log\left(\frac{P_{out}}{P_{in}}\right) \quad [dB] \quad (4.1)$$

For most modulators these days extinction ratio is usually several (20-30) dB, because of their short optical intersection length. There is another way of defining, ratio of the average received optical energy of a logic “1” pulse to the average received optical energy of a logic “0” pulse. The maximum extinction ratio decreases because of the incomplete confinement of the optical field.

b) Bias Voltage: The smaller the applied voltage the better it is for the electronic circuit. Low driving voltage operation is the key point bringing such modulators into practical use because this eliminates the need for high speed electrical amplifiers. The voltage applied to the modulator from a direct current source causes the crystal (substrate) to modulate the phase of the light by π radians. In order to attain the highest possible extinction ratio, the substrate must be at quadrature. This means that complete destructive interference will result in logic “0” and complete constructive interference will result in logic “1.” To get the substrate to “quadrature,” a bias voltage field must be applied to it. This optimum voltage, known as V_{π} DC, often drifts back and forth over a period of time. This causes problems because it diminishes the extinction ratio (the difference between logic “1” and logic “0”). If the extinction ratio diminishes, the optical receiver cannot differentiate as well between “on” and “off” and the bit error rate increases. Studies have shown that V_{π} DC drifts as a result of age and is accelerated by heightened temperatures (Nagata 2000). Studies have also shown that a higher V_{π} DC results in a higher rate of change of V_{π} DC (Maack, 1999). Conversely, a lower V_{π} DC results in a lower rate of change, making it more desirable to have a modulator whose V_{π} DC is near zero. Not only does it require less power, but it also will dampen the effect of the V_{π} DC drift. It is also desirable to have a near-zero V_{π} because a large drift may require more voltage than the available voltage from a given power source.

c) Chirping: Changes or oscillations which are not periodic (increase and decrease) of the emitted laser light and its unstable wavelength is defined as chirping. This ratio affects the laser emitting linewidth. As pulse travels from the

laser source with time it broadens and gets chirped. This phenomenon increases instability of the modulator. Moreover, the reduction of the chirp parameter is a hot topic in research on ultra high bit rate and long haul optical fibre transmission systems. It has been reduced but the price has been increased insertion loss and reduced extinction ratio. Therefore it is necessary to optimize the device characteristics for overall practical use, as we have done in this work for both LiNbO₃ and GaAs electrooptic modulators. External LiNbO₃ modulators can show an adjustable frequency chirp (free chirp).

d) Frequency modulation: Frequency modulation and chirping are intrinsically similar phenomena. There are three regions of frequency domains in laser diode response:

- 1) Lower frequency region below 10MHz.
- 2) Medium frequency region between 10MHz- 1GHz.
- 3) Higher frequency region, above 1GHz (as our LiNbO₃ and GaAs modulators are operating).

e) Bandwidth: The speed of an optical modulator is dependent on its bandwidth, the higher bandwidth yields higher speed modulator. The speed of the modulator is the speed at which the modulator processes data, measured in Gb/sec. The bandwidth requirements for modulators is varying from: digital stereo sound 10⁶ bit/sec, digital TV 10⁸ bit/sec (100 Mbit/sec), high resolution TV up to 1Gbit/sec, 3D TV and teleconferencing 100 Gbit/sec. The modulator bandwidth is primarily restricted by the velocity (speed) mismatch between microwave and optical carrier, conductor loss impedance mismatch and dielectric loss (at high frequency modulation). The mismatch between the electrical and the optical signals is very important in order to achieve maximum bandwidth. In other words, the effective index of electrical signals $N_m = \sqrt{\epsilon_e}$ has to be equal to the effective index of optical signals, N_o .

Under the impedance matching condition, which is often set to 50 Ω , the bandwidth is limited by the velocity mismatch and the total microwave loss.

Under both impedance and phase matched conditions, and $N_m=N_o$, the bandwidth is limited by the microwave loss only. Different designs of the metal electrode have been reported in order to achieve velocity and impedance matching. In the calculation of optical bandwidth often only the conductor loss is considered. However, the dielectric loss at high frequency plays a significant role in bandwidth reduction; therefore it has to be taken into account. The dielectric loss can arise from different lossy microwave regions (layers). Presented in this work are some of the most successful approaches in simultaneous velocity and impedance matching, leading to the significant increase of the overall bandwidth of the modulator. Bandwidth calculation will be discussed in the next section.

- f) **Insertion loss:** The insertion loss is the power loss that results from the insertion of a device such as a connector or coupler into a fibre optic system. The insertion loss consists the combination of the transmission, reflection and coupling loss. Transmission loss is caused by absorption loss of the material, free carrier loss, and scattering loss. In other words transmission loss depends on the refractive index profile. Coupling loss is due to mode-spot size mismatch between the incident light and the guided light.

There are many other parameters which have an important role on the design improvements of the modulator performances. However, it has been confirmed from the research in manufacturing technology that above factors have the most impact on the long term high-speed, compactness and reliability of the modulators.

4.4 Electrooptic effect

The electrooptic (or Pockels) effect is associated with an external electric field applied in the top of the substrate to modify the index of a substrate or dielectric medium. When an electric field is applied to a crystal, the ionic constituents move to new locations determined by the strength of the applied field, the charge on the ions and the restoring force. In cases when these effects can be described as being linearly proportional to the

applied field then the crystal exhibits the *linear* electrooptic effect as illustrated in the Fig. 4.8. In the design of an electrooptic modulator, it is usually desirable to achieve a required modulation depth with the smallest consumption of modulation power, leading to the largest possible bandwidth.

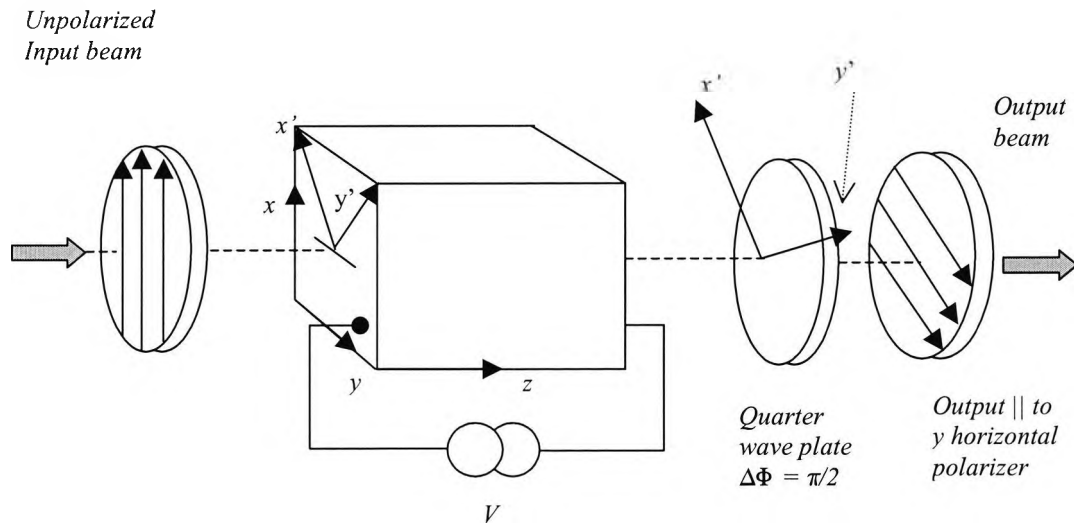


Fig. 4.8 Electrooptic amplitude modulation.

The voltage applied to the electrodes placed over the substrate along the waveguide will create the electric fields in x -direction and y -direction, as shown in the Fig. 4.8. The electric field may be applied either in the direction of the wave propagation or perpendicular to it. The induced polarization due to the change in the distribution of the electrons within the substrate will depend on the magnitude and also the direction of the applied voltage. Starting from Maxwell's equation relations in the material media:

$$\mathbf{D} = \epsilon_0 \mathbf{E} + \mathbf{P} \quad (4.2)$$

$$\mathbf{B} = \mu_0 \mathbf{H} + \mathbf{M} \quad (4.3)$$

where \mathbf{P} and \mathbf{M} are the electric and magnetic polarization vectors, respectively.

$$\mathbf{P} = \varepsilon_0 \sum \chi_{ij}^e \mathbf{E}_j \quad (4.4)$$

$$\begin{bmatrix} \mathbf{P}_x \\ \mathbf{P}_y \\ \mathbf{P}_z \end{bmatrix} = \varepsilon_0 \begin{bmatrix} \chi_{11}^e & \chi_{12}^e & \chi_{13}^e \\ \chi_{21}^e & \chi_{22}^e & \chi_{23}^e \\ \chi_{31}^e & \chi_{32}^e & \chi_{33}^e \end{bmatrix} \begin{bmatrix} \mathbf{E}_x \\ \mathbf{E}_y \\ \mathbf{E}_z \end{bmatrix} \quad (4.5)$$

$$\varepsilon_{ij} = \varepsilon_0 (1 + \chi_{ij}^e) \quad (4.6)$$

where χ_{ij}^e is susceptibility tensor and \mathbf{P} and \mathbf{E} are usually complex amplitudes of harmonics, time varying quantities. This is the basis of electrooptic modulation and this phenomenon is used to control the refractive index change of the crystal in the directions of the ordinary and extraordinary rays due to the application of an electric field. This phenomenon can be described as *index ellipsoid*, expressed (Yariv 1985):

$$\frac{x^2}{n_x^2} + \frac{y^2}{n_y^2} + \frac{z^2}{n_z^2} = 1 \quad (4.7)$$

where x, y, z are the principal dielectric axes, the directions in the crystal where \mathbf{D} and \mathbf{E} are parallel. In the presence of an external applied electric field \mathbf{E} the equation of the ellipsoid takes the general form of:

$$\left(\frac{1}{n^2}\right)_1 x^2 + \left(\frac{1}{n^2}\right)_2 y^2 + \left(\frac{1}{n^2}\right)_3 z^2 + 2\left(\frac{1}{n^2}\right)_4 yz + 2\left(\frac{1}{n^2}\right)_5 xz + 2\left(\frac{1}{n^2}\right)_6 xy = 1 \quad (4.8)$$

If we choose $x, y,$ and z to be parallel to the principle dielectric axes of the crystal, then with zero applied field, the equation (4.8) reduces to equation (4.7);

$$\left. \begin{aligned} \left(\frac{1}{n^2}\right)_{1,E=0} &= \frac{1}{n_x^2} \quad ; \quad \left(\frac{1}{n^2}\right)_{2,E=0} = \frac{1}{n_y^2} \quad ; \quad \left(\frac{1}{n^2}\right)_{3,E=0} = \frac{1}{n_z^2} \\ \left(\frac{1}{n^2}\right)_{4,E=0} &= \left(\frac{1}{n^2}\right)_{5,E=0} = \left(\frac{1}{n^2}\right)_{6,E=0} = 0 \end{aligned} \right\} \quad (4.9)$$

The linear change in $\left(\frac{1}{n^2}\right)_i$ ($i = 1, 2, 3, \dots, 6$) due to an arbitrary electric field \mathbf{E} defined by:

$$\Delta\left(\frac{1}{n^2}\right)_i = \sum_{j=1}^3 r_{ij} \mathbf{E}_j \quad (4.10)$$

where $\mathbf{E}_1 = \mathbf{E}_x$, $\mathbf{E}_2 = \mathbf{E}_y$ and $\mathbf{E}_3 = \mathbf{E}_z$. In matrix form the equation (4.10) can be expressed as:

$$\begin{bmatrix} \Delta\left(\frac{1}{n^2}\right)_1 \\ \Delta\left(\frac{1}{n^2}\right)_2 \\ \Delta\left(\frac{1}{n^2}\right)_3 \\ \Delta\left(\frac{1}{n^2}\right)_4 \\ \Delta\left(\frac{1}{n^2}\right)_5 \\ \Delta\left(\frac{1}{n^2}\right)_6 \end{bmatrix} = \begin{bmatrix} r_{11} & r_{12} & r_{13} \\ r_{21} & r_{22} & r_{23} \\ r_{31} & r_{32} & r_{33} \\ r_{41} & r_{42} & r_{43} \\ r_{51} & r_{52} & r_{53} \\ r_{61} & r_{62} & r_{63} \end{bmatrix} \begin{bmatrix} \mathbf{E}_1 \\ \mathbf{E}_2 \\ \mathbf{E}_3 \end{bmatrix} \quad (4.11)$$

So for example

$$\Delta\left(\frac{1}{n^2}\right)_1 = r_{11}\mathbf{E}_x + r_{12}\mathbf{E}_y + r_{13}\mathbf{E}_z \quad (4.12)$$

4.5 Electrooptic effect of LiNbO₃ modulators (transverse electrooptic modulation)

It is more convenient to apply the electric field transversely along electrodes placed on the side faces of the crystal as shown in the Fig. 4.9 and Fig. 4.10 for both crystal orientations. The choice of axes with respect to the crystal orientation is very important in defining the susceptibility tensors. A waveguide electrooptic modulator with CPW electrodes on either sides of the waveguide is shown in Fig. 4.9, where the vertical electric field is employed with the hot electrode placed directly over the waveguide, and in Fig. 4.10 where the horizontal electric field is used. Based on this approach, the Z-cut crystal orientation (Fig. 4.9) of LiNbO₃ modulator is investigated in this work. This is the basis of the electrooptic modulation and this phenomenon is used to control the refractive index change of the crystal in the directions of the ordinary and extraordinary rays due to the application of an electric field.

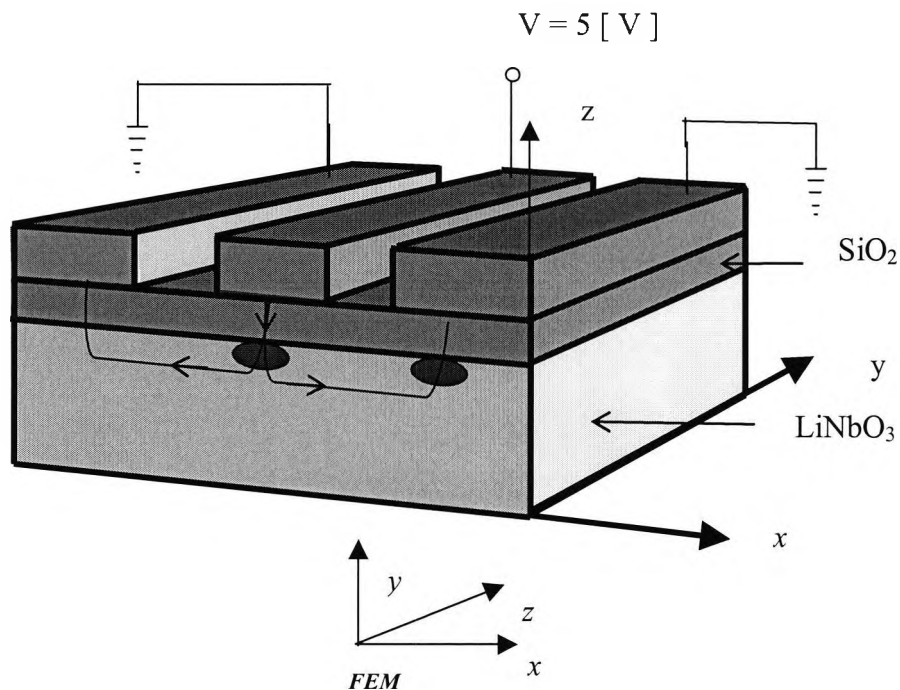


Fig. 4.9 CPW Z-cut electrooptic modulator with vertical field ($E \perp$) TM mode.

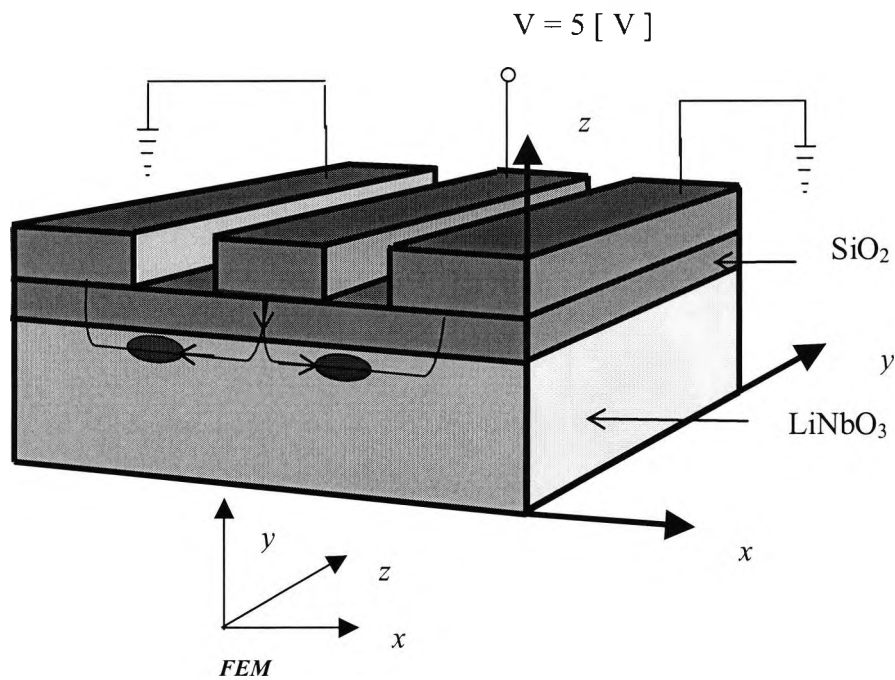


Fig. 4.10 CPW X-cut electrooptic modulator with horizontal field ($E \parallel$) TE mode.

By using the equations (4.8) and (4.11) and the rules for the matrix multiplication under the external field $E(E_x, E_y, E_z)$ this phenomenon can be described as the *index ellipsoid*, expressed (Yariv 1985):

The electrooptic coefficients for Z-cut crystal orientation are:

$$[r_{ij}] = \begin{bmatrix} r_{12} & 0 & r_{13} \\ -r_{12} & 0 & r_{13} \\ 0 & 0 & r_{33} \\ 0 & r_{42} & 0 \\ r_{51} & 0 & 0 \\ 0 & -r_{12} & 0 \end{bmatrix} \quad (4.13)$$

where the nonzero tensors are:

$$\left. \begin{aligned}
 r_{13} &= 8.6 \cdot 10^{-12} \frac{m}{V} \\
 r_{22} &= -r_{12} = r_{61} = 3.4 \cdot 10^{-12} \frac{m}{V} \\
 r_{33} &= 30.9 \cdot 10^{-12} \frac{m}{V} \\
 r_{51} &= r_{42} = 28 \cdot 10^{-12} \frac{m}{V}
 \end{aligned} \right\} \quad (4.14)$$

The electrooptic coefficients for *X*-cut orientation can be expressed in the form:

$$[r_{ij}] = \begin{bmatrix} 0 & -r_{22} & r_{13} \\ 0 & r_{22} & r_{13} \\ 0 & 0 & r_{33} \\ 0 & r_{51} & 0 \\ r_{51} & 0 & 0 \\ -r_{22} & 0 & 0 \end{bmatrix} \quad (4.15)$$

where nonzero tensors are:

$$\left. \begin{aligned}
 r_{12} &= -r_{21} = -r_{62} = 3.4 \cdot 10^{-12} \frac{m}{V} \\
 r_{33} &= 30.9 \cdot 10^{-12} \frac{m}{V} \\
 r_{13} &= r_{23} = 8.6 \cdot 10^{-12} \frac{m}{V}
 \end{aligned} \right\} \quad (4.16)$$

In this research work there will be an investigation of the LiNbO₃ electrooptic modulator with the Z-cut crystal orientation. With lithium niobate in the 3m crystallographic group with nonzero elements as above, its index ellipsoid will be expressed in the form:

$$\left(\frac{1}{n_o^2} + r_{12}\mathbf{E}_y + r_{13}\mathbf{E}_z\right)x^2 + \left(\frac{1}{n_o^2} + r_{22}\mathbf{E}_y + r_{23}\mathbf{E}_z\right)y^2 + \left(\frac{1}{n_e^2} + r_{33}\mathbf{E}_z\right)z^2 + 2(r_{42}\mathbf{E}_y)yz + 2(r_{51}\mathbf{E}_x)xz + 2(r_{61}\mathbf{E}_x)xy = 1 \quad (4.17)$$

In general form, under the external electric field applying the ellipsoid equation with new coordinate system, x' , y' and z' in which the equation of the ellipsoid (4.17) does not contain the mixed terms, it can be expressed as:

$$\frac{x'^2}{n_{x'}^2} + \frac{y'^2}{n_{y'}^2} + \frac{z'^2}{n_{z'}^2} = 1 \quad (4.18)$$

As is illustrated in the Fig. 4.9 our FEM crystal orientation is presented in such a way that electric field is parallel to y -direction and \mathbf{E}_y is presented in Z -direction. In other words our FEM y -direction is presented with Z in real crystal orientation. However, the electrooptic effect is investigated in accordance with real crystal orientation shown in the above figures. The effect of the field has been to render the crystal biaxial and rotate the indicatrix in the xy plane. Let it be assumed that the indicatrix has been rotated so that its new principle axes are x' , y' are at an angle θ to the original principal axis with \mathbf{E}_y applied, as no cross term involved z has been introduced into the equation as illustrated in the Fig. 4.11. (see Appendix 1).

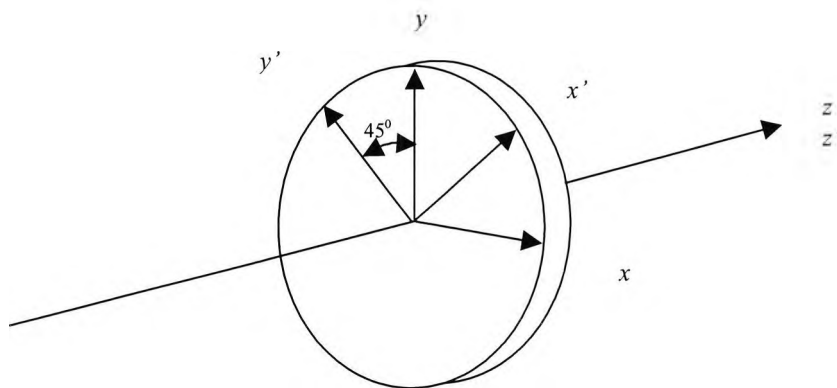


Fig. 4.11 Intersection of index ellipsoid with x - y plane.

$$x = \frac{1}{\sqrt{2}}(x' + y') = x' \cos 45^\circ + y' \sin 45^\circ \quad (4.19)$$

$$y = \frac{1}{\sqrt{2}}(-x' + y') = -x' \sin 45^\circ + y' \cos 45^\circ \quad (4.20)$$

$$n_x = n_o + \frac{n_o^3}{2} r_{33} E_y \quad (4.21)$$

$$n_{y'} = n_o - \frac{n_o^3}{2} r_{33} E_y \quad (4.22)$$

$$n_{z'} = n_z = n_e \quad (4.23)$$

Insert the electrooptic tensors from:

$$\Delta \left(\frac{1}{n^2} \right)_i = \sum_{j=1}^3 r_{ij} E_j \quad \text{or} \quad (\Delta n)_i = -\frac{n^3}{2} \sum_{j=1}^3 r_{ij} E_j \quad (4.24)$$

$$\Delta n_{ij} = \frac{-n^3}{2} \begin{bmatrix} -r_{22} E_y + r_{13} E_z & -r_{22} E_x & r_{15} E_x \\ -r_{22} E_x & r_{22} E_y + r_{13} E_z & r_{15} E_y \\ r_{15} E_x & r_{51} E_y & r_{33} E_z \end{bmatrix} \quad (4.25)$$

where n is either the ordinary n_o or extraordinary n_e . If the voltage is applied along y direction, the electrooptic induced index change for light polarized along the y direction, which sees the extraordinary index and the highest value of the tensors, in this case r_{33} coefficient is:

$$\Delta n_e = -\frac{n_e^3}{2} r_{33} E_y \quad (4.26)$$

In this case the refractive index change under the voltage applied is:

$$\Delta n(x, y, V) = -\frac{n^3}{2} r E_y(x, y) \quad (4.27)$$

The new refractive index is:

$$n_{new}(x, y, V) = n_{old}(x, y) + \Delta n(x, y, V) \quad (4.28)$$

The off diagonal elements of (4.22) have to be utilized for the waveguide polarization modulation. Lithium niobate is an *anisotropic*, uniaxial crystal where $n_o = n_x = n_y = 2.23$ and $n_e = n_z = 2.15$ at $\lambda = 1.55 \mu\text{m}$. Due to the crystal symmetry in LiNbO_3 we have presented in Fig. 4.9 and Fig. 4.10 two useful crystal orientations, Z-cut and X-cut. With Z-cut, Y- propagation crystal orientation, where electric field is perpendicular to the waveguide, the strongest electrooptic diagonal coefficient is r_{33} , therefore this configuration provides maximum modulation for the TM mode (polarization in the plane of the substrate). For a Z-cut it is important to have an optical isolating layer to avoid increase of optical loss, such as use of SiO_2 . The X-cut and Y-propagation configuration offers utilization of the largest diagonal coefficient r_{33} for TE mode (polarization in the plane of the substrate).

4.6 Electrooptic effect of the GaAs (modulators) crystal orientation

Practical modulators are operating as *transverse electrooptic modulators* where the electric field is applied normal to the direction of the propagation, as illustrated in Fig. 4.12. As shown in figure 4.12 the whole structure is deposited on very thick insulating GaAs substrate. In these cases a $0.1 \mu\text{m}$ thick *highly doped* (1×10^{18})/ cm^3 GaAs layer below the lower cladding is considered as the ground electrode, placed between the

10%AlGaAs layer and the substrate, while the hot electrode, $V \neq 0$ is deposited on the top of the buffer AlGaAs layer. The crystal structure of the III-V is $\bar{4}3m$ or Zinc blend, where the crystal orientation is (001) in Miller indices plane as illustrated in Fig. 4.13.

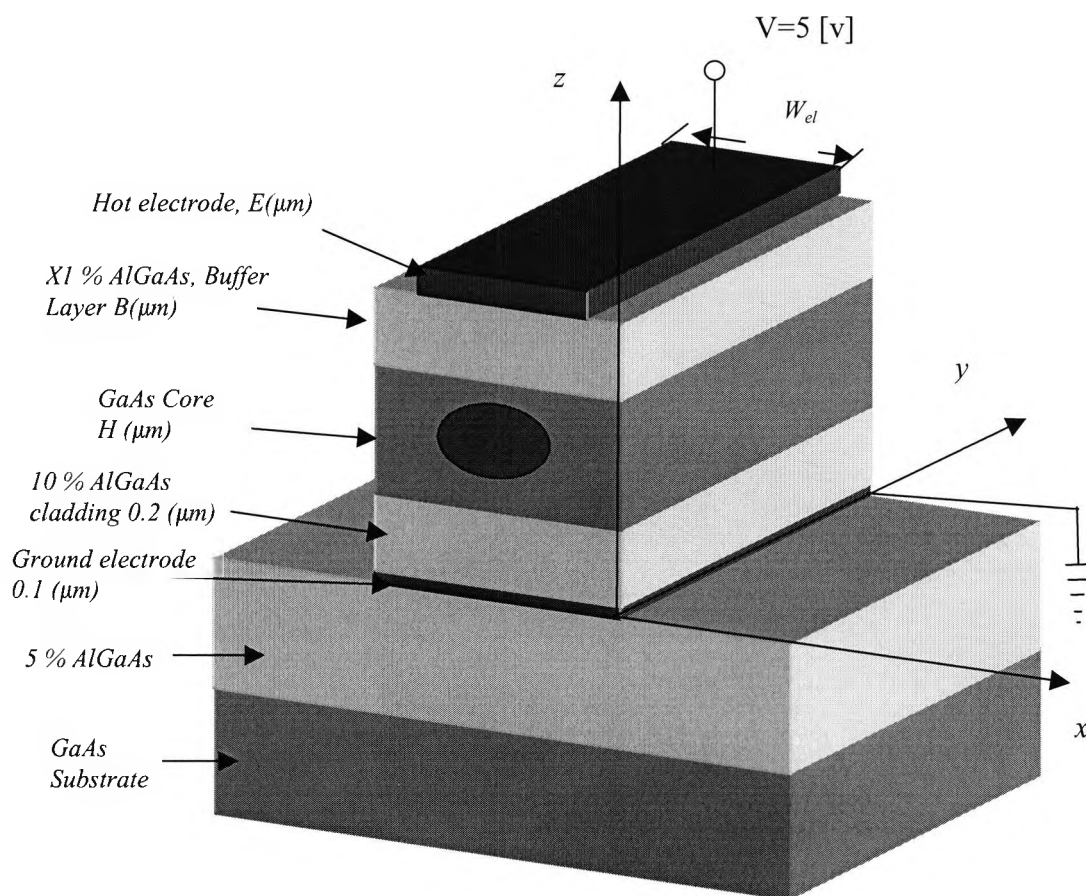


Fig. 4.12 Deeply-etched semiconductor electrooptic modulator.

The vertical electric field applied in the (001) direction increases the index of refraction by Δn in (011) direction and decreases in $(01\bar{1})$. In other words, the index increases along one of the two mutually orthogonal directions parallel to the surface of the crystal. The decrease happens by the same amount in the other orthogonal direction. No index change is observed in (001) direction which implies that a vertical applied electric field to an (001)-oriented crystal will only modulate the TE mode of the optical waveguide in

which the main electric field component of the optical mode is either in (011) or $(01\bar{1})$ directions, in other words it is tangential to the surface. It is important to mention that no modulation will result for the TM mode which has its main electric field component in (001) direction, normal to the surface of the crystal (Wang 1988).

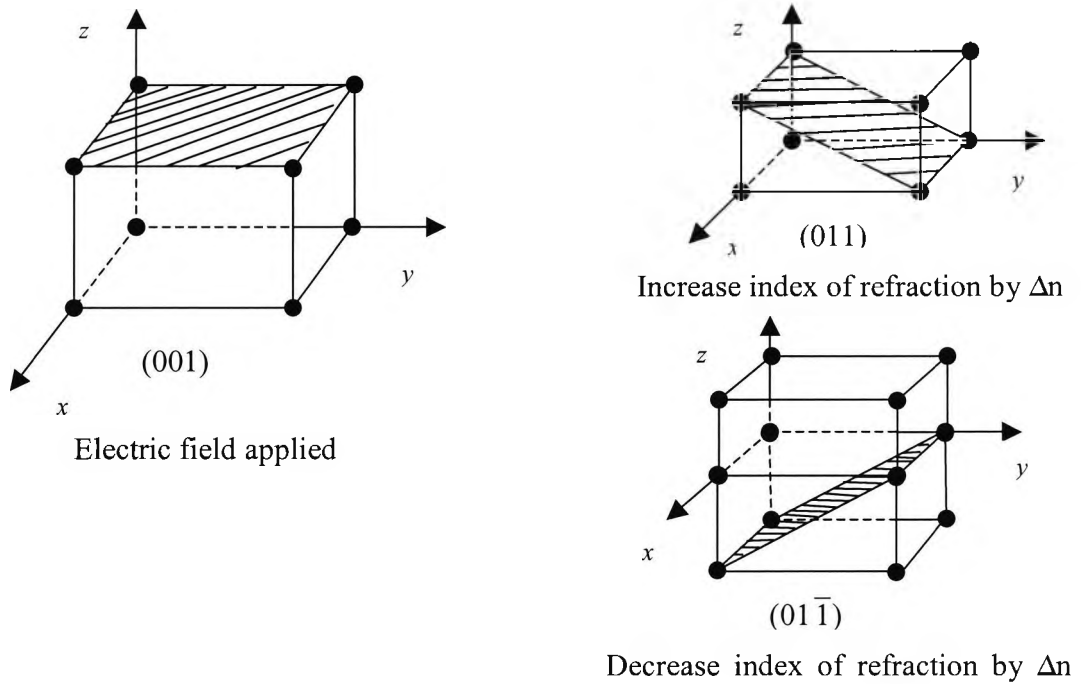


Fig. 4.13 Miller Indices.

The equation (4.11) for a GaAs crystal orientated as presented above will take the form:

$$[r_{ij}] = \begin{bmatrix} 0 & 0 & 0 \\ 0 & 0 & 0 \\ 0 & 0 & 0 \\ r_{41} & 0 & 0 \\ 0 & r_{52} & 0 \\ 0 & 0 & r_{63} \end{bmatrix} \quad (4.29)$$

where nonzero tensors are:

$$r = r_{41} = r_{52} = r_{63} = 1.4 \cdot 10^{-12} \frac{m}{V} \quad (4.30)$$

Thus substituting equation (4.11) and (4.12) into (4.8) yields:

$$\frac{x^2}{n_o^2} + \frac{y^2}{n_e^2} + \frac{z^2}{n_e^2} + 2r_{41}E_x yz + 2r_{41}E_y xz + 2r_{63}E_z xy = 1 \quad (4.31)$$

In general form, under the external electric field applying the ellipsoid equation with new coordinate system, x' , y' and z' in which the equation of the ellipsoid (4.17) does not contain the mixed terms it can be expressed as:

$$\frac{x'^2}{n_x'^2} + \frac{y'^2}{n_y'^2} + \frac{z'^2}{n_z'^2} = 1 \quad (4.32)$$

where, n_x' , n_y' and n_z' are the semi-major axes of the new ellipsoid, with coordinates in which x' and y' are related to x and y via a 45° rotation, as illustrated in the Fig. 4.11. After substituting equations (4.19) and (4.20) for x' and y' in the equation (4.31) and (4.32) the new refractive index will become (see Appendix 1):

$$\frac{1}{n_x'^2} = \frac{1}{n^2} - rE_z \quad (4.33)$$

Since;

$$d\left(\frac{1}{n_x'^2}\right) = \frac{-2}{n_x'^3} dn_x' \approx \frac{-2}{n^3} dn_x' \quad \text{as} \quad (rE_z \ll \frac{1}{n^2}) \quad (4.34)$$

$$d(n_x') \approx \frac{-n^3}{2} d\left(\frac{1}{n_x'^2}\right) = \frac{n^3}{2} rE_z \quad (4.35)$$

Similarly

$$d(n'_y) = \frac{-n^3}{2} r E_z \quad (4.36)$$

since

$$n'_{x,y} = n + d(n'_{x,y}) \quad (4.37)$$

$$n'_x = n + \frac{n^3}{2} r E_z \quad (4.38)$$

$$n'_y = n - \frac{n^3}{2} r E_z \quad (4.39)$$

$$n'_z = n_z = n \quad (4.40)$$

In this case E_z plays the role of E_y from Laplace and z is the direction of the propagation.

Therefore the refractive index distribution becomes a 3x3 tensor and depends on the electric field applied as given by:

$$\bar{n}(x, y) = \begin{bmatrix} n(x, y) + \Delta n_{xx}(x, y) & \Delta n_{xy}(x, y) & 0 \\ \Delta n_{yx}(x, y) & n(x, y) + \Delta n_{yy}(x, y) & 0 \\ 0 & 0 & n(x, y) + \Delta n_{zz}(x, y) \end{bmatrix} = \quad (4.41)$$

$$\begin{bmatrix} n_{xx} & n_{xy} & n_{xz} \\ n_{yx} & n_{yy} & n_{yz} \\ n_{zx} & n_{zy} & n_{zz} \end{bmatrix}$$

where $n(x, y)$ is the refractive index distribution of the structure in the case where the external field is not applied, whereas, Δn_{xx} , Δn_{xy} , Δn_{yx} , and Δn_{zz} are the changes in the refractive index occurring due to the electrooptic effect and these are related to the external field applied via

$$\Delta n_{xx} = -\Delta n_{zz} = \frac{n^3(x, y)}{2} r_{41} \mathbf{E}_y(x, y), \quad \Delta n_{yy} = 0 \quad (4.42)$$

$$\Delta n_{xy} = \Delta n_{yx} = \frac{n^3(x, y)}{2} r_{41} \mathbf{E}_x(x, y) \quad (4.43)$$

The phenomenon of *birefringence* does not apply with *isotropic* media such as GaAs substrate.

4.7 Calculation of half-wave length product $V_\pi L$

Low driving voltage operation is the key point bringing electrooptic modulators into practical use because this eliminates the need for high speed electrical amplifiers. The low power and high-frequency operation of the modulator will make these devices useful for external modulators. The drive voltage must be very low, because the electrical driver has very low output and needs a large bandwidth amplifier. For MZ modulators, a phase shift π appears between two arms. If the output waveguides of the modulator are single-mode the total optical power at the output can be considered to a first approximation as a weighted sum of the optical power from two arms. As discussed above the usual voltage for a π phase shift is several volts. The term $V_\pi L$ is the product of the half-wave voltage, V_π and the interaction length, L , of the device and it is the key parameter of an electrooptic modulator. The 3 dB optical bandwidth is the electrical small signal 3 dB band under the condition that the modulators are biased in the linear region or at phase quadrature region where the optical output intensity is approximately a linear function of the applied voltage, with V_π the DC bias voltage required to generate a phase difference $\Delta\beta$. In order to obtain a low V_π , the overlap integral is to be maximized, which can be achieved by fabrication of a Ti: LiNbO₃ (Titanium diffused

lithium niobate) waveguide which could support the tightest confined optical fundamental TE or TM mode.

The process of amplitude modulation of an optical signal is illustrated in Fig. 4.14. The modulator is biased with a fixed retardation to the 50% transmission point.

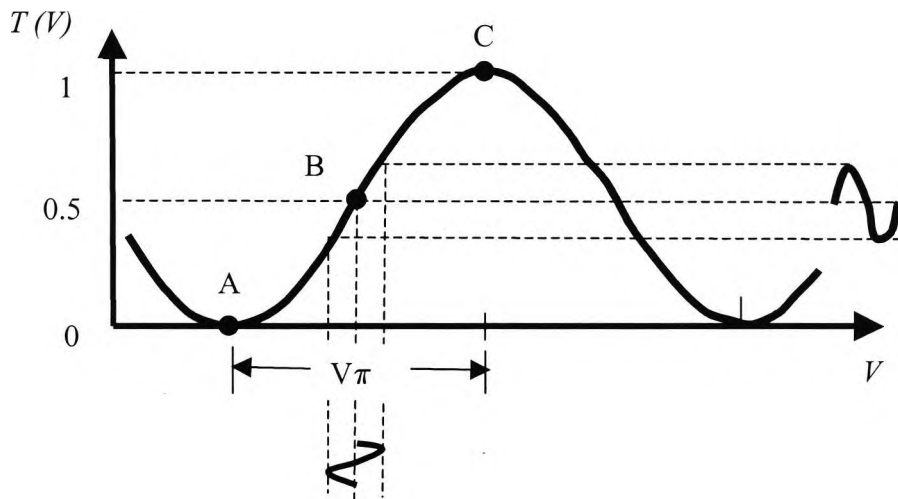


Fig. 4.14 The process of the modulation of an optical signal.

This bias can be achieved by applying a voltage $V = 1/2 V_{\pi}$, where a small sinusoidal modulation voltage will cause a nearly sinusoidal modulation of the transmitted intensity as illustrated in the Fig. 4.14 The transmission of the light T is:

$$T(\%) = \sin^2\left(\frac{\pi V}{2 V_{\pi}}\right) \quad (4.44)$$

The operation of the LN electrooptic modulator is primarily through the phase difference, $\Delta\phi$, obtained between two arms of the device by applying voltage, where

$$\Delta\phi = \Delta\beta \cdot L \quad (4.45)$$

In this case the refractive index change under the voltage applied is:

$$\Delta n(x, y, V) = -\frac{n^3}{2} E_y(x, y) \quad (4.46)$$

The new refractive index is:

$$n_{new}(x, y, V) = n_{old}(x, y) + \Delta n(x, y, V) \quad (4.47)$$

$$n = n_{linear} + \Delta n_{electrooptic} \quad (4.48)$$

After solving waveguide equations for $V=0$ and $V=V_{applied}$, in other words after getting the propagation constant β for both cases in both arms for LN, then;

$$\Delta\beta = \beta_{V=V_{applied}} - \beta_{V=0} \quad (4.49)$$

the device length (Alferness, 1988) is:

$$L = \frac{\pi}{\Delta\beta} \quad (4.50)$$

Therefore the figure of merit is:

$$V_\pi \cdot L = V \cdot \frac{\pi}{\Delta\beta} \quad (4.51)$$

where V is the applied voltage, for Z -cut LN crystal orientation, the polarized mode is TM, where the H_{11}^x is the (quasi-TM) fundamental mode. Whereas for the semiconductor modulator considered in this research work, assuming that the two waveguide branches of the MZ arrangement are sufficiently separated not to have coupling between their isolated guided modes, the product, $V_\pi L$ can be calculated using equation (4.51) where, $\beta_{V=0}$ $\beta_{V=V_{applied}}$ and with the propagation constants of the

fundamental H_{II}^y modes of the MZ arms with and without the applied voltage. As can be deduced from the electrooptic effect the H^y (or E^x) modes are mainly affected by the refractive index change in the x-direction, namely Δn_{xx} , which are directly proportional to E_y , while the H^x (or E^y) modes are, on the other hand, affected by the refractive changes in the y-direction, Δn_{yy} , which is zero. That is why only the H^y mode (quasi-TE) will be considered throughout the semiconductor modulator investigation, However, if an asymmetry has been brought to the structure, the horizontal field component, E_x , will not be symmetric, giving rise to a nonzero Δn_{xy} : an off-diagonal refractive index component which can cause a coupling between the two orthogonal TE and TM modal states.

4.8 Driving power calculation of the electrooptic modulators

In the design of the electrooptic modulators, the microwave attenuation and phase velocity mismatch between the optical wave and the microwave are the two main concerns, both of which depend critically on how the metal electrodes are designed. It is very important to optimize the design of the electrodes in order to achieve both a high bandwidth and a low driving power. In Chapter 5 of this thesis, the calculation of the microwave parameters is investigated in detail. Given the impedance of the microwave source, Z_S , the driving power P_{in} can be calculated from (Hui, 1998)

$$P_{in} = \frac{V_{\pi}^2}{8Z_S \left[1 - \left(\frac{Z_S - Z_C}{Z_S + Z_C} \right)^2 \right]} \quad (4.52)$$

where Z_S usually is set to be 50Ω , V_{π} is the half-wave voltage calculated under the section of optical properties equation (4.51). Obviously, a low half-wave voltage is required in order to achieve low driving power modulator design. Various attempt have been made in order to achieve low driving power, primarily in the optimisation of the device parameters, such as electrode thickness, buffer layer thickness and soon. Therefore, in this research work many device parameters are investigated, involving

electrode designs to achieve high bandwidth and low driving power. These results will be illustrated in the subsequent result sections on the work carried on both types of modulators, in LN and GaAs.

Summary

In this chapter we have presented briefly describes of most of commonly used optical modulators, their characteristics and performance through many years on the market. The role of the optical modulators in high speed communications systems is also briefly discussed, including their characteristics which make these devices even more drivable sources for future ultra-high speed communication systems. Various types of the modulators are investigated in this section, in particular the LiNbO_3 electrooptic modulator and deeply-etched waveguide GaAs electrooptic modulator and their electrooptic effects are also investigated in detail. This effect is described in terms of third-rank tensors, r_{ij} expressing the linear dependence of the coefficients of the index ellipsoid on the applied electric field. Arrangements with different crystal orientations are discussed, involving Z -cut and X -cut LN crystal orientation used in LiNbO_3 electrooptic modulators for future analysis, such as FEM analysis in the modeling of electrooptic modulators. The details of electrooptic effect for general case are calculated in Appendix I. A similar approach has been applied for the deeply-etched semiconductor modulator, but in accordance with the use of a semiconductor as the *isotropic* material, their crystal orientation is based on the Miller Indices. The optical properties of both LN and GaAs modulator are investigated. The half-wave voltage length product, $V_\pi L$ calculation for both modulators is presented in this chapter, with respect to achieving low driving power. Based on the study in this chapter, performance results for both LiNbO_3 and GaAs modulators will be illustrated in subsequent chapters.

Microwave properties of the electrooptic modulators

5.1 Introduction

Electrode design is one of the most important aspects of modulator characteristics; usually a first step in electrode design is to choose a proper transmission line structure. In this chapter, the focus is on the design issues in achieving high-speed operation using travelling-wave electrode structures. The optical response of a modulator is determined by the microwave propagation characteristics of the electrode, namely, the potential distribution, the electric fields, the capacitance calculation, the effective index of the microwave, N_m , the characteristic impedance, Z_c , and the propagation losses, α_c and α_d . These microwave propagation parameters can be calculated by using the quasi-TEM techniques for their optimizations. Amongst various quasi-static approaches, Kitazawa *et al.*, 1992, used the spectral domain approach and Keen *et al.*, 1990, employed the method-of-lines to optimize LN optical modulators.

Pantic and Mittra (1986) have used the finite element method (FEM), which is one of the most versatile methods for the simulation of many electromagnetic field problems. Zhang and Miyoshi, 1995, have used the FEM along with the conformal transformation to model open-type structures. Simple quasi-TEM analysis using a scalar field does yield useful results, even in the high frequency range. The finite element method is capable of handling transmission lines with rather arbitrary configurations, such as thick metal electrodes, slanted wall of the ridge type structures, besides the anisotropic permittivity and lossy metal and dielectric materials, as encountered in practical devices. Because of its generality, the FEM is employed in this research work for the analysis of LiNbO₃ and GaAs electrooptic modulators illustrated in the Fig. 5.1-5.2 as coplanar and microstrip type transmission lines, respectively. The analysis is based on a quasi-TEM model

which is adequate for microwave frequencies in communication applications, typically for high-speed digital circuits.

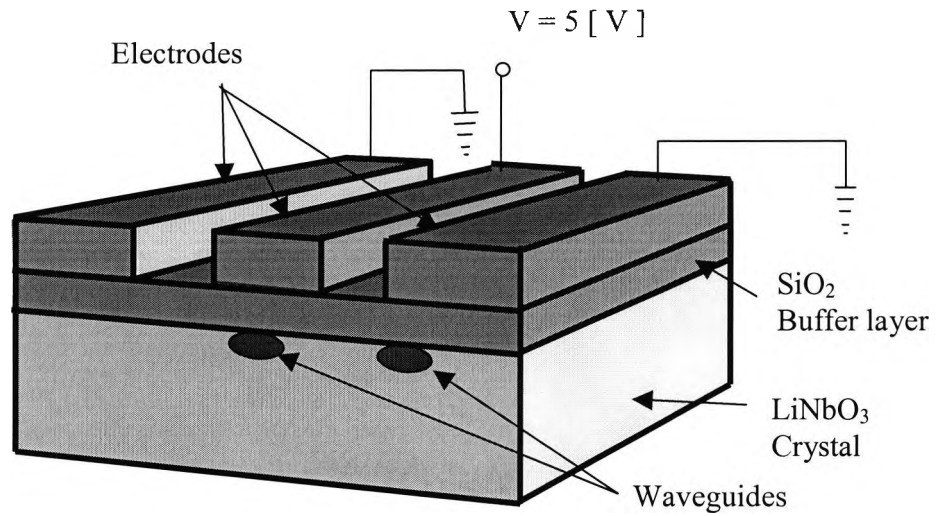


Fig. 5.1 Coplanar waveguide (CPW) LiNbO₃ electrooptic modulator.

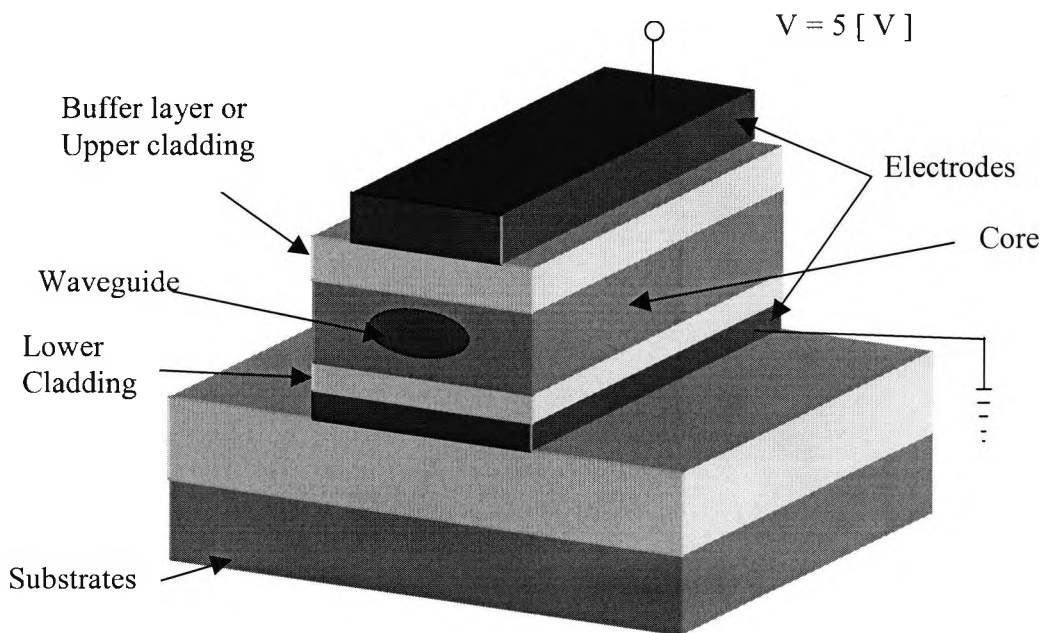


Fig. 5.2 Microstrip type Semiconductor electrooptic modulator.

The term “coplanar lines” is used for those transmission lines for which all the conductors are in the same plane; namely on top surface of the dielectric substrate. These transmission lines include (CPW) coplanar waveguide, (CPS) coplanar strips. The term “microstrip line” is used for those transmission lines for which the conductors are in the same vertical plane; the hot electrode is placed on the top of the dielectric surface and at the bottom of the dielectric surface is placed the ground electrode. In this research work, the dielectric conductivity of the bottom electrode shown here in the Fig. 5.2, is ignored.

5.2 Quasi-TEM analysis of electrooptic modulators by the finite element method.

Coplanar waveguide consists of a centre strip with two ground planes located parallel to and in the plane of the strip. The main components of fields are electric and magnetic, the wave propagating along the line is called TEM mode. This approximation reduces the problem to that of finding the scalar potential function at every node for the entire domain.

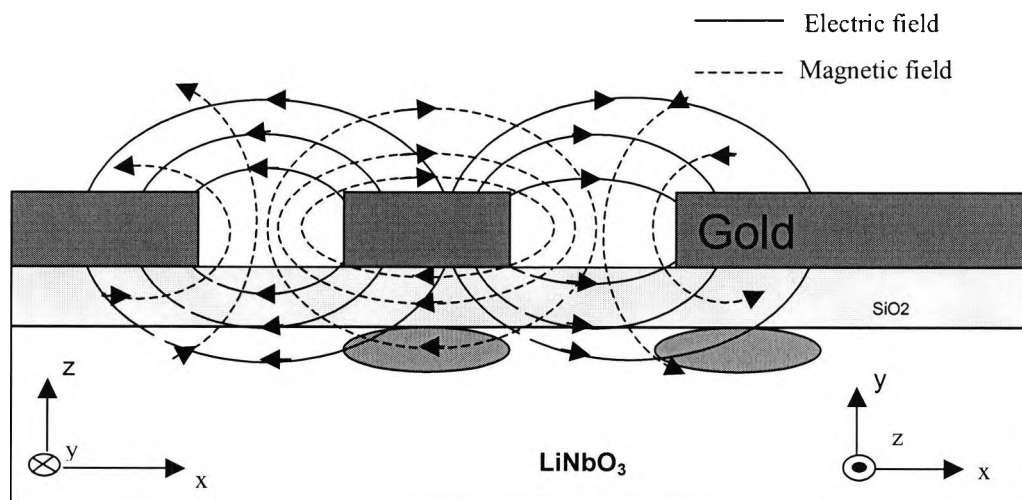


Fig. 5.3 Electrooptic LiNbO₃ CPW modulator fields distributions.

The electric and magnetic field configurations for quasi-static approximation are shown in Fig. 5.3. The electric field is represented with solid lines, whereas magnetic field is shown with dashed lines. It is obvious that electric field lines and magnetic field lines are perpendicular to each other, which conforms to Maxwell's equations (given in the Chapter 3 of this thesis).

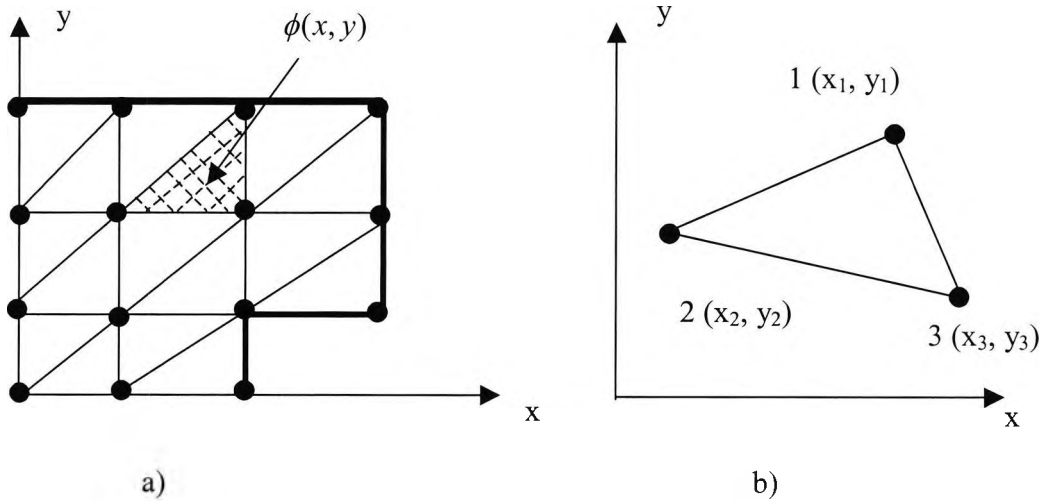


Fig. 5.4 a) Triangle elements over an L-shape region b). Typical triangle element in x - y plane.

A simple and fast quasi-TEM FEM is used in this work to analyze numerically the modulator structure illustrated in the Fig. 5.3. In the quasi-static approximation, the scalar potential function $\phi(x, y)$ is governed by Laplace's equation, as given below:

$$\epsilon_x \frac{\partial^2 \phi(x, y)}{\partial x^2} + \epsilon_y \frac{\partial^2 \phi(x, y)}{\partial y^2} = 0 \quad (5.1)$$

or

$$\nabla^2 \phi = 0 \quad (5.2)$$

To construct an approximation solution by a simple FEM, the problem region is subdivided into triangle elements as indicated in Fig. 5.4. The potential distribution over first-order triangle elements represents the nodal value and is defined as:

$$U(x, y) = a_i + b_i x + c_i y \quad (5.3)$$

where $\phi(x, y) = U(x, y)$ and coefficients a_i , b_i , and c_i are calculated under the Chapter 3 equation (3.38)-(3.40). It then follows immediately from the local (area) coordinates of definition that:

$$L_1 + L_2 + L_3 = 1 \quad (5.4)$$

where, L_1 , L_2 , and L_3 are local coordinates and (x, y) are global coordinates, the usual Cartesian coordinates, their relation is defined as:

$$\left. \begin{aligned} x &= x_1 L_1 + x_2 L_2 + x_3 L_3 \\ y &= y_1 L_1 + y_2 L_2 + y_3 L_3 \end{aligned} \right\} \quad (5.5)$$

The potential value of the element, which consists of three nodes is:

$$U = \sum_{i=1}^3 U_i \alpha_i(x, y) \quad (5.6)$$

where,

$$\alpha_1 = \frac{1}{2A} \{ (x_2 y_3 - x_3 y_2) + (y_2 - y_3)x + (x_3 - x_2)y \} \quad (5.7)$$

where A represents the surface area of the triangle. The remaining two functions (α_2 and α_3) can be obtained by cycling interchange of subscripts. It can be noted that the newly

defined functions are *interpolatory* on the three vertices of the triangle, that each function vanishes at all vertices but one, and that it has unity value at that one:

$$\alpha_i(x_j, y_j) = \begin{cases} 0 & \text{for } i \neq j \\ 1 & \text{for } i = j \end{cases} \quad (5.8)$$

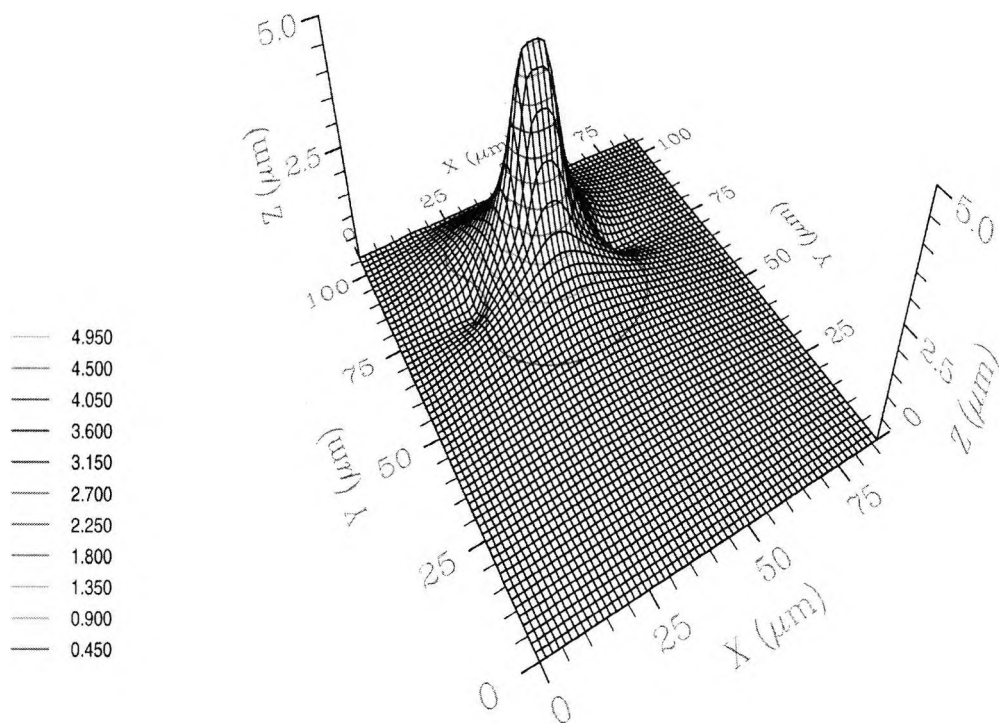


Fig. 5.5 Potential distribution for the LiNbO₃ electrooptic modulator considered at voltage applied, V = 5 volt.

The potential distribution for all elements is associated with an assemblage of many elements. In general, the sum of all the potential distribution of the individual elements is defined as;

$$U = \sum_{\text{all elements}} U^e \quad (5.9)$$

The potential gradient within the element can be found as:

$$\nabla U = \sum_{i=1}^3 U_i \nabla \alpha_i \quad (5.10)$$

$$\nabla^2 U = \sum_{\text{all el.}} \sum_{i=1}^3 U_i \nabla^2 \alpha_i \quad (5.11)$$

Equation (5.9) represents the potential distribution at every node for the entire region, illustrated in Fig. 5.5. It can be seen that the voltage applied is 5 volt, for the considered structure shown in Fig. 5.3. Similarly there is calculated the potential distribution for the GaAs electrooptic modulator structure shown here in the Fig. 5.2 as microstrip line.

5.3 Electric fields calculations

Central to the analysis of electrooptic modulator structure, such as LiNbO₃ and GaAs modulators, is the solution of the Laplace equation for the potential distribution, $\phi(x, y)$. From the Laplace equation given in the equation (5.1), the following Lagrangian function can be obtained (Yong, 1988).

$$L = \iint \left[\varepsilon_x \left(\frac{d\phi}{dx} \right)^2 + \varepsilon_y \left(\frac{d\phi}{dy} \right)^2 \right] dx dy \quad (5.12)$$

where, ε_x and ε_y are the permittivity in the x and y directions respectively. For LN, as *anisotropic* media, $\varepsilon_x = 43$ and $\varepsilon_y = 28$, whereas for GaAs as *isotropic* media $\varepsilon_x = \varepsilon_y = 12$.

By discretizing the modulator cross-section with many triangular elements and solving the highly sparse resultant algebraic equation generated, after the application of the Galerkin procedure, the nodal values of the potential ϕ are obtained for the given applied voltage, with the electrodes as boundary conditions. Once $\phi(x, y)$ is determined, both the horizontal, $E_x(x, y)$ and the vertical, $E_y(x, y)$ modulating electric field components can also be determined using:

$$\mathbf{E}(x, y) = -\nabla\phi(x, y) \left[\frac{V}{\mu m} \right] \quad (5.13)$$

The negative sign is required in order that the electric field's intensity point towards a *decrease* in potential, according to the usual convention. Results on the electrode configuration involving electric fields distribution, $E_x(x, y)$ and $E_y(x, y)$ for both electrooptic modulators including LiNbO₃ and GaAs will be discussed in more details in the subsequent chapters.

5.4 Capacitance calculation of the electrooptic modulators.

Various methods have been reported for the capacitance calculation of coplanar transmission lines. Some of these methods are conformal mapping method (CMM) (Ramer, 1982), variational method in Fourier transformed domain (VMFD) (Yamashita, 1968). These methods cannot be applied to the three strip lines where the strip lines have a finite width and nonzero thickness. Therefore, a finite element method is capable of handling structures whose cross-section geometry is illustrated in the Fig. 5.6.

From the Laplace equation, the Lagrangian functional in the equation (5.12) and by applying the finite element method, the potential values at every node are obtained as explained above under the section of the potential distribution. The source of the potential is the middle electrode, sometimes denoted as the "hot electrode".

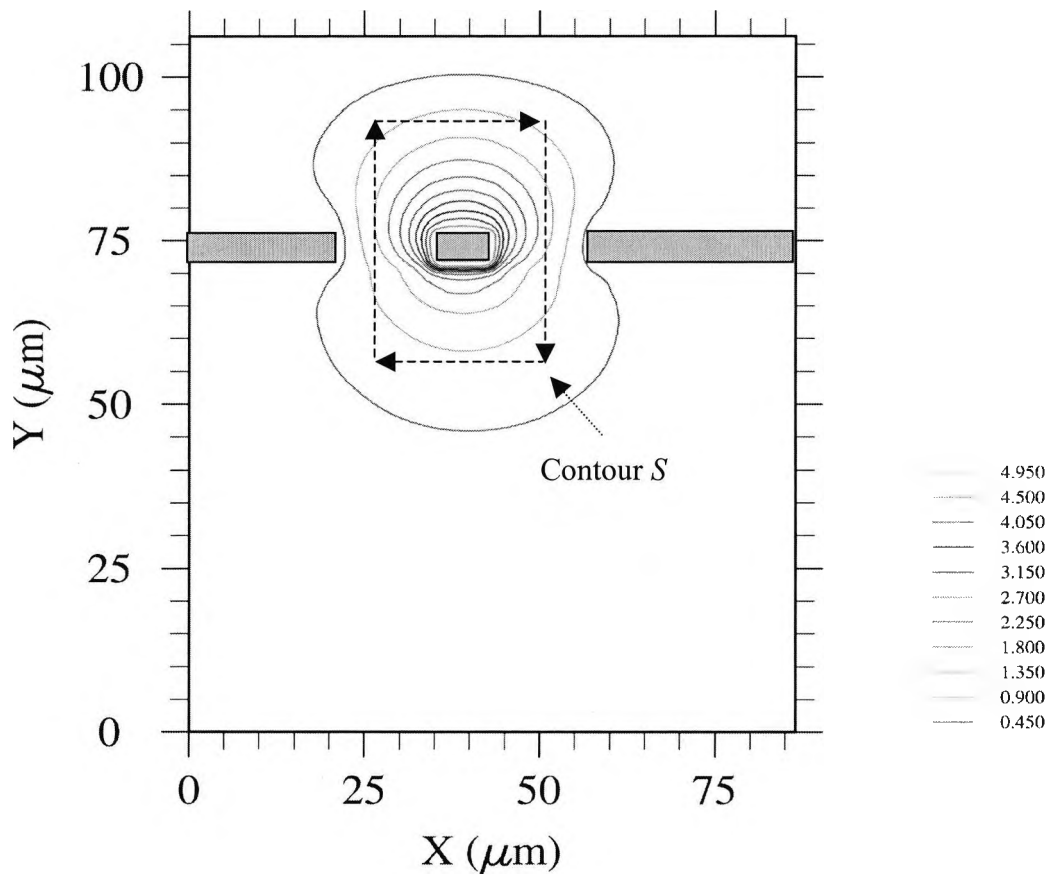


Fig. 5.6 Cross-section geometry of three parallel strip lines, equipotential lines (potential lines) with integration path.

The potential distribution for all elements is defined from the equation (5.9). From these potential values, the capacitance, C per unit length can be evaluated using the divergence theorem, given in Appendix 2:

$$C = \frac{Q}{V} \quad (5.14)$$

where, Q is the electrostatic charge defined as:

$$Q = \int_V \nabla \cdot \mathbf{D} dv \quad (5.15)$$

Illustrated by the divergence theorem, Appendix 2, equation (A2.6) gives

$$\mathbf{D} = \epsilon_0 \epsilon_n \mathbf{E} = -\epsilon_0 \epsilon_n \frac{\partial \phi}{\partial \mathbf{n}} \quad (5.16)$$

where, \mathbf{D} is the normal component of the electric flux, \mathbf{E} is the normal component of electricity intensity, ϕ is node potential distribution along the line, and \mathbf{n} is the normal vector.

$$\int_V \nabla \cdot \mathbf{D} dv = \oint_S \epsilon_0 \epsilon_n \mathbf{E} \cdot d\mathbf{l} \quad (5.17)$$

after substituting equations (5.16) and (5.17) into equation (5.15) the capacitance formulation is:

$$C = \frac{1}{V_0} \oint_S \epsilon_0 \epsilon_n \frac{d\phi}{dn} dl \quad (5.18)$$

where V_0 is the magnitude of applied voltage, as illustrated in the Fig. 5.6 hot electrode, S is the integration contour, and the subscript \mathbf{n} means normal to the contour of integration. The integration contour S is designed to encircle all the electrodes, where the voltage is applied. In our case the contour is encircling the hot electrode which is placed

on the top of the waveguide and in sides, left and right, with ground electrodes, with zero potential values. This method of capacitance calculation is very useful, because it can be applied to arbitrary shaped electrodes in anisotropic and inhomogeneous dielectric media. Furthermore, this procedure can reduce computer time compared with the conventional variational techniques.

The substrate interface between the layers has to be taken into consideration, especially when dealing with anisotropic media such as LN, where the permittivity constant changes in x and y directions. In such situations, the permittivity at these points is taken as an average value between two dielectric constants. The same approach is applied for capacitance calculation of the deep-etched semiconductor electrooptic modulator. The contour path is encircling the hot electrode as illustrated in Fig. 5.6 and the dielectric constant of GaAs does not change along x and y direction.

5.5. Microwave index calculation of the electrooptic modulators

Microwave effective index is defined as ratio between capacitance per unit length of the actual line of the modulator structure and free space line capacitance, C_0 . Free space line capacitance calculation, involves the same procedure as capacitance per unit length calculation, except the dielectric constants now are replaced by air, $\epsilon_r = 1$. After the capacitance per unit length of the actual line and free space line capacitance the microwave group velocity or phase velocity will be defined as (Gupta, 1979).

$$v_m = \frac{c}{N_m} \quad (5.19)$$

where, $c = 3.0 \times 10^8$ m/s is the velocity of electromagnetic wave in free space, N_m is microwave effective index defined as:

$$N_m = \sqrt{\frac{C}{C_0}} \quad (5.20)$$

The effective (dielectric) permittivity is defined as:

$$\epsilon_{eff} = \frac{C}{C_0} = N_m^2 \quad (5.21)$$

The velocity mismatch factor, μ_d is defined as difference between optical and microwave group velocities, with N_o and N_m the optical and microwave group refractive indices, defined as:

$$\mu_d = \frac{N_m - N_o}{c} \quad (5.22)$$

where, microwave and optical group refractive indices depend primarily on the dielectric constants involved in the modulator fabrication and the modulator structure. For the LN electrooptic modulators, considered in this research work, $N_o = 2.15$, whereas N_m has to be calculated from the eq. (5.20). Also for deeply-etched semiconductor electrooptic modulator structure investigated here the typical optical effective index is $N_o = 3.35$. Velocity matching between optical and microwave signals involves a great deal of the modulator design, therefore this issue will be discussed widely in the separate section of this research work.

5.6. Characteristic impedance calculation of the electrooptic modulators

After the capacitance per unit length of the actual line and free space line capacitance the characteristic impedance is defined as (Koshiba, 1999).

$$Z_c = \frac{1}{c\sqrt{CC_0}} \quad [\Omega] \quad (5.23)$$

where, c , C and C_0 are defined above, under the microwave index section. The expression (5.23) is for a single line, but the same procedure can be applied to find the capacitance and characteristic impedance for even and odd modes of two coupled lines or to find the capacitance for a system of n lines. The electromagnetic field distribution can also be defined

$$E_0 = -\nabla\phi \quad (5.24)$$

$$H_0 = -\frac{1}{\eta} E_0 \times \hat{z} \quad (5.25)$$

where, \hat{z} is unit vector in the z direction and η is the intrinsic impedance of the medium

$$\eta = \sqrt{\left(\frac{\mu_0}{\epsilon_0}\right) \frac{1}{\epsilon_{eff}}} = \frac{Z_0}{N_m} = \frac{377[\Omega]}{N_m} \quad (5.26)$$

where, Z_0 is free space impedance, and other parameters are defined above.

A “coupled line” configuration consists of two transmission lines such as microstrip lines placed parallel to each other and in close proximity as illustrated in the Fig. 5.7. In this case a coupling between the electromagnetic fields in two lines is caused. Because of the coupling of electromagnetic fields, a pair of coupled lines can support two different modes of propagation (Hatsuda, 1975). Therefore, these modes have different characteristic impedances.

For quasi-static analysis of coupled microstrip lines, the calculation of even and odd impedance must be employed. The integration path would be the same as the capacitance calculation for single strip line, except now we have two different hot electrodes. Odd mode is considered when the voltage is applied in both hot electrodes, V_1 and V_2 , but with different polarization as illustrated in Fig. 5.7 ($V_1 = 10$ V, $V_2 = -10$ V). Even mode is the opposite of the odd, where both hot electrodes have the same polarity ($V_1 = V_2 = 10$ V). Therefore, according to the electrodes polarizations, we have

even and odd characteristic impedance. On the bases of the quasi-TEM assumptions the calculation of even and odd characteristic impedance is employed.

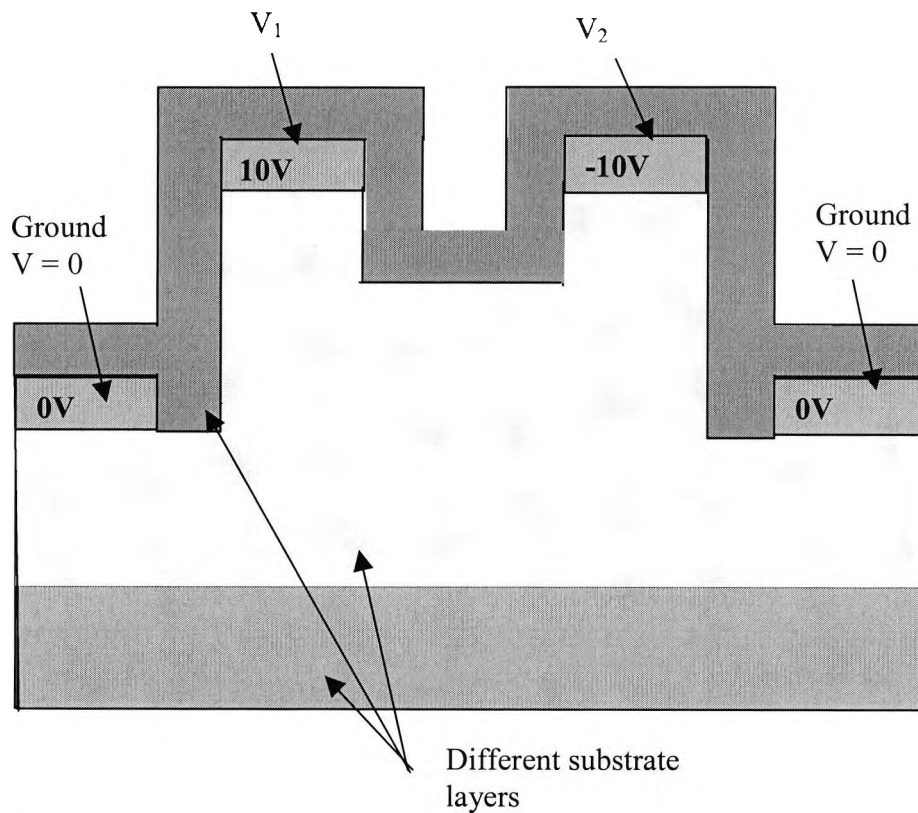


Fig. 5.7 Traveling-wave electrooptic modulator with coupled electrode (V_1 and V_2).

The odd and even impedances are expressed in terms of the capacitance as

$$Z_{odd} = \frac{1}{\sqrt{cC_{odd}C_{0odd}}} \quad [\Omega] \quad (5.27)$$

$$Z_{even} = \frac{1}{\sqrt{cC_{even}C_{0even}}} \quad [\Omega] \quad (5.28)$$

where, C_{odd} is calculated when, $V_1 = V_2 = 10$ V, and C_{even} is calculated when $V_1 = -10$ V and $V_2 = 10$ V. Usually Z_{odd} is almost twice the Z_{even} value. The variation of these characteristic impedances for different structures such as LiNbO₃ electrooptic modulator, semiconductor electrooptic modulator and for the electrooptic modulator illustrated in the Fig. 5.7 will be shown in the results chapter.

5.7 Conductor loss calculation

Losses for nonmagnetic substrate are discussed in this subsection. Conductor losses are losses caused by imperfect conductors, in this case metal (gold) electrodes. Conductor loss or attenuation constant in this research work is investigated by using the “incremental inductance rule” (Koshiba, 1999). In this method the series surface resistance R per unit length is expressed in terms of that part of the total inductance per unit length which is attributable to the skin effect, i.e., the inductance produced by the magnetic field within the conductors.

The attenuation constant because of conductor loss (ohmic) loss is defined as:

$$\alpha_c = \frac{R_s}{2\mu_0 Z_C} \frac{\partial L}{\partial n} = \frac{R_s}{2Z_0 Z_C} \frac{\partial Z_{C0}}{\partial n} \quad (dB/\sqrt{GHz} \cdot cm) \quad (5.29)$$

where, Z_C characteristic impedance and Z_0 free space impedance are defined under the impedance calculation subsection, R_s is the surface resistance of the conductors at frequency of 1 GHz is defined as:

$$R_s = \sqrt{\pi\mu_0 f \rho} \quad (5.30)$$

and resistivity, or conductivity of the gold is;

$$\sigma = \frac{1}{\rho} = 4.1 \times 10^7 \frac{s}{m} \quad (5.31)$$

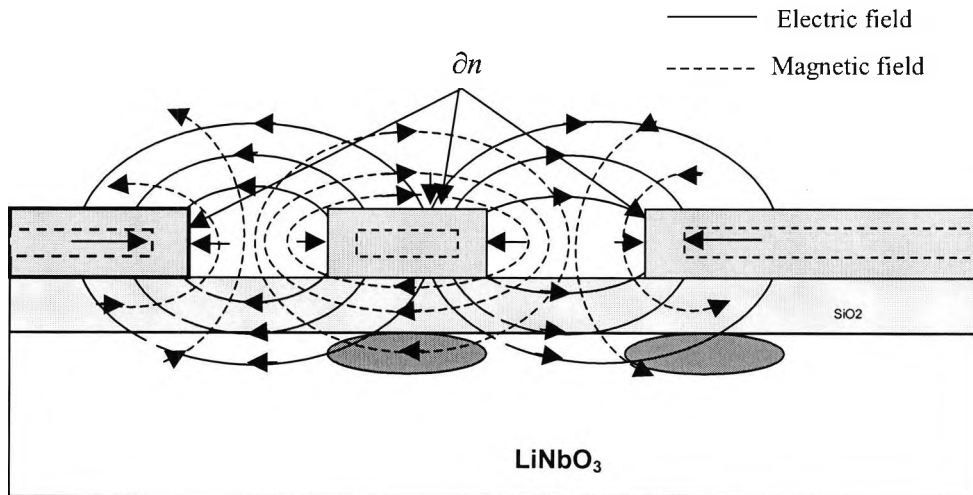


Fig. 5.8 Recession of conducting walls of LiNbO₃ modulator structure.

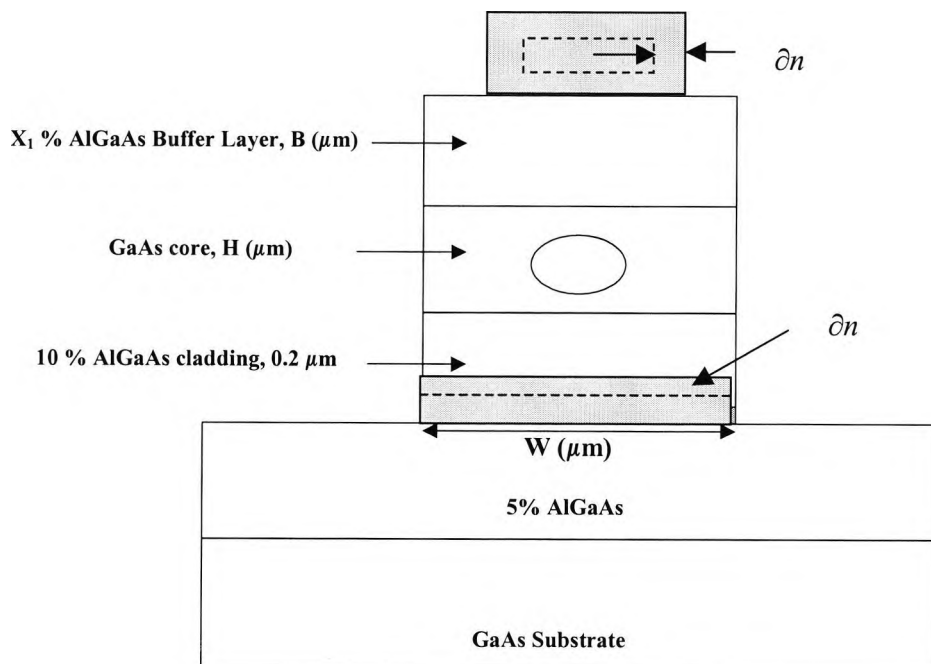


Fig. 5.9 Recession of conducting walls of GaAs modulator structure.

The term $\partial Z_{C0}/\partial n$ denotes the derivative of Z_{C0} with respect to the incremental recession of the surface electrodes illustrated in the Fig. 5.8 for the LiNbO₃ modulator structure and Fig. 5.9 for the GaAs modulator structure. Usually the unit for attenuation constant is in neper where, $1\text{neper} = 8.686\text{dB}$. The amount of recession is equal to the skin depth $\delta = (2/\omega\mu\sigma_c)^{1/2}$. The effects of the electrode design and the conductor losses of both electrooptic modulators, LN and GaAs, are illustrated in the subsequent chapters, where device performances are investigated in details.

5.8 Dielectric losses

Attenuation due to the dielectric loss of the media is caused by the molecular absorption of the dielectric. If there is a loss in dielectric, the dielectric constant ϵ is a complex quantity. Thus,

$$\epsilon = \epsilon' - j\epsilon'' \quad (5.32)$$

where, ϵ' is the real part of the dielectric constant and ϵ'' is the imaginary part of the dielectric constant.

$$j\omega\epsilon E = \omega\epsilon'' E + j\omega\epsilon' E \quad (5.33)$$

Therefore, for relative permittivity yields,

$$\epsilon_r = \epsilon_r' - j\epsilon_r'' \quad (5.34)$$

The loss tangent of the dielectric material is given by;

$$\tan \delta = \frac{\epsilon_r''}{\epsilon_r'} \quad (5.35)$$

Microwave loss due to lossy dielectrics can be calculated by using the perturbation theory (Pantic and Mittra, 1986).

$$\alpha_d = \frac{P_d}{2P_0} \quad (5.36)$$

where P_d and P_0 are the time-averaged powers dissipated in the dielectrics and the total power. From the scalar potential profile $\phi(x, y)$, the transverse components of the electric fields E_x and E_y (defined above) may be calculated and these fields profiles can subsequently be used to obtain P_0 and P_d as follows:

$$P_d = \omega \epsilon \tan \delta \int_{S_{diel}} |\mathbf{E}_0|^2 ds = \omega \epsilon \tan \delta \int_{S_{diel}} (|E_x|^2 + |E_y|^2) ds \quad (5.37)$$

where, tangent $\tan \delta$ is assumed to be very small in the way that perturbation fields can be approximated to the fields for the lossless condition, $\mathbf{E}_0, \mathbf{H}_0$, $\omega = 2\pi f$ is the angular frequency, and in our calculation, $f = 1 \text{ GHz}$, and S_{diel} is the area of the dielectric.

$$P_0 = \text{Re} \int_S (\mathbf{E}_0 \times \mathbf{H}_0^*) \cdot \hat{z} ds \quad (5.38)$$

where, S is complete cross section of the line. According to Maxwell's equations;

$$\mathbf{E}_0 = -\nabla \phi = x\mathbf{E}_x + y\mathbf{E}_y = -x \frac{\partial \phi}{\partial x} - y \frac{\partial \phi}{\partial y} \quad (5.39)$$

whereas magnetic field is

$$\mathbf{H}_0 = -\frac{1}{\eta} \mathbf{E}_0 \times \hat{z} = -\frac{1}{\eta} (-\hat{y}\mathbf{E}_x + \hat{x}\mathbf{E}_y) = \hat{x}\mathbf{H}_x + \hat{y}\mathbf{H}_y \quad (5.40)$$

After substituting equations (5.39) and (5.40) and applying the cross and dot product yields:

$$P_0 = \frac{1}{\eta_s} \int_s (|E_x|^2 + |E_y|^2) \cdot ds \quad (5.41)$$

After substituting equations (5.41) and (5.37) into equation (5.36) the dielectric loss can be calculated for different dielectric layers, with its corresponding $\tan \delta$. The dielectric loss in this research work is calculated for LiNbO₃ and GaAs electrooptic modulators. For electrooptic modulator dielectric loss is calculated for LN and SiO₂ layers, their $\tan \delta$ are $\alpha_{LN} = 0.004$ and $\alpha_{SiO_2} = 0.016$ (Minakata, 2001). For the semiconductor electrooptic modulator dielectric losses are calculated separately for every GaAs/Al_xGa_{1-x}As layer and for the coating thickness of Ta₂O₅, their $\tan \delta$ are: (Wu, 1991) $\tan \delta_{GaAs / AlGaAs} = 0.0003$ and $\tan \delta_{Ta_2O_5} = 0.053$ (Khan, 1993). The effects of the dielectric losses on the device performances for both electrooptic modulators, LN and GaAs, respectively are illustrated under the subsequent chapters.

5.9 Bandwidth calculation

The potential bandwidth of the electrooptic waveguide modulators is, in practice, always limited by distributed-circuit effects. The electrooptic effect is an electronic phenomenon that has a sub-picosecond response time. The achievable modulation speed depends upon several factors. The speed of the modulator is the speed at which the modulator processes data, measured in Gb/sec. The speed of the modulator is dependent on its bandwidth. A higher bandwidth yields higher speed modulator. The optical response of a modulator is determined by the microwave propagation characteristics of the electrode, namely, the effective index of the microwave, N_m , the characteristic impedance, Z_C , and the overall propagation losses. The modulator bandwidth is primary restricted by the velocity (speed) mismatch between microwave and optical carrier, conductor loss impedance mismatch and dielectric loss (at high frequency modulation). The mismatch between the electrical and the optical signals is very important in order to

achieve maximum bandwidth. The general equation of the optical response is given (Koshiya, 1999) as:

$$m(f) = \left| \frac{1 - S_1 S_2}{(1 + S_2)[e^{j2u_+} - S_1 S_2 e^{-2ju_-}]} \times \left[e^{ju_+} \frac{\sin u_+}{u_+} + S_2 e^{-ju_-} \frac{\sin u_-}{u_-} \right] \right| \quad (5.42)$$

where

$$u_{\pm} = \frac{1}{c} \pi f L (N_m \mp N_o) - j \frac{1}{2} \alpha L \quad (5.43)$$

$$S_1 = \frac{Z_1 - Z_C}{Z_1 + Z_C} \quad (5.44)$$

$$S_2 = \frac{Z_2 - Z_C}{Z_2 + Z_C} \quad (5.45)$$

Where, L is electrode length, c is the velocity of light in a vacuum, Z_C , Z_1 , and Z_2 are the microwave characteristic impedance, the microwave generator internal impedance, and the shunted loaded impedance, respectively. Here N_m is microwave effective index, N_o is optical effective index, α represents overall microwave and dielectric losses, and c is the velocity of light. After applying mathematical formulas such as:

$$\sin u = \frac{e^{ju} - e^{-ju}}{2j} \quad (5.46)$$

Under the impedance matching condition $Z_C = Z_1 = Z_2$, which is often set to 50Ω , the bandwidth is limited by the velocity mismatch and the total microwave loss, and thus the optical response equation is reduced to:

$$m(f) = \left| e^{-ju_+} \frac{\sin u_+}{u_+} \right| \quad (5.47)$$

Under both impedance and phase matched conditions $Z_C=Z_l=Z_2$, and $N_m=N_o$ where N_o is often taken as 2.15 at $\lambda=1.55 \mu\text{m}$, for LiNbO_3 modulator structure whereas for GaAs is taken as 3.35 at $\lambda=1.55 \mu\text{m}$. The bandwidth is limited by the microwave loss only, and then the optical response equation is further reduced, with the 3dB optical bandwidth, Δf , and is given by (Minakata, 2001):

$$\Delta f = \left(\frac{6.84}{\alpha_c L} \right)^2 \quad (5.48)$$

where α_c is conductor loss in dB per unit length normalized at 1 GHz. However, in the estimation of the modulator bandwidth the critical factor is the velocity mismatch, and when this is not achieved, the 3dB optical bandwidth, Δf , is determined approximately by (Minakata, 2001):

$$\Delta f = \frac{2c}{\pi |N_o - N_m| L} \quad (5.49)$$

The optical 3dB bandwidth corresponds to the electrical 6dB bandwidth. For optical modulators operating beyond 40 GHz, the total dielectric loss will play a significant role in the determination of the overall speed of the modulator. In the calculation of optical bandwidth often only the conductor loss is considered. However, when the dielectric loss is included, then the total frequency dependence loss may be given by:

$$\alpha(f) = \alpha_c \sqrt{f} + \alpha_d f \quad (5.50)$$

If α_c and α_d are normalized at 1 GHz, then f is given in GHz. Here α_c is conductor loss in $\text{dB} / \sqrt{\text{GHz}} \cdot \text{cm}$ and α_d total dielectric loss in units of $\text{dB} / \text{GHz} \cdot \text{cm}$. The

dielectric loss can arising from different lossy microwave regions and in this for LiNbO₃ electrooptic modulator case,

$$\alpha_d = \alpha_{dL} + \alpha_{dS} \quad (5.51)$$

where α_{dL} and α_{dS} are the dielectric losses in the LN and SiO₂ regions respectively. The dielectric loss arisen from different lossy microwave regions in semiconductor electrooptic modulator case are;

$$\alpha_d = \alpha_{AlGaAs / GaAs} + \alpha_{Ta_2O_5} \quad (5.52)$$

where $\alpha_{AlGaAs / GaAs}$ and $\alpha_{Ta_2O_5}$ are the dielectric losses in the AlGaAs/GaAs (layers) and Ta₂O₅ regions, respectively.

The effect of the impedance mismatch, conductor loss, dielectric loss and velocity mismatch on the bandwidth and subsequent attempt to match both N_m and Z_C and their effects on the bandwidth are presented in the subsequent chapters for both LN and GaAs electrooptic modulators.

5.10 Velocity matching techniques

Travelling wave electrooptic modulators fabricated in the substrate materials for which the optical and microwave velocities are equal offer the potential of very high modulation bandwidth. However, for important materials such as lithium niobate and gallium arsenide there is an inherent mismatch between the optical and microwave velocities. As a result, the maximum achievable drive frequency decreases as the modulator length is increased. Conversely, to lower the drive voltage and drive power, a longer device length is required, which is reducing the device performances for high-speed communications systems.

The velocity mismatch factor μ_d is defined as the difference between optical and microwave group velocities, with N_o and N_m the optical and microwave group refractive indices, defined in the equation (5.22) where microwave and optical group refractive

indices depend primarily on the dielectric constants involved in the modulator fabrication and the modulator structure. For the LN electrooptic modulators considered in this research work $N_o = 2.15$, whereas, N_m has to be calculated from the eq. (5.20). Also for deeply-etched semiconductor electrooptic modulator structure which is investigated here the optical velocity is $N_o = 3.35$.

In order to achieve velocity matching between two signals, for LN electrooptic modulator the microwave velocity has to be increased, whereas for GaAs electrooptic modulator the microwave velocity has to be reduced.

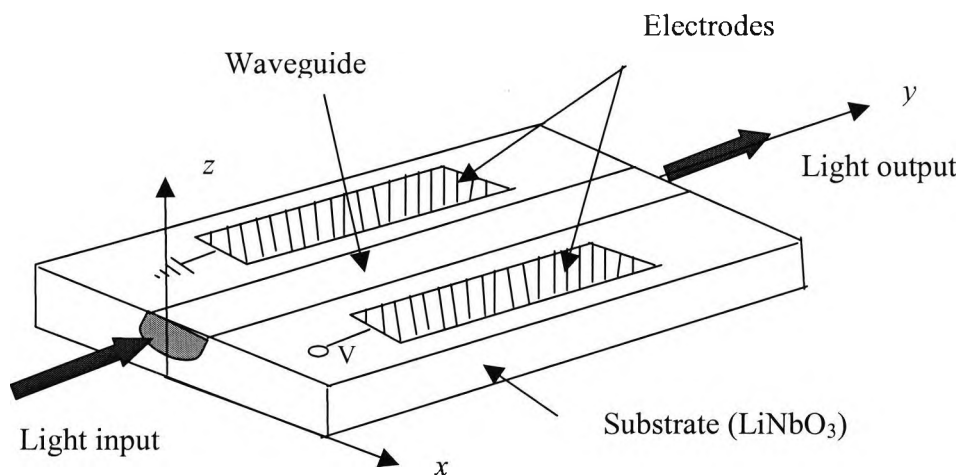


Fig. 5.10 General principal work of the traveling wave phase LiNbO_3 electrooptic modulator.

The optical response of a modulator is determined by the microwave propagation characteristics of the electrode, namely, the effective index of the microwave, N_m , the characteristic impedance, Z_c , and the overall propagation losses. The basic traveling wave phase electrooptic modulator is illustrated in Fig. 5.10. Under the impedance matching condition, $Z_c = Z_1 = Z_2$, which is often set to 50Ω , the bandwidth is limited by the velocity mismatch and the total microwave loss, and thus the optical response equation is given by equation (5.47). However, in the estimation of the modulator bandwidth the critical factor is the velocity mismatch, and when this is not achieved, the 3dB optical bandwidth, Δf , is determined approximately by the equation (5.49).

Several techniques which can be generally described as real-velocity matching and artificial-velocity matching have been proposed for LN electrooptic modulators. In artificial-velocity-matching techniques, one seeks not necessary to increase the bandwidth of the modulator, but rather the shape and shift of the frequency response. New design electrode configurations are proposed, which are referred to as reverse phase electrodes, where velocity matching is achieved by periodic phase reverse electrode configuration (Alferness, 1984). Also proposed, has been a combination of phase reverses and intermittent interaction electrodes, to achieve velocity-matching. Kawano and Noguchi (Kawano and Noguchi, 1991) proposed a shielded plane velocity-matched LiNbO_3 electrooptic modulator.

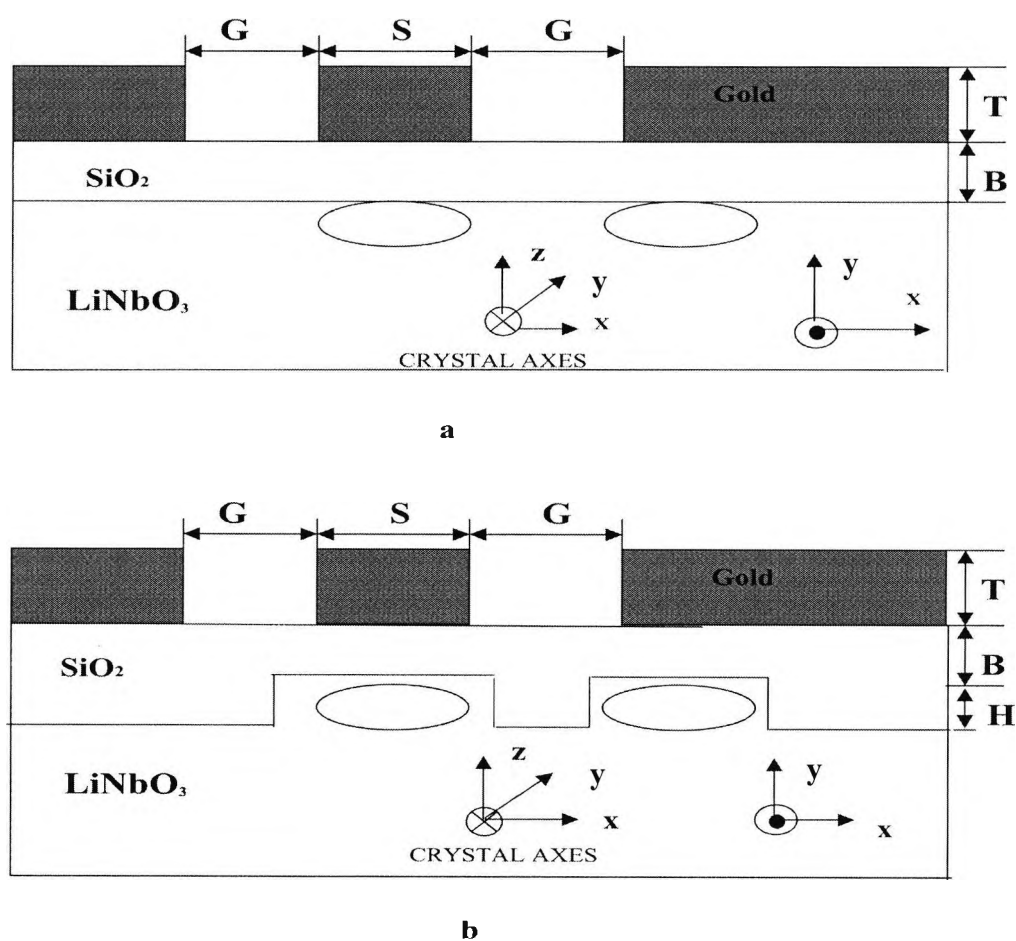


Fig. 5.11 Cross-section of the LiNbO_3 (a) un-etched and (b) etched Mach-Zehnder modulator.

In real velocity matching techniques once the structure is designed, then an attempt is made to modify the effective propagation velocity of either optical or, more typically, the electrical signal to equalize N_o and N_m . These techniques applied for LiNbO₃ electrooptic modulators include a high-index overlayer and etching of the lithium niobate to increase electrical field into the lower-index air to speed up the electrical signal. Such technique is applied in this research work, achieving the velocity matching and impedance matching simultaneously, showing a significant increase of the bandwidth of the modulator. Most high-speed modulators are based on the Mach-Zehnder approach fabricated on Z-cut LN substrates and operating with a vertical electric field to utilize the largest electrooptic coefficient r_{33} of LN, illustrated in Fig. 5.11 for etched and unetched structures. The relative dielectric constants of z-cut LN substrate were 28 and 43 in the perpendicular and parallel directions to the substrate surface respectively. To reduce optical loss due to lossy metal electrode, often a SiO₂ buffer layer is used, which also assists in the phase matching. The relative dielectric constant of the SiO₂ buffer layer is taken as 3.9. The coplanar waveguide (CPW) electrode is commonly used as a travelling-wave electrode for Ti:LN optical modulator because it provides good connection to an external coaxial line.

Although GaAs electrooptic modulators suffer from a relatively smaller electrooptic coefficient, compared to the traditional materials like LiNbO₃ this is however partly compensated by their higher refractive indices. Often travelling-wave designs are employed to increase the interaction length between the optical signal and the electrical signal and thus reduce the modulator half-wave voltage (V_π). These designs will increase the interaction length up to a point, but they are still limited by the velocity mismatch between the optical signal and the microwave signal. In this work, illustrated in Fig. 5.12, a newly proposed structure for a deep-etched electrooptic modulator is employed where the velocity matching is achieved by introducing a tantalum pentoxide, Ta₂O₅, coating which has a high relative dielectric constant at the microwave frequency, $\epsilon_r = 27$, but a low refractive index at the optical frequency, $n=2.03$. Tantalum pentoxide (Ta₂O₅) has been investigated over the past decade and is a low-absorption material, suitable for optical coating. Two types of tantalum pentoxide Ta₂O₅ overlayer arrangement structures have been investigated, designated *A* and *B*, shown in Fig. 5.12.

In the structure *A* as shown in Fig. 5.12 a, tantalum pentoxide is deposited all around the mesa. In the structure *B* as shown in Fig. 5.12 b, the Ta_2O_5 thickness is deposited on the two sides of the mesa. In these cases a $0.1 \mu\text{m}$ thick *highly doped* (1×10^{18})/ cm^3 GaAs layer below the lower cladding is considered as the ground electrode.

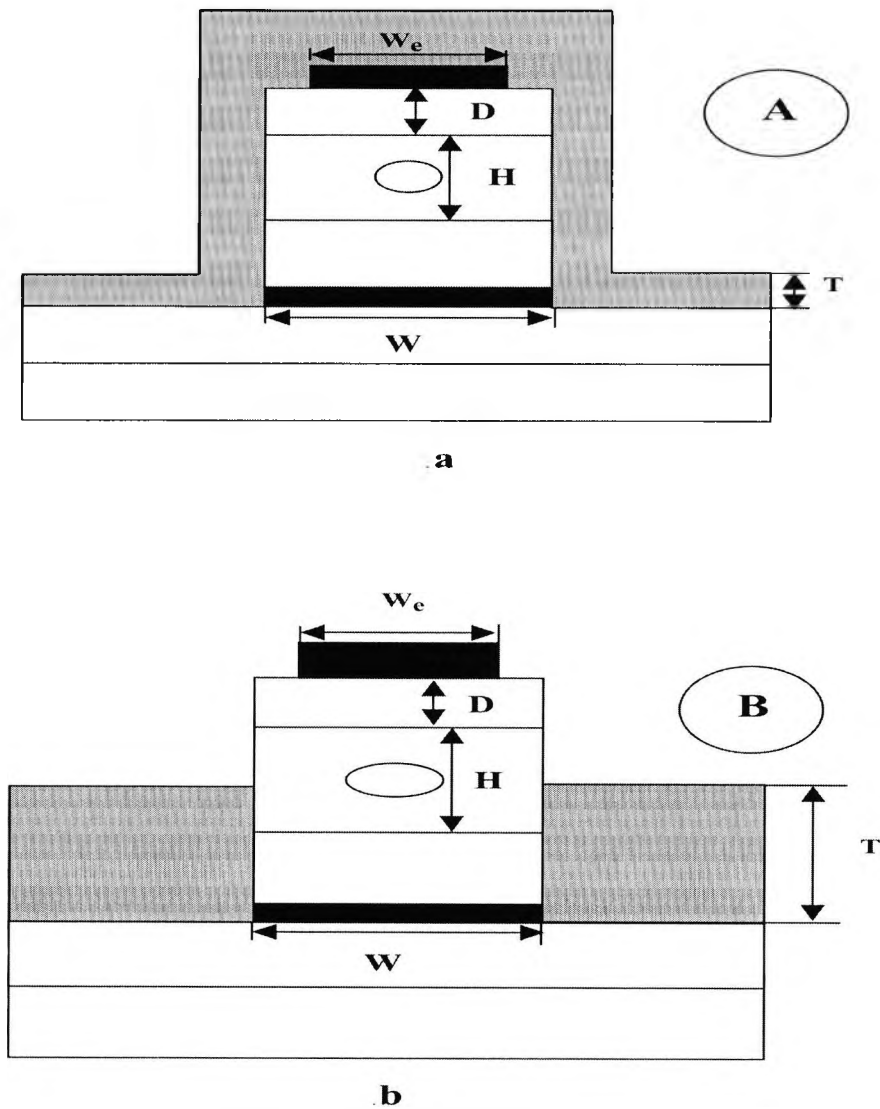


Fig. 5.12 Schematic diagrams of a deep-etched GaAs/AlGaAs of the semiconductor electrooptic modulators for two types of the Ta_2O_5 overlayers arrangements, *A* and *B*.

Various attempts have been made to achieve velocity matching, such as by placing a GaAs superstrate over the GaAs (Nees, 1989) travelling-wave modulator, where the velocity of the electrical signal is reduced to that of optical signal. However earlier work reported (Nees, 1989) indicates that the product of the half-wave voltage length product $V_{\pi}L$, was too high, at 288 V. The use of slow-wave electrodes, fabricated on undoped epitaxial layers by Spikerman, 1996, has enabled the achievement of near velocity matching, with an impedance Z_0 of $46 \pm 1 \Omega$, a bandwidth greater than 40 GHz and a value $V_{\pi}L$ product of 16.8 V. Another approach which combines p-i-n and coplanar features has also been reported (Tan, 1990) with a bandwidth up to 15 GHz. A travelling wave modulator with the bandwidth around 50 GHz and a value of V_{π} in the region of 10 volts at 1300nm has been reported by Walker, 1994, in which the velocity matching was achieved by means of a loaded (slow-wave) transmission-line. Recently (Craig, 1997) reported a technique to deposit an amorphous hydrogenated silicon cover on the coplanar electrical waveguide of the electrooptic modulator, where the silicon acts as both a cladding for the optical waveguide and a slow-wave structure to the electrical signal and the approximate value of the bandwidth has been measured as 20 GHz, with the switching voltage being 54 Volts at $1.55 \mu\text{m}$ and showing a velocity matched intersection length of 8.3 millimeters.

To date, most of the work reported has focused only on obtaining the velocity matching condition as one of the essential aims of the design process. For the next generation of ultra-high-speed modulators, it is necessary to optimize the electrode structures to achieve simultaneous matching of the velocity and impedance along with a reduced overall microwave loss.

Summary

In this chapter an investigation into microwave properties of electrooptic modulators, in particular LiNbO_3 and semiconductor modulators has been reported. Both types of modulator structures have been presented in this section. An analytical approach using quasi-TEM and FEM has been presented in the calculation of microwave parameters. Starting with potential distribution for both structures, the electric field and magnetic field components have been investigated in detail. The capacitance calculation through

the line integral based on the divergence theorem (given in the Appendix 5) has been presented in details in this chapter. Attenuation constants for both conductor loss and dielectric loss have been explained, and their effects on the device performance briefly discussed. The bandwidth calculation has been presented and the effects of conductor and dielectric loss on the bandwidth calculation has also investigated. One of the most important parameters in the overall bandwidth determination of the electrooptic modulator is the velocity mismatch between the optical carrier and electrical signal, carried in this chapter. The effect of the impedance mismatch on the bandwidth and a subsequent attempt to match both N_m and Z_C and their effects on the bandwidth have also been presented. Based on the study in this chapter a future investigation of the microwave properties, and velocity matching for both LiNbO_3 and GaAs modulators, will be illustrated in subsequent chapters.

Unetched Lithium Niobate Electrooptic Modulator

6.1 Introduction

Various studies have been reported concerning optical modulators that use titanium-diffused lithium niobate (Ti: LiNbO₃) for optical modulators that are applicable to high-speed optical communication, optical information processing and optical sensing systems. Optical modulators are essential components for digital and analog fibre optic transmission. Even though there has been considerable interest in electrooptic waveguides made from dielectric crystals such as LiNbO₃, over the past few decades, there is still a strong demand for devices fabricated from this material because of its advantageous properties such as its low transmission loss, large electro-optical coefficient, as well as the low chirp and high bandwidth with which it is associated (Wooten, 2000). However, because of the nature of dielectric crystals, the material cannot be integrated with other electro-optic materials such as semiconductors, and it is because of this that LiNbO₃ modulators are used for external modulation applications.

The guiding in LiNbO₃ is achieved by the introduction of another material, of which Ti-indiffusion (Korotky, 1987) and annealed proton exchanges (APE) (Charczenko, 1993) are the better known techniques. However, Ti-in diffusion is mainly used in LiNbO₃-based modulator devices and the technique which is used throughout research work in etched and unetched structures.

The most important performances of the optical modulators are determined by optical 3 dB bandwidth, B (GHz), and the driving power, P (mW), where these two factors are in a trade-off relationship. Also, the main restriction in the broad-band improvement of LN modulators is caused by phase velocity mismatch between microwaves and optical waves. Impedance mismatch plays significant bandwidth reduction also.

There are many waveguide devices which are fabricated using LiNbO₃ such as directional couplers (Anwar, 1999), Mach-Zehnder interferometers (Anwar, 2002), amplifiers (Kawano, 1992), wavelength filters and switches (Pohlmann, 1991). and

polarisation controllers (Heismann, 1994). However, in this research work only the design of LiNbO₃ modulators is addressed.

Most high-speed modulators are based on the Mach-Zehnder approach fabricated on Z-cut LN substrates and operate with a vertical electric field to utilize the largest electrooptic coefficient r_{33} of LN. The relative dielectric constants of Z-cut LN substrate were 28 and 43 in the perpendicular and parallel directions to the substrate surface, respectively. For modulators signal frequency to reduce optical loss due to lossy metal electrode, often a SiO₂ buffer layer is used, which also assists in the phase matching. The relative dielectric constant of the SiO₂ buffer layer is taken as 3.9. The coplanar waveguide (CPW) electrode is commonly used as a traveling-wave electrode for Ti:LN optical modulator because it provides good connection to an external coaxial line, a schematic cross section of which is shown in Fig. 6.1.

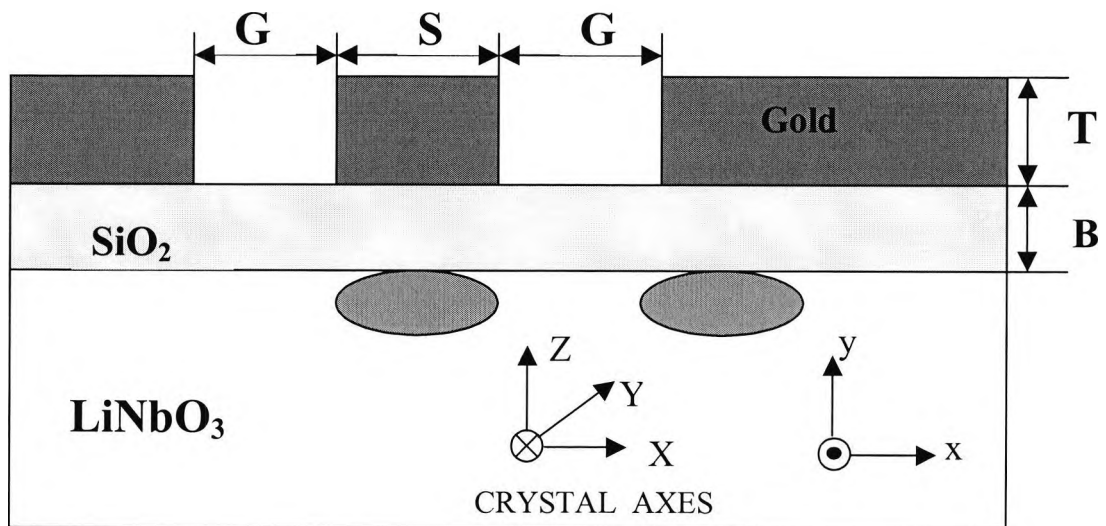


Fig. 6.1 Cross section of Z-cut unetched lithium niobate electrooptic modulator.

The gold electrode thickness is identified with T (μm), the SiO₂ buffer layer thickness, B (μm), G , represents the gap between the hot electrode and the ground electrodes (left and right), in this case the hot central-electrode (strip) width is identified with S (μm).

6.2 Modulator Fabrication

Lithium niobate has very large intrinsic modulation bandwidth, but the device switching speeds are mainly limited by a variety of physical constraints. Modulation is produced by applying voltage to the gold electrode, causing voltage-induced change in the refractive index. The changed refractive index is very small; therefore either large voltage or long electrode lengths are needed to obtain sufficient light modulation. For the length that allows reasonable voltages, the capacitance of the lumped element gold electrodes would limit the bandwidth to less than 1 GHz (Wooten, 2000).

A lithium niobate electrooptic modulator can usually be several centimeters long, therefore preservation of the cross-section dimensions along the length of the device presents a real challenge not only from the fabrication point of view, but also in the choice, compatibility and reliability of the materials used. Characteristics of the Ti-diffused LiNbO₃ electrooptic modulators depend very much upon crystal quality and fabrication parameters. Required materials for lithium niobate electrooptic modulators include the electrooptic substrate, electrode (gold) metal, electrode adhesion layer, buffer layer and the dopant used for fabrication of the optical waveguides. Modulators also require special packaging in order to minimize bias drift due to charge migrating and buildup of pyroelectric charges (interferences).

6.3 Titanium diffused waveguide fabrication

Lithium niobate has been material of choice for the fabrication of electrooptic modulators due to its high electrooptic coefficients and high optical transparency in the near infrared wavelength used for telecommunications. Its high Curie temperature (1100 °C-1180 °C) makes it practical for fabrication. It is also thermally, mechanically and chemically stable and is compatible with conventional integrated-circuit processing technology (Wooten, 2000). The fabrication procedure of titanium diffused waveguides involves four steps. The process is straightforward, but precautions must be taken to suppress the

out-diffusion of Li from the surface of the substrate, because the Li-diffusion surface can result in unwanted planer waveguide for z-polarized light which can seriously affect modulator performances. LiNbO₃ waveguides have been fabricated by indiffusion of Ti usually near 1000 °C. The typical step to fabricate waveguides is by lifting-off patterning as illustrated in the Fig. 6.2-6.5 (Alferness, 1988)

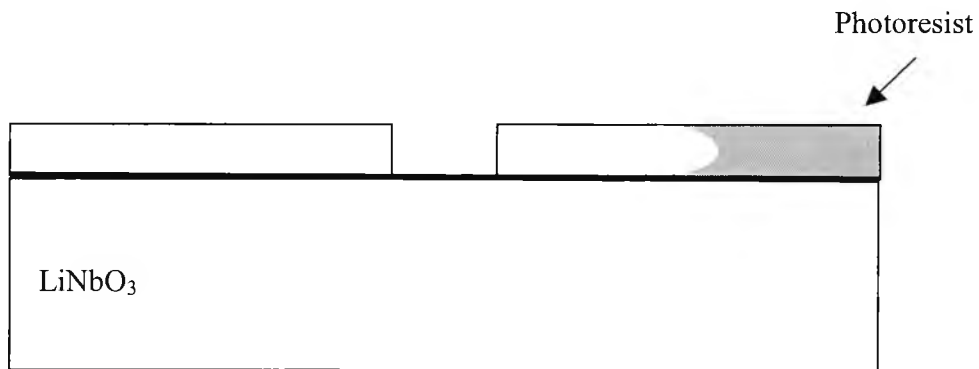


Fig. 6.2 Step one expose waveguide pattern.

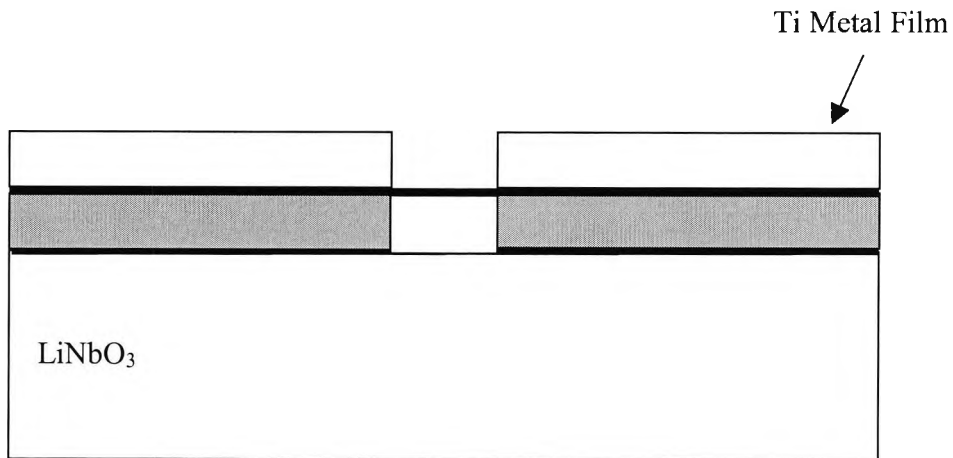


Fig. 6.3 Step two deposit titanium dopant.

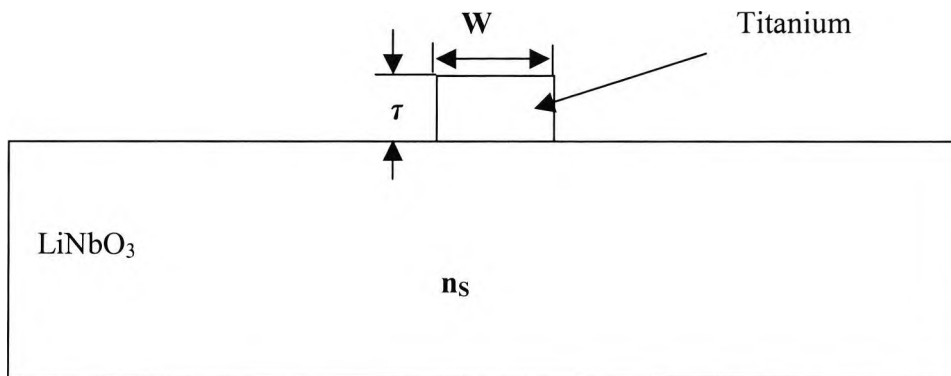


Fig. 6.4 Step three liftoff process.

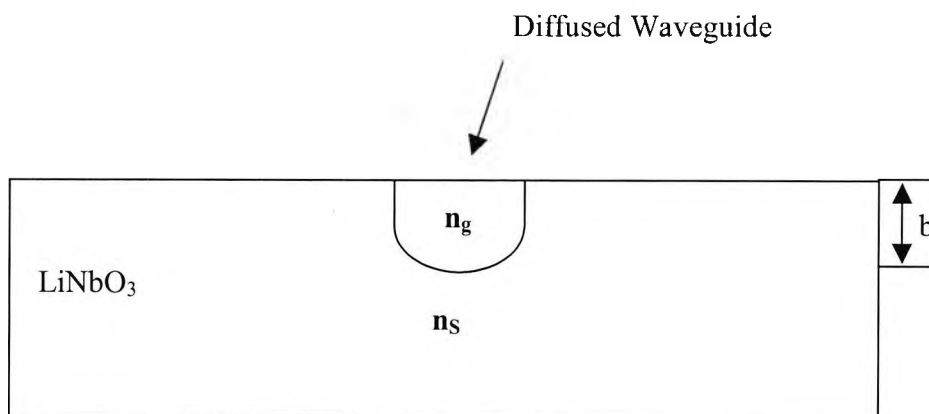


Fig. 6.5 Step four diffused waveguide.

LiNbO₃ waveguides have been fabricated by indiffusion of Ti usually near 1000 °C. The typical step to fabricate waveguides is by lifting-off patterning as illustrated in Fig. 6.2-6.5. The process of crystal cleaning is carefully done with photoresistor, and then a mask with the desired waveguide pattern is placed in contact with the crystal as shown in Fig. 6.2 which is exposed to uv (ultra violet) light illustrated in the Fig. 6.3. Upon developing to remove the exposed photoresist, a window corresponding to the waveguide pattern is left in the photoresist shown in the Fig. 6.4. Titanium is deposited over the entire crystal by rf sputtering, by e-beam deposition or by using a resistively heated evaporation illustrated in the Fig. 6.5. After this process, the crystal is placed in a photoresist solvent in order to remove the photoresist and the unwanted titanium, leaving the desired strip of titanium. There is another way of patterning, instead of the liftoff process, the patterning can also be achieved by depositing titanium over the entire, then selectively removing it outside the desired waveguide region.

The crystal of LiNbO₃ then is placed in a diffusion furnace for diffusion at temperatures that range from 980⁰ to 1050 °C for typical diffusion times of 4-10 hours. After diffusion process, cooling down is performed in flowing oxygen to allow reoxidating of the crystal to compensate for oxygen loss during diffusion process. Typically, 80% relative humidity in the flow gas is sufficient to eliminate unwanted guiding for diffusion temperature below 1000⁰. However, the technique has been successfully used at temperature as high as 1050 °C. Many techniques have been reported in order to eliminate the unwanted guiding (outdiffusion), but none of them totally eliminates the outdiffusion. They work sufficiently well to keep unwanted planar guiding from being a problem under most circumstances.

Characteristics of the Ti-diffused LiNbO₃ optical waveguides largely depend upon crystal quality and fabrication parameters such as waveguide depth, d , diffusion time, t , diffusion temperature, T , and to a lesser extent on the titanium strip width. With respect to the former, the characteristics are related to the deviation of the Li/Nb ratio (or refractive index) degree of induced defects, and impurities such as Fe in the wafer. With respect to the latter, they are related to the Ti-film thickness and width deviations, diffusion conditions (atmosphere, temperature and time), etc. In order to fabricate

optical waveguide, while still maintaining excellent characteristics and good reproducibility, it is necessary to control tightly each of these factors (Kawano, 1989).

The diffusion model for entire simulation process for LiNbO₃ electrooptic modulator is carried out using the Finite Element Method (FEM), and involves first finding the refractive index profile, $n(x,y)$, which is generally described in terms of the exponential function (exp) and the error function (erf) (Korotky and Alferness, 1987).

$$C(x, y) = \frac{\tau}{d_y} \frac{1}{\sqrt{\pi}} \cdot \exp\left[-\left(\frac{y}{d_y}\right)^2\right] \cdot \left[\operatorname{erf}\left(\frac{\frac{W}{2} + x}{d_x}\right) + \operatorname{erf}\left(\frac{\frac{W}{2} - x}{d_x}\right) \right] \quad (6.1)$$

where,

τ the thickness of the titanium layer as illustrated in the Fig. 6.2.

W width of the titanium layer or the effective width of the guide, Fig. 6.4.

$d_{x,y}$ the diffusion length along the x, y axes

$C(x, y)$ the titanium concentration profile in the transverse plane,

$$d_{x,y} = 2\sqrt{D_{x,y}t} \quad (6.2)$$

where, $D_{x,y}$ is the diffusion coefficients along the x, y axes respectively which follows the Arrhenius law (Fouchet, 1987).

$$D_{x,y} = D_O^{x,y} e^{-(E_O^{x,y})/kT} \quad (6.3)$$

where, $D_O^{x,y}$ are the diffusion constants along x, y axes, which depends on the crystal orientation (crystal cut), (Fukuma, 1980).

$E_O^{x,y}$ the activation energies in the x, y directions;

k the Boltzmann constant;

T the diffusion temperature in Kelvin;

t the diffusion time in hours.

These equations are with respect to a single waveguide, but for weakly coupled DC devices the equation for Ti concentration $\hat{C}(x, y)$ becomes ((Januar, 1992).

$$\hat{C}(x, y) = C \left[\left(x - \frac{W}{2} - \frac{G}{2} \right), y \right] + C \left[\left(x + \frac{W}{2} + \frac{G}{2} \right), y \right] \quad (6.4)$$

where, G is the gap between two waveguides of the modulator structure. In the optical frequency range, the ordinary and extraordinary refractive index profiles of the Ti: LiNbO₃ optical waveguide n_o and n_e are given by (Koshiha, 1999)

$$n_o = n_{oS} + \Delta n_s [f(x)g(y)]^{0.55} \quad (6.5)$$

$$n_e = n_{eS} + \Delta n_e f(x)g(y) \quad (6.6)$$

$$f(x) = \frac{\operatorname{erf}\left(\frac{2x+W}{2d_x}\right) - \operatorname{erf}\left(\frac{2x-W}{2d_x}\right)}{2\operatorname{erf}\left(\frac{W}{2d_x}\right)} \quad (6.7)$$

$$g(y) = \exp\left[-\left(\frac{y}{d_y}\right)^2\right] \quad (6.8)$$

For the left waveguide, x is replaced by $x - G$. At operating wavelength $\lambda = 1.55 \mu\text{m}$

$n_{oS} = 2.214$, $n_{eS} = 2.138$, $\Delta n_o = 0.0062$, $\Delta n_e = 0.0146$, when, $W = 6 \mu\text{m}$, $d_x = 4.850 \mu\text{m}$, and $d_y = 4.105 \mu\text{m}$. The refractive indexes of the Z-cut crystal orientation are given $n_x = n_z = n_o$ and $n_y = n_e$ and the refractive indexes of the SiO₂ buffer layer and gold electrodes are 1.45 and 0.379-j10.75, respectively.

Obviously, the expression for Δn_e is very nearly proportional to C (the Ti concentration) and Δn_o has a nonlinearity relationship with C and they are given (Korotky and Alferness, 1987).

$$\Delta n_e = bC_o \quad (6.9)$$

$$b(\lambda) = 0.552 + \frac{0.065}{\lambda^2} \quad (6.10)$$

$$C_o = \frac{2}{\sqrt{\pi}} \cdot \frac{\tau}{d_y} \operatorname{erf}\left(\frac{W}{2d_x}\right) \quad (6.11)$$

Δn is the change in refractive index of the LiNbO₃ due to titanium diffusion. Since LiNbO₃ is a uniaxially anisotropic crystal, the refractive index is viewed as n_e (extraordinary refractive index) along the optic axis of the crystal (usually taken along the Z axis of the crystal) and n_o (ordinary refractive index) along the other two axes. In this research work, the expressions for n_e , n_o , Δn_e and Δn_o used for device simulation are those given by Korotky and Alferness and Fouchet and have been chosen because both equations give a clear representation of the diffusion mechanism, since most if not all of the diffusion parameters have been incorporated into these equations.

The refractive index profiles depend primarily on the fabrication parameters as mentioned above and via the diffusion constants, d_x and d_y , which are adjusted to enable an understanding of their effects on the modulator performance.

6.4 Fabrication of buffer layer SiO₂

It is obvious that Ti-diffused LiNbO₃ waveguide devices have characteristics of instabilities due to DC and thermal drift (characteristic changes caused by environmental temperature changes). These problems can be solved by optimising the buffer layer properties of SiO₂. When voltage is applied the DC drift occurs because electric charges move on the surface of the LiNbO₃ crystal or with the buffer layer. When a DC electric

field is applied between electrodes, then the effective electric field applied to the waveguide decreases.

Buffer layer is needed to reduce current induced heating losses to the TM polarized (light polarized perpendicular to the crystal). The silica buffer layer is deposited by atmospheric chemical vapour deposition (CVD) (Alferness, 1988). This method decreases damage to the crystal, and permits formation of high-quality films at a low temperature, and enables drastic changes in the characteristics by changing the film forming conditions. The thickness (CVD) of SiO₂ layer eliminates measurable loading loss. In general introduction of buffer layer thickness has significantly improved modulator performances. However, the drift is always associated with the finite (and deposition dependent) conductivity of the buffer layer.

6.5 Fabrication of gold electrodes

Gold is generally used for fabrication of high-speed lithium niobate electrooptic modulators, because of high purity metal, small grain size, minimum features distortion, and reasonable plating rate. The fabrication of the RF gold electrode involves several steps illustrated on the Fig. 6.6 (Alferness, 1988).

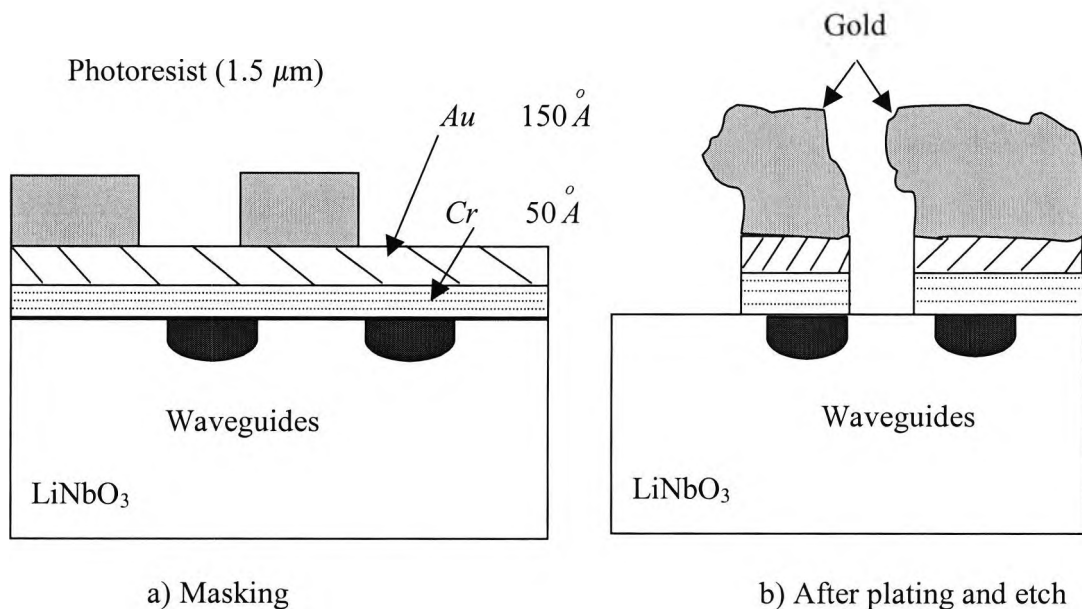


Fig. 6.6 Fabrication steps of the gold electrodes for LiNbO₃ electrooptic modulator.

For electrode-forming an electroplating method has been employed in order to reduce conductor loss. A thin gold seed layer is deposited over the entire crystal in top of SiO₂ buffer layer. The electrode pattern is then photolithographically defined. The photoresist is spun, shown in the Fig. 6.2, and the electrode pattern aligned over the waveguides, which open a window in the resist. Then, the crystal is placed in a plating bath and gold plated to thickness of 2-3 μm . After this process, the gold seed layer is removed in the gap region illustrated in the Fig. 6.3. Gold plate fabricated using this method has conductivity comparable to bulk conductivity. A similar approach can be applied for fabrication of the modulator design investigated in this research work with some small difference in that this design involves two ground electrodes on left and right with the hot electrode in the middle as illustrated in Fig. 6.1.

6.6 Dicing, polishing, pigtailling, packaging, and testing of electrooptic modulators.

The crystal end faces are cut at an angle to the waveguides in order to eliminate reflections and are then polished to an optical finish (Wooten 2000). A good optical finish and a sharp edge are necessary at both the input and output optical faces of the modulator in order to ensure good fibre-to-waveguide coupling. Debris (scattered fragments) from dicing (dice box) and particulates from polishing compounds during fabrication process are contaminants which can negatively affect the modulator performance and long-term reliability of the device. Therefore they must be removed during chip cleaning operations. Applications of the LiNbO₃ in the real world require the integrated-optic chip to be pigtailed (plait of hair hanging from the back of the head, according to dictionary) and packaged in order that optical and electrical signals can be effectively and efficiently directed into and away from the modulator. LiNbO₃ can be packaged in either hermetic or nonhermetic housing depending upon the application and environmental operation. Due to polarization dependence of the electrooptic effect, the polarization state of the input light supplied from the laser to the modulator must be carefully controlled and maintained in order to achieve optimum performance. Packaging and installation in the real world requires numerous procedures and precautions which have to be followed throughout the process. Key parameters that have

to be measured during final test include: optical loss, switching voltage, optical on/off extinction, bias stability and microwave properties such as S_{11} and S_{21} . Usually these measurements are performed during the design verification and validation stages.

6.7 Simulated results for unetched lithium niobate waveguide electrooptic modulators.

Based on the theoretical analysis performed in this section and in the previous chapters, simulated results during this research work for unetched LiNbO₃ electrooptic modulator are discussed in this section. The schematic and layout of the Z-cut Y-propagating unetched LiNbO₃ electrooptic modulator used throughout this work is shown in Fig. 6.7. In total, 22400 irregular triangular mesh have been used to represent more than 100 μm by 100 μm transverse cross section of the modulator structure. Distribution of electric and magnetic lines is illustrated in this figure. It is obvious that the electromagnetic field around the hot electrode has reached the peak value. Finite element coordinate axes and crystal orientation are also presented in this figure, including buffer layer thickness, B gap between electrodes, G strip width, S and applied voltage, $V = 5$ voltage.

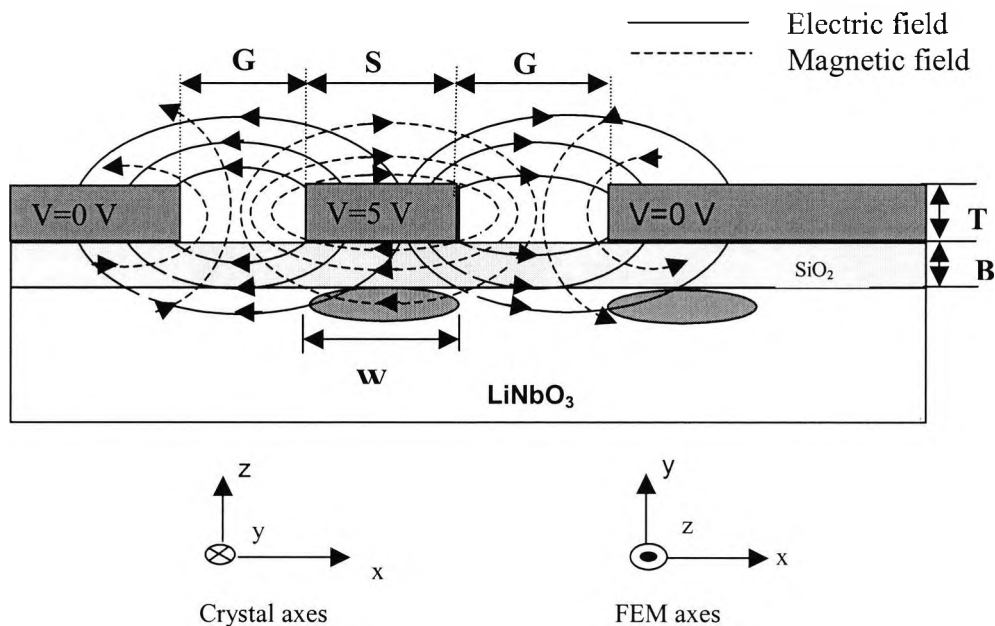


Fig. 6.7 Schematic illustration of unetched LiNbO₃ electrooptic modulator.

The relative dielectric constants of the Z-cut LN substrate are 28 and 43 in the perpendicular and parallel directions to the substrate surface respectively. To reduce optical loss due to lossy metal electrode, often a SiO₂ buffer layer is used, which also assists in the phase matching. The relative dielectric constant of the SiO₂ buffer layer is taken as 3.9. The coplanar waveguide (CPW) electrode is commonly used as a traveling-wave electrode for Ti: LN optical modulator because it provides good connection to an external coaxial line.

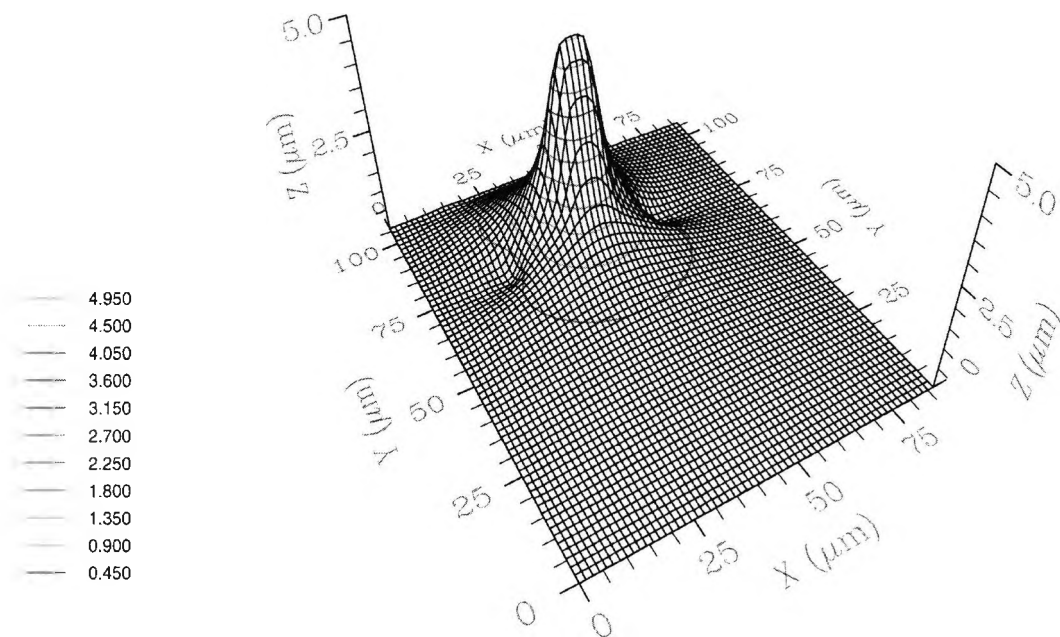


Fig. 6.8 3D potential distribution for unetched LN electrooptic modulator for $V = 5$ volts.

The coplanar waveguide-type structure arrangement for the electrode (i.e., a “hot” or central electrode with two ground electrodes) was chosen so that maximum interaction takes place in the waveguide under the central electrode in this unetched structure.

The scalar potential, $\phi(x,y)$ is calculated from the equation (5.9) using the FEM. As expected the potential value is heavily concentrated around the hot electrode, with the peak value almost 5 voltages, shown in Fig. 6.8 in 2 dimensional plane.

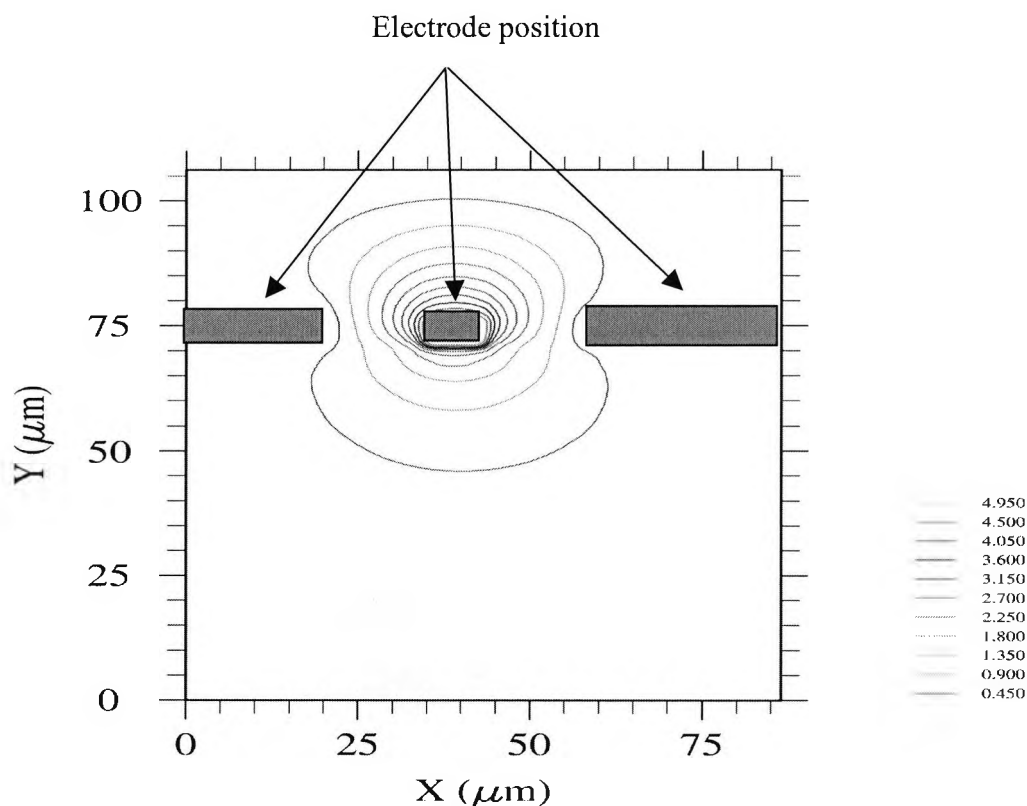


Fig. 6.9 2-D illustration of potential distribution for unetched LN electrooptic modulator.

Potential distribution depends critically on how the electrodes are designed. It is obvious that the potential distribution for the structure presented in this research work is symmetric in x and y direction. The potential distribution is exponential flattened towards the ground electrodes (left and right) until is flattened with zero value, which is exactly the voltage of the ground electrodes as illustrated in the Fig. 6.9 in one

dimensional plane. Initially, parameters for this structure are chosen: the electrode gap is, $G=15 \mu\text{m}$ electrode width, $S=8 \mu\text{m}$, electrode thickness, $T=5 \mu\text{m}$, buffer layer thickness, $B=1.2 \mu\text{m}$, and the waveguide width is, $W=9 \mu\text{m}$. Forced boundary condition is employed around the structure, where the potential value is assumed to be zero.

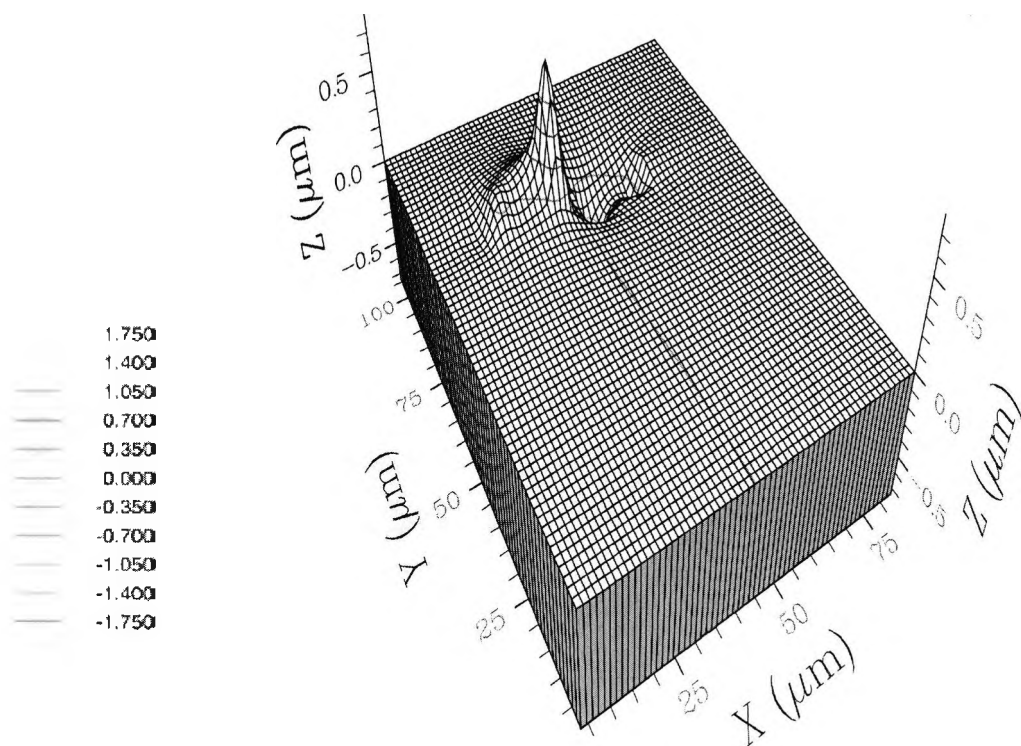


Fig. 6.10 3D illustration of the electric field concentration in x direction (E_x).

The x -component of the vector modulating electric field $E_x(x, y)$, is calculated from the scalar potential, $\phi(x, y)$, using the FEM eq. (5.13). Electric field concentration in x direction is presented in three dimensional plane in Fig. 6.10. It can be seen that due to

its asymmetry the field concentration is maximum and reaches the large peak value at the edges of the hot electrode, and is exponentially decaying. Its minimum point (zero) is in the middle of the hot electrode. Its maximum value is $0.9 \text{ (V}/\mu\text{m)}$ exponentially decaying through zero value and reaches the minimum value at $-0.6 \text{ (V}/\mu\text{m)}$, illustrated on the legend of this figure. From this presentation it is very clear that the symmetry of the electric field is very accurate, which gives confidence in further calculation of other parameters of the modulator structure. The field acting in the waveguide is very small, almost zero, therefore its effect on the waveguide can be ignored. Its profile is also illustrated in two dimensional plane presented in Fig. 6.11, where its symmetry is depending on the electrodes design.

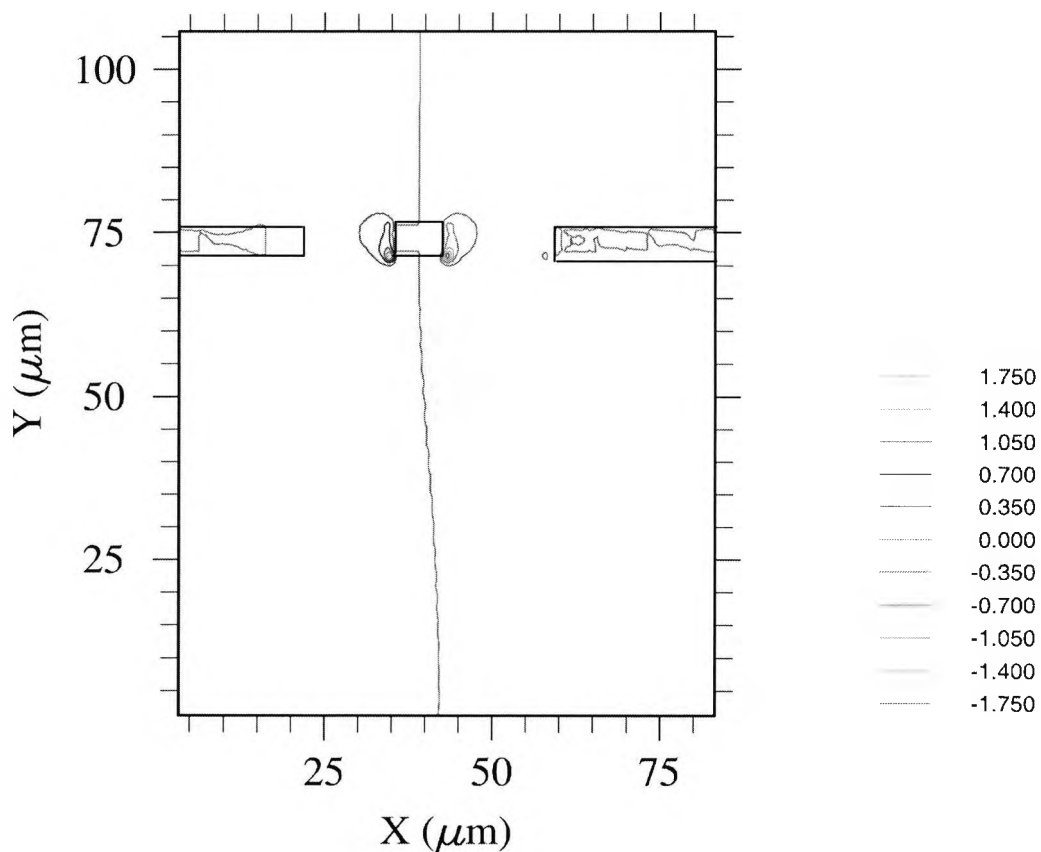


Fig. 6.11 Two dimensional presentation of $E_x(x, y)$ component.

The change in the refractive index profile produced by this electric field is neglected, because of its zero effect on the waveguide.

The y -component of the vector modulating electric field $E_y(x, y)$ is also calculated from the scalar potential, $\phi(x, y)$ using FEM eq. (5.13) and this, as well as the electrode position, is illustrated here for, 3D and 2D plots Fig. 6.12 and Fig. 6.13, respectively.

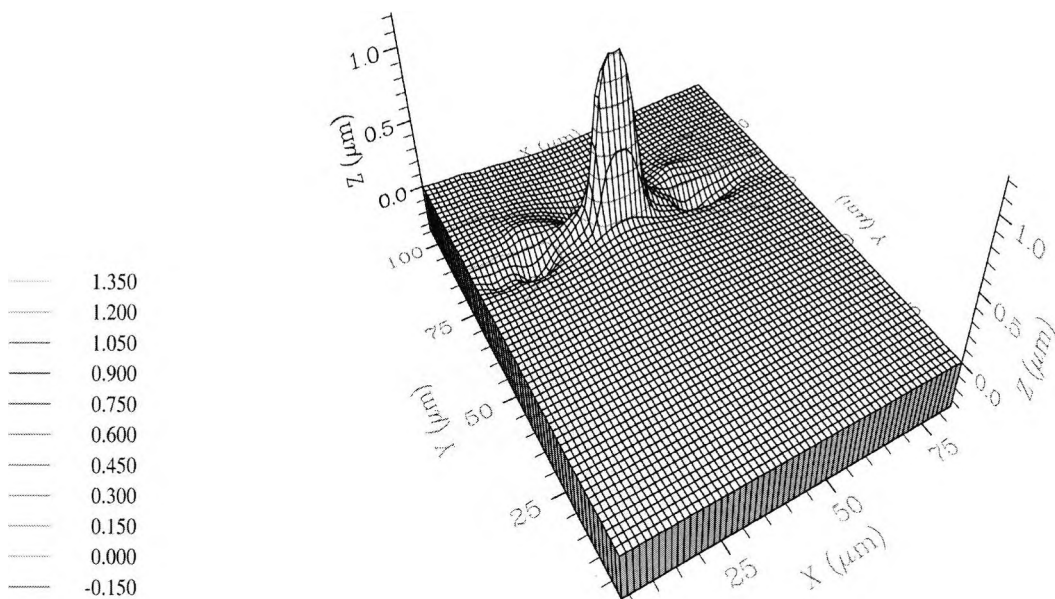


Fig. 6.12 3D plot of the modulating electric field $E_y(x, y)$ for unetched LN modulator.

As expected, the field is heavily concentrated under the hot electrode but evidence of a lower concentration under the two ground electrodes is also present. It is obvious that, due to the symmetrical placement of the gold electrodes, the modulating field acting in the second waveguide, which is placed under the one ground electrodes seen here on the

right, is small compared with that of the first waveguide, which is placed directly under the hot electrode.

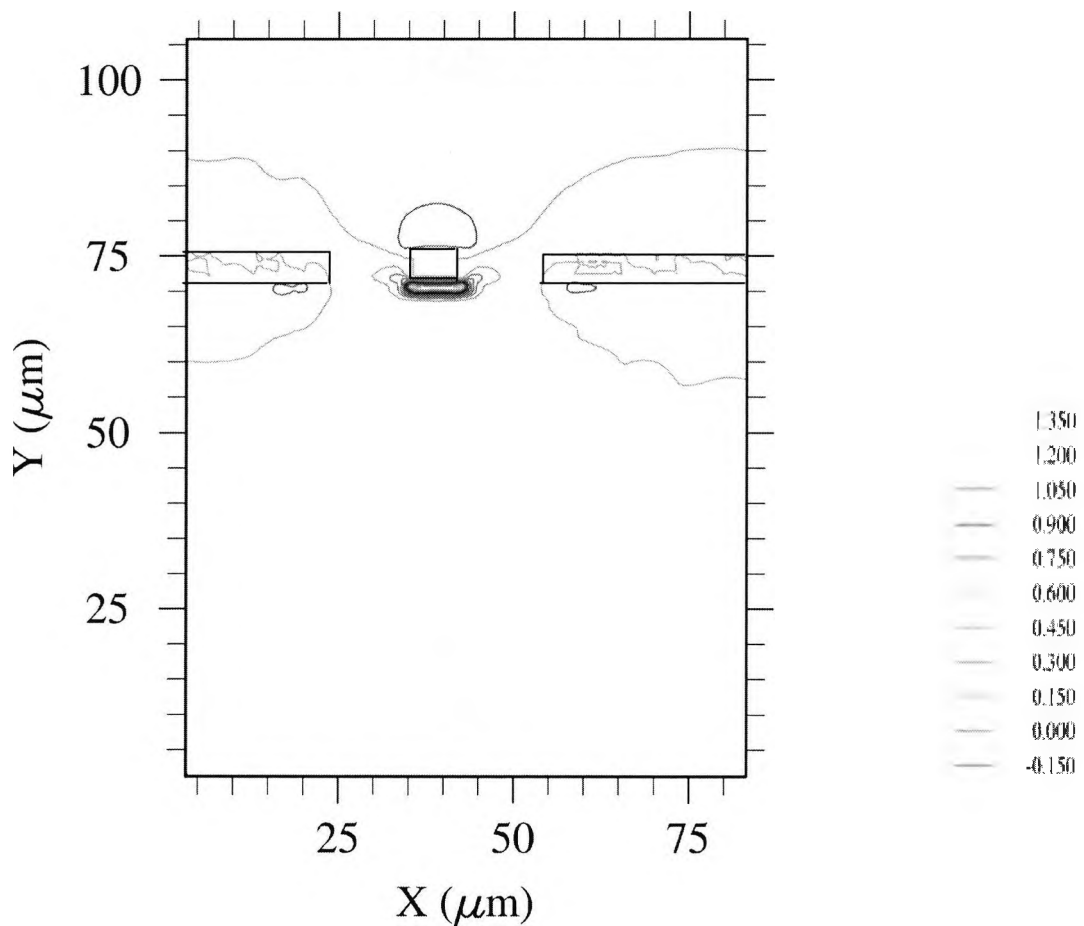


Fig. 6.13 2D plot of the $E_y(x, y)$ electric field for unetched LN electrooptic modulator.

Due to the presence of the SiO₂ buffer layer thickness, B , which is essential in order to minimize the optical loss due to the metal electrodes for TM-polarization light, it can be seen that a reasonable proportion of the modulating field is acting in the buffer layer, because of the flatter profile of the modulating electric field. Therefore, the overlap

between the optical and modulating electric field is not so high as would be the case if no buffer layer were present.

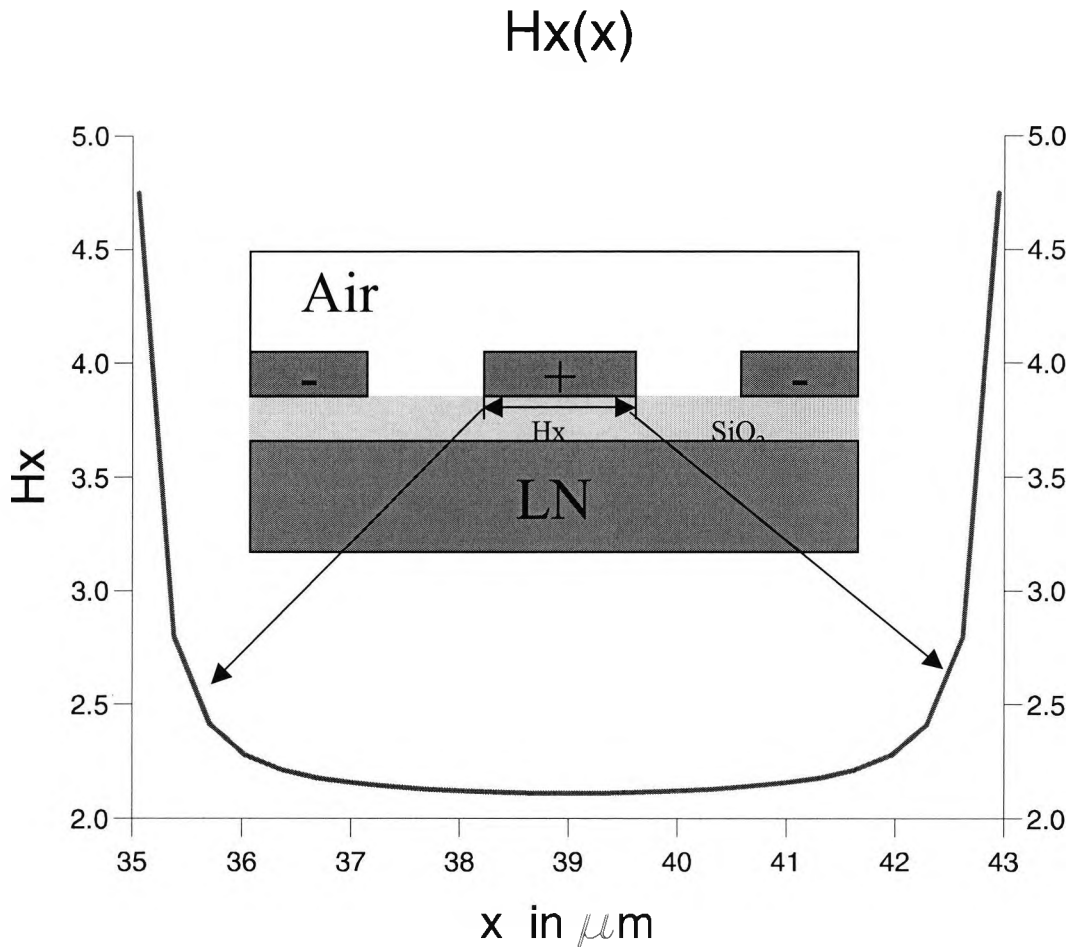


Fig. 6.14 Variation of magnetic field component along x -direction, H_x .

Concentration of magnetic field along x - direction of the hot electrode is illustrated in Fig. 6.14. It can be seen that the magnitude of the field along x direction reaches its maximum value at $35 \mu\text{m}$, then it is decreasing until it is flattened at the center of the hot electrode, after which it again starts to increase to its maximum value at the end of the hot electrode, at $43 \mu\text{m}$. This field variation is prescribing the whole width of the hot

electrode from left to right at exact value of the electrode width from 8 μm . The magnetic field is heavily concentrated on the edges of the hot electrode (left and right). Due to its symmetry the magnetic field has two maximum peaks, left and right of the strip.

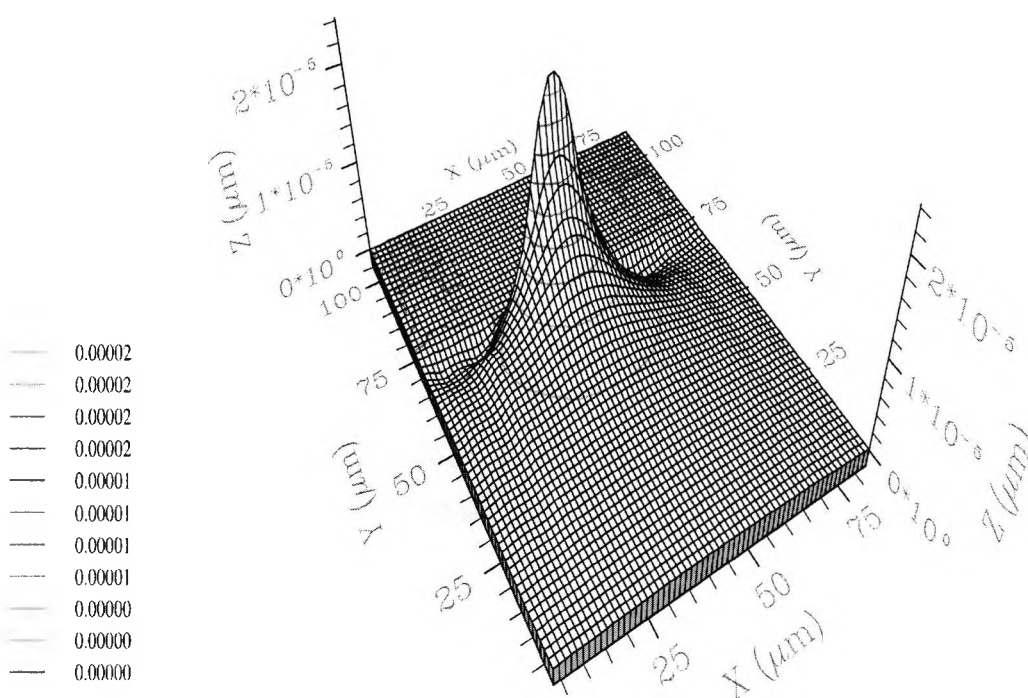


Fig. 6.15 3D plot of the change in refractive index due to an applied electric field, for an applied voltage of 5 V for unetched LiNbO₃ electrooptic modulator.

After the voltage is applied the diffused extraordinary refractive index change profile is calculated according to the equation (4.25). It can be seen that refractive change profile is mainly concentrated in the first waveguide region under the hot electrode, as result of

y -component modulating electric field, E_y , whereas its concentration is much smaller on the second waveguide, because the field value in this region is weaker as a result of the electrode position.

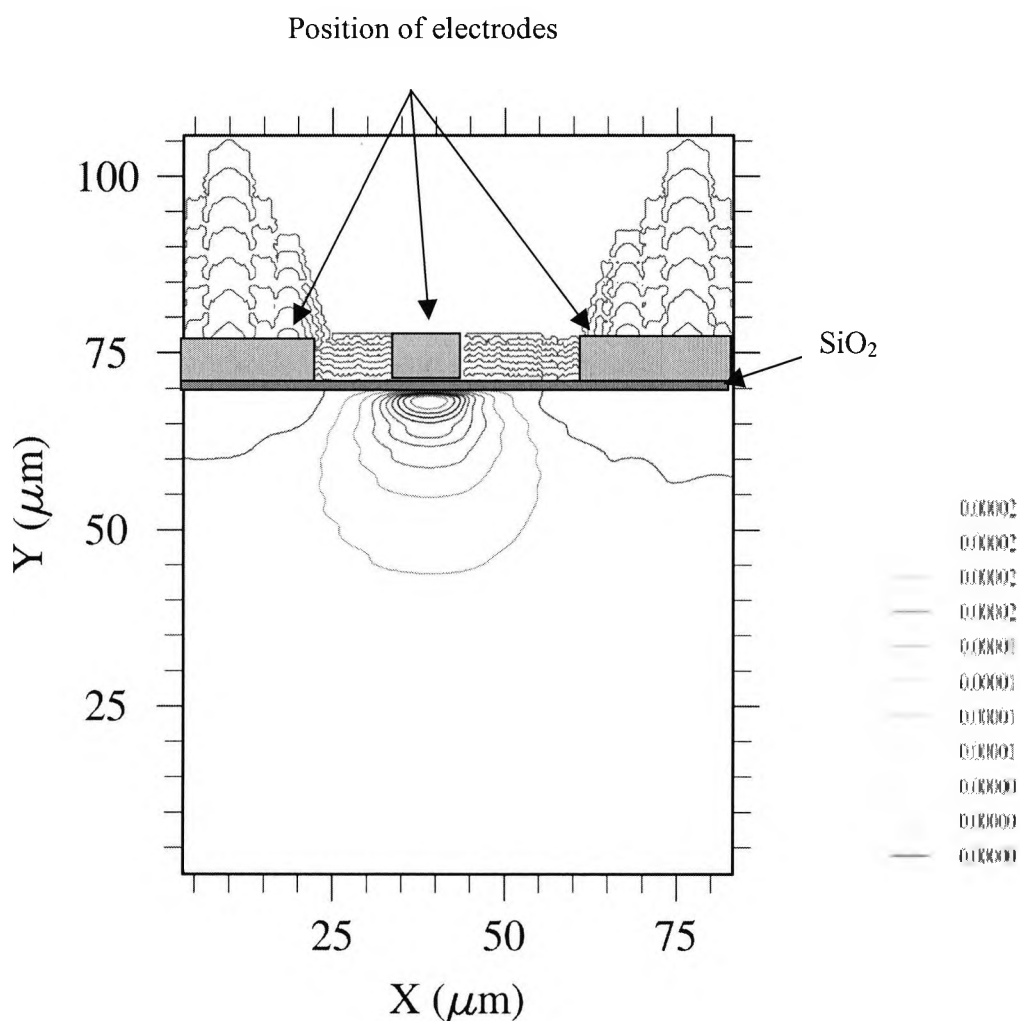


Fig. 6.16 2D plot for refractive index change due to the electric field, for an applied voltage of 5 V for unetched LiNbO₃ electrooptic modulator.

Refractive index profile and the electrode position is illustrated in Fig. 6.16. It can be seen that refractive index is heavily concentrated under the hot electrode, and largely depends upon the electrode position. It is obvious that due to electrode symmetry the refractive index profile is also symmetrically concentrated along x axis. Its concentration is mainly in the desired waveguide region. As result of electric field applied in both waveguides, $\Delta\beta_{Left} = 0.0000959$ and $\Delta\beta_{Right} = -0.0000074$, whereas the total change is; $\Delta\beta_{Total} = 0.0001033$.

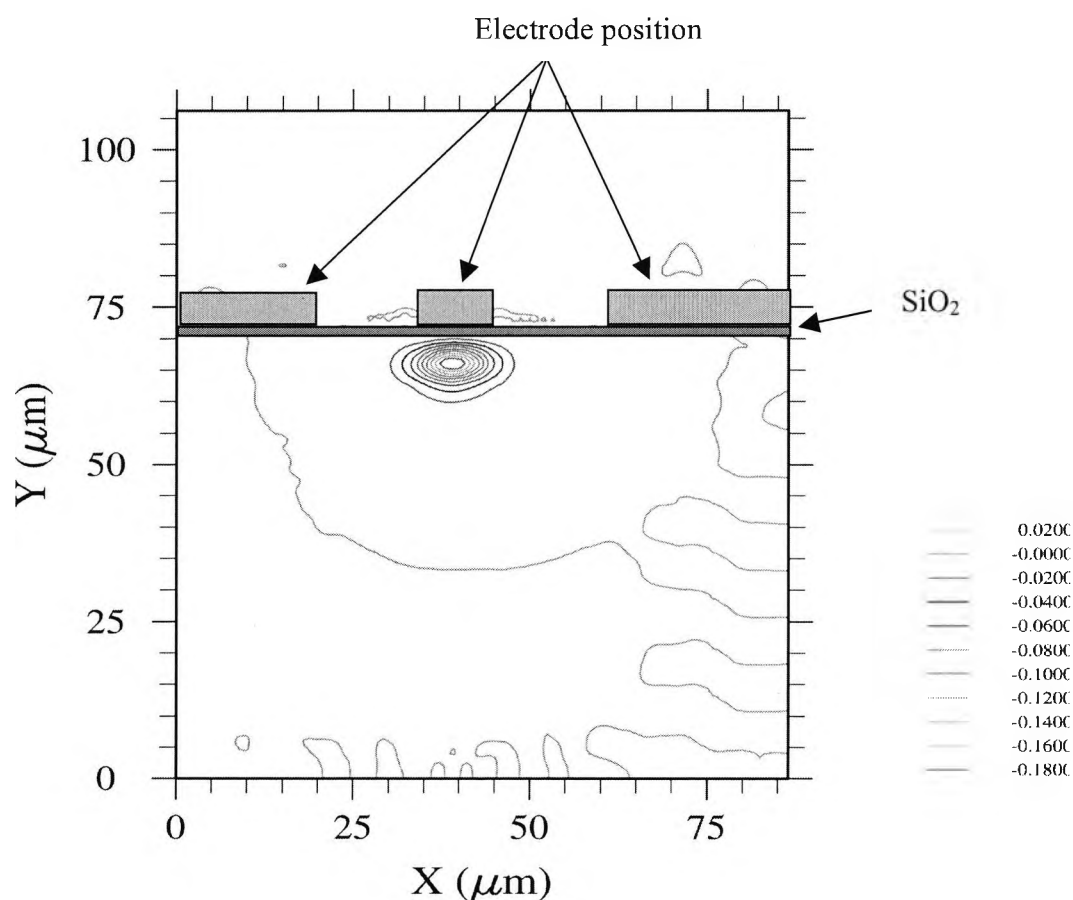


Fig. 6.17 The optical field H_x contours of the quasi-TM mode for unetched LiNbO₃ electrooptic modulator.

The optical field profile for TM-polarized light, where the H_{11}^x is the quasi-TM fundamental mode, is illustrated in Fig. 6.17 for electrode gap, $G=15 \mu\text{m}$, buffer layer

thickness, $B=1.2 \mu\text{m}$, center electrode width, $S=8 \mu\text{m}$, electrode thickness, $T=5 \mu\text{m}$, and waveguide width, $W=9 \mu\text{m}$. The propagation constant for left waveguide, for this LiNbO₃ unetched modulator structure with its parameters as defined here is $\beta = 8.6765654$, whereas for the right waveguide it is $\beta=8.6755614$. It can be seen that, due to the fact that the waveguide index profile, $n_{e,o}(x,y)$, is diffused, the optical mode is not so well confined in the lateral dimension, yet it supports only the fundamental mode for each polarization. For this mode, the dominant H_x optical field profile is in only one of the guides for the unetched structure with its parameters determined above. The position of electrodes and the buffer layer thickness role are also illustrated in this figure. It has been confirmed that, for $V=5$ volts, when the buffer layer thickness B is reduced to $0.75 \mu\text{m}$ the propagation constant for left waveguide is $\beta=8.6765913$ and for the right waveguide is $\beta=8.6755586$. It can be noted that when buffer layer thickness is increased the propagation constant is reduced on the left waveguide, whereas it is increased on the right waveguide, which will increase the $V_\pi L$ product.

For the unetched structure with buffer layer thickness, $B=1.1 \mu\text{m}$, electrode gap, $G=15 \mu\text{m}$, electrode thickness, $T=5 \mu\text{m}$, width of center electrode, $S=8 \mu\text{m}$, and width of the waveguide, $W=9 \mu\text{m}$. When the voltage is zero the values of the propagation constant for left and right waveguide modes are, $\beta_{L,V=0}=8.6764701$ and $\beta_{R,V=0}=8.6755610$, respectively. For the same parameters under the voltage applied the value of propagation constant for left and right waveguides are, $\beta_{L,V=5}=8.6765702$, $\beta_{R,V=5}=8.6755610$. The propagation constant changes due to electric field applied for left and right waveguides are, $\Delta\beta_L = \beta_{L,V=0} - \beta_{L,V=5} = 0.0001001$, and $\Delta\beta_R = \beta_{R,V=0} - \beta_{R,V=5} = 0.0000082$, respectively. From these two values and using equation (4.50) from the Chapter 4, the half-wave voltage length can be calculated, at which the phase difference between two arms of the unetched MZI (Mach-Zehnder-Inferometric) is π radian. The length of the electrodes is one of the most important characteristics for guided wave electrooptic modulators. The role of the buffer layer thickness is also essential in the modulator design. The half-wave product usually decreases as buffer layer is decreasing, but at the very small buffer layer thickness, the optical loss will be very high, therefore the optical losses of the electrooptic modulators depend critically on the buffer layer thickness.

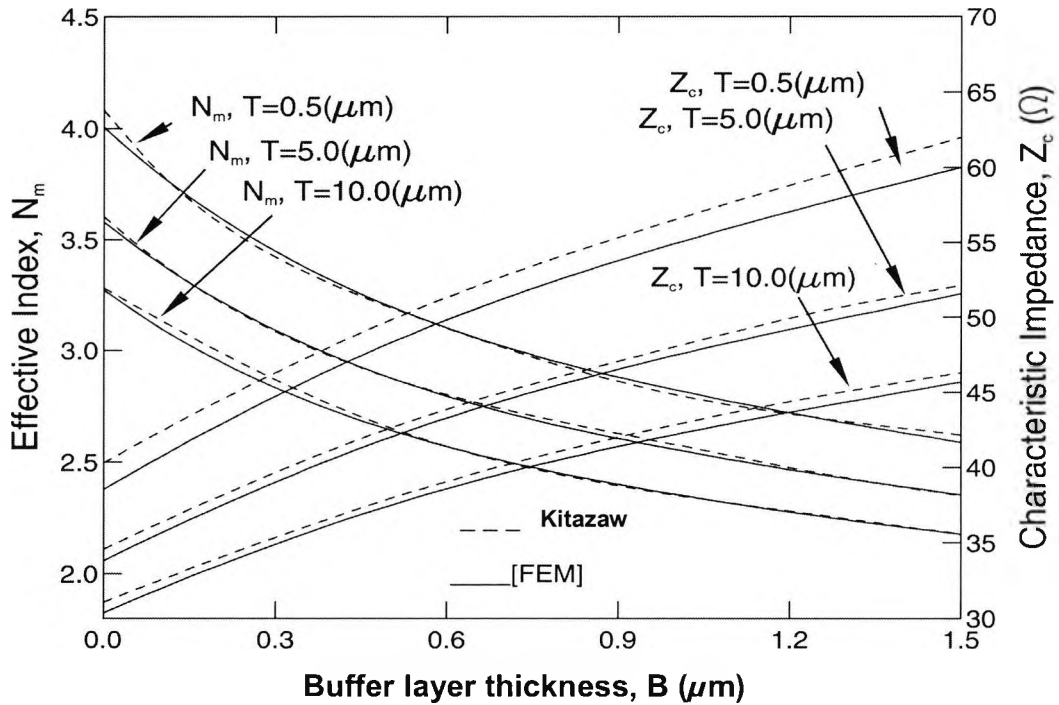


Fig. 6.18 Variation of microwave index, N_m and characteristic impedance, Z_C with the buffer layer thickness, B .

Calculation of microwave index and characteristic impedance are performed by employing the FEM based on the quasi-TEM analysis equation (5.20) and (5.23), given in chapter 5. Fig.6.18 shows the variations of the N_m and Z_C with the buffer layer thickness, B , for various gold electrode thicknesses, T . In this case the hot central-electrode (strip) width, S , and gap width, G , were taken as 8 μm and 15 μm, respectively. The results agree well with those reported by Kitawaza *et al.* 1992, which are shown by dashed lines. It can be noted that N_m decreases as B or T is increased. It can also be noted that Z_C increases as B is increased but Z_C reduces when T is increased. The wave velocity of the optical carrier wave or its equivalent parameter, the effective index, N_o , of a modulator structure depends on various fabrication parameters, such as the titanium thickness, diffusion time and temperature. For unetched structure, this parameter can be accurately calculated by using an optical modal solution approach, such as the FEM; however, for this study it is assumed that a typical value would be 2.15

for the purpose of its subsequent phase matching. It can be noted that for lower electrode thickness, such as $T = 0.5 \mu\text{m}$, the buffer layer has to be very thick to achieve the velocity matching. However, it is well known that as B is increased, the overlap between the microwave and optical modes would reduce and as a consequence the $V_{\pi}L$ value would also increase. To avoid this drawback, as can be noted from Fig. 6.18, the electrode thickness could be increased, but that would also reduce Z_C . It may not be easy to match both N_m and Z_C simultaneously, however, for this case, when $S = 8 \mu\text{m}$ and $G = 15 \mu\text{m}$, both of them could be satisfied *only* when $T = 8 \mu\text{m}$ and B is $1.7 \mu\text{m}$.

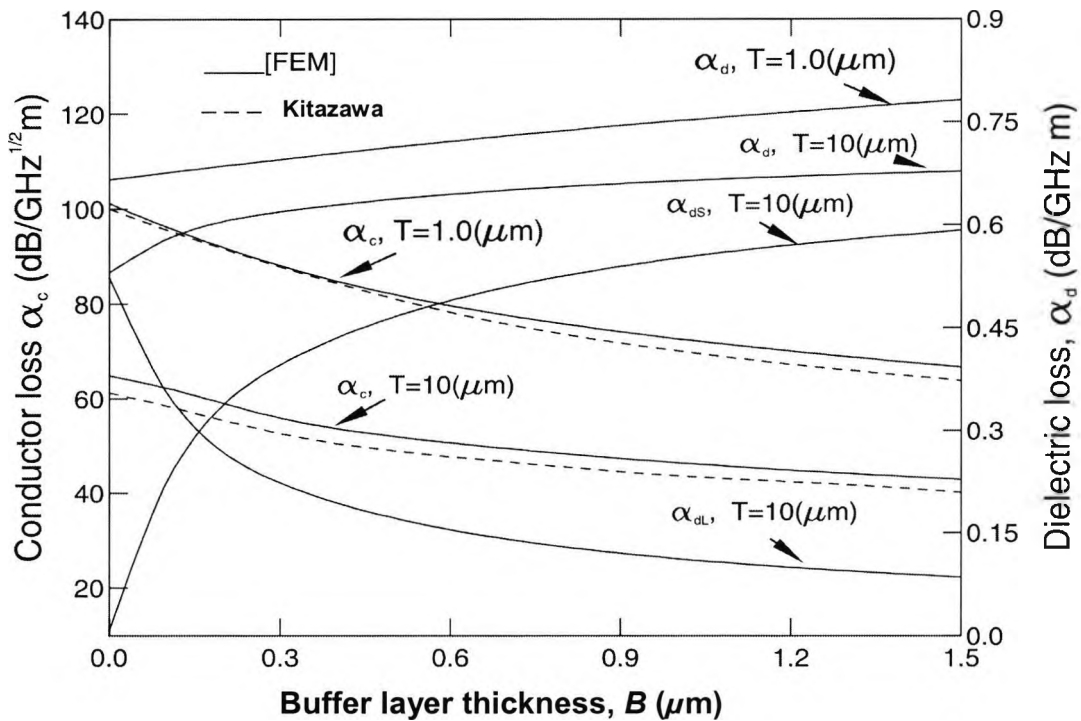


Fig. 6.19 Variation of conductor and dielectric losses, α_C and α_d , normalized at 1 GHz, with buffer layer thickness, B for unetched LN structure.

Conductor loss or attenuation constant in this research work is investigated by using the “incremental inductance rule” eq. (5.29). The amount of recession is taken equal to the skin depth $\delta = (2/\omega\mu\sigma_c)^{1/2}$ of the conductor (gold) electrodes. The dielectric losses on

the dielectric regions are calculated by using the perturbation theory equation (5.36) in the Chapter 5. The conductor loss also strongly depends on the electrode thickness, T . Variation of the conductor loss, α_C , and dielectric losses, α_d , normalized at 1 GHz are shown in Fig. 6.19. It can be seen as B is increased, α_C reduces monotonically and this value reduces considerably when a thicker electrode is used. The frequency dependent surface resistance for gold, R_S , is calculated from its conductivity, $\sigma = 4.1 \times 10^7$ s/m. The simulated results presented here agree well with the published work (Kitazawa, 1992), which are also shown here as dashed lines. The dielectric loss in silica (buffer) layer, α_{ds} , in the lithium niobate crystal, α_{dL} , and the total dielectric loss, α_d , for $T = 10 \mu\text{m}$ are shown in Fig. 6.19. In this work, the loss tangent values for LN and silica are taken as 0.004 and 0.016 (Noguchi, 1998). It can be observed that α_{dL} reduces and α_{ds} increases, as the B is increased. It can be also noted that for typical buffer layer thickness losses in the silica layer are much higher than that of the LN crystal, similar as reported by Noguchi, 1998. It can also be observed that, when electrode thickness is reduced to $1.0 \mu\text{m}$, total dielectric loss is increased, due mostly to additional loss in the buffer layer. At 1 GHz, for this structure the conductor loss is two orders of magnitude larger than the dielectric loss. However, as the dielectric loss is proportional to the operating frequency, f , compared to the conductor loss, which is proportional to the \sqrt{f} , so at 100 GHz they would be comparable. A high-speed optical modulator with a thicker buffer layer dielectric loss would increase further, and in this case at 100 GHz with $B=1.5 \mu\text{m}$, the conductor and dielectric losses would be 4.5 dB/cm and 0.7 dB/cm, respectively.

Besides the buffer thickness, B and electrode thickness, T , the electrode gap, G the width of the center (hot) electrode, S , also play an important role in the design and performance of optical modulators. Variations of effective index, N_m and the characteristic impedance, Z_C with the central electrode's width, S , for various gaps between the electrodes, G , are shown in Fig.6.20.

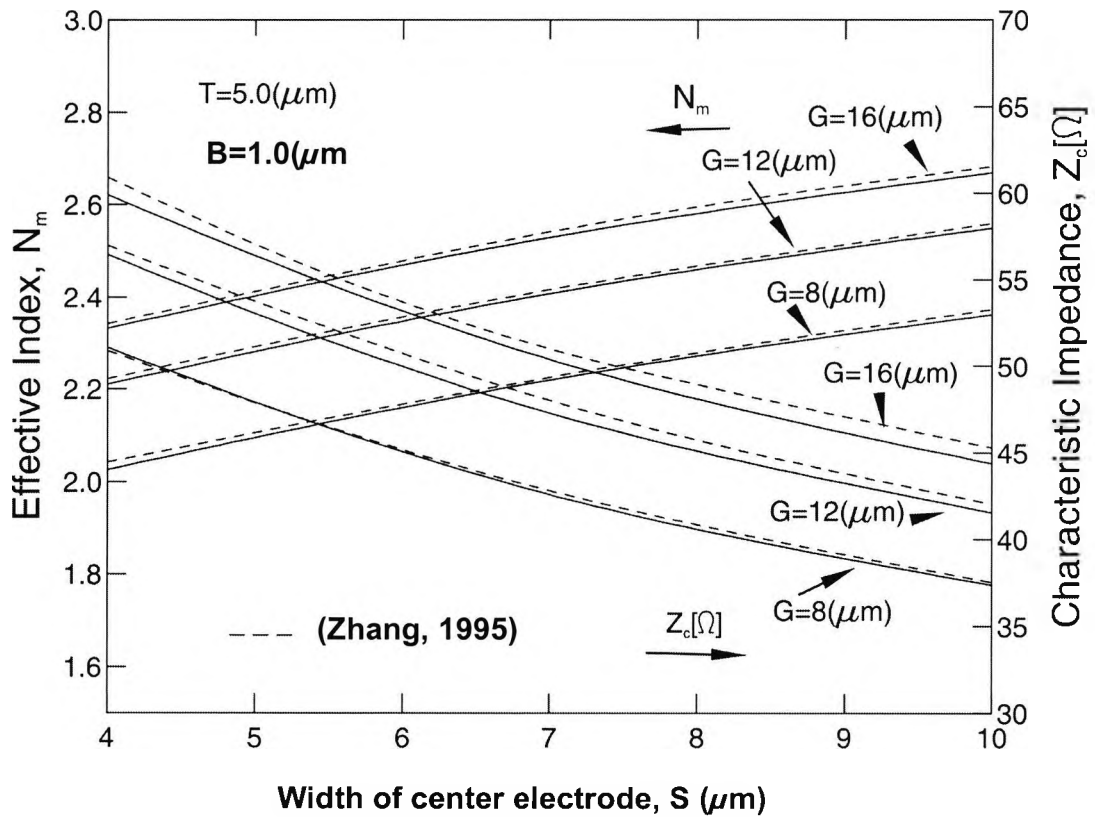


Fig. 6.20 Variation of microwave effective index, N_m and characteristic impedance, Z_c with central electrode width, S .

It can be observed that microwave effective index, N_m increases as the centre electrode width S is increasing; however, when the width of the centre electrode is increasing the characteristic impedance, Z_c is decreasing. On the other hand effective index N_m and characteristic impedance Z_c increase when the gap between electrodes G is increased. The results obtained in this study agree reasonably well with previous work published by Zhang and Miyoshi, 1995, which are also illustrated here in this graph with dashed lines. It can be noted that in this case the dominant loss component of conductor loss, α_c does

not depend strongly on width of the centre electrode S but its value reduces considerably with the increase of the gap between electrodes, G .

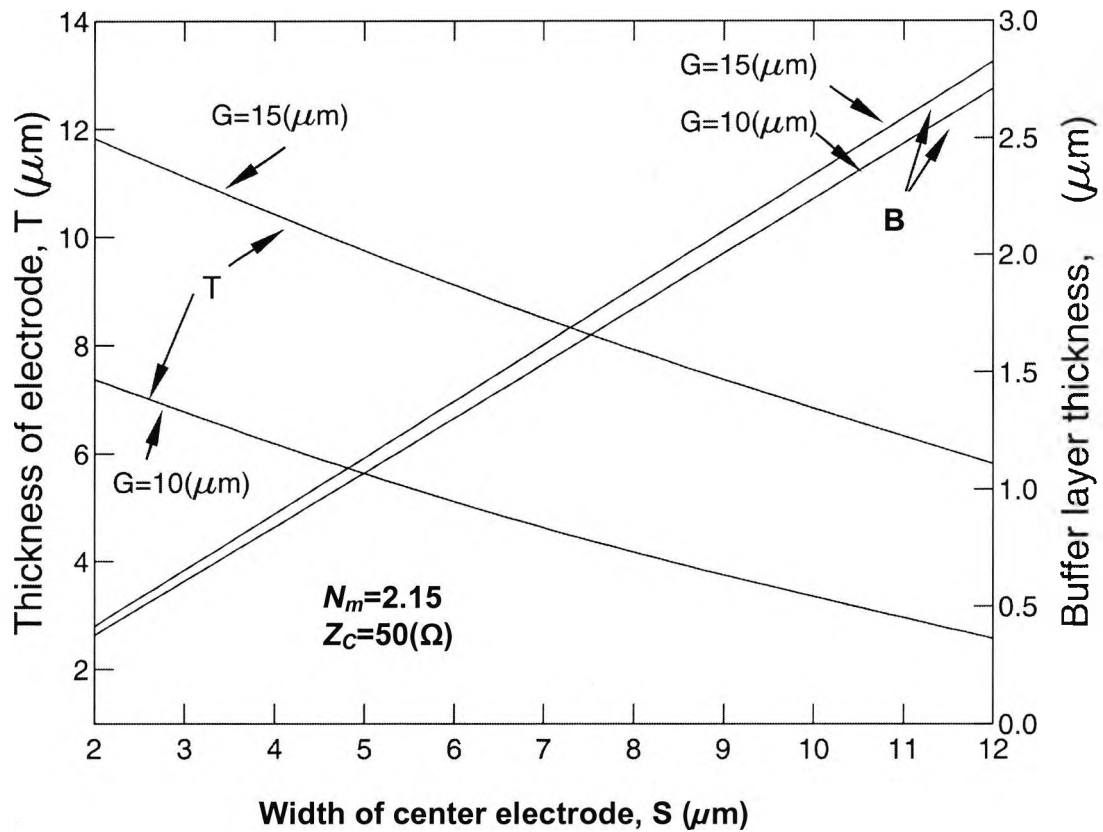


Fig. 6.21 Required electrode thickness, T , and buffer layer thickness, B , values for simultaneous matching of N_m and Z_C with the electrode width, S .

Next, the simultaneous matching of both the microwave effective index, N_m , and the characteristic impedance, Z_C , is performed. For two values of gap between electrodes, G , equal to $15 \mu\text{m}$ and $10 \mu\text{m}$, variations of the electrode thickness, T , and buffer layer thickness, B , are evaluated in order to achieve simultaneous matching for both, N_m and Z_C . The necessary centre electrode width, S , under simultaneous matching condition is illustrated in Fig. 6.21. It can be observed that as centre electrode width, S , is increased, the necessary electrode thickness is reduced, but the required buffer layer thickness is

increased and consequently the $V_{\pi}L$ value would also increase. The required buffer layer thickness, B , does not depend strongly on the electrode gap, G , however as the gap, G , is increased the necessary metal electrode thickness, T , would increase. However, an increase in electrode gap, G , is expected to increase the product of the half-wave voltage length, $V_{\pi}L$.

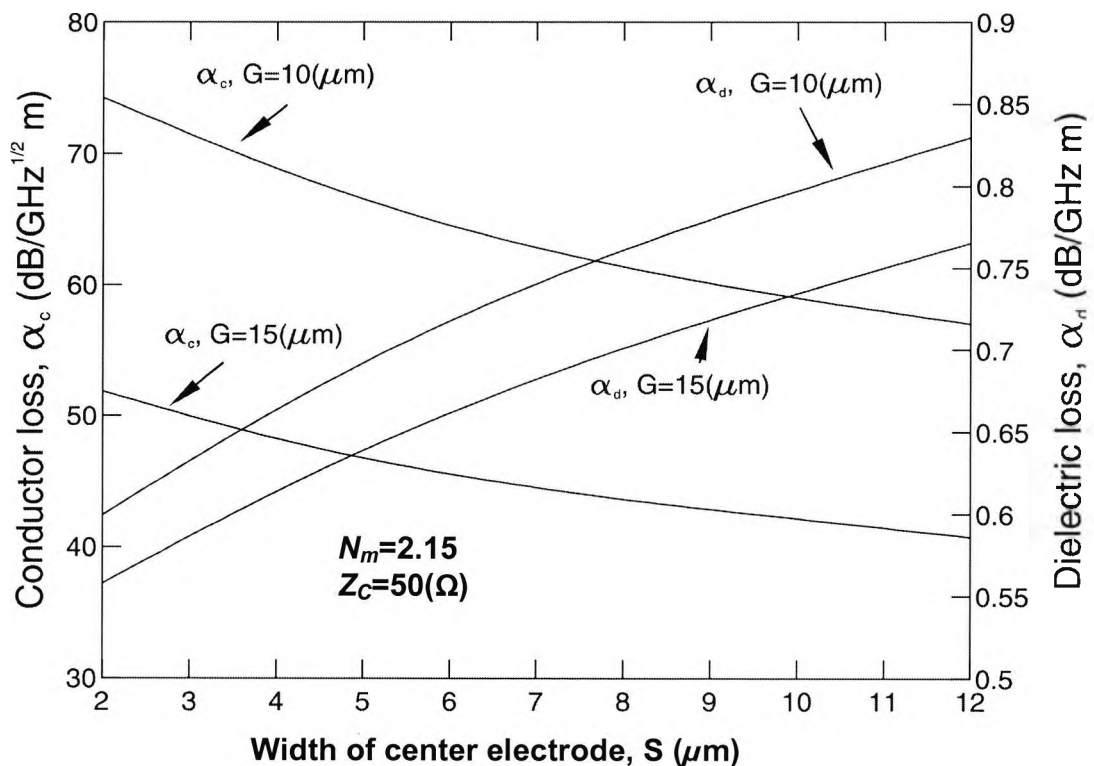


Fig. 6.22 Variation of the α_c and α_d with S when both N_m and Z_C are simultaneously matched.

It is also essential to identify the dielectric and conductor losses under simultaneous matching condition for microwave effective index, N_m , and characteristic impedance, Z_C . Variations of total dielectric loss α_d and electrode loss α_c with width of centre electrode S and electrode gap G are performed in Fig. 6.22. It can be noted that by increasing both width of hot electrode S and gap between the electrodes G conductor loss can be

significantly reduced. However, it should be noted that an increase in S would also increase the buffer layer thickness required (as shown in Fig.6.21), which would require a higher half-voltage length product, $V_{\pi}L$ value. Obviously, the overall bandwidth of the modulator depends critically on the simultaneous matching of both microwave index, N_m , and characteristic impedance, Z_C . However, the conductor loss and dielectric loss at high frequency plays a significant role on the device bandwidth. Therefore, their behaviour under the simultaneous matching condition of both N_m and Z_C are illustrated in this research work presented in the Fig. 6.22.

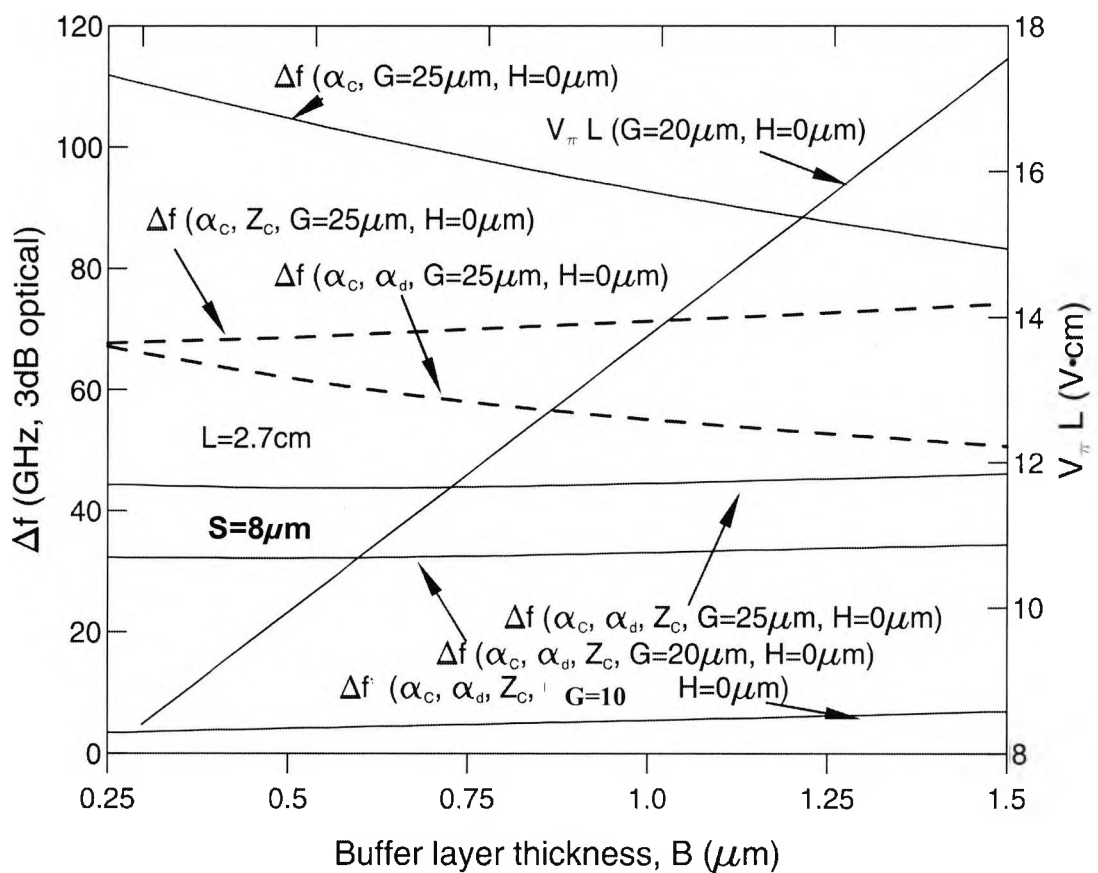


Fig. 6.23 Variation of the modulator bandwidth, Δf and half-wave length product $V_{\pi}L$ with buffer layer thickness, B .

From variation of the bandwidth Δf with buffer layer thickness, B for three different values of the electrode gap G equal to 10 μm , 20 μm and 25 μm , it can be observed that

when only conductor loss is considered, for electrode gap, $G=25 \mu\text{m}$ the bandwidth is significantly high and it reduces when the buffer layer thickness is decreased. Its magnitude has reached the maximum point at buffer layer thickness, $B=0.25 \mu\text{m}$, but at this buffer layer thickness, the optical loss will be very high; therefore an optimum buffer layer thickness would be around $1.0 \mu\text{m}$. Variation of the bandwidth with buffer layer thickness, when the conductor loss and impedance mismatch are considered, is illustrated with dashed line in the Fig. 6.23. It can be seen that the impedance mismatch has negative impact on the device bandwidth, therefore its effect cannot be ignored. When conductor loss and dielectric loss are taken into consideration, the bandwidth versus buffer layer is performed with dashed lines and it can be noted that when the buffer layer thickness is increased the bandwidth decreases. Significant bandwidth reduction happens when conductor loss, dielectric loss and impedance mismatch are taken into consideration; it can be seen that its reduction is almost (30-40) %. Electrode gap design is essential for the modulator, for the same parameters when the gap between electrode is increased from $20 \mu\text{m}$ to $25 \mu\text{m}$ the bandwidth has been increased for 30 %. Variation of the bandwidth when conductor loss, dielectric loss and impedance mismatch are included is illustrated in this graph for three different values of electrode gap, $10 \mu\text{m}$, $20 \mu\text{m}$ and $25 \mu\text{m}$. Based on this study it is necessary to design a modulator where velocity and impedance matching are achieved simultaneously.

Variation of the half-wave product $V_{\pi}L$ for electrode gap, $G=20 \mu\text{m}$, with buffer layer thickness, B , is illustrated on the right-hand side of this graph. It can be seen that when the buffer layer thickness B is increased the $V_{\pi}L$ product is increasing. The lowest value of the $V_{\pi}L$ product is achieved at buffer layer value of $0.27 \mu\text{m}$, but as mentioned above at this point the optical loss would be very high. The length of the modulator for this investigation is taken at 2.7 cm .

When the phase matching and impedance matching are achieved, by varying electrode thickness T and electrode width S , the overall bandwidth depends on the total microwave losses (Minakata, 2001). Variations of the 3dB optical bandwidth for unetched LN modulator with the buffer layer thickness, B , are shown in Fig. 6.24. Variation of the 3 dB optical bandwidth with buffer layer thickness when only the conductor loss is considered under velocity and impedance matching conditions is illustrated by dashed

lines. It can be seen that when the buffer layer thickness is increasing the bandwidth is also increasing under this condition. However if this dielectric loss is included, the resulting bandwidth can be calculated from the conductor loss and dielectric loss, by using a simple iteration approach to estimate the effective loss coefficients, which are shown by solid lines. It is obvious that when the dielectric loss is included the bandwidth is reduced and its reduction is more visible when the buffer layer thickness is increased.

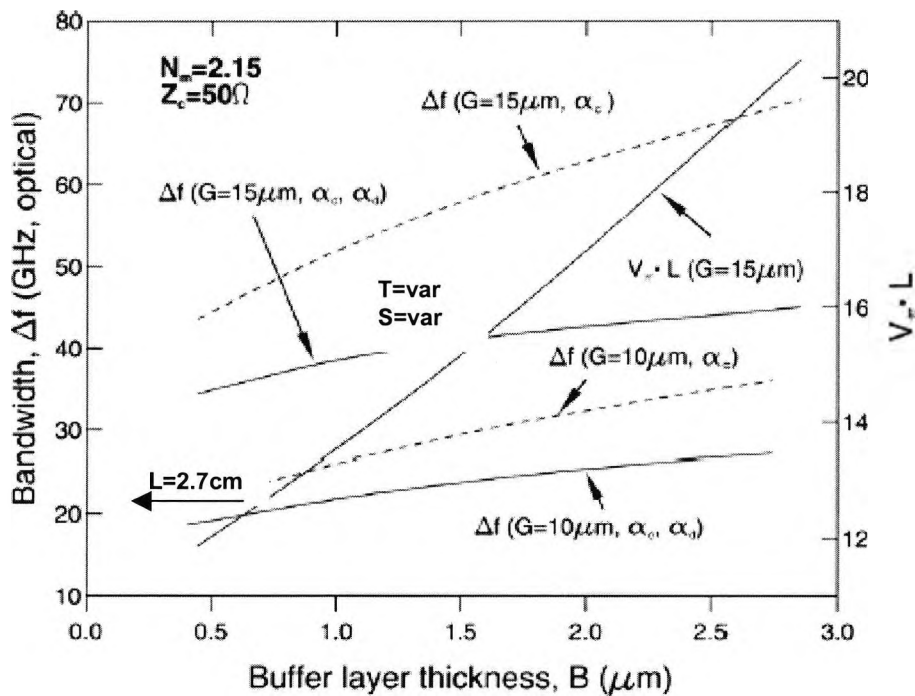


Fig. 6.24 Variation of the modulator bandwidth with the buffer layer thickness, B , and Variation of the product $V_{\pi}L$ with buffer layer thickness, B , under velocity and impedance matching conditions.

Variation of the product $V_{\pi}L$ with the buffer layer, B , for electrode gap, $G=15\mu\text{m}$ under the velocity and impedance matching condition is performed in this figure also. With respect to the $V_{\pi}L$ product under velocity and impedance matching condition, as a result the driving power of the modulator is reasonably increased. Therefore the study that has taken place in this research work was mainly concerned in simultaneous matching of

both velocity and impedance in order to achieve a high-speed electro optic modulator which is essential for optical communications systems.

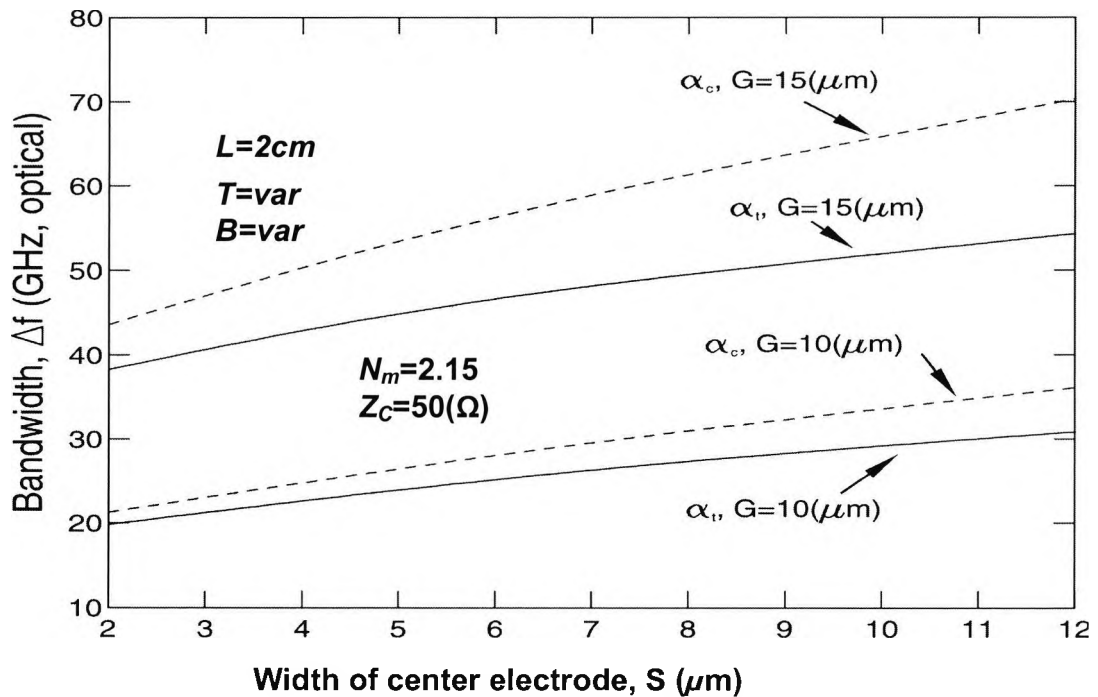


Fig. 6.25 Variation of the modulator bandwidth with the electrode width, S under velocity and impedance matching conditions.

When phase and impedance matching are achieved by varying the electrode thickness, T , and buffer layer thickness, B , the overall bandwidth depends on the total microwave losses. Variations of the 3dB optical bandwidth for a 2 cm long unetched LN modulator with the strip width, S , are illustrated in Fig. 6.25. Variation of the 3dB optical bandwidth with hot electrode width when only conductor loss is included is illustrated by dashed lines. However if the dielectric loss is included in this calculation, the resulting bandwidth can be calculated from the total loss, α_t , by using a simple iteration approach to estimate the effective loss coefficients, which are shown by solid lines. It can be noted when dielectric loss is ignored the overall bandwidth can be overestimated by nearly 50%. From this study it can be seen that when the width of centre electrode is increased the bandwidth is also increasing, and when the gap between electrodes is

increased the 3dB optical bandwidth is increased. Based on this study a higher gap between electrodes and higher width of the hot electrodes have positive impact on the device performance.

Summary

In this chapter thesis details of unetched LiNbO₃ fabrication procedures have been explained starting from Ti-diffusion technique for obtaining low-loss waveguide and high-quality buffer layer SiO₂ thin film fabrication and electrode fabrication techniques have been performed in sequence steps in this study.

A numerical approach based on the efficient finite element method is developed to study some of the key unetched LN modulator parameters. In this section we have investigated the unetched LN electrooptical modulators, which have the feature that use the buffer layer of SiO₂ in order to reduce velocity mismatch between microwave and optical waves as well as employing coplanar waveguide travelling-wave electrodes to improve impedance and propagation mode mismatch between the electrode and the external circuit. Potential distribution, electromagnetic fields, microwave effective index, characteristic impedance, conductor loss, dielectric loss, bandwidth calculation and the product of half-wave voltage length have been investigated in order to improve the modulator performances. Details of different modulator parameters have been also widely investigated.

The effects of various key device parameters such as buffer layer thickness, centre electrode width, electrode thickness and gap between electrodes, for simultaneous velocity and impedance matching are considered in this chapter. The effect of conductor, loss impedance mismatch and dielectric loss in the bandwidth determination for unetched LN electrooptic modulator have also been presented. The research shows that dielectric loss in buffer layer is much higher than that in the lithium niobate substrate and, for optical modulators operating beyond 40 GHz, the total dielectric loss will play a significant role in the determination of the overall speed of the modulator. Software implementation of FEM, LSBR and quasi-TEM analysis are illustrated in the Appendix 3.

Ultra-Broad-Band LiNbO₃ optical Modulator with Ridge Structure

7.1 Introduction

The most important factors for an effective electrooptic modulator are the optimization of the modulator bandwidth and the driving voltage. The bandwidth of a high-speed optical modulator with a traveling-wave electrode is primarily limited by the velocity mismatch between the optical carrier wave and the modulating microwave signal. The lack of a velocity-mismatch between the optical and the microwave signals is the dominant problem which prevents the design and fabrication of optimized high-speed electrooptic modulators. Various attempts with different electrode designs and different structures have been reported to achieve velocity-matching and low drive voltage electrooptic modulators. Noguchi *et al.* 1993, employed ridge a structure with a shielding plane with a relatively low microwave propagation loss and a large interaction between the optical and the microwave signals. Recently Yoshida, 1999, introduced an unetched LN electrooptic modulator with a shielded plane using a superconductive electrode in order to achieve velocity matching. A ridge structure with coplanar waveguide electrode (CPW) proposed by Mitomi, 1995, can provide a broader bandwidth, lower driving voltage and is relatively easy to fabricate. It has been reported relatively recently (Mitomi, 1995, Noguchi, 1998, Dagli, 1999, Wooten, 2000, Minakat, 2001) that in the case of this ridge type modulator with an etched LN substrate, the overlap between the optical and modulating fields can be significantly increased and, as

a consequence, for a given operating voltage the interaction length can be shortened which will also increase the modulator bandwidth. The cross-sections of an etched modulator shown in Fig. 7.1.

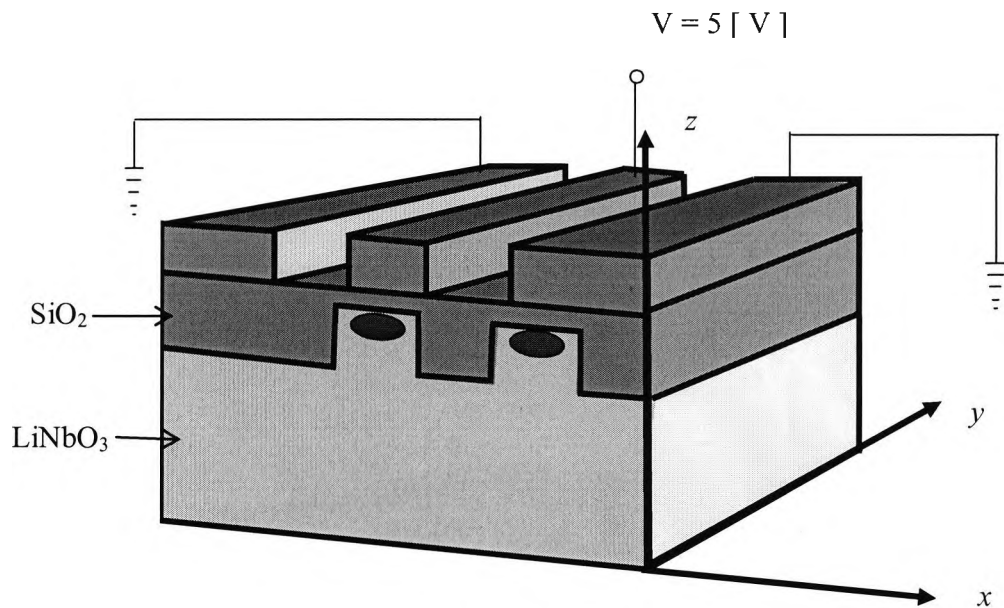


Fig. 7.1 a)

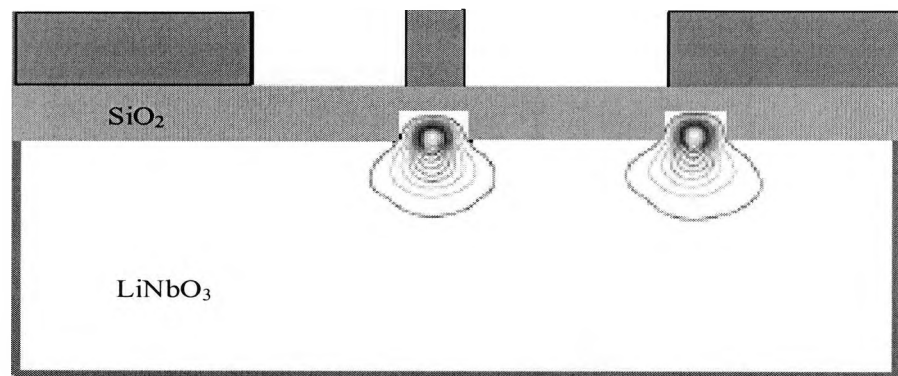


Fig. 7.1. b)

Fig. 7.1 3-D and 2-D cross sections of ridged structure LiNbO₃ electrooptic modulator

7.2 Etching substrate fabrication

Optical waveguides can be fabricated in the z-plane of a LiNbO₃ substrate by diffusing Ti patterns at 1000°C for 10 hours in a wet O₂ atmosphere. The LiNbO₃ substrate is etched using an RF –biased electron cyclotron resonance (ECR) system with Ar and C₂F₆ gases to form the ridge, with a typical etching rates of 15 nm/min. The substrate is etched to form ridges with dimension of 9 μm wide and 3.6 μm high (Noguchi, 1994). During the etching of LiNbO₃ substrate some of the ridge ends up with some range of tilt (a rough surface) which has some small effect on the microwave properties. After the mask is removed in hydrofluoric acid, a dual buffer layer of SiO₂ is deposited on the etched substrate in order to improve the thermal stability of the modulator. The thicknesses of the lower and the upper layer can be of the order of 1.0 and 0.2 μm. After that a thick gold plate CPW electrode could be formed following the steps given in Chapter 6. The ridge width is chosen to be slightly more than the optical waveguide width in order to make the degradation of the optical propagation loss negligible in comparison with that of the conventional planar (unetched) waveguide. The substrate then is cut into chips and its end faces are then polished. After that the modulator can be pigtailed with polarized maintaining (PANDA) fibres using an ultraviolet cured adhesive.

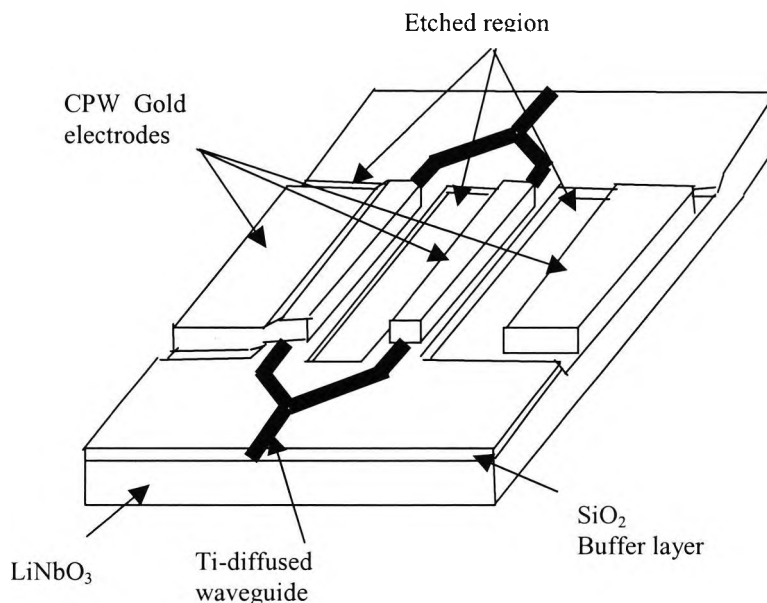


Fig. 7.2 Picture of a LiNbO₃ electrooptic modulator.

With respect to the fabrication procedure involved in the Ti: diffusion, buffer layer, forming of gold electrodes, polishing and testing steps more details can be found in Chapter 6 of this thesis.

7.3 Simulated results for ridge electrooptic modulator and its advantage over conventional planar structure.

This study has concentrated on the ridged electrooptic modulator and in particular a comparison between the etched and unetched structure is carried out using the finite-element method (FEM), which is one of the most versatile and powerful methods for modelling optical devices of any complexity.

The high-speed electrooptic modulator represented in this study is based on the Mach-Zehnder approach and is fabricated on Z-cut LN substrates, operating with a vertical electric field to utilize the largest electrooptic coefficient, r_{33} , of the LN. The relative dielectric constants of the Z-cut LN substrate were 28 and 43 in the perpendicular and parallel directions to the substrate surface respectively.

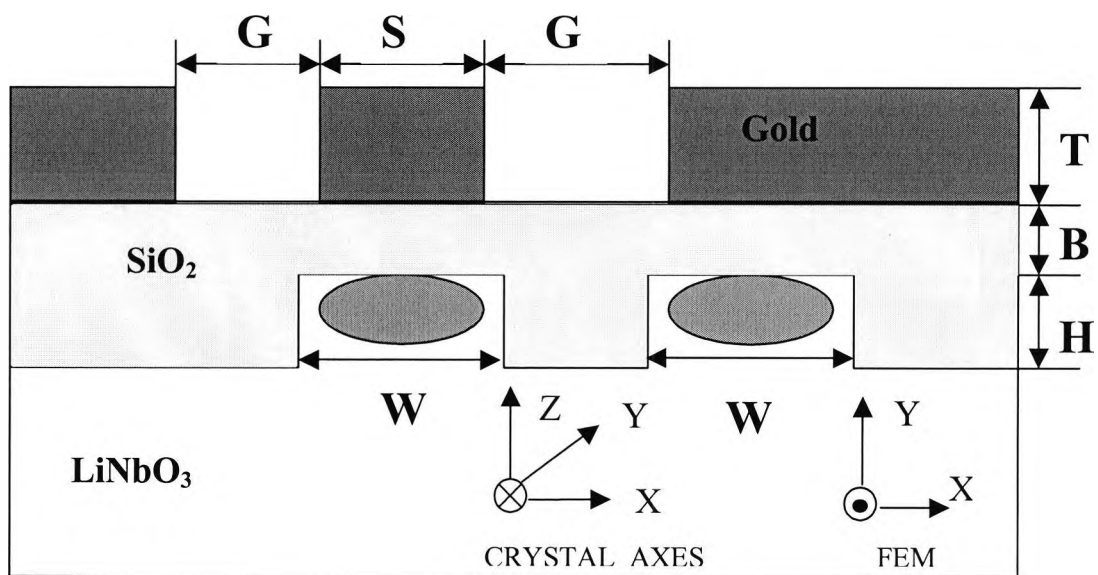


Fig. 7.3 Ridged LiNbO₃ electrooptic modulator

To reduce the optical loss due to the lossy metal electrode, a SiO₂ buffer layer is often used, which also assists in the phase matching. The relative dielectric constant of the SiO₂ buffer layer is taken as 3.9. In the calculation, the etched regions are buried by silicon oxide. The coplanar waveguide (CPW) electrode is commonly used as a travelling-wave electrode for a Ti: LN optical modulator because it provides a good connection to an external coaxial line. It has been reported relatively recently (Mitomi, 1995) that for a ridge type modulator with an etched LN substrate, the overlap between the optical and modulating field can be significantly increased and as a consequence, for a given operating voltage, the interaction length can be shortened which will also increase the modulator bandwidth. In this paper the important optical and microwave properties of an etched Z-cut LN modulator are presented. The cross section of ridged LN electrooptic modulator with its crystal orientation and its parameters such as waveguide width, W , electrode gap, G , electrode width, S , ridge height, H , and buffer layer thickness, B , is illustrated in Fig. 7.3.

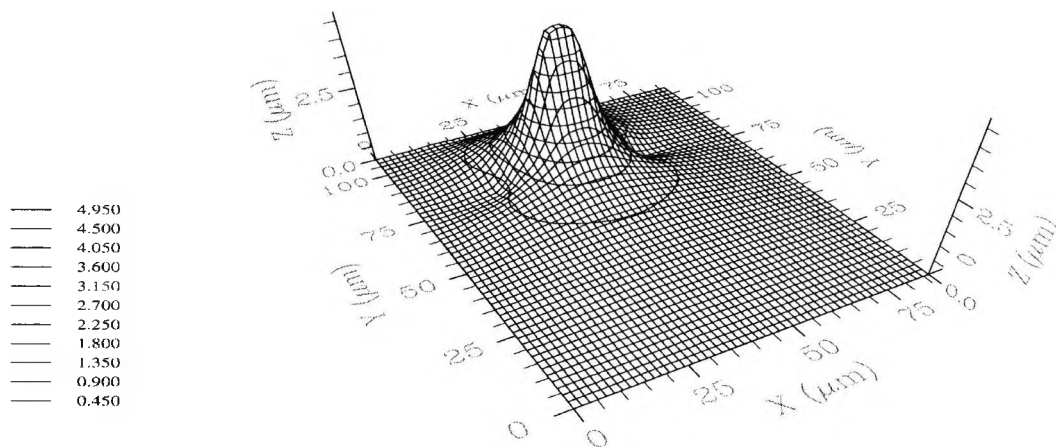


Fig. 7.4 3-D potential distribution for ridge LN electrooptic modulator at $V=5$ voltage.

The ridge type coplanar waveguide (CPW) structure arrangement for the central electrode with two ground electrodes on the sides was chosen so that the maximum interaction takes place in the waveguide under the central electrode. The scalar potential, $\phi(x,y)$ is calculated from equation (5.9) using the FEM at ridge height, $H=3 \mu\text{m}$, electrode gap, $G=15 \mu\text{m}$, strip width, $S=8 \mu\text{m}$, buffer layer, $B=1.2 \mu\text{m}$, electrode thickness, $T=5 \mu\text{m}$, and waveguide width, $W=9 \mu\text{m}$. The potential value is heavily concentrated in and around the hot electrode, with the peak value almost 5 V which is equal to the voltage applied to the hot electrode, shown in the Fig. 7.4. in a 2 dimensional plane.

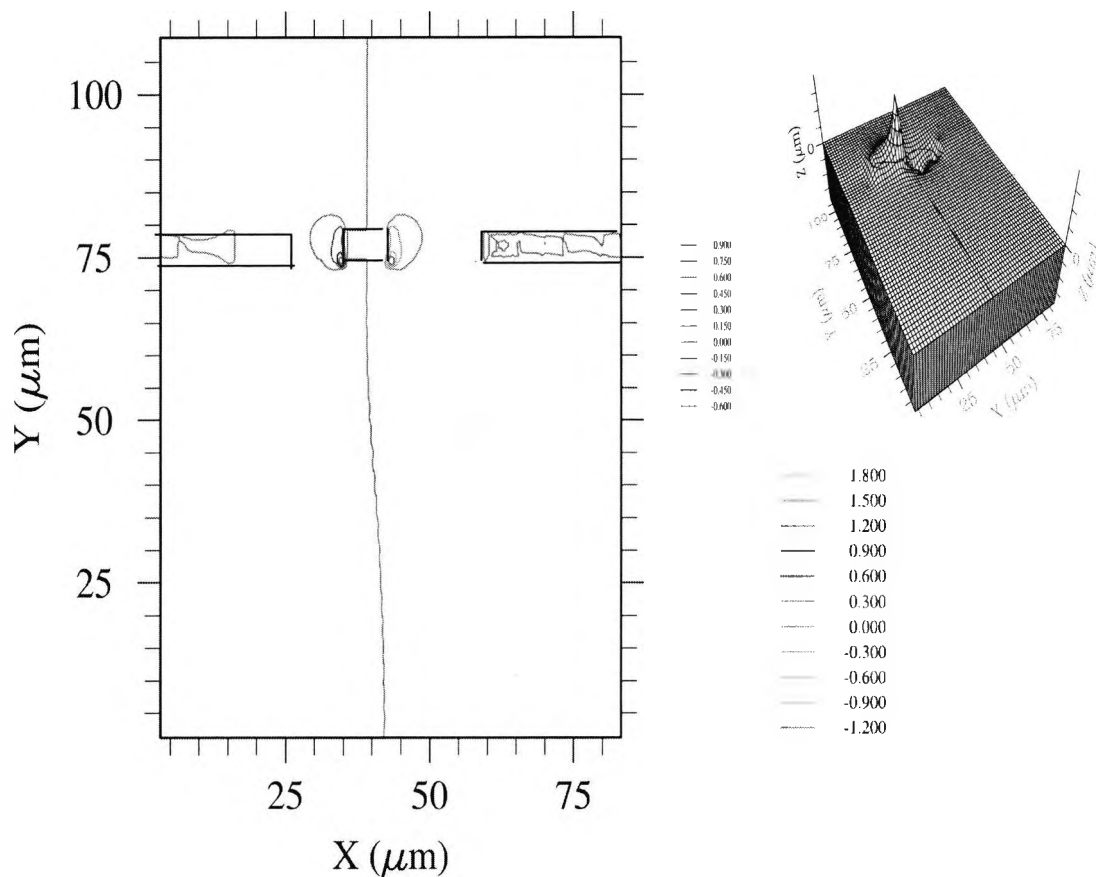


Fig. 7.5 2-D and 3-D (small scale) illustration of the electric field concentration in x direction (E_x).

The x -component of the vector modulating electric field $E_x(x, y)$, may be calculated from the scalar potential, $\nabla\phi(x, y)$, using the FEM eq. (5.13). The electric field concentration in x direction is presented in the 2 and 3 dimensional plane in Fig. 7.5. It can be seen that due to its a symmetry, the field concentration is maximum and reaches the large peak value at the edges of the hot electrode and is exponentially decaying, with its minimum point (zero) in the middle of the hot electrode. Its magnitude taken from the figure 2-D, is 1.800 (V/ μm) and exponentially decays through the zero value, reaching the minimum value at -1.200 (V/ μm), as illustrated on the legend of this figure, compared to the unetched structure given in Chapter 6, (Fig. 6.11) where these peak values show a maximum of 1.750 (V/ μm) and a minimum of -1.750 (V/ μm). From this presentation it is very clear that the symmetry of the electric field is very accurately represented and the electric field in the x direction is slightly higher than the electric field for unetched structure. In a similar way to the unetched structure, the field acting in the waveguide is small and, being positive and negative in two sides of the waveguide its overall effect on the waveguide can be ignored. Its 2-D and 3-D profiles are also illustrated in the same figure where its symmetry depends on the electrodes design.

The y -component of the vector modulating electric field, $E_y(x, y)$, calculated from the scalar potential, $\phi(x, y)$, using the FEM equation (5.13), as well as the electrode position is illustrated for 2-D and 3-D plots in Fig. 7.6. The field is more concentrated around the centre electrode, and therefore in the waveguide directly placed under this electrode, for this etched structure compared with the unetched structure given in Chapter 6, (Fig. 6.13). It is evident the electric field of a lower concentration under the two ground electrodes is also present. It is obvious that, due to the symmetrical placement of the gold electrodes, the modulating field acting in the second waveguide, which is placed under the one ground electrode seen in Fig. 7.6 on the right, is small compared with that of the first waveguide, which is placed directly under the hot electrode. Hence most of the modulating electric field is acting in the first guide with virtually no field present in the second waveguide, and this has a much less “push-pull” effect than in the case of the unetched waveguide electrooptic modulator. Due to the presence of the SiO₂ buffer layer thickness and its low refractive index on the sides of the waveguide, which is essential for the modulating field, it can be seen that a reasonable proportion of the modulating

field is acting in the buffer layer. Therefore, the overlap between the optical and modulating electric field is much higher than compared to the unetched structure.

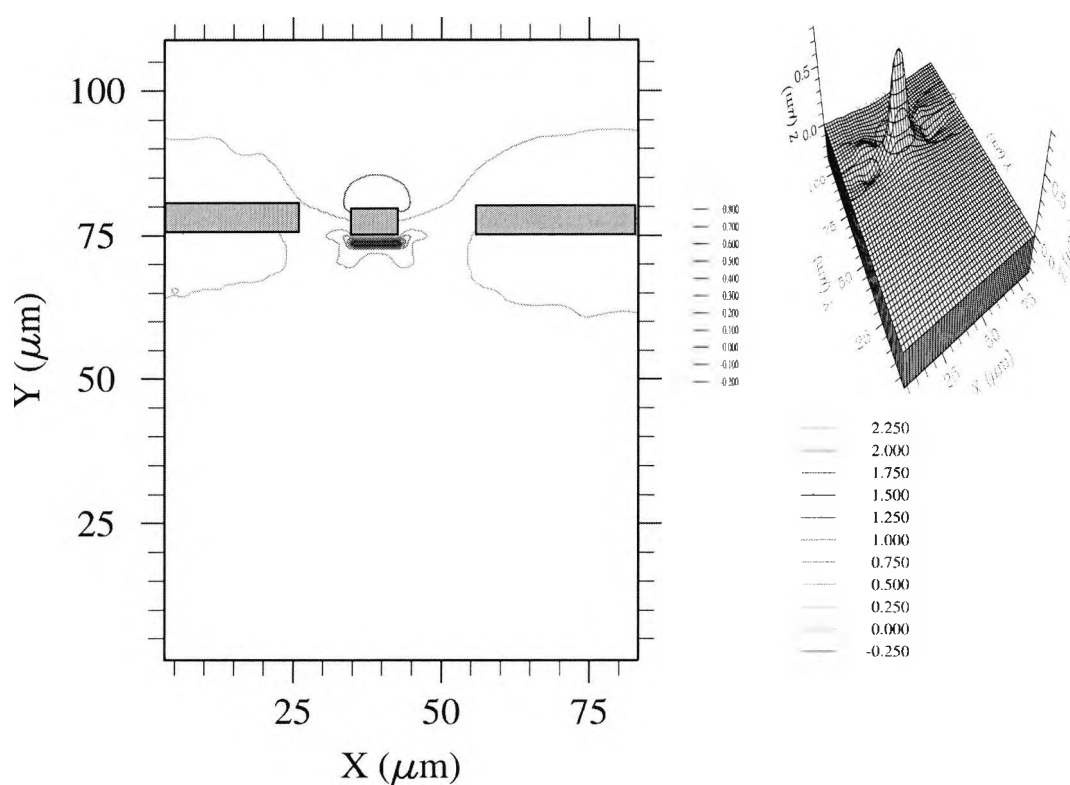
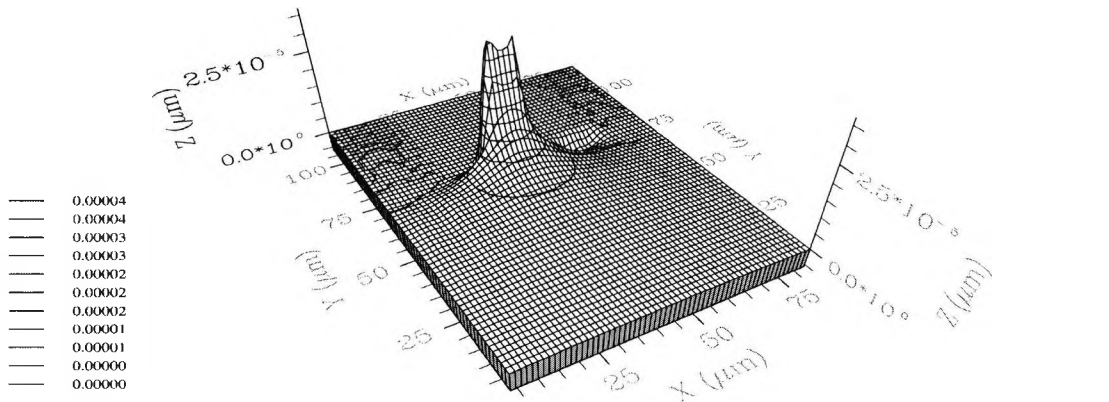
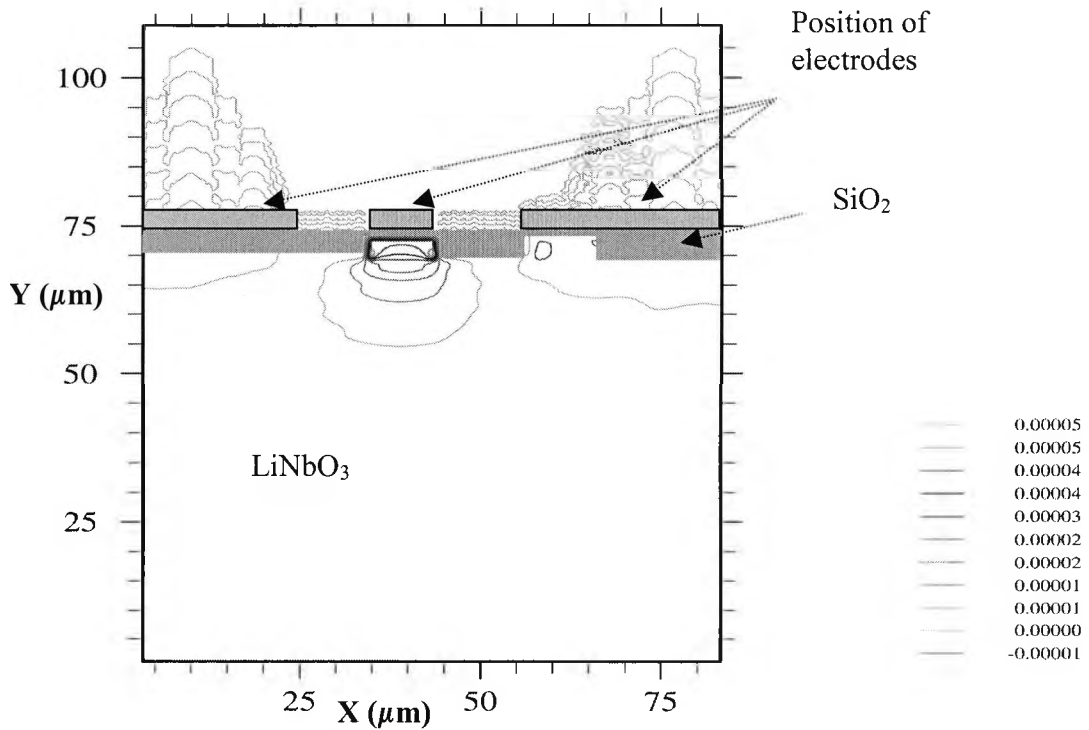


Fig. 7.6 2-D and 3-D (small scale) plot of the $E_y(x, y)$ electric field for ridge electrooptic modulator.

The y component of electric field $E_y(x, y)$ is selected in order to calculate the refractive change under the applied voltage. Therefore based on this approach a further investigation of the ridge modulator structure has been carried in this study.



a). 3-D plot



b) 2-D plot

Fig. 7.7 The change of refractive index due to an applied electric field for ridge structure, $H=3 \mu\text{m}$, 3-D plot a) and 2-D plot b).

When the voltage is applied the diffused extraordinary refractive index change profile is calculated from the equation (4.25). It is obvious that the refractive change profile is mainly concentrated in the first waveguide region under the hot electrode, as a result of the y -component of the modulating electric field, E_y , whereas its concentration is much smaller on the second waveguide, because the field value in this region is weaker as a result of the electrode position. The refractive index change profile for the right waveguide and the electrode position is illustrated in the Fig. 7.7. It can be seen that refractive index is heavily concentrated under the hot electrode and largely depends upon the electrode position and ridge depth. It is obvious that, due to electrode symmetry, the refractive index profile is also symmetrically concentrated along x axis and is mainly in the desired waveguide region. The refractive index change in the first waveguide is much higher and better confined in the ridge area than for the unetched structure shown in the Fig. 6.15 of Chapter 6. As a result of electric field applied in both waveguides, left and right, the refractive index change profile calculated from equation (4.46) is $\Delta n_{Left} = 0.0001437$ and $\Delta n_{Right} = -0.0000167$, whereas the total refractive index change is $\Delta n_{Total} = 0.0001607$.

It can be observed that the maximum refractive change under the voltage applied for the etched left waveguide is $\Delta n_{max,Left} = 0.00004$ and for the unetched $\Delta n_{max,Left} = 0.00002$. As a result of this difference, the half-wave voltage will be much lower for etched structure, which is a significant advantage for etched LN modulators over unetched LN modulators. Next to be considered is the optical field profile for TM-polarized light for the etched modulator shown in Figure 7.8. The optical field profile for the TM-polarized light, where the H_{11}^x is the quasi-TM fundamental mode, is investigated for an electrode gap, $G=15 \mu\text{m}$, a buffer layer thickness, $B=1.2 \mu\text{m}$, a centre electrode width, $S=8 \mu\text{m}$, an electrode thickness, $T=5 \mu\text{m}$, a waveguide width, $W=9 \mu\text{m}$ and a ridge height, $H=3 \mu\text{m}$. The propagation constant for the left waveguide, for this LiNbO₃ etched modulator structure with its parameters as defined here, is $\beta = 8.6782526$, whereas for the right waveguide it is $\beta=8.6778874$. It can be seen that due to the fact that the waveguide index profile, $n_{e,o}(x,y)$, is diffused, the optical mode is very well confined in the lateral

dimension. For this mode, the dominant H_x optical field profile is only one of the guides for the etched structure with its parameters determined above. The position of the electrodes and the buffer layer thickness role with its ridge are also illustrated in this figure.

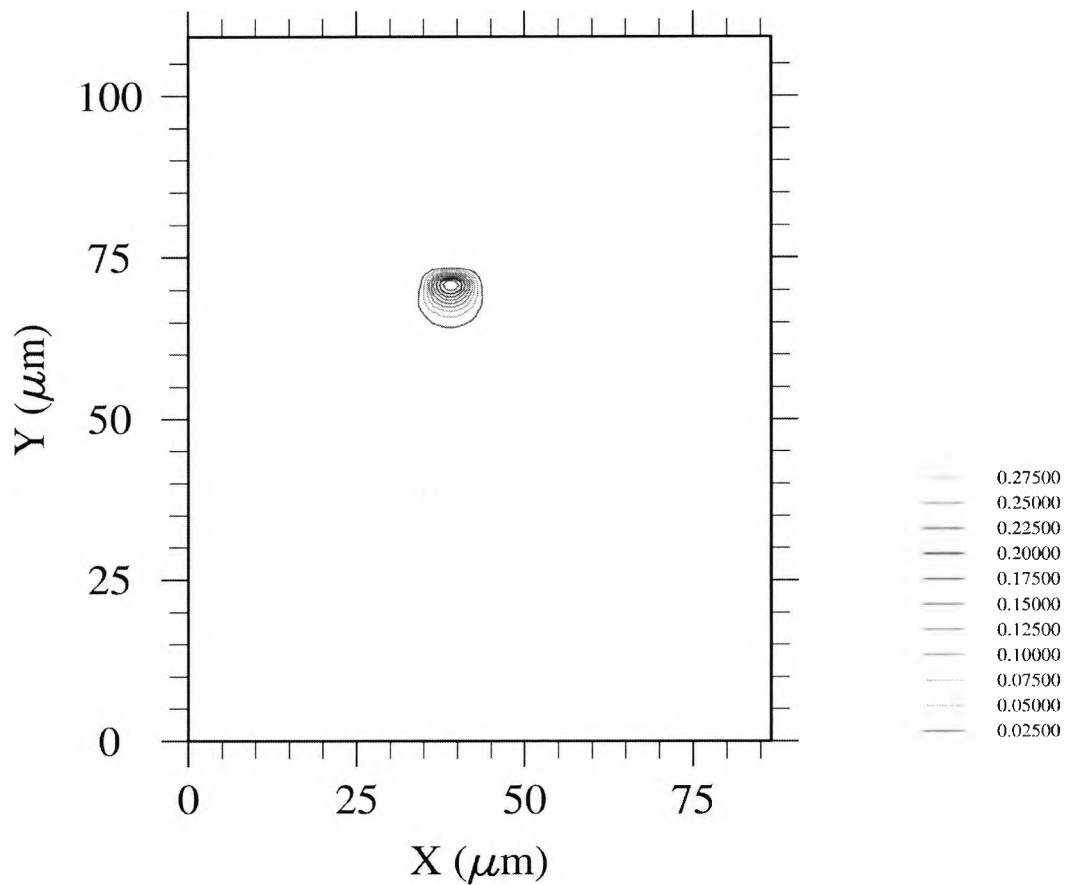


Fig. 7.8 The optical field H_x contours of the quasi-TM mode for an etched structure with ridge height, $H=3 \mu\text{m}$.

It has been confirmed that propagation constants for the ridge structure are $\beta_{V=0,Left} = 8.6781145$ and $\beta_{V=5,Left} = 8.6782526$ the $\Delta\beta_{Left} = 0.0001381$, whereas for the right waveguide are $\beta_{V=0,Right} = 8.6779031$ and $\beta_{V=5,Right} = 8.6778874$,

$\Delta\beta_{Right} = -0.0000157$ and the total $\Delta\beta_{Total} = 0.0001538$. The optical mode is much more confined for this structure due to the nature of the ridge waveguide, as can be seen in Fig. 7.8.

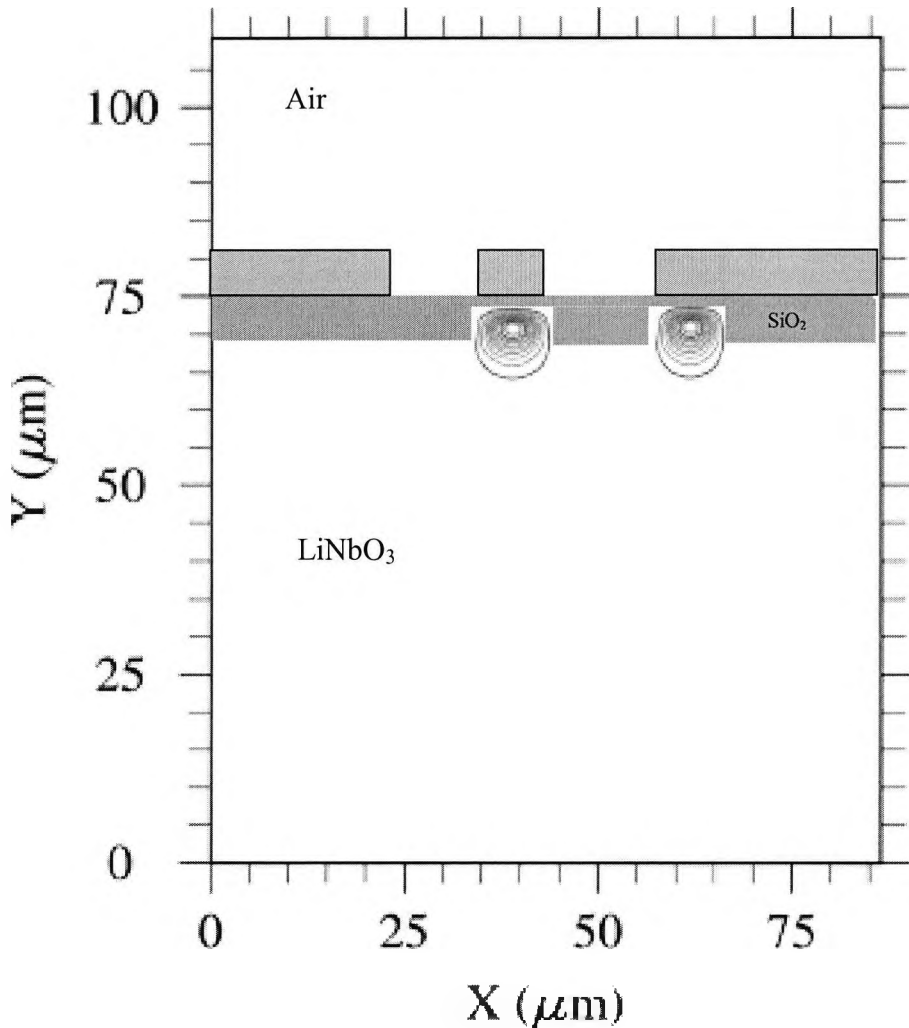


Fig. 7.9 The optical field H_x contours of quasi-TM modes for left and right waveguides.

The TM modes for both waveguides, at ridge height, $H=3 \mu\text{m}$ are illustrated in Fig. 7.9. The unetched high-speed electro-optic modulator considered here is based on the Mach-Zehnder approach and fabricated on Z-cut LN substrates, operating with a vertical electric field to utilize the largest electrooptic coefficient, r_{33} , of the LN. The relative dielectric constants of the Z-cut LN substrate were 28 and 43 in the perpendicular and

parallel directions to the substrate surface, respectively. To reduce the optical loss due to the lossy metal electrode the SiO₂ buffer layer is used, which also assists in the phase matching. The relative dielectric constant of the SiO₂ buffer layer is taken as 3.9. The coplanar waveguide (CPW) electrode is commonly used as a travelling-wave electrode for a Ti:LN optical modulator because it provides a good connection to an external coaxial line. It has been reported relatively recently (Mitomi, 1998) that for a ridge type modulator with an etched LN substrate, the overlap between the optical and modulating field can be significantly increased and as a consequence, for a given operating voltage, the interaction length can be shortened which will also increase the modulator bandwidth. In this paper the important optical and microwave properties of an etched Z-cut LN modulator are presented.

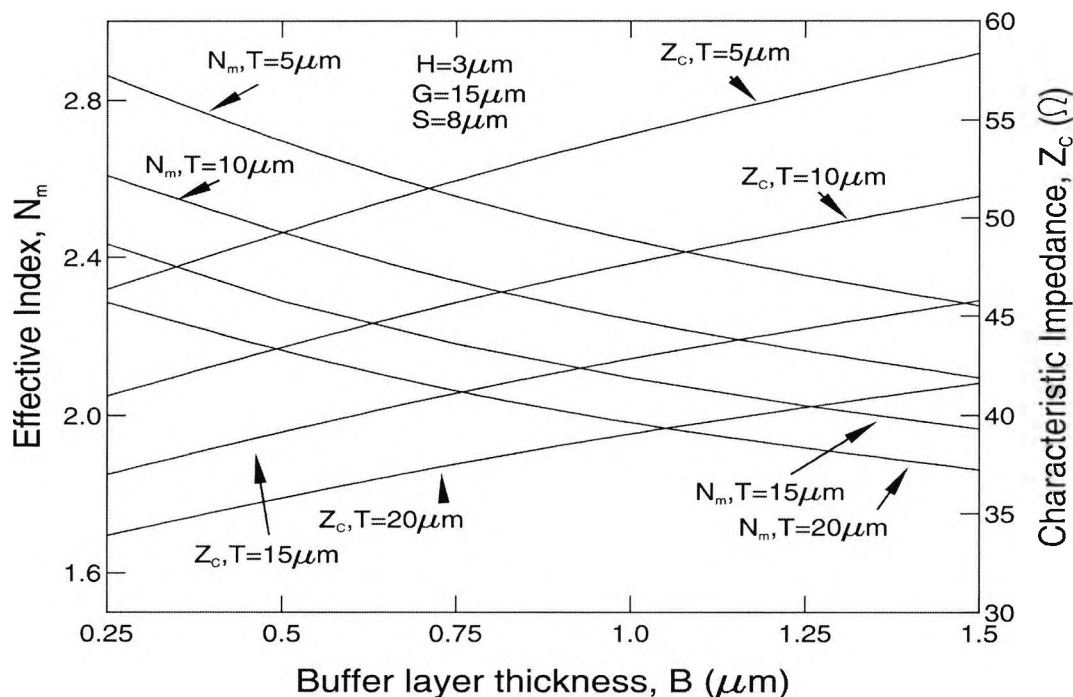


Fig. 7.10 Variation of the microwave index, N_m and the Characteristic Z_c with the buffer layer thickness, B .

The buffer thickness, B , is an important parameter in the design of an optical modulator. Variations of N_m and Z_C with the buffer layer thickness, B , for various electrode thickness, T , are shown in Fig.7.10. In this case, the ridge height, H , the hot-electrode (strip) width, S , and the gap between the electrodes, G , are taken as 3.0 μm , 8.0 μm , and 15 μm , respectively. It can be noted that N_m reduces and Z_C increases with the increase of B . It can also be observed that the microwave index, N_m and the characteristic impedance Z_C decrease as T is increased. The velocity of the optical carrier wave or its equivalent parameter, the effective index, N_o , of a modulator structure depends on various fabrication parameters, such as the titanium thickness, the diffusion time and the temperature. For a given structure, this parameter can be accurately calculated by using an optical modal solution approach, such as the FEM; however, for this study a typical value of 2.15 is assumed for the purpose of phase matching.

It can be observed from Fig. 7.10 that for $T = 5 \mu\text{m}$, the buffer layer has to be thicker than 1.5 μm to match the phase velocity. On the other hand, as T is increased, a thinner buffer layer would be adequate to match the phase velocity. In this particular case, when T equals in from 10, 15, and 20 μm , the necessary buffer layer thicknesses are 1.31, 0.84 and 0.53 μm , respectively, for the phase matching. Similarly, for electrode thicknesses of 5 and 10 μm , buffer layer needs to be 0.57 and 1.32 μm respectively, for impedance matching. However, the buffer layer needs to be thicker than 1.32 μm when the electrode thickness is more than 10 μm . At the same time, it is well known that as B is increased, the overlap between the microwave and optical modes is reduced and as a consequence the $V_{\pi L}$ value would also increase.

Variations of the microwave index, N_m , and characteristic impedance, Z_C , with the etch depth, H , for various gold electrode thickness, T , are illustrated in Fig. 7.11. In this case the hot central-electrode (strip) width, S , gap width, G , and buffer layer thickness, B , were taken as 8 μm , 15 μm , and 1.2 μm respectively. It can be noted that N_m decreased as the ridge height, H , increases; also it can be observed from this figure that the electrode thickness, T , is increasing when the ridge is increased. It can also be noted that the characteristic impedance, Z_C , increased as H was increased but the value of Z_C reduced when the electrode thickness, T , was increased. Our results agree well with those reported by Mitomi *et al.* (1995), which are illustrated by dashed lines on the

figure. It is essential that for an electrode thickness, $T=5\ \mu\text{m}$, the velocity and impedance matching cannot be achieved at any value of ridge depth, whereas for an electrode thickness $T=10\ \mu\text{m}$, it can be achieved relatively easily.

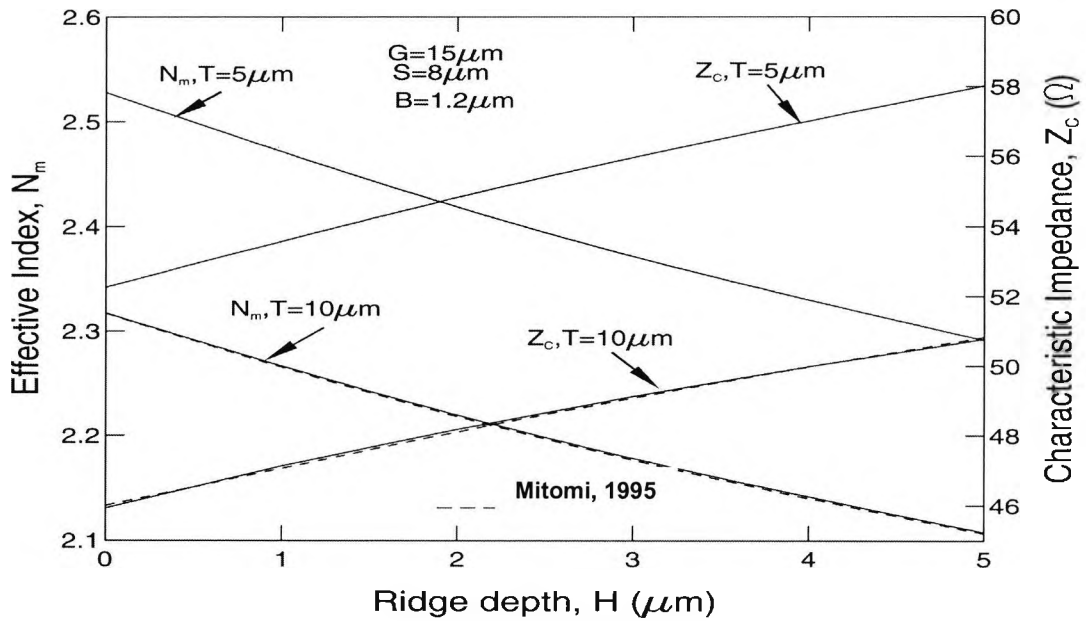


Fig. 7.11 Variation of the microwave parameters N_m and Z_C with ridge depth, H .

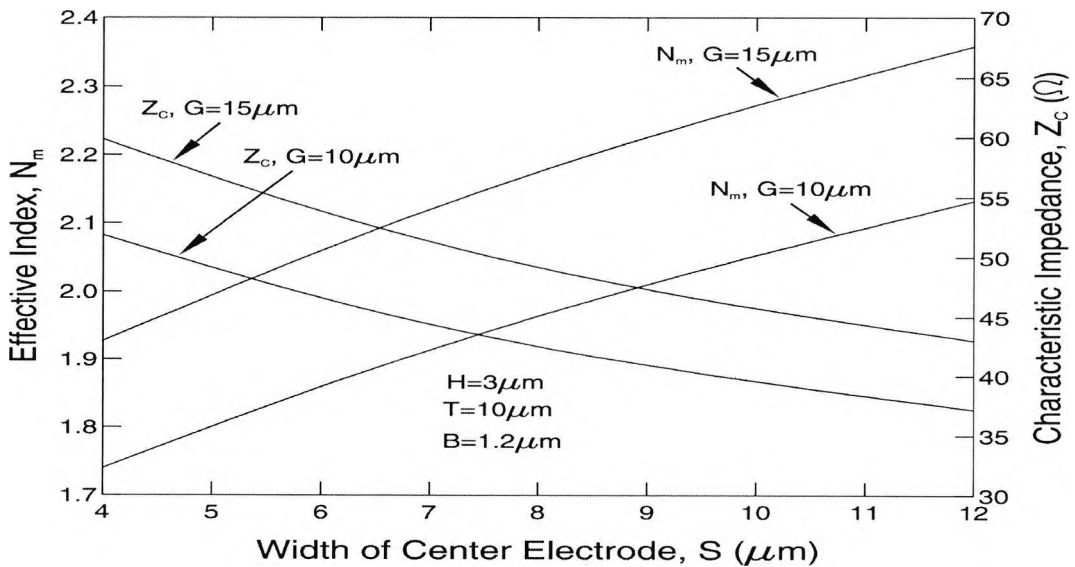


Fig. 7.12 Variation of microwave parameters N_m and Z_C with the central electrode, S .

Besides the ridge depth, H , the buffer layer thickness, B , and the electrode thickness, T , the hot-electrode and gap the widths also play important roles in the design of optical modulators. Variations of N_m and Z_C with the width, S , of the hot-electrode for two gaps between the electrodes, G , are shown in Fig.7.12. It can be observed that N_m increases with the S , however Z_C decreases. On the other hand both N_m and Z_C increase with the increase of the gap between the electrodes G . It can be noted (is not shown here) that in this case the dominant loss component, α_c , does not depend strongly on S , but this loss reduces considerably with the increase of G .

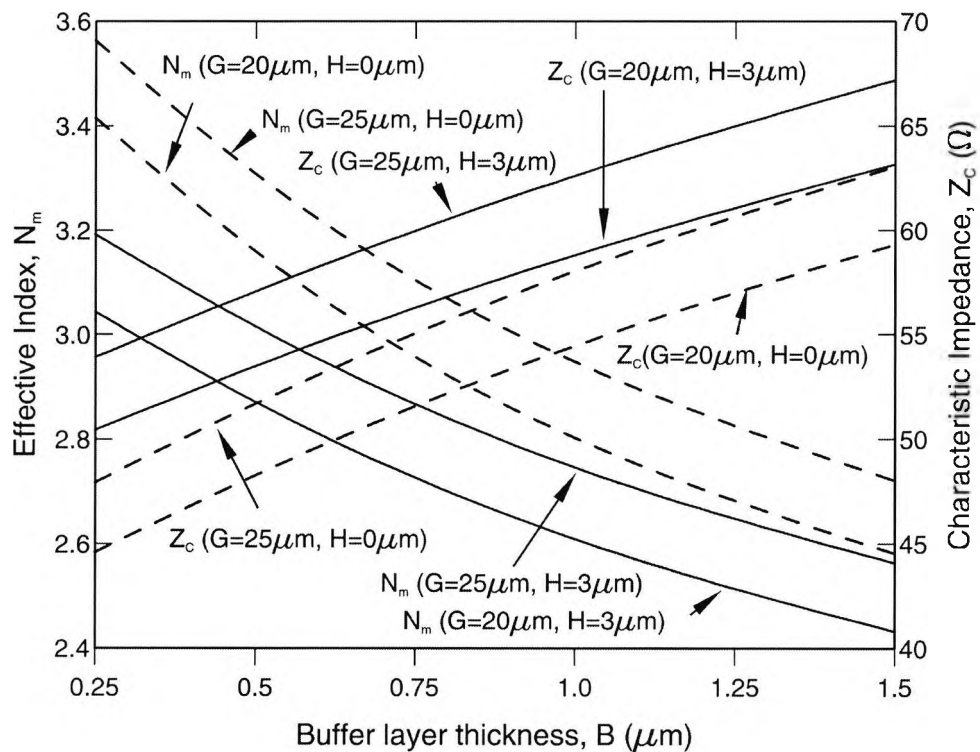


Fig. 7.13 Variation of the microwave index, N_m , the characteristic impedance, Z_C as a function of the buffer layer, B , for an electrode gap, $G=20 \mu\text{m}$ and $G=25 \mu\text{m}$ and for the ridge depth, $H=0 \mu\text{m}$ and $H=3 \mu\text{m}$ when the electrode thickness, $T=5 \mu\text{m}$.

In the design of the optical modulator, besides the minimization of $V_{\pi}L$, the microwave parameters N_m and Z_C play an important role in determining the bandwidth of the modulator. Variations of N_m and Z_C with the buffer layer thickness, B , are shown in Fig. 7.13. In this case the electrode thickness, T , and the waveguide width, W , were kept constant at 5.0 μm and 9.0 μm , respectively. Results for ridge heights of 0 μm and 3.0 μm are shown by dashed and solid lines respectively, for two values of G . It can be observed that N_m reduces and Z_C increases as B is increased. On the other hand, both N_m and Z_C reduce as G is reduced. It can also be observed that N_m reduces but Z_C increases, as H is increased. The wave velocity of the optical carrier wave or its equivalent parameter, the effective index, N_o , of a modulator structure depends on various fabrication parameters, such as the titanium thickness and the diffusion time and temperature. For this study it is assumed that a typical value would be 2.15 for the purpose of subsequent phase matching. For the range considered here, it can be noticed that for none of the cases is N_m matched. By considering a higher value of B , it should be possible to match N_m , but as a consequence $V_{\pi}L$ would also be larger. However, it can be observed that by etching the LN substrate, since N_m is also reduced, it would then be easier to match the value of N_m with a lower value of B . It can also be noted that in most cases it is not possible to match both N_m and Z_C simultaneously by adjusting only B , unless the other parameters are carefully tailored.

For high-speed LN electrooptic modulators, when the phase matching between the optical and the microwave signals are achieved, then the overall modulator bandwidth depends on the total microwave loss. Variations of α_C and α_d , normalized at 1 GHz, with the buffer layer thickness, B , are shown in Fig. 7.14. It can be observed that the dominant loss factor, α_C , reduces slightly as the buffer layer thickness is increased and this coefficient also reduces if the electrode thickness, T , is increased. On the other hand, the dielectric loss in the LN layer, α_{dL} , reduces, but α_{ds} and the total dielectric loss, α_d , increase as the buffer thickness is increased. It can be noticed that the dielectric loss in the silica layer is much higher than that in the LN substrate. The total dielectric loss, α_d , is also reduced when the electrode thickness, T , is increased. Conductor loss, α_C , being dominant at the low frequency operation and particularly at 1 GHz, has a value between 20 to 70 times higher than that of the total dielectric loss. It can be noted that conductor

loss calculated here in this study agrees well with the conductor loss reported by Noguchi 1998, illustrated on the figure with dashed lines.

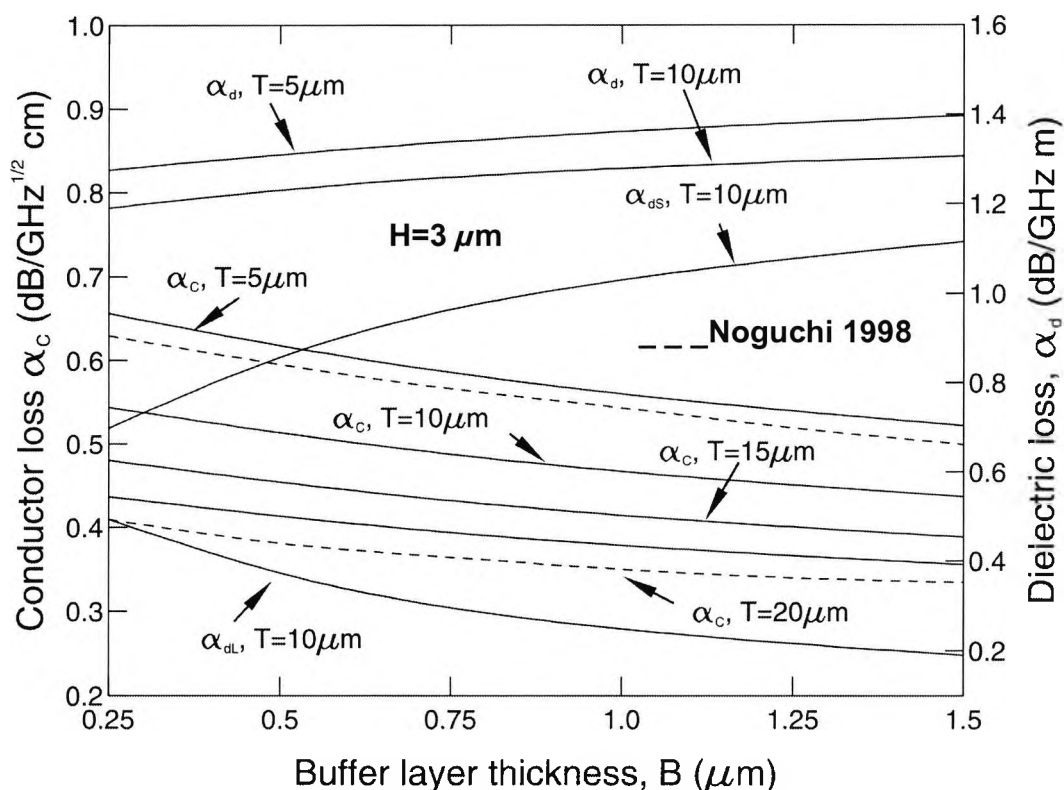


Fig. 7.14 Variation of the conductor loss and dielectric loss with buffer layer thickness normalized at 1 GHz, for ridge height, $H=3 \mu\text{m}$.

It is essential to notice that the results of the conductor loss calculated in this figure are for four different values of the electrode thickness, T , $5 \mu\text{m}$, $10 \mu\text{m}$, $15 \mu\text{m}$ and $20 \mu\text{m}$. In this work, the loss tangent values for LN and the silica are taken as 0.004 and 0.016 (Noguchi 1998). It can be observed that both α_{dL} and α_d increase slightly, as the value of H is increased. It can be also noted that for typical buffer layer thicknesses, the losses in the silica layer are much higher than that of the LN crystal, similar to that reported in Noguchi, 1998.

The variations of the conductor loss, α_c , and dielectric losses, α_d , (normalized at 1 GHz) with the etch depth, H , are shown in Fig. 7.15. The frequency dependent surface

resistance for gold, R_s , is calculated from its conductivity, $\sigma = 4.1 \times 10^7$ s/m. It can be observed that as H is increased, α_c reduces slightly. The conductor loss depends strongly on the electrode thickness, T , and reduces considerably when a thicker electrode is used.

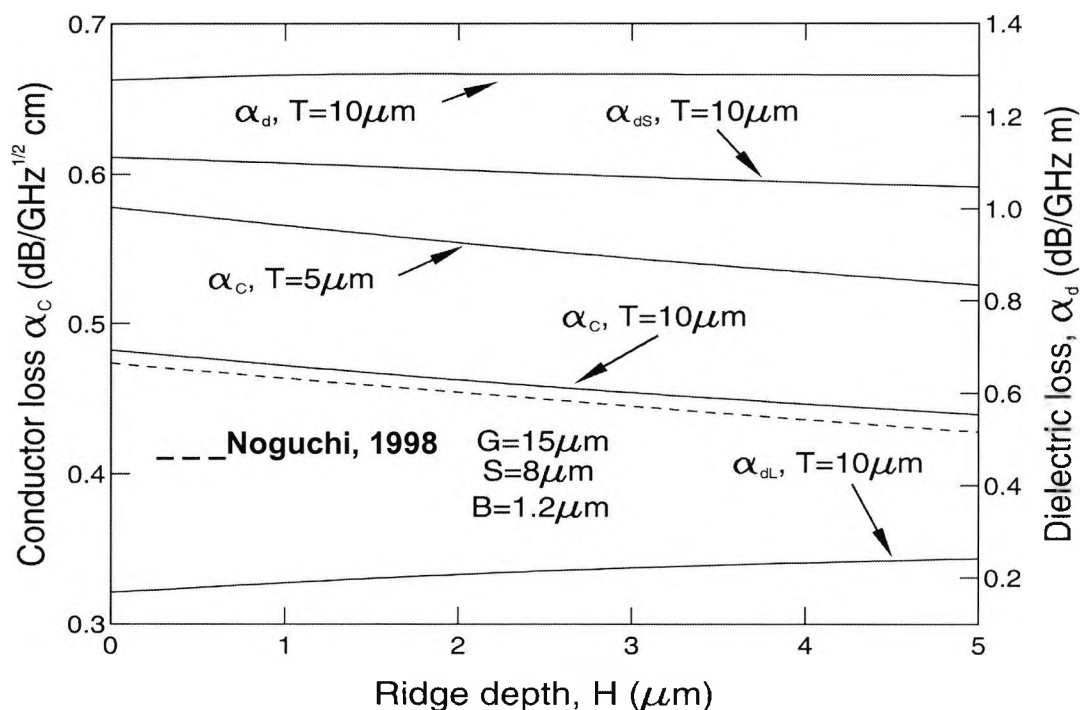


Fig. 7.15 Variation of the conductor loss and dielectric losses with the ridge depth.

The simulated results presented here agree reasonably well with that in the published work (Noguchi, 1998), also shown here by dashed lines. The dielectric loss in silica (buffer) layer, α_{ds} , in the lithium niobate crystal, α_{dl} , and the total dielectric loss, α_d , for $T = 10 \mu\text{m}$ are also shown in this figure.

The conductor loss has significant impact on the bandwidth determination; however, when the operating frequency is higher, the dielectric loss also plays an important role in determining its bandwidth. It can also be observed in Fig. 7.16 that the dielectric loss, α_d increases as the buffer layer is increased, as more of the modulating field is confined in the silica layer, which has a higher loss coefficient. It can be observed that the dielectric

loss, α_d , is increased as the electrode gap, G , is reduced, or the ridge height H is increased. The results presented in this work on dielectric losses agree well with the results of a similar study reported by Gopalakrishnan *et al.* 1993, indicating that, as the operating frequency of the next generation of ultra-high-speed modulators is increased the effect of dielectric loss would increase significantly.

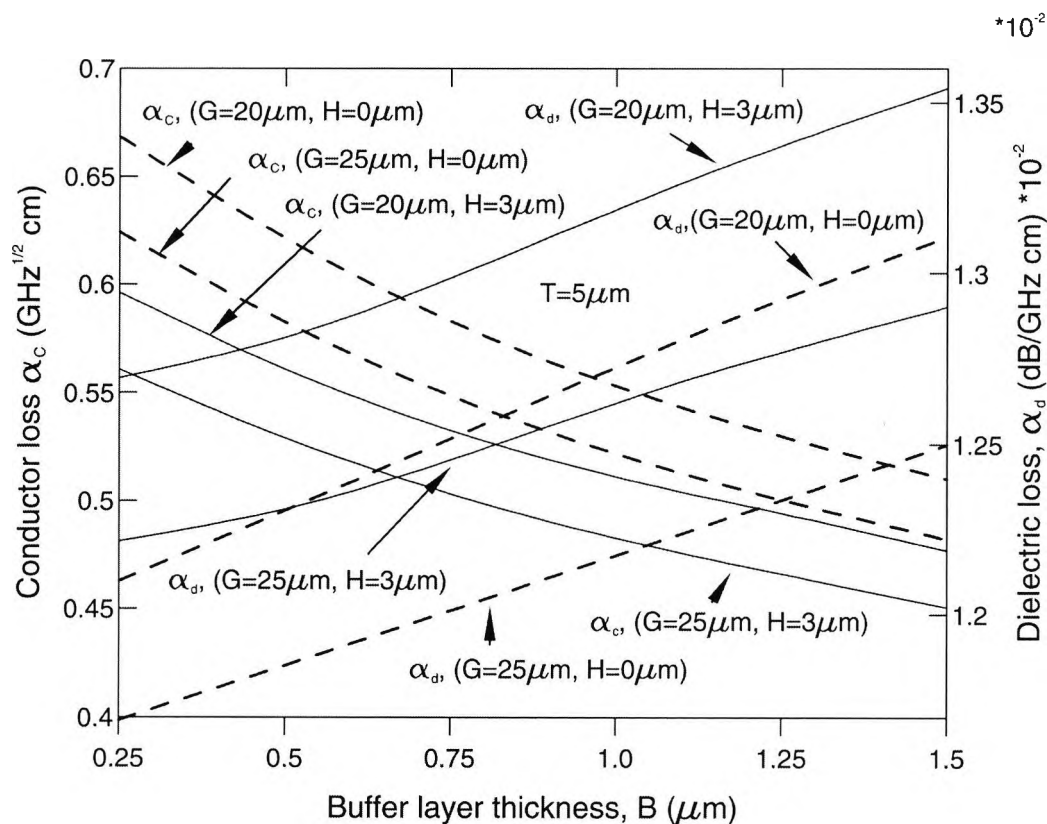


Fig. 7.16 Variation of conductor loss and dielectric loss with the buffer layer thickness, normalized at 1 GHz, for an electrode gap, $G=20 \mu\text{m}$ and $G=25 \mu\text{m}$ and for the ridge depth, $H=0 \mu\text{m}$ and $H=3 \mu\text{m}$ when the electrode thickness, $T=5 \mu\text{m}$.

At 1 GHz, for this structure, the conductor loss is two orders of magnitude larger than the dielectric loss. However, since the dielectric loss is proportional to the operating frequency, f , compared to the conductor loss, which is proportional to \sqrt{f} , for ultra-high-speed modulators the dielectric loss cannot be neglected. It can be noted that both conductor loss and dielectric loss are reduced when electrode gap G is increased, and

this parameter plays an important role in bandwidth determination for high-speed LN electrooptic modulators.

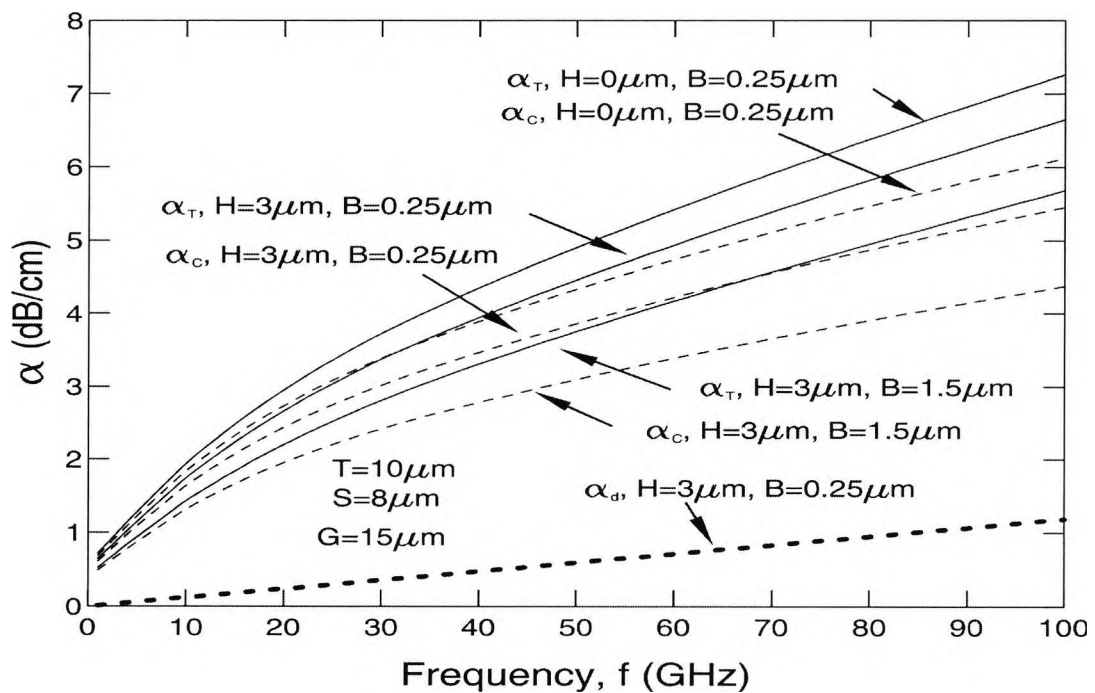


Fig. 7.17 Variation of conductor loss, α_C dielectric loss, α_d and total dielectric, α_T loss with the operating frequency f .

At 1 GHz, for etched and unetched structures the conductor loss is two orders of magnitude larger than the dielectric loss. However, since the dielectric loss is proportional to the operating frequency, f , compared to the conductor loss, which is proportional to the \sqrt{f} , so for ultra-high-speed modulators dielectric loss cannot be neglected. The variation of the conductor loss, dielectric loss and the total microwave losses with the operating frequency are illustrated in Fig. 7.17, by dashed, dotted, and solid lines, respectively. It can be observed noted that at 100 GHz, dielectric loss could easily be 15% of the total loss, and this loss cannot be neglected in the calculation of the modulator bandwidth. This research work has confirmed that the effect of the etched compared to unetched modulator structure is significant. Fig. 7.17 investigates the effect

of the total conductor loss for three different buffer layer thicknesses, with the operating frequency. It can be observed from this figure that, at high operating frequency, the effect of etched structure is positively significant.

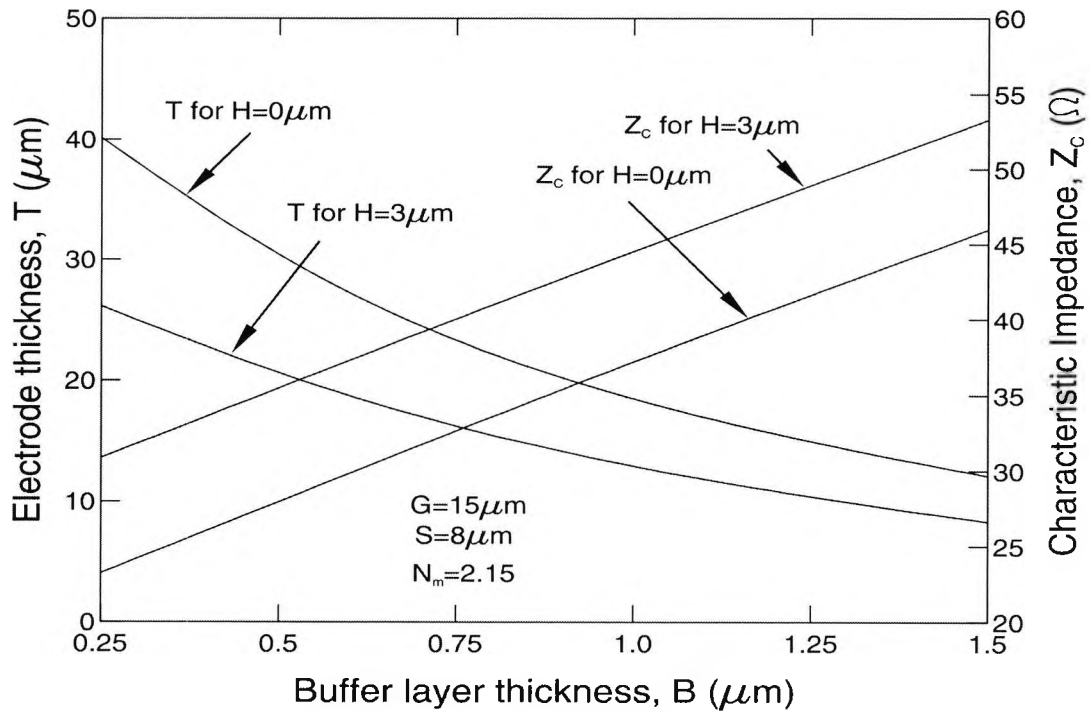


Fig. 7.18 Required electrode thickness to achieve the phase matching and the corresponding characteristic impedance, Z_C for certain buffer layer thickness, B .

It is possible to match the most important parameter for a travelling wave modulator, the microwave effective index, N_m , by varying fabrication parameters. The electrode thickness necessary to achieve the phase matching for a given buffer layer thickness is shown in Fig. 7.18, for both $H = 0$ (unetched structure) and $3 \mu\text{m}$ (etched structure). It can be observed that as buffer layer is reduced a much thicker electrode is necessary to match the phase velocity. It can also be noted that it is easier to match phase velocity for etched structure as a considerably reduced metal thickness would be necessary. The variation of Z_C with B , when phase velocity is matched is also shown in this figure. It can be noted that, although N_m is matched, however, mostly Z_C is not matched to 50Ω ,

except only for $H=3\ \mu\text{m}$, when $B=1.30\ \mu\text{m}$ and $T=10\ \mu\text{m}$, where both phase velocity and Z_C are matched simultaneously. When etched LN structure is employed ($H=0\ \mu\text{m}$), it can be noted that necessary buffer thickness and electrode thickness would be $1.7\ \mu\text{m}$ and $10\ \mu\text{m}$ respectively for simultaneous matching of N_m and Z_C .

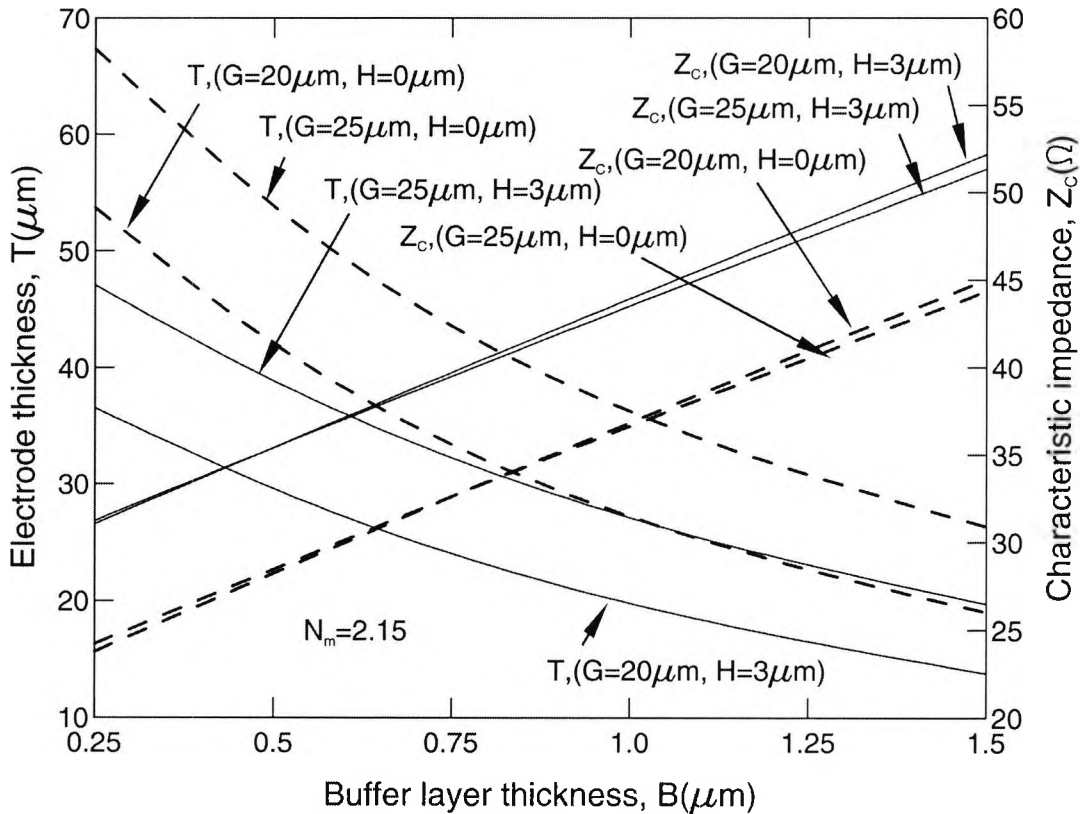


Fig. 7.19 Required electrode thickness, T , to achieve velocity matching, $N_m = 2.15$ and the variation of the characteristic impedance, Z_C , under this condition as a function of the buffer layer, B .

In the design of such high-speed modulators first of all it is necessary to match the microwave impedance to the optical impedance. Amongst the other parameters, this can easily be achieved by increasing the electrode metal thickness, T . Moreover, the $V_\pi L$ product does not change significantly with electrode thickness. However, the electrode thickness is a key parameter to optimise the velocity and impedance matching. The variations of electrode thickness, T , necessary to match the value of $N_m (= 2.15)$, for

different buffer layer thickness, B , are shown in Fig. 7.19. It can be noted that as the buffer layer thickness is reduced to a lower $V_{\pi}L$ product, the value of T required would be higher to achieve the phase matching. However, it can also be observed that for an etched LN the required metal thickness is smaller than that of unetched LN for the same buffer layer thickness. Variations of Z_C with the buffer layer, when the structure is phase matched, are also illustrated in this figure. It is demonstrated that when the buffer layer is increased, Z_C is increased. It can be noted that in most cases, when the modulator is phase matched, the impedance is not matched. The impedance matching is slightly worse when the LN is not etched. Phase matching depends strongly on the ridge depth, H , and this figure shows that for a certain buffer layer, B , and electrode gap, G , the required electrode thickness, T , is higher for an unetched structure. For a ridge height $H=3\ \mu\text{m}$, it is possible to achieve both phase and impedance matching when the buffer layer thickness $B=1.49\ \mu\text{m}$: however for $H=0\ \mu\text{m}$ both impedance and phase matching is not achievable for these particular parameters. The electrode gap, G , does not have significant role in impedance matching, but when the electrode gap G is higher, a higher electrode thickness is required to achieve phase matching, which reduces the conductor loss.

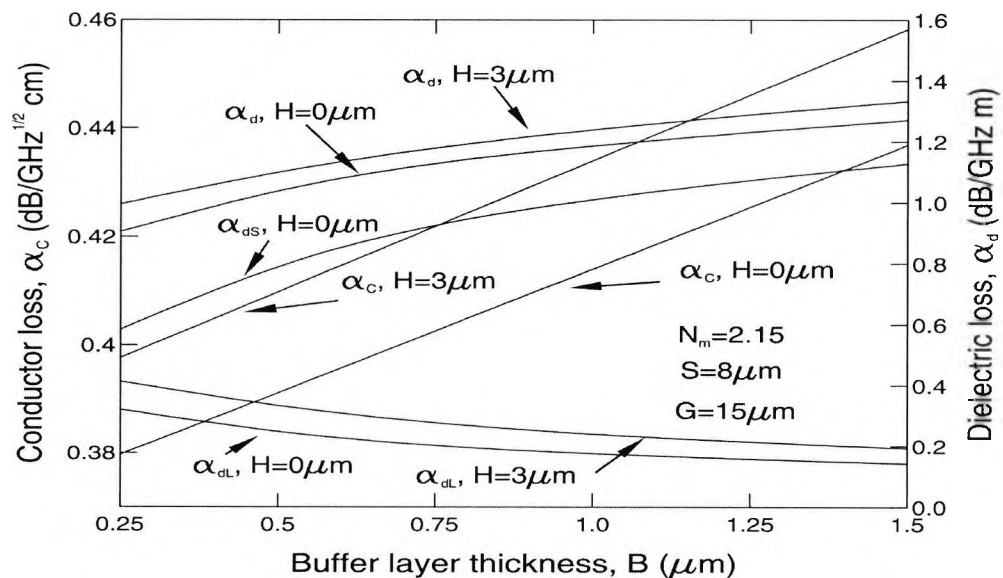


Fig. 7.20 Variation of conductor loss, dielectric loss in LN and SiO₂ with buffer layer thickness, under velocity matching condition.

Variations of the conductor loss, α_C and dielectric loss, α_d with the buffer layer, B , under velocity matching condition, N_m is illustrated in Fig. 7.20. It can be observed that for both unetched, $H = 0 \mu\text{m}$, and etched structures, $3 \mu\text{m}$, conductor loss, α_C , is increased when the buffer layer thickness, B , is increased. It can also be observed that dielectric loss in the LN substrate, α_{dL} , reduces, but both dielectric loss on SiO₂ buffer region α_{dS} and total dielectric loss (sum of dielectric losses of LN and SiO₂ regions) α_d are increased when buffer layer is increased. It can also be noted that for etch depth $3.0 \mu\text{m}$, α_C is slightly higher than that for when LN is not etched.

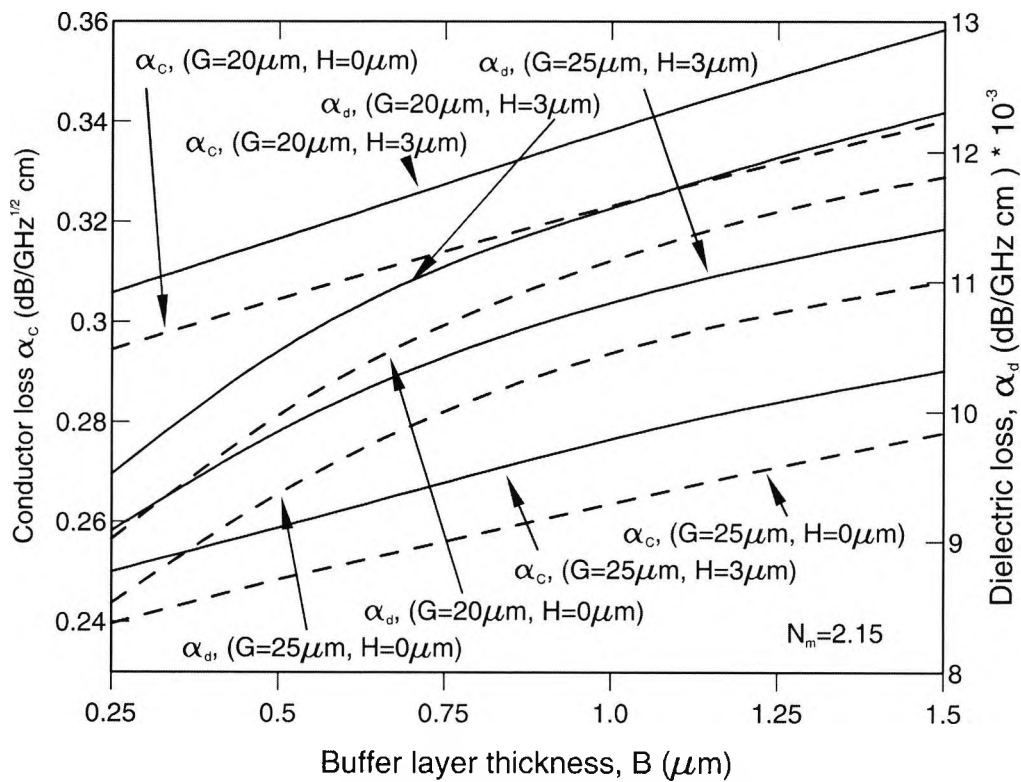


Fig. 7.21. Variation of the conductor loss and the dielectric loss with the buffer layer thickness, B , normalized at 1 GHz for an electrode gap, $20 \mu\text{m}$ and $25 \mu\text{m}$ and ridge depth $0 \mu\text{m}$ and $3 \mu\text{m}$ under the velocity matching condition.

In Fig. 7.21. are illustrated the variation of the conductor loss α_C , and the dielectric loss, α_d , normalized at 1 GHz with the buffer layer thickness, B , when the electrode thickness, T , has been adjusted to achieve phase matching. Solid and dashed lines shown are for $H=3 \mu\text{m}$ and $0 \mu\text{m}$, respectively. It can be observed that for a given ridge height value and a fixed electrode gap, G , the value of α_C is increased when the buffer layer thickness, B , is increased. This increase of conductor loss is due to the reduced electrode thickness necessary for the phase matching. The electrode gap, G , has a significant role on the conductor losses, when electrode gap, G , is increased from $G=20 \mu\text{m}$ to $G=25 \mu\text{m}$. The conductor losses, α_C , are reduced by nearly 20% for a fixed ridge height, H . The dielectric losses are increased when the buffer layer thickness, B , is increased for a value of the ridge height and a fixed electrode gap, G . It can be seen that when the electrode gap, G , is increased, the dielectric losses, α_d , is decreased, in a similar way to the conductor loss. Hence a larger electrode gap, G , is expected to increase the modulator bandwidth.

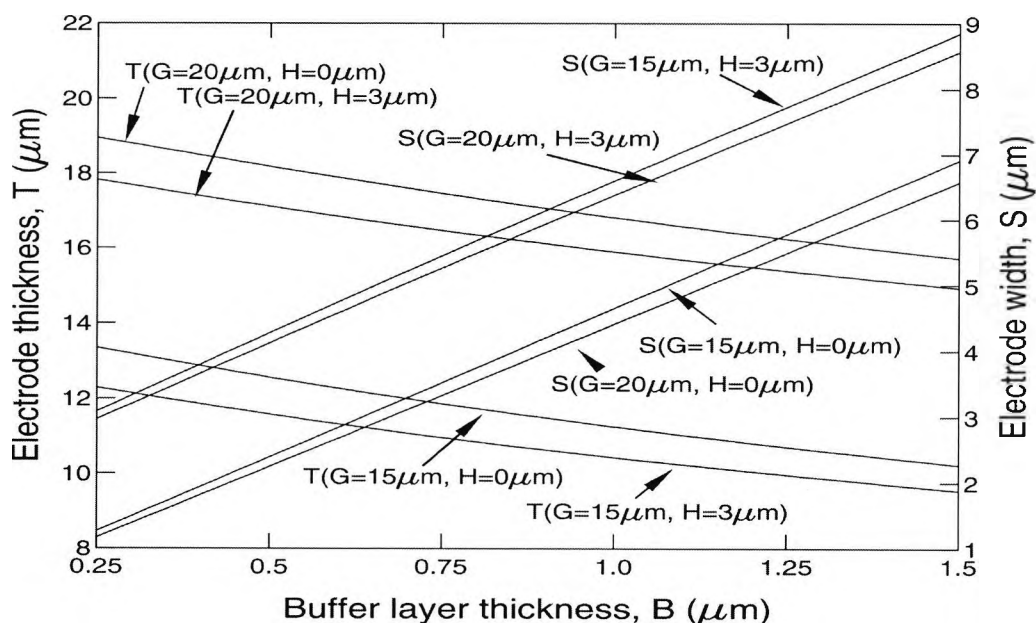


Fig. 7.22 Variation of the electrode thickness T and electrode width S with the buffer layer thickness B under the simultaneous matching condition of N_m and Z_C .

It has been confirmed that simultaneous matching of both N_m and Z_C is not possible by varying only one parameter such as the ridge depth, H , buffer layer thickness, B , or electrode thickness, T , at a time. But it is also investigated that for a specific combination of T and B , it may be possible to match both of them simultaneously. In general, by changing any of the two parameters from B , T , H , S and G , it may be possible to match both N_m and Z_C simultaneously. Next, the simultaneous matching of both the N_m and Z_C is undertaken. For each buffer layer thickness, B , both the electrode thickness, T , and the hot-electrode width, S , are varied together to match N_m and Z_C simultaneously. Simulated results are shown in Fig. 7.22, for two values of the gap between the electrodes, G , 15 and 20 μm , and for two values of ridge depth, H , 0 μm and 3 μm , respectively. It can be observed that the necessary electrode thickness, T , is increased and the electrode width, S , is reduced when buffer layer thickness is reduced.

With respect to simultaneous matching it has been observed that when G is increased, electrode thickness necessary for the phase matching is also increased. When an etched LN is used, the necessary T value is slightly reduced. It can be noted that as G is changed, necessary hot-electrode width, S , does not change much. However, one important factor can be noted here that, for etched LN structure ($H = 3 \mu\text{m}$), for a given hot-electrode width, S , buffer layer could be thinner. It should also be noted here that, to match the optical spot-size of the modulator to that of a single mode fibre, it is often necessary to have the LN ridge width and also the hot-electrode width, S , in the range of 6-10 μm , which would also restrict the centre electrode width S .

It is also very important to identify the dielectric and conductor losses under velocity and impedance matching condition, N_m and Z_C respectively. The variation of conductor loss, α_C and dielectric loss, α_d with the buffer thickness, B , are illustrated in Fig. 7.23, when both N_m and Z_C are matched simultaneously. It can be noted that as buffer thickness is reduced the α_C is increased, which would reduce bandwidth if length of the modulator is fixed. However, when thinner buffer layer is used, the corresponding $V_{\pi}L$ will be significantly reduced; hence the modulator length can be reduced to increase the optical bandwidth. It has been confirmed that conductor loss α_C reduces as electrode gap, G is increased, but this value reduces significantly when a ridge structure is used ($H = 3 \mu\text{m}$) compared to planar LN structure ($H = 0 \mu\text{m}$).

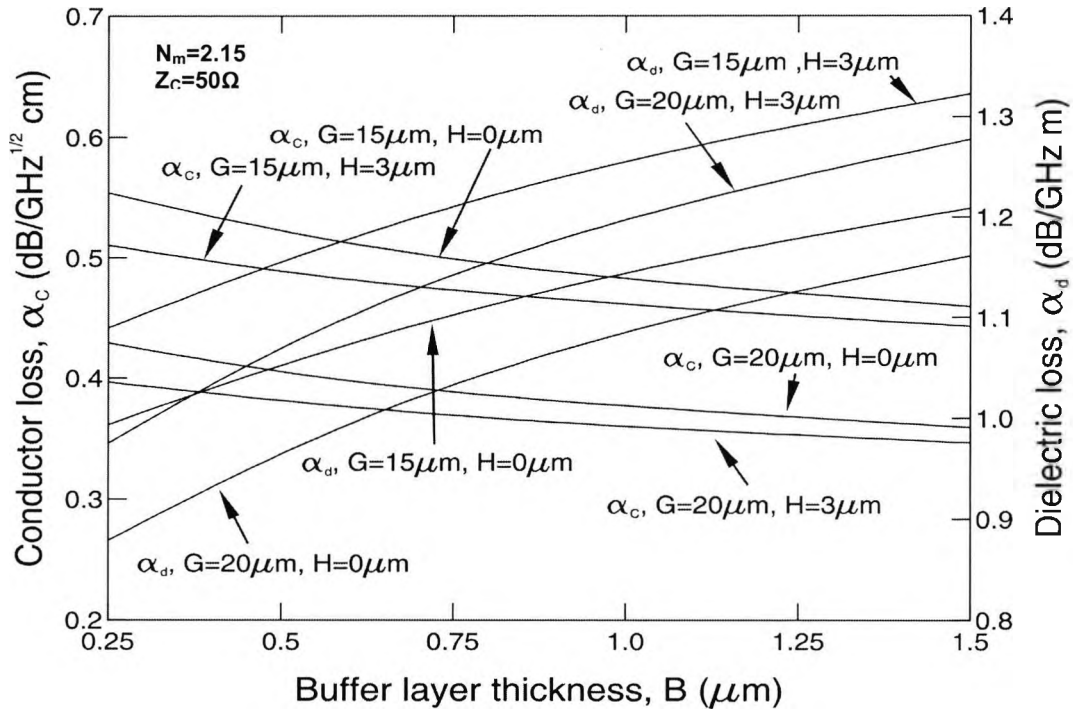


Fig. 7.23 Variation of the conductor loss and dielectric loss with buffer layer thickness under simultaneous matching condition of N_m and Z_C .

It should be mentioned that both $V_{\pi}L$ and α_c reduce when etched LN electrooptic modulator is considered, which can positively impact on the performance of the modulator. The term $V_{\pi}L$ is the product of the half-wave voltage, V_{π} and the interaction length, L , of the device and it is the key parameter of an electrooptic modulator. Fig. 7.24 shows the variation of $V_{\pi}L$, as a function of ridge depth, H , for two different values of the buffer layer thickness, B . It can be observed that for the electrode width, $S=8\ \mu\text{m}$, a waveguide width, $W=9\ \mu\text{m}$, and the electrode gap, $G=15\ \mu\text{m}$, the product $V_{\pi}L$ decreases as the ridge depth H is increased from zero and reaches its minimum value when H is between $3\ \mu\text{m}$ to $5\ \mu\text{m}$ where the present optimum value is consistent with the observations reported earlier by various authors such as Minakata, 2001 and Mitomi, 1995. The decrease of $V_{\pi}L$ is due to the optical field being more confined in the lateral direction, and consequently showing an increased overlap with the modulating electric

field. It can also be observed that the product $V_{\pi}L$ reduces as the buffer layer is reduced from $B=1.2\ \mu\text{m}$ to $0.75\ \mu\text{m}$.

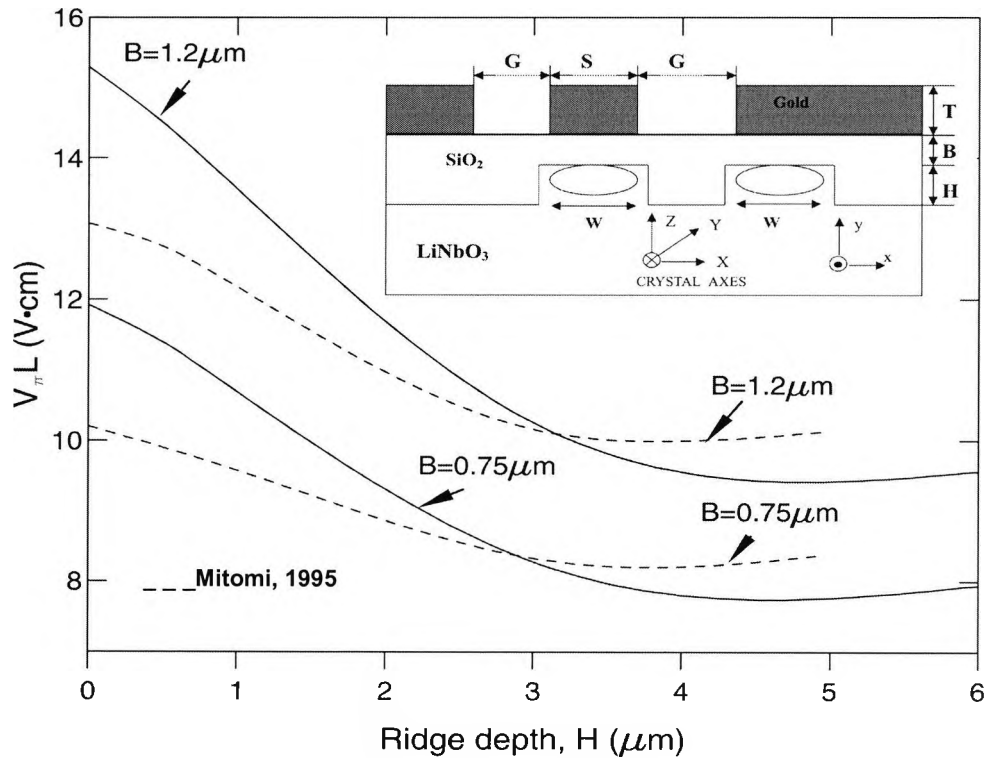


Fig. 7.24 Variation of the product $V_{\pi}L$ as a function of the ridge depth, H for two different buffer layer thicknesses, B and the structure of modulator.

Results for similar types of structures, as reported by Mitomi *et al.* 1995 are shown by dashed lines: however, an exact comparison was not carried out due to the lack of the key optical parameters necessary for the optical simulations. Since further reduction of H may not reduce $V_{\pi}L$, considering these results and the ease of fabrication, the optimum ridge depth is often set to $3.0\ \mu\text{m}$ for comparison with the planar LN structures and also for further optimization of the microwave characteristics.

The buffer thickness, B , is an important parameter in the design of an optical modulator. The variations of the $V_{\pi}L$ product with the buffer layer thickness, B , for three ridge depths, H , and two electrode gaps, G , are shown in Fig. 7.25. It shows that $V_{\pi}L$ decreases linearly as the buffer layer thickness B is reduced, but for a very small buffer layer

thickness, the penetration of the optical field into the metal electrode would also increase the optical losses, as shown in previous work by Anwar, 2002.

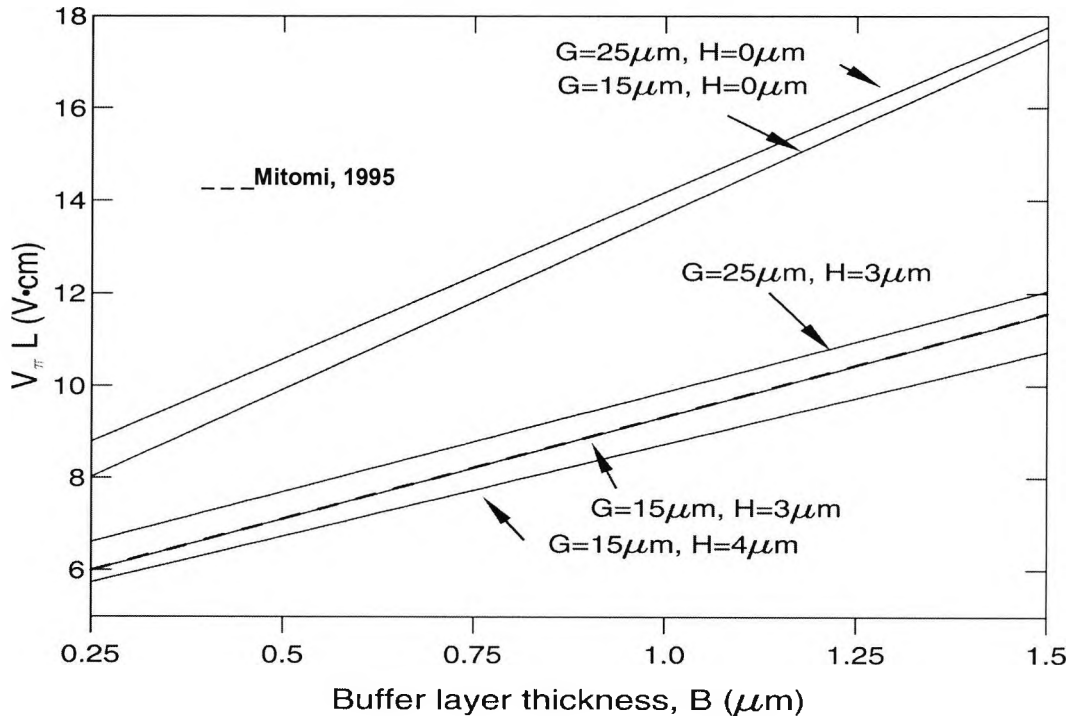


Fig. 7.25 Variation of $V_{\pi}L$ as a function of the buffer layer, for an electrode gap, $G=15$ μm and $G=25$ μm for etched, ($H=3$ μm , $H=4$ μm) and unetched, ($H=0$ μm) structures.

It can be observed that by increasing the ridge depth from 0 μm to 4 μm , the $V_{\pi}L$ product decreases by more than 30% over the range of B considered here. It can also be observed that by increasing the electrode gap, G , from 15 to 25 μm and keeping the other parameters fixed, the product $V_{\pi}L$ increases slightly. This observation is consistent with the results reported by Mitomi *et al.* 1995, for a similar type of structure, shown here by a dashed line for a ridge depth of $H=3$ μm .

Although the gap between electrodes, G , does not play a significant role in determining the $V_{\pi}L$ product, it will be shown later, that the electrode gap, G , does influence other microwave parameters such as the microwave losses and bandwidth. The variations of the $V_{\pi}L$ product with the electrodes gap, G , are shown in Fig. 7.26. For $H=4$ μm the product $V_{\pi}L$ reduces as the electrode gap reduces until G is very small. In this case, when the electrode gap, G , is below 5 μm , the Mach-Zehnder section behaves rather like

a directional coupler due to the evanescent coupling between the two adjacent optical waveguides.

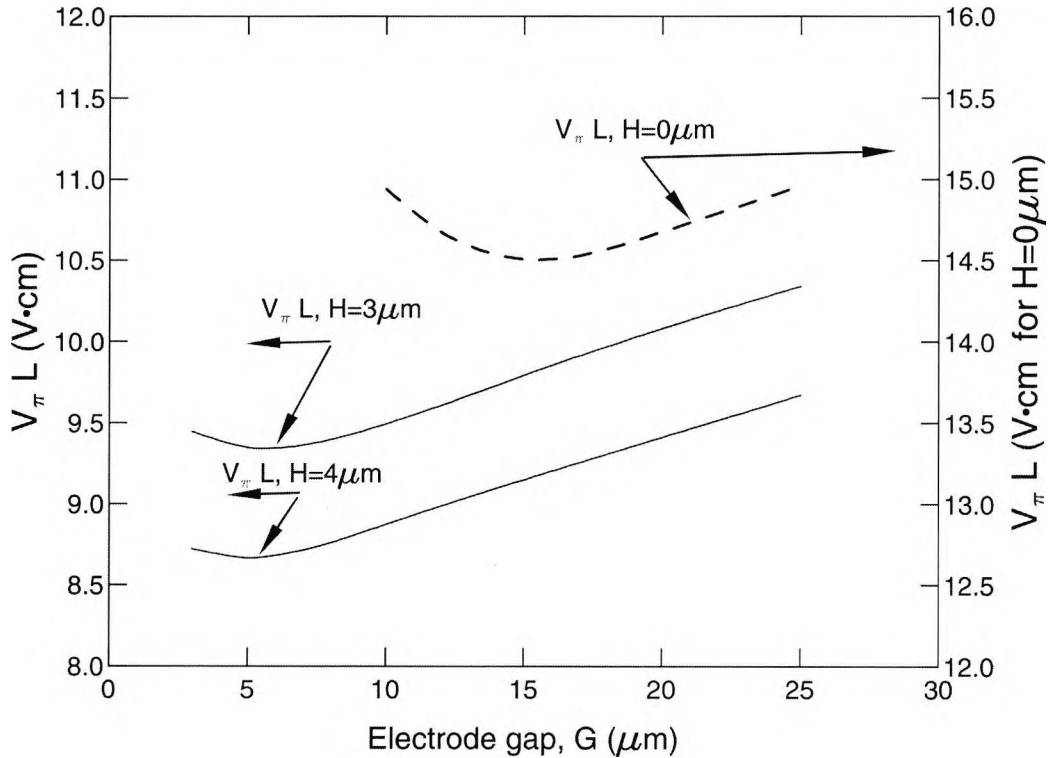


Fig. 7.26 Variation of the product $V_{\pi}L$ with the electrode gap, G , for values of ridge depth, $H=0 \mu\text{m}$, $H=3 \mu\text{m}$ and $H=4 \mu\text{m}$.

Since for $H=0 \mu\text{m}$, the resulting product $V_{\pi}L$ is quite large, its variation with the electrode gap, G , is shown by a dashed line with its scale on the right hand side. For the ridge depth $H=0 \mu\text{m}$, this mode coupling between the arms can be detected even when the electrode gap, G , is around $15 \mu\text{m}$, due to the much weaker lateral confinement of the modal fields of the unetched guides. As in this situation there is a significant coupling between the two arms of the Mach Zehnder branches, and a simple value $\Delta\beta$ for the two isolated waveguides would not give the correct $V_{\pi}L$ product.

The optimization of the waveguide and the hot-electrode width are also important. Fig. 7.27 shows the dependence of the $V_{\pi}L$ product on the width of the central hot-electrode, S , for different waveguide widths. The other parameters, such as $B=1.1 \mu\text{m}$, $G=15 \mu\text{m}$, $T=5 \mu\text{m}$ and $H=3 \mu\text{m}$ are kept fixed. It can be observed that the $V_{\pi}L$ product is reduced

as the electrode width, S , is increased for a given waveguide width, W . As S is increased, the peak value of Δn (due to electrooptic effect) spreads outward and the overlap between the optical field increases.

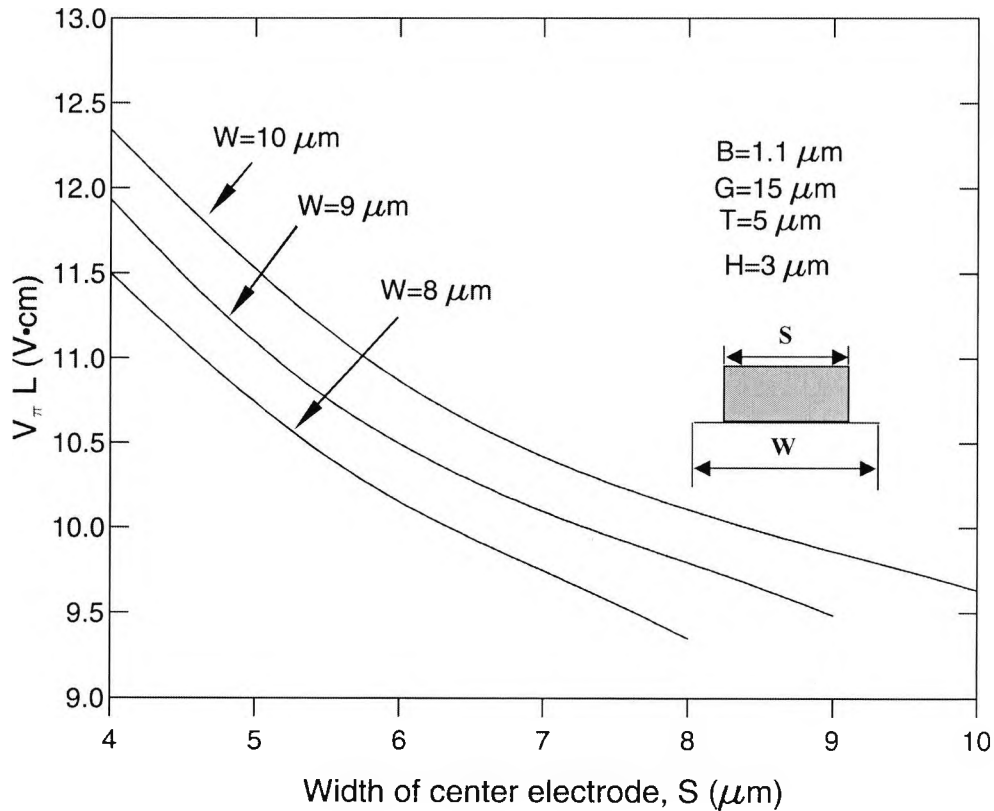


Fig. 7.27 Variation of the product $V_{\pi}L$ with the width of center electrode, S , for a waveguide width, $W=8 \mu\text{m}$, $W=9 \mu\text{m}$ and $W=10 \mu\text{m}$.

The $V_{\pi}L$ product keeps decreasing as the width of center electrode, S , increases until it equals that of the ridge width. It can also be observed that when the width of the waveguide is reduced, the $V_{\pi}L$ product is also reduced, as the optical field is more confined in the guide. However, it is interesting to observe that when S and W are equal, i.e. when the electrode covers the whole waveguide width, the $V_{\pi}L$ values are the lowest and nearly constant for the range of values of S and W considered here. For H lower than $3 \mu\text{m}$, the trends are similar but the $V_{\pi}L$ values would be larger.

The modulator bandwidth primarily depends on the mismatching between the optical and microwave phase velocities. However, when they are matched, the maximum optical bandwidth can be achieved, and this maximum value depends on the microwave loss. The variations of the 3 dB optical bandwidth with the buffer layer thickness for different electrode thickness are shown in Fig. 7.28. The length of the electrodes is taken as $L=2.7$ cm, the waveguide width, $W=9$ μm , the electrode width, $S=8$ μm and the electrode gap, $G=15$ μm . In this case the effects of phase and impedance mismatching and electrode losses are considered.

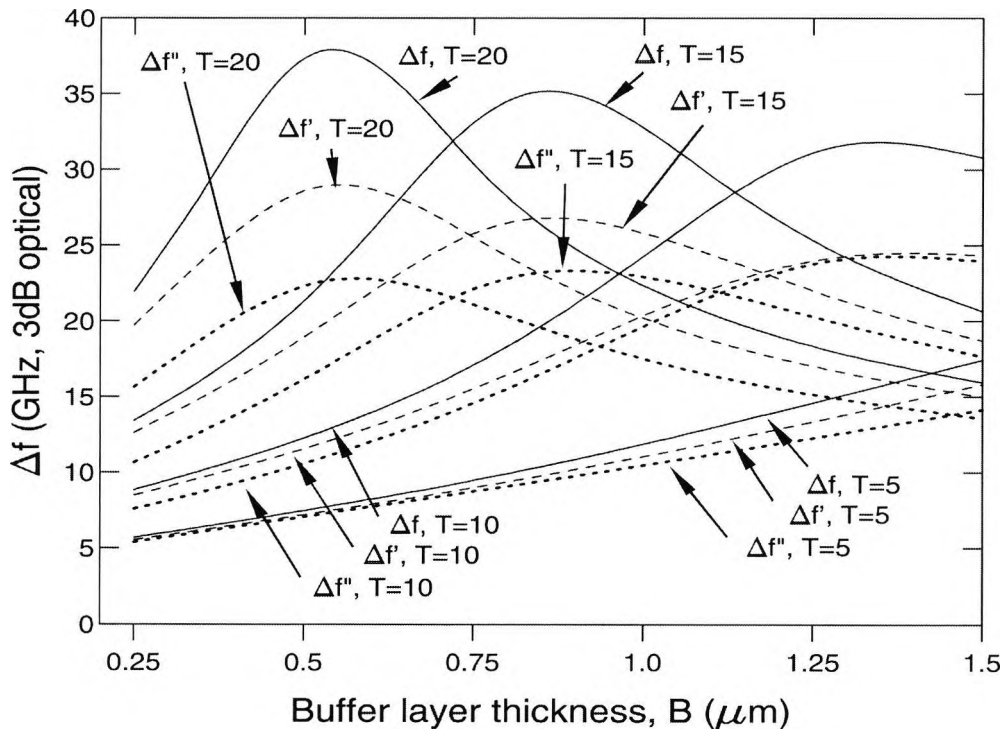


Fig. 7.28 Variation of the 3dB optical bandwidth, with buffer layer thickness, B , for different values of electrode thickness, T .

When only the conductor loss is considered and the dielectric loss and impedance mismatch are neglected, the bandwidths calculated by using equation (5.48) (Chapter 5) are shown by the solid lines. It can be noted that for $T=20$ μm , a 38 GHz maximum bandwidth is achieved when $N_m = N_o$, at the buffer layer thickness, B , equal to 0.52 μm . It can be also noted that for $T=15$ μm , the maximum bandwidth of 35 GHz is achieved

when $B = 0.83 \mu\text{m}$, as the microwave loss in this case increases. The dashed lines show the variations of the optical bandwidths with the buffer layer thickness, B , when the effect of the dielectric losses is included. It can be noted that by neglecting the dielectric loss, the optical bandwidth could be over estimated by as much as 30%. This error will be even higher when the operating frequency is also higher as the dielectric loss increases faster than the conductor loss with the operating frequency. It is obvious that at higher operating frequencies, when the dielectric loss is ignored, the total microwave loss can be significantly underestimated. The dotted line represents the variation of the $\Delta f'$ bandwidth with the buffer layer thickness, B , when the conductor loss, the dielectric loss and also the effect of impedance mismatch are considered, and it can be observed that the maximum value of the bandwidth has been reduced significantly, by almost 45%. It can be noted that for an electrode thickness, $T=5 \mu\text{m}$, the maximum bandwidth can be achieved, but at a large value of buffer layer thickness, B .

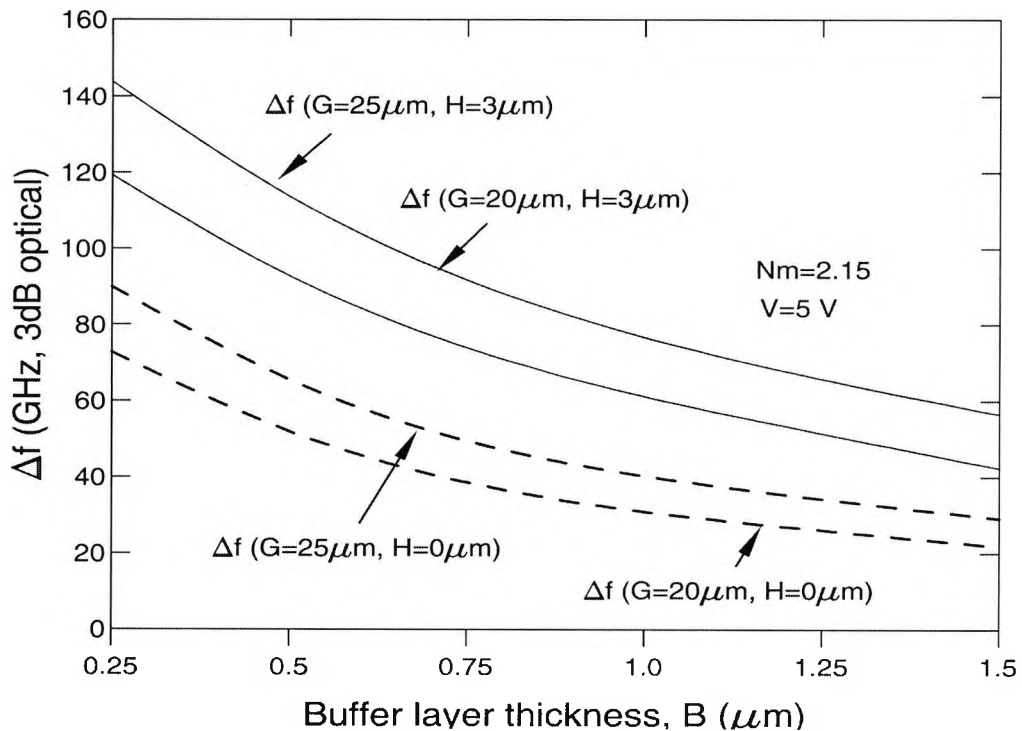


Fig. 7.29 Variation of the 3dB optical bandwidth for etched and unetched structures, with the buffer layer thickness, B , at a fixed voltage $V=5 \text{ V}$ under the velocity matching condition.

Since $V_{\pi}L$ varies strongly with buffer layer thickness, B , it is also important to evaluate the design developed for a fixed operating voltage, by adjusting the device length. In this case it is assumed that the operating voltage is 5 V and the electrode thickness, T , is adjusted to achieve phase matching as illustrated in Fig. 7.29. The variations of the bandwidth, Δf , with the buffer layer thickness, B , are shown in Fig. 7.30, after taking into account the effects of the conductor loss, α_c , dielectric loss, α_d and the impedance, Z_c , mismatch. It can be noted that the bandwidth, Δf , increases as the buffer layer, B , decreases. It is also obvious that the bandwidth increases as the electrode gap, G , increases. However, as B is reduced, the optical loss at the metal electrode would also increase. It has been demonstrated that for a ridge depth, $H=3 \mu\text{m}$, the overall bandwidth, Δf , increases significantly, compared with the unetched structure.

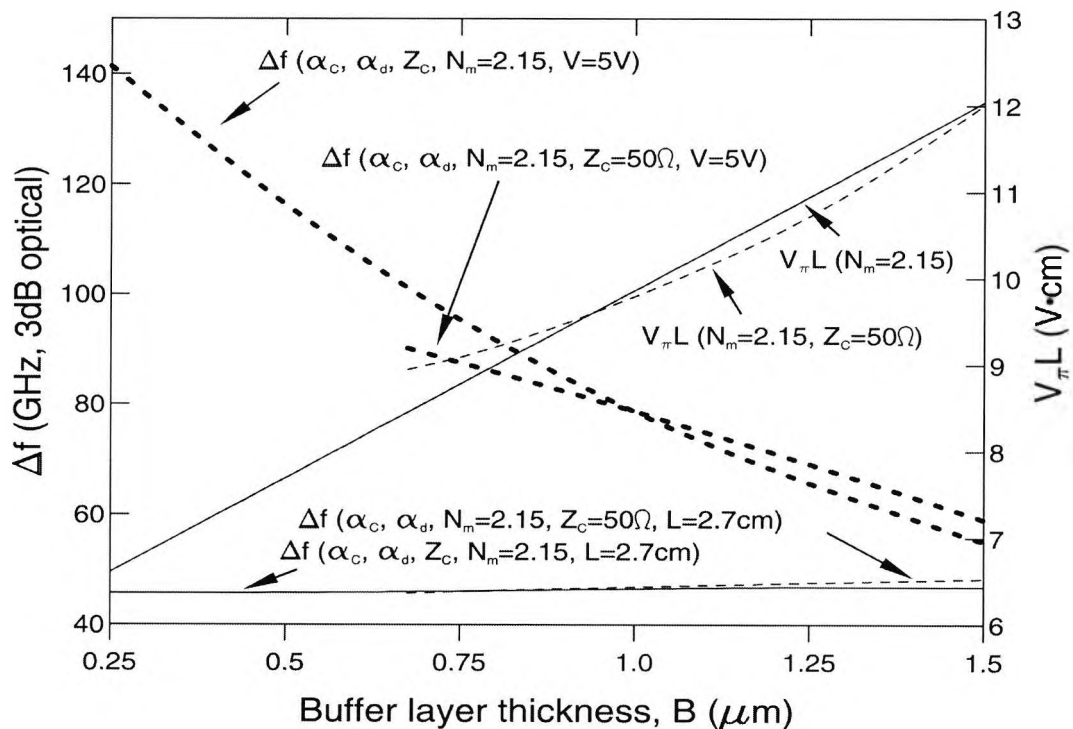


Fig. 7.30 Variation of the 3dB optical bandwidth and the product $V_{\pi}L$ with buffer layer thickness, B , under velocity and impedance matching conditions.

Next, a study of the simultaneous matching of both N_m and Z_c is undertaken. In general, by changing any of the two parameters from the group B , T , H , S and G , it may be possible to match both N_m and Z_c simultaneously. In this study, for each buffer layer

thickness, B , both the electrode thickness, T , and the hot-electrode width, S , are varied together to match N_m and Z_C simultaneously. The waveguide width, W , is kept $1\ \mu\text{m}$ higher than the electrode width, S . Results for both fixed device length ($L=2.7\text{cm}$) and fixed operating voltage ($V=5\text{V}$) are shown. The variation of the parameter $V_\pi L$ is also shown in Fig. 7.30, by the dashed lines, under velocity and impedance matching conditions. In this case the electrode length, L , is kept at 2.7cm , the ridge height, H , is $3\ \mu\text{m}$ and the electrode gap, G , is $25\ \mu\text{m}$. In the bandwidth calculation the effect of the conductor loss and the dielectric loss are considered under velocity and impedance matching conditions. By adjusting the electrode thickness, T , and the electrode width, S , the matching condition can be achieved, but only for particular values of buffer layer thickness. It has been confirmed that for a buffer layer thickness, B , less than $0.70\ \mu\text{m}$, the device does not behave as a Mach-Zehnder modulator because of the coupling between the waveguides. This is due to the small waveguide width, W , which is required to achieve phase and impedance matching simultaneously. It can be noted that the product $V_\pi L$ increases when the buffer layer increases under the velocity and impedance matching conditions shown by the dashed line. The solid line represents the variation of the product $V_\pi L$ with the buffer layer thickness under the velocity matching condition only.

The variation of the bandwidth with the buffer layer thickness, B , when the voltage V is fixed at $5\ \text{V}$, rather than the electrode length, is shown also in this figure by a dot line for the electrode gap, $G=25\ \mu\text{m}$, and a ridge depth, $H=3\ \mu\text{m}$. It can be seen that by keeping the voltage fixed under the velocity matching condition, the bandwidth has been increases significantly, and it decreases rapidly with the buffer layer thickness. In this case the effect of the conductor loss, the dielectric loss and the impedance mismatch are included. The variation of the bandwidth with the buffer layer thickness, B under the velocity and impedance matching condition is also shown by the dashed lines. Under these velocity and impedance matching conditions for a buffer layer thickness, B , less than $0.70\ \mu\text{m}$, the device cannot operate as a modulator.

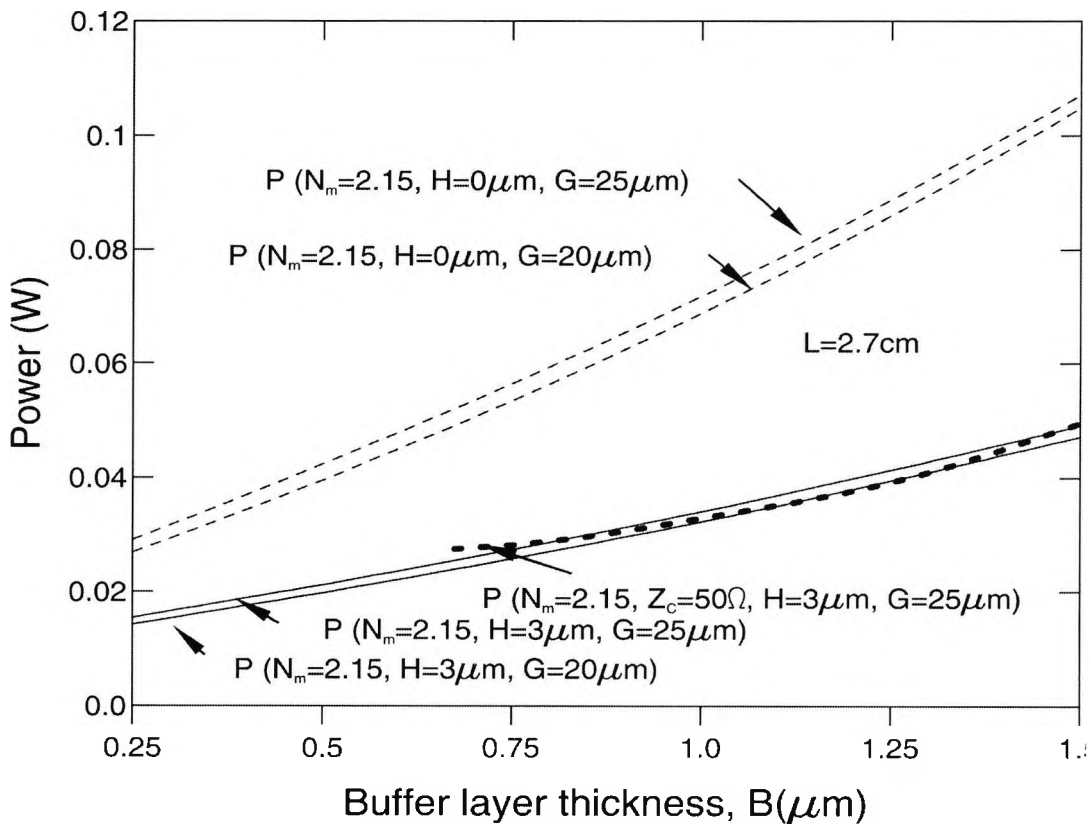


Fig. 7.31 Variation of the driving power with buffer layer thickness under velocity and impedance matching condition for etched and unetched structure.

Next the driving power is calculated from the equation (4.52). As stated before the driving power primarily depends on the product of half-wave voltage length $V_{\pi}L$ and the characteristic impedance, Z_C . Obviously a low half-wave voltage and characteristic impedance value close to 50Ω are required in order to achieve low driving power. For this reason many LN electrooptic modulators are designed and their electrodes are optimized in order to achieve impedance matching and low half-wave voltage. Fig. 7.31 shows variation of the driving power under velocity matching condition for both structures, etched and unetched. It can be seen that the value of driving power for the same parameters under velocity matching condition for unetched structure is very high compared to etched, its value being almost 60% higher at the desirable buffer layer thickness, $B=1.25 \mu\text{m}$. The driving power increases when the buffer layer increases as a result of the impedance mismatch and increased half-wave voltage length. Also its value

increases slightly when the gap between electrodes is increased. From this figure it is essential to confirm that the lowest value for the driving power is under velocity and impedance matching condition at electrode gap, $G=25 \mu\text{m}$ for etched structure, illustrated with a dotted line. It is very important to see that the required buffer layer thickness for low driving power LN electrooptic modulator with its length $L=2.7 \text{ cm}$ is in the range between $0.6 \mu\text{m}$ and $1.5 \mu\text{m}$.

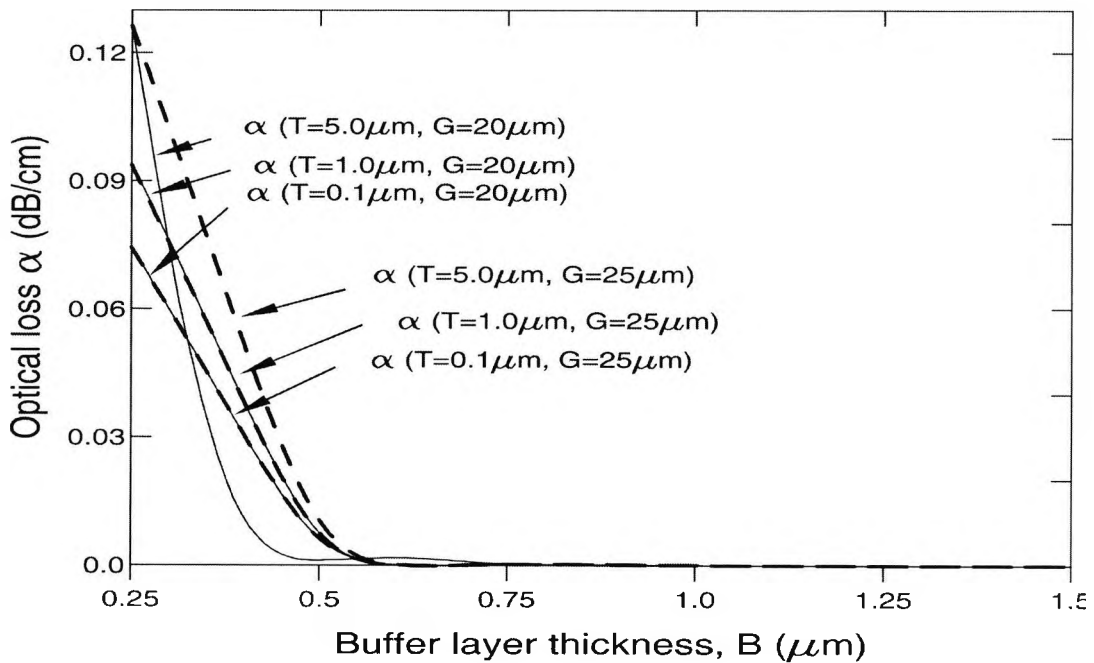


Fig. 7.32 Variation of the optical loss with buffer layer thickness for different electrode thickness and gap between electrodes.

Electrode design is an important consideration in minimizing the overlap between the optical and modulating fields. The buffer layer thickness is required to reduce the optical loss due to the lossy metal electrodes, particularly for TM-polarized light. The calculation of the optical loss due to the electrode is determined using the perturbation method, in conjunction with the FEM (Themistos, 1995). Variation of the optical loss with buffer layer thickness for electrode thickness, T equal to 0.1, 1.0 and $5.0 \mu\text{m}$ for electrode gap, G equal to 20 and $25 \mu\text{m}$ is illustrated in the Fig. 7.32. It can be seen that

optical loss decreases when the buffer layer thickness increases, also optical loss increases when the electrode thickness is decreased and electrode gap is decreased. This reduction of optical loss is due to a decreasing penetration of the optical field into the metal electrode, the source of the optical loss, due to increase in the buffer layer thicknesses, there is a trade-off between loss due to the electrode and half-wave voltage $V_{\pi}L$. However there is a slight increase of optical loss when the electrode thickness is increased.

7.4 Summary

In this chapter a numerical approach based on the efficient finite element method has been established to study some of the key etched and unetched modulator parameters. Simulated results are illustrated including the potential distribution, capacitance calculation, electric and magnetic field distribution, microwave index, characteristic impedance, optical field confinement, conductor loss, dielectric loss for different regions of the substrate, half-wave voltage length, bandwidth, driving power and optical loss, investigated for etched structure. Results of etched and unetched structures are also investigated, in particular the advantage of etched over unetched structure on the device performance. The material and structural dispersion of CPW LN has been reported to be almost constant at frequencies up to 200 GHz so a quasi-static approach is considered here. The effects of various key device parameters to achieve simultaneous velocity and impedance matching are presented. The lack of velocity and impedance mismatch which is the dominant problem preventing the modulator high performance is also thoroughly investigated. For optical modulators operating beyond 40 GHz, the total dielectric loss will play a significant role in the determination of the overall speed of the modulator. It is shown that the etch depth plays an important part in reducing the voltage, or driving power. It also reduces the device length and increases the optical bandwidth. It is further shown that the electrode gap width plays an important role in the bandwidth of a high-speed modulator. The effect of the impedance mismatch on the bandwidth and subsequent attempt to match both effective index, N_m , and characteristic impedance, Z_C , and their effects on the bandwidth are also presented in this chapter.

Deeply-Etched Semiconductor Electrooptic Modulator

8.1 Introduction

External high-speed optical modulators of multi-gigahertz bandwidth and high optical power handling capacity are key components (Walker, 1991) in current optical communications systems and valuable for future optical signal processing technology. Excellent external modulators, made from titanium-diffused lithium niobate in a Mach-Zehnder type structure with a travelling-wave electrode (Mitomi, 1995) are available as standard commercial products and 40 Gb/s modulators are also emerging on the market after successful prototype demonstrations due to their large electrooptic coefficients, low bias drift, and zero or adjustable frequency chirp. However, there is a continued demand for the design of more efficient ultra-high-speed semiconductor electrooptic modulators, (Walker, 1991), (Wang, 1988), (Khan, 1993) and GaAs/Al_xGa_{1-x}As travelling-wave electrooptic modulators offer the obvious advantage of monolithic integration of active/passive photonic and electronic devices to form opto-electronic integrated circuits (OEIC) and/or laser sources. GaAs is the material of choice in many optoelectronic components such as lasers and detectors. Although GaAs electrooptic modulators suffer from a relatively small electrooptic coefficient, compared to the traditional materials like LiNbO₃ this is however partly compensated by their higher refractive indices. Often travelling-wave designs are employed to increase the interaction length between the optical signal and the electrical signal and thus reduce the modulator half-wave voltage

(V_π). These designs will increase the interaction length up to a point, but they are still limited by the velocity mismatch between the optical signal and the microwave signal.

8.2 Design and fabrication of deeply-etched semiconductor waveguide electrooptic modulator

The schematic diagram of the deeply-etched semiconductor electrooptic modulator is illustrated in Fig. 8.1. The parameters of this structure are a $0.2 \mu\text{m}$ 10%AlGaAs layer, a thick GaAs core with a height, $H(\mu\text{m})$, and a buffer layer thickness AlGaAs with an aluminium concentration of $X_1\%$ and its height, $B(\mu\text{m})$, deposited on a $2 \mu\text{m}$ thick 5% AlGaAs spacer layer.

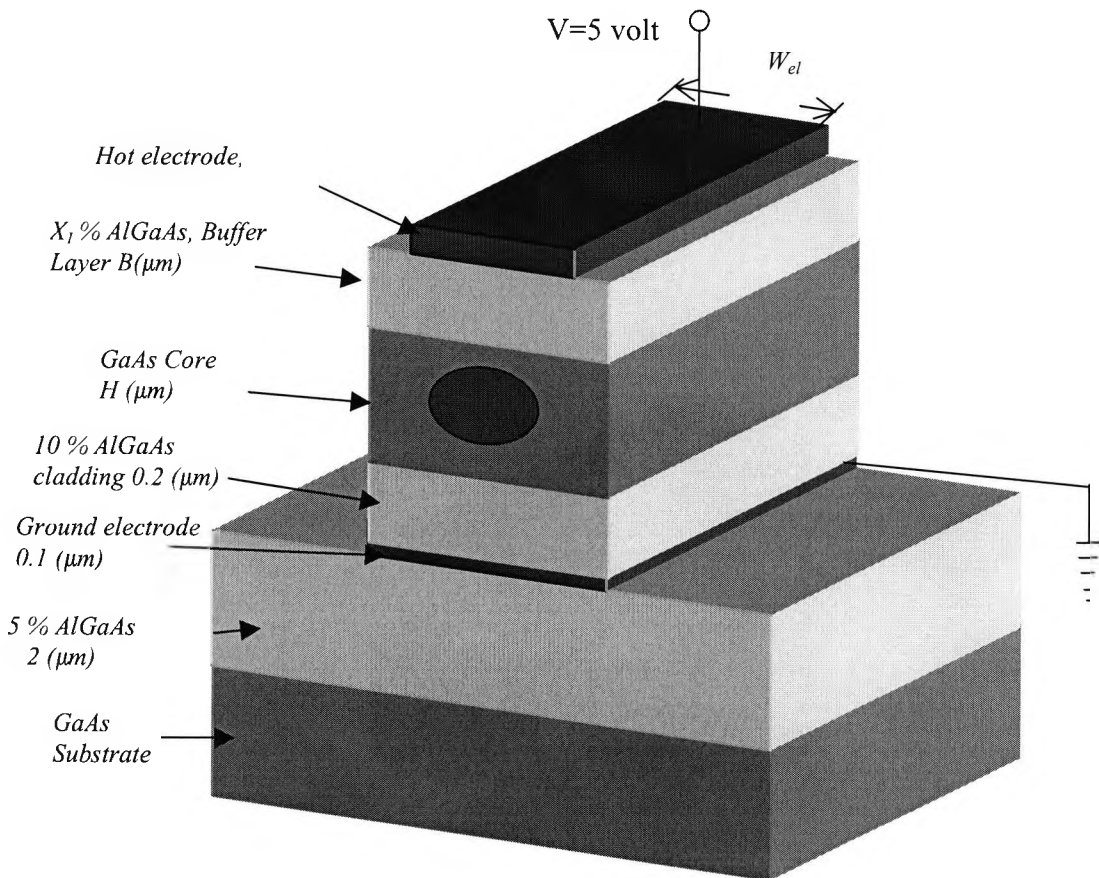


Fig. 8.1 Deeply-etched AlGaAs/GaAs semiconductor electrooptic modulator.

The whole structure is deposited on the very thick insulating GaAs substrate. In these cases a $0.1 \mu\text{m}$ thick *highly doped* (1×10^{18})/ cm^3 GaAs layer below the lower cladding is considered as the ground electrode, with $V = 0$ placed between the 10%AlGaAs layer and the substrate, while the hot electrode, $V \neq 0$, is deposited on the top of the buffer AlGaAs layer. The waveguide width is W (μm), while the electrode width is W_{el} (μm) and the modulator operating wavelength is taken as $\lambda = 1.55 \mu\text{m}$. Deeply-etched waveguide structures are known to suffer from lower bending loss, therefore more compact system design is possible than that for the shallow-etched counterparts. Theoretically this waveguide structure is multimoded, when the waveguide width is greater than $2.5 \mu\text{m}$. However, from the practical point of view, the use of a high index of GaAs substrate leads to a situation where these higher order modes suffer very high leakage radiation losses into the substrate, while the fundamental mode shows virtually no leakage loss (Heaton, 1999), so effectively behaving like a single-moded guide.

In this research work the deeply-etched semiconductor electrooptic modulator is theoretically investigated. As far as fabrication procedure is concerned, it is assumed to be similar to the deeply-etched waveguide fabrication (Heaton, 1999), where the wafers were grown by both metallorganic vapour phase epitaxy (MOVPE) and molecular beam epitaxy (MBE). It is difficult to grow 1%AlGaAs by MOVPE procedure, because in some reactors this procedure involves using an aluminium precursor gas flow rate which is very close to the limit. Therefore, the core in wafer design which is grown by MOPE is 5%AlGaAs, rather than GaAs, to achieve the required small core/cladding index step with greater accuracy. Most of the AlGaAs alloy concentration compositions are not very critical, which is an advantage of this deeply-etched waveguide. The upper cladding B (μm) is used to keep the light away from any possible attenuating metal (gold) electrodes on the top of the surface of the guide, which usually does not need very accurate Al mole fraction and thickness. The core, H (μm), is usually undoped GaAs with its refractive index well defined, and has not much effect on the number of horizontal modes supported. First $0.1 \mu\text{m}$ and second $0.1 \mu\text{m}$ lower claddings Al mole fraction are also not critical and is not difficult to fabricate. In particular they have to be thick enough to prevent too much light leaking from the fundamental mode into substrate.

The only critical parameter in designing this deeply-etched waveguide is to determine guide width for a given wafer.

The waveguide pattern is formed on each wafer in photoresist using the standard photolithography and then etched using SiCl₄ RIE machine. This machine (RIE) has a laser reflectometer attachment which can detect changes from one AlGaAs alloy composition to another during the etching process. After etching and removing the resist, a Dektak surface profile measurement has to be used to determine the etched depth. In order to give chips with high-quality input and output faces, the wafer has to be skipe-scribed and cleaved.

X₁(%) Al mole concentration on the (%GaAs)	Optical refractive index n
GaAs or 0%	3.376
5%	3.353
6%	3.346
9%	3.334
10%	3.329
11%	3.324
15%	3.305
20%	3.281
25%	3.256
30%	3.232
40%	3.183
50%	3.158
60%	3.134
70%	3.109
80%	3.084

Table 8.1 Al mole concentration on the %GaAs composition.

The AlGaAs alloy composition is calculated from;

$$\varepsilon_{STAT} = 13.18 - 3.12 \cdot X_1\% \quad (8.1)$$

Where, $X_1\%$ is the percentage of the Al mole concentration, however the optical refractive index for the corresponding value of $X_1\%$ is taken from the Table 8.1.

8.3 Velocity matching techniques for the semiconductor electrooptic modulator

In this research work, a newly proposed structure for a deep-etched electrooptic modulator is employed where the velocity matching is achieved by introducing a tantalum pentoxide, Ta_2O_5 , coating which has a high relative dielectric constant at the microwave frequency, $\varepsilon_r = 27$, but a low refractive index at the optical frequency, $n=2.03$ (Khan, 1993). Tantalum pentoxide (Ta_2O_5) has been investigated over the past decade, and is a low-absorption material, suitable for optical coating. Previously Khan *et al.* 1993 have reported velocity matching by using a Ta_2O_5 coating. However, as they used the less flexible finite difference approach with a regular grid, the solution accuracy they achieved was rather limited. The bandwidth of a high-speed optical modulator is primarily limited by the velocity mismatch between the optical carrier wave and the modulating microwave signal. For high-speed modulators, when velocity matching is achieved, the next limiting factor is the overall microwave propagation losses. At lower operating frequencies, the electrode conduction loss, α_C , dominates; however, as the operating frequency is extended beyond 40 GHz, the dielectric loss, α_d , is expected to play an increasingly important role in the bandwidth determination (Haxha, 2002, Haxha, 2003). In practical applications, the characteristic impedance, Z_C , of the electrode also affects the performance of a high-speed modulator, which is typically matched to an external circuit of impedance 50Ω .

Various attempts have been made to achieve velocity matching, such as by placing a GaAs superstrate over the GaAs (Nees, 1989) travelling-wave modulator, where the

velocity of the electrical signal is reduced to that of optical signal. The same structure is investigated in this study shown in Fig. 8.2.

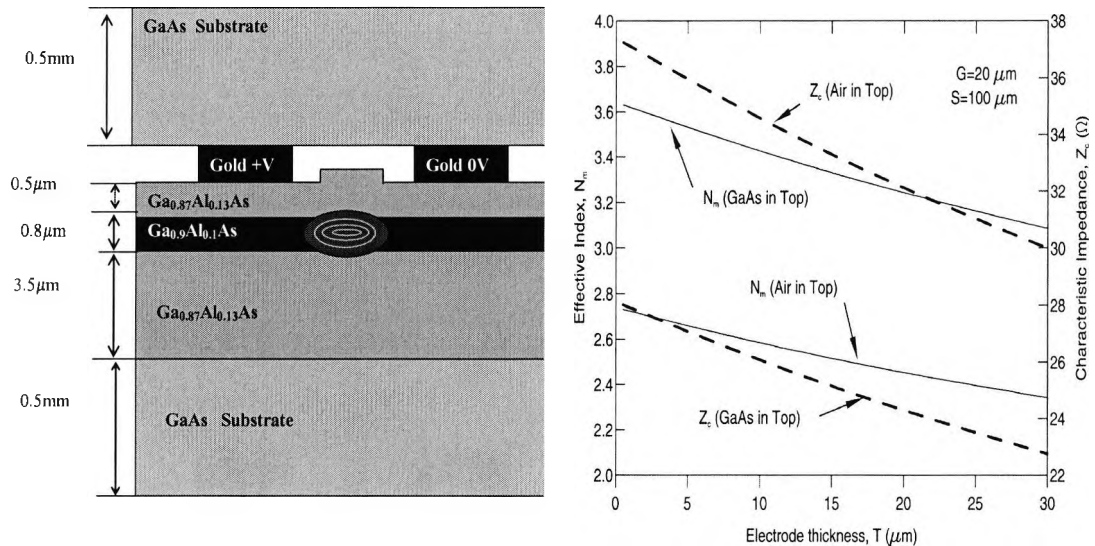


Fig. 8.2 a) Cross section (Nees, 1989) of the GaAs electrooptic modulator and b) variation of the effective index, N_m and characteristic impedance, Z_c , with electrode thickness, T , with and without GaAs substrate placed in top of the structure.

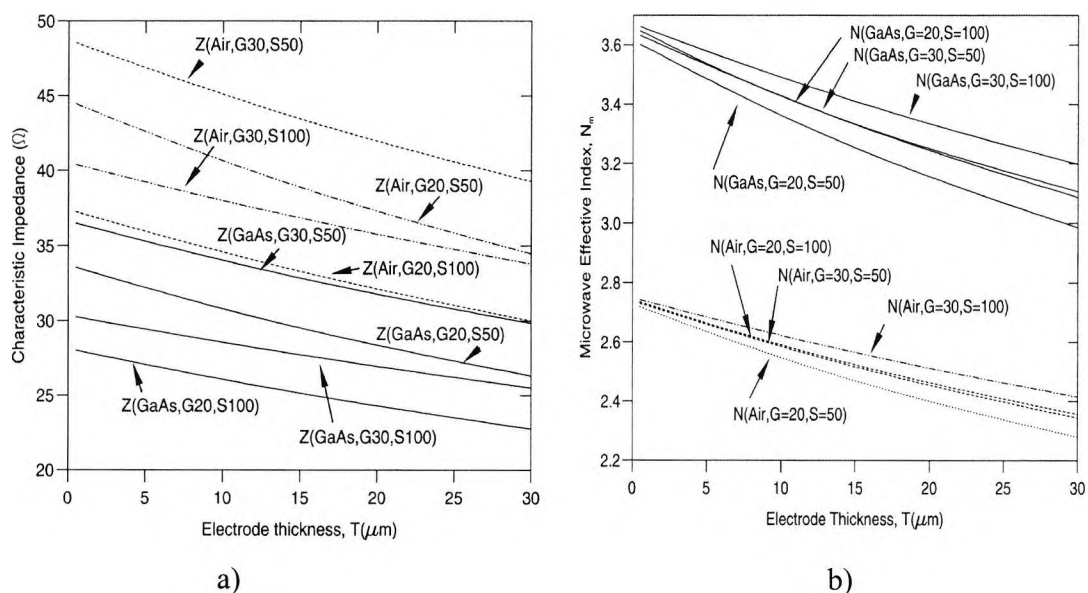


Fig. 8.3 Variation of the characteristic impedance a) and microwave index b) with electrode thickness for different value of gap between electrodes, G , and electrode width, S , when GaAs substrate is placed in top of the structure.

The effect of the substrate GaAs layer placed on the top of the structure on the microwave effective index and characteristic impedance can be seen in Fig. 8.2 and Fig. 8.3. Further investigation on this structure (Nees, 1989) has been done with respect to velocity matching for various electrode thickness, T , electrode width, S , and gap between electrodes, G , as illustrated in Fig. 8.3. It can be seen that velocity matching can be achieved easily, when the GaAs substrate is placed on top of the structure, however the characteristic impedance deteriorates. Also the value of Z_C can be slightly improved for smaller electrode width, S . Our simulated results agree with the experimental results reported by Nees, 1989. A similar idea has been employed in this research on deeply-etched electrooptic modulator, but with different coating thickness material. However earlier experimental work reported (Nees, 1989) indicates that the product of the half-wave voltage length product $V_\pi L$, was too high, at 288 V. For the comparison reason our result simulation on $V_\pi L$ was 285 V which agrees well with their work. Their (Nees, 1989) simulation results did not match with experimental one.

The use of slow-wave electrodes, fabricated on undoped epitaxial layers by Spikerman *et al.* (1996) has enabled the achievement of near velocity matching, with an impedance Z_0 of $46 \pm 1 \Omega$, a bandwidth greater than 40 GHz and a value $V_\pi L$ product of 16.8 V. Another approach which combines p-i-n and coplanar features has also been reported by Tan *et al.* (1990) with a bandwidth up to 15 GHz. A travelling wave modulator with bandwidth around 50 GHz and a value of V_π in the region of 10 volts at 1300nm has been reported by Walker (1994) in which the velocity matching was achieved by means of a loaded (slow-wave) transmission-line. Recently Craig *et al.* (1997), reported a technique to deposit an amorphous hydrogenated silicon cover on the coplanar electrical waveguide of the electrooptic modulator, where the silicon acts as both a cladding for the optical waveguide and a slow-wave structure to the electrical signal and the approximate value of the bandwidth has been measured as 20 GHz, with the switching voltage being 54 Volts at $1.55 \mu\text{m}$ and showing a velocity matched intersection length of 8.3 millimeters.

To date, most of the work reported has focused only on obtaining the velocity matching condition as one of the essential aims of the design process. For the next generation of

ultra-high-speed modulators, it is necessary to optimize the electrode structures to achieve simultaneous matching of the velocity and impedance along with a reduced overall microwave loss. In this research work, using the numerically efficient and versatile finite element method, for a new proposed structure of deep-etched electrooptic modulator, the velocity matching is achieved by introducing a coating of tantalum pentoxide, Ta_2O_5 . Besides the calculation of the dominant conductor loss, α_C , the dielectric loss α_d , which is not small for a high-speed modulator, has also been calculated and its effect of the bandwidth estimation is illustrated. Numerically simulated results are shown for the deep-etched electrooptic modulator and various types of Ta_2O_5 overlayer arrangements have been considered. Optimization of their microwave and optical characteristics are also addressed in this study.

8.4 Simulated results for deeply-etched semiconductor electrooptic modulator

The solution of the Laplace equation given under the Chapter 5 equation (5.1) is essential to calculate the potential distribution for entire deeply-etched semiconductor electrooptic modulator illustrated in Fig. 8.4.

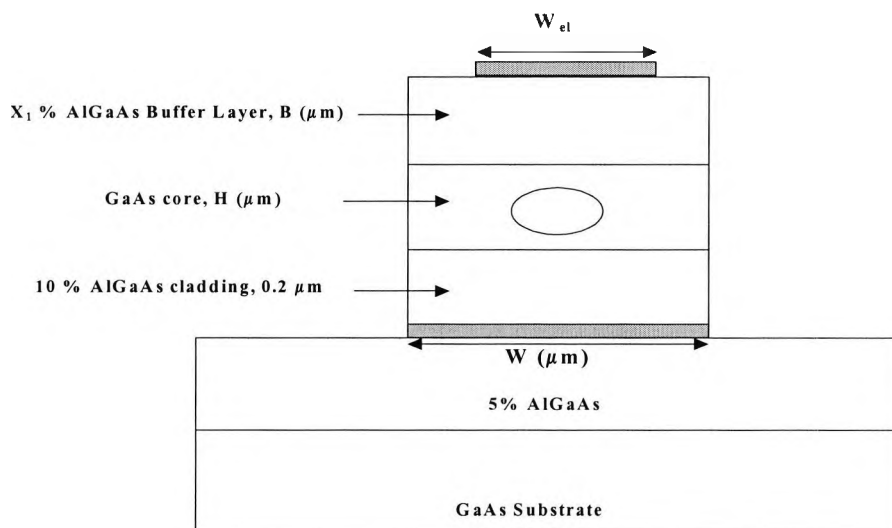


Fig. 8.4 Schematic illustration of cross section of the deeply-etched semiconductor electrooptic modulator.

Once the potential distribution is calculated, x component of the electric field, $E_x(x, y)$ can be calculated using equation (5.13). Figure 8.5 shows the contour plot of the horizontal electric field profile, $E_x(x, y)$ under the voltage applied of 5 volts, when the waveguide width is $5 \mu\text{m}$, the electrode width is $4.9 \mu\text{m}$, the core height is $1.5 \mu\text{m}$, the buffer layer thickness is $1.1 \mu\text{m}$ with its Al mole concentration of 30%.

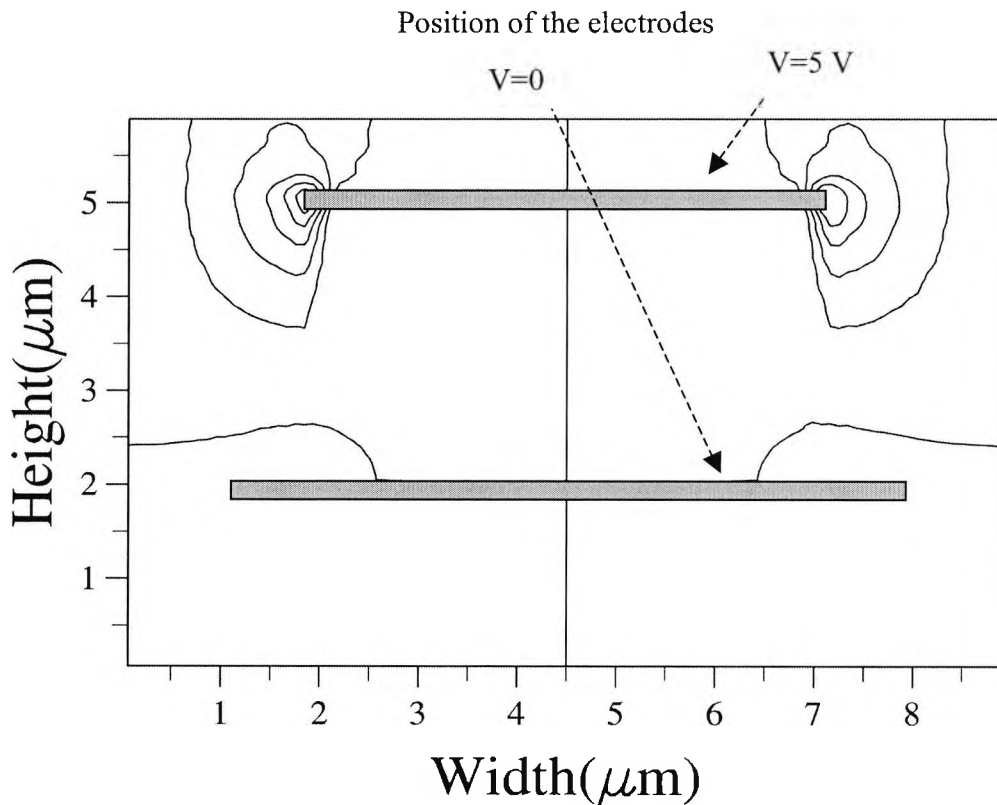


Fig. 8.5 Horizontal or x component of the electric field profile $E_x(x, y)$

It can be observed that electric field $E_x(x, y)$ is asymmetric and nearly zero in the desired waveguide region, with its maximum around the left and right corners of the hot electrode. Therefore the refractive index change on the x direction is almost zero and it can be neglected.

Contour plot of the electric field y component is illustrated in the Fig. 8.6. It should be noted that the electric field $E_y(x, y)$ is heavily concentrated and symmetric, nearly uniform to the desired core waveguide region. The vector field profile would be nearly

vertical, except close to the left and right edges of the hot electrode. According to the equations (5.13), (4.42) and (4.43), H^y or E^x modes are mainly affected due to refractive index change in the x direction.

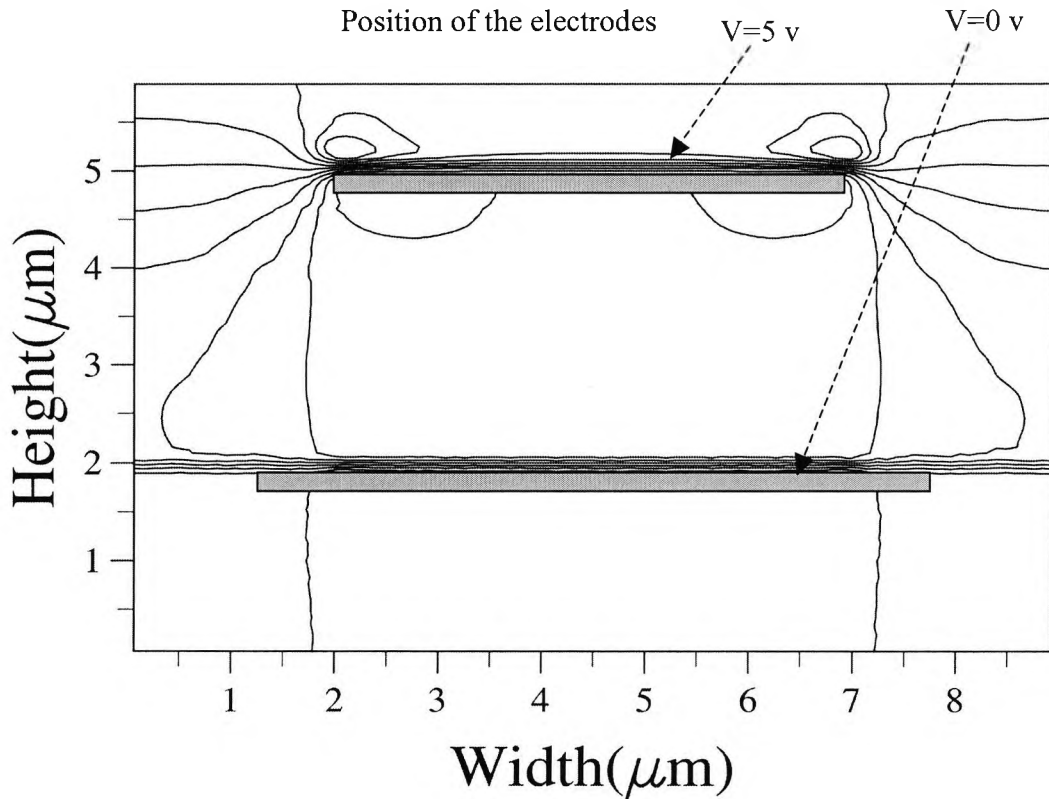


Fig. 8.6 Vertical or y component of the electric field $E_y(x, y)$

It would appear that the refractive index change is according to the equation (4.42) Δn_{xx} which is directly proportional to y component of the electric field $E_y(x, y)$. On the other hand the H^x or E^y modes are directly related to the refractive change in the y direction, Δn_{yy} , which in this case is zero. This is the reason why only the H^y mode (quasi-TE) will be considered throughout this research work. If an asymmetry has been brought to the structure, then the horizontal field component E_x will not be symmetric, which gives rise to a nonzero Δn_{xy} , an off-diagonal refractive index component which will cause a coupling between the two orthogonal TE and TM modal states. Due to the restriction of the thesis length, optical field profiles and refractive change index will not be shown here for V=5 voltage.

Variation of the half-wave voltage length product, $V_{\pi}L$, with buffer layer thickness, B , for different values of the Al mole concentration, X_l of the buffer layer, are illustrated in Fig. 8.7. The value of the waveguide width W in this case is $5 \mu\text{m}$, the electrode width, W_{el} is $4.9 \mu\text{m}$, and the core height H is $1.5 \mu\text{m}$.

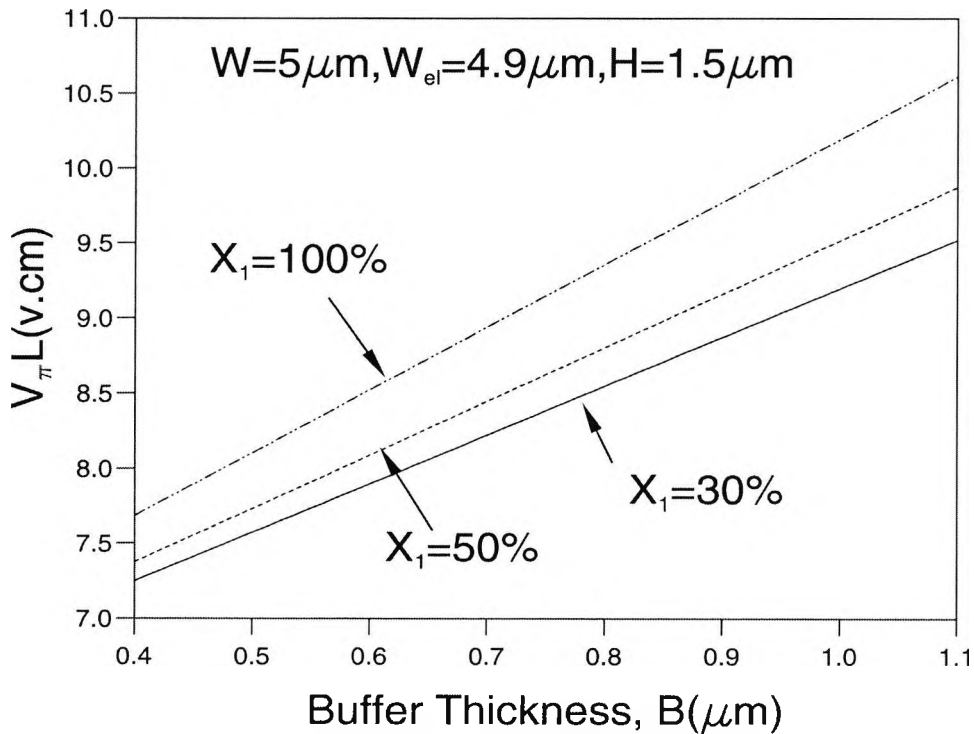


Fig. 8.7 Variation of the $V_{\pi}L$ product with buffer layer thickness for different values of Al mole concentration of the buffer layer, X_l .

It can be seen that when the buffer layer thickness B is increasing the product $V_{\pi}L$ is also increasing. For a given value of buffer layer thickness, B , the product $V_{\pi}L$ is slightly increased as X_l increases from 30% to 50% and to 100%. In particular, when the buffer layer thickness, B , is $0.4 \mu\text{m}$, $V_{\pi}L$ increases from $7.3 \text{ V}\cdot\text{cm}$ to $7.4 \text{ V}\cdot\text{cm}$ and then to $7.7 \text{ V}\cdot\text{cm}$, when X_l increases from 30% to 50% and to 100% respectively, this indicates that at this stage the aluminum concentration of the buffer layer thickness has only a smaller influence on the design of optical modulators.

Next the variation of the microwave index, N_m and the microwave characteristic impedance, Z_C , with the buffer layer thickness, B , for two different values of the core

height, H , are illustrated in Fig. 8.8. The waveguide width, W , the electrode width, W_{el} , the Al mole concentration of the buffer layer, X_I , and the electrode thickness, T , are $5\ \mu\text{m}$, $4.9\ \mu\text{m}$, 30% and $0.1\ \mu\text{m}$, respectively. Although the present model can deal with electrodes of finite conductivities, as a reasonable approximation, however, the doped semiconductor ground lower electrode has been considered as a perfect conducting metal electrode in order to simplify the calculations.

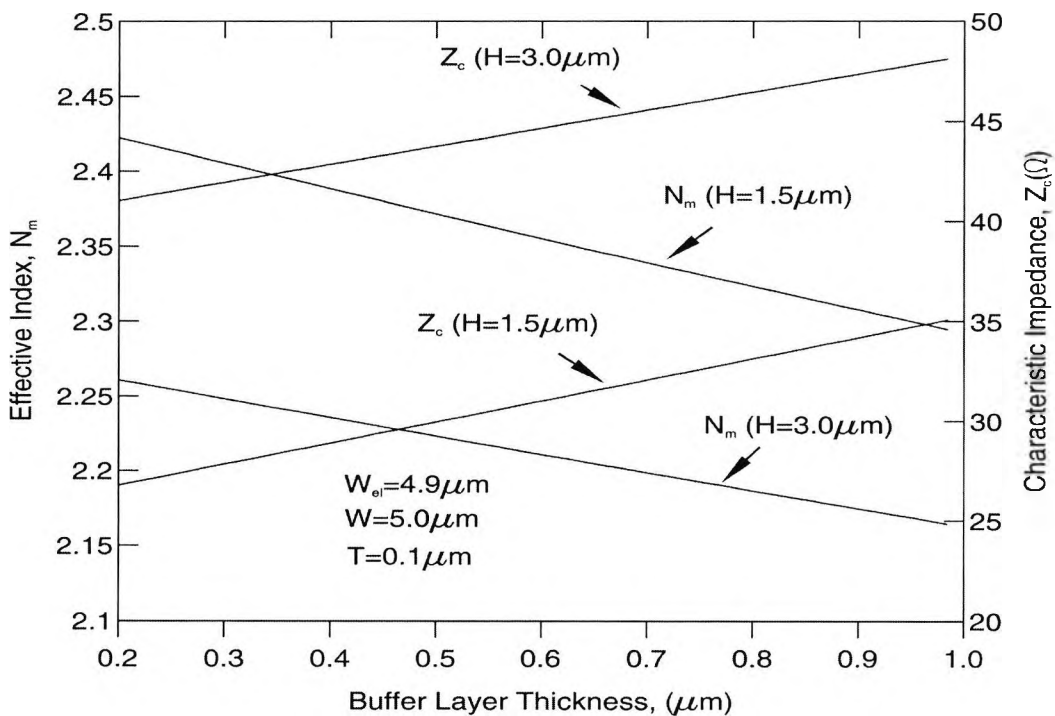


Fig. 8.8 Variation of microwave index N_m and characteristic impedance Z_C with buffer layer thickness B for two different values of the core height H .

It can be seen that microwave index, N_m , reduces linearly, while the characteristic impedance, Z_C , increases linearly with the increase in the buffer layer thickness, for both values of core height, H . For velocity matching between the microwave and optical signals, the value of N_m should be equal to the value of the effective index of the optical fundamental mode, H_{11}^v , (n_{eff}), while the impedance matching should be equal to $50\ \Omega$. If the electrode thickness is increased then the conductor loss will reduce; however the

optical and microwave signals will deteriorate. At this stage, for these particular modulator parameters, matching between optical and microwave signals is not possible. In this research work, using the numerically efficient and versatile finite element method, for a new proposed structure of deep-etched electrooptic modulator, the velocity matching is achieved by introducing a coating of tantalum pentoxide, Ta_2O_5 as illustrated in the Fig. 8.9.

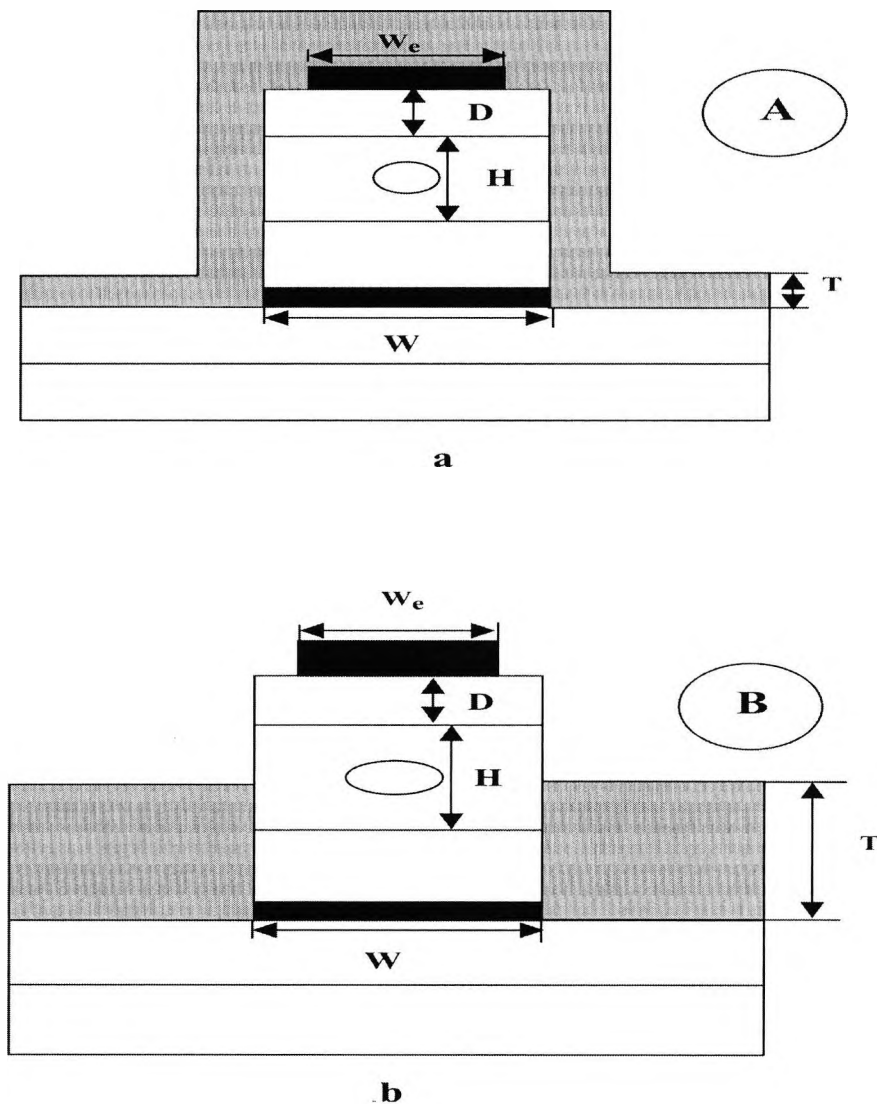


Fig. 8.9 Schematic diagrams of a deep-etched GaAs/AlGaAs of the semiconductor electrooptic modulators for two types of the Ta_2O_5 over layers arrangements, *A* and *B*.

The waveguide layers for the design of our deep-etched waveguide structure considered here are shown in Fig.8.9. Etching through the upper cladding layer, the waveguide core and part of the lower cladding gives a very strong horizontal confinement of the light, and as a result the bending loss reduces, as does the crosstalk, the background scatter at the output surface (Heaton, 1999). The waveguide width, W , and its core thickness, H , are taken as $5 \mu\text{m}$ and $1.5 \mu\text{m}$ respectively. The upper cladding (buffer) thickness, D , is varied, but the lower cladding thickness is taken as $0.5 \mu\text{m}$. The hot electrode width W_e is $4.9 \mu\text{m}$ with its conductivity of $\sigma=4.1 \times 10^7 \text{ s/m}$. The refractive indices of the core, the upper layer, and the lower cladding are taken as 3.37, 3.322 and 3.329, respectively at the operating wavelength $\lambda=1.55 \mu\text{m}$. Two types of tantalum pentoxide, Ta_2O_5 overlayers arrangement structures have been investigated, designated A and B , shown in Fig.8.9. In the structure A , as shown in Fig. 8.9. a, tantalum pentoxide is deposited all around the mesa. In the structure B , as shown in Fig. 8.9. b the Ta_2O_5 thickness is deposited on the two sides of the mesa. In these cases a $0.1 \mu\text{m}$ thick *highly doped* ($1 \times 10^{18} \text{ /cm}^3$) GaAs layer below the lower cladding is considered as the ground electrode.

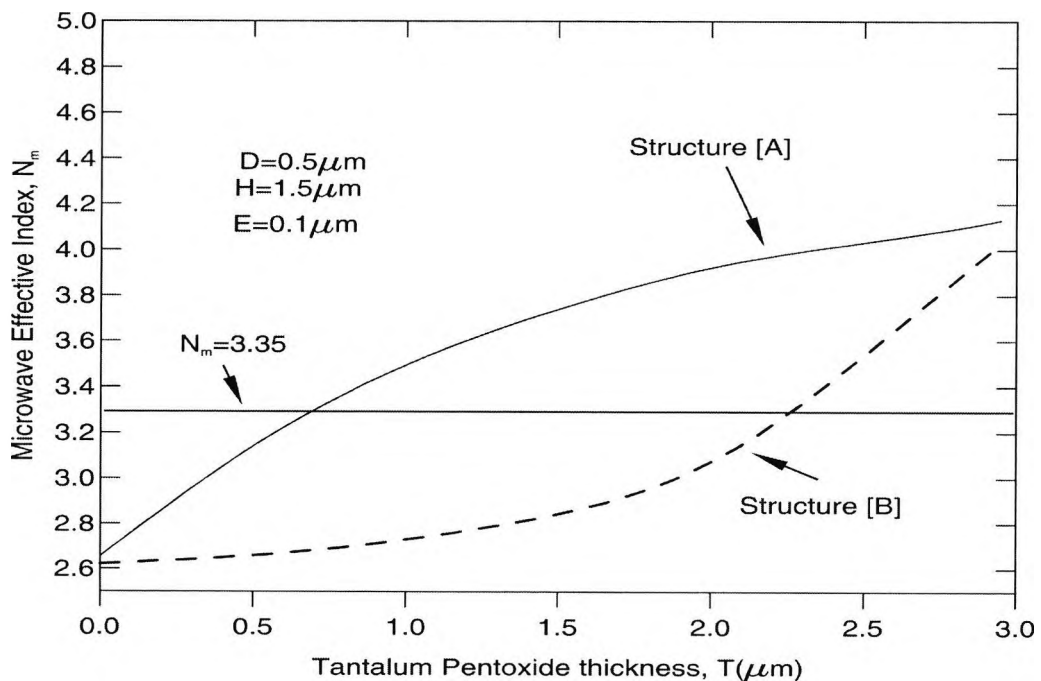


Fig. 8.10 Variation of microwave index, N_m with Ta_2O_5 for the structures A and B .

Fig. 8.10 shows the variation of microwave effective index N_m , with the Ta_2O_5 coating thickness for the structures A and B . Buffer layer thickness, D , core thickness, H , and electrode thickness, E , are set to values of $0.5 \mu\text{m}$, $1.5 \mu\text{m}$ and $0.1 \mu\text{m}$, respectively. It can be observed that when the coating thickness of the Ta_2O_5 is increased, the microwave effective index is significantly increased, for both the cases studied here. The required coating thicknesses, for velocity matching for structures A and B , are $0.75 \mu\text{m}$ and $2.25 \mu\text{m}$, respectively. However, the numerical simulations in this work indicate, (but they are not shown here) that it is not possible to reduce the velocity mismatch significantly, even when a $5.0 \mu\text{m}$ thick layer of Ta_2O_5 is deposited *only* on the top of the hot electrode. For a given structure the optical effective index N_0 can be calculated accurately by using an optical modal solution approach, such as the FEM (Rahman, 1984) and depends on the waveguide parameters; however, for this study it is assumed that a typical value would be around 3.35 for the purpose of subsequent velocity matching. It is very important to note that for the structure A the required Ta_2O_5 coating thickness to achieve velocity matching is smaller compared to the structure B .

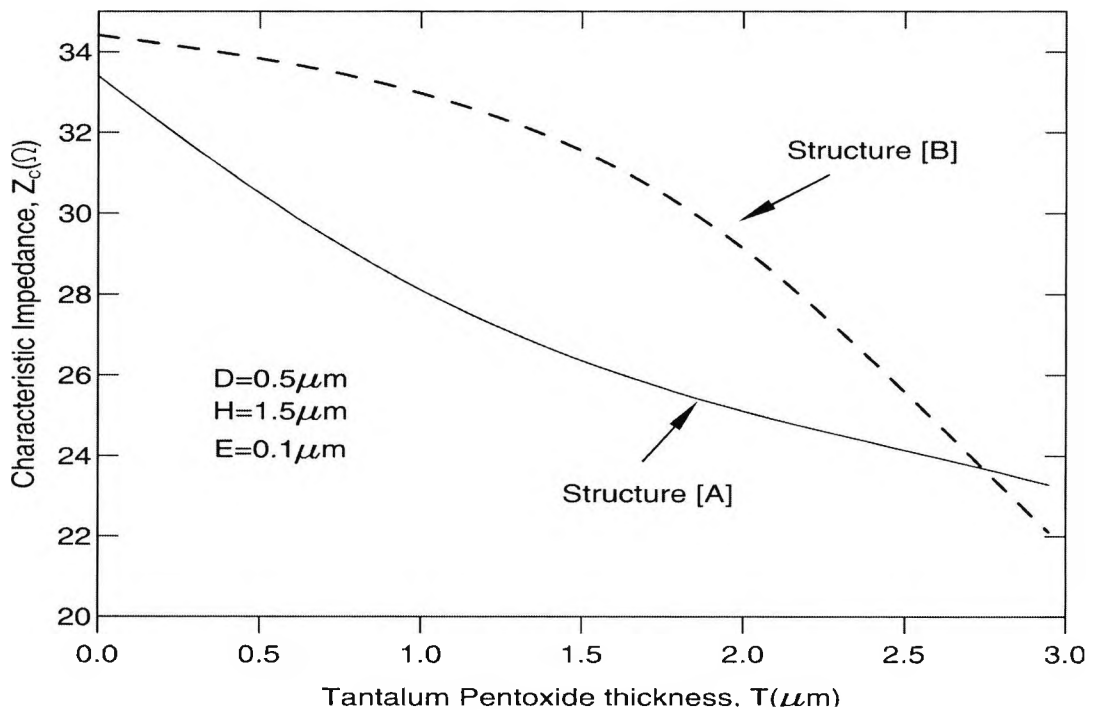


Fig. 8.11 Variation of characteristic impedance, Z_C with coating thickness, Ta_2O_5 for the structures A and B .

The overlayer with a high dielectric constant of the Ta_2O_5 material increases the concentration of the electric field in the epitaxy layers, more specifically in the core region and the upper cladding. By contrast, in the structure *B*, this phenomenon is more visible when the coating thickness on the side starts to submerge the core region.

The characteristic impedance also plays an important role in the performance of the electrooptic modulators. Variations of their characteristic impedances, Z_C , with the Ta_2O_5 coating thickness are shown in Fig. 8.11 for both structures, *A* and *B*. However as the Ta_2O_5 thickness increases, unfortunately, the characteristic impedance also reduces. For the range considered here, it can be noticed that in both these cases Z_C is not matched. The results show that when the coating thickness Ta_2O_5 is adjusted to match the wave velocities, the corresponding values of the characteristic impedance are reduced to 29Ω and 26.5Ω for structures *A* and *B* respectively.

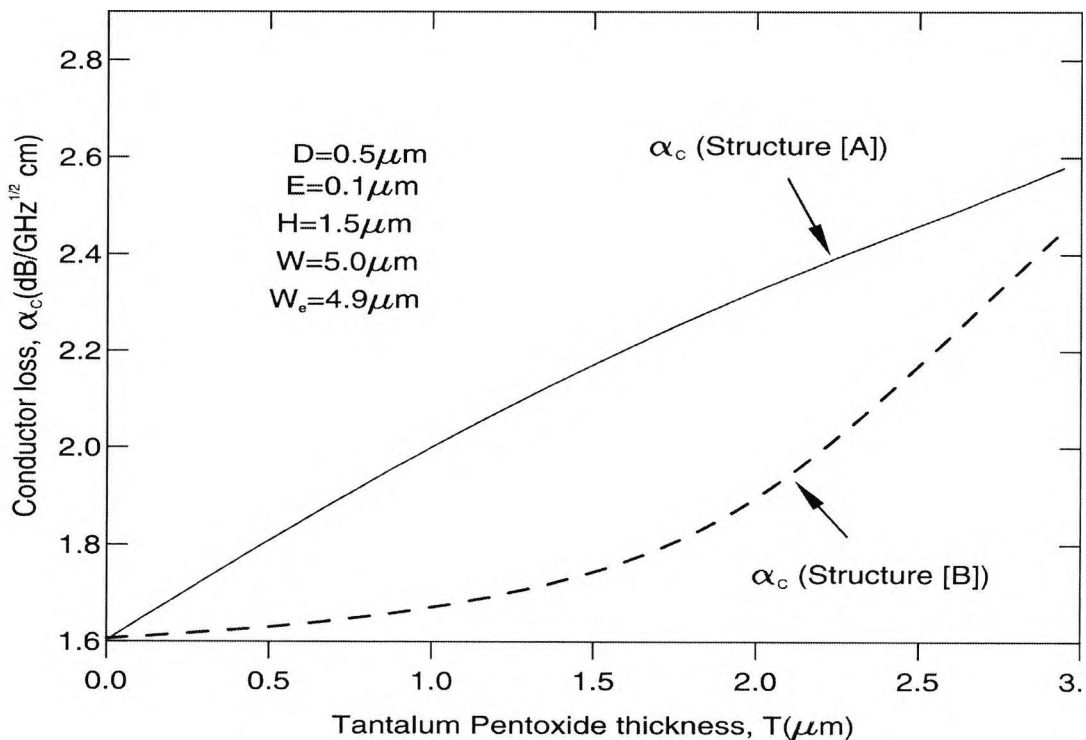


Fig. 8.12 Variation of the conductor loss, α_c for two structures *A* and *B*.

The low value of Z_C would adversely effect the optical bandwidth. By varying the different parameters of the structure, impedance matching may be achieved.

For high-speed modulators, where velocity matching is achieved, then the overall modulator bandwidth depends on the total microwave loss. The conductor loss depends strongly on the electrode thickness, E , and reduces considerably when a thicker electrode is used. Variations of the conductor loss, α_c , (normalized at 1 GHz), with the Ta_2O_5 coating thickness, are shown in Fig. 8.12 for the structures, A and B . The frequency-dependent surface resistance, R_s , for gold is calculated from its conductivity, σ ($= 4.1 \times 10^7 \text{ S/m}$). It can be observed that for a given value of the electrode thickness, $E=0.1 \mu\text{m}$, the conductor loss increases as the Ta_2O_5 coating thickness is increased for both the structures presented in this paper. When the coating thickness is adjusted to achieve velocity matching the corresponding conductor losses are $1.91 \text{ (dB}/\sqrt{\text{GHz}\cdot\text{cm}}$) and $2.074 \text{ (dB}/\sqrt{\text{GHz}\cdot\text{cm}}$) for structures A and B respectively. For the case where only the hot electrode is covered by a coating of thickness of $3 \mu\text{m}$ (not shown here), the conductor loss is increased to almost $2.4 \text{ (dB}/\sqrt{\text{GHz}\cdot\text{cm}}$).

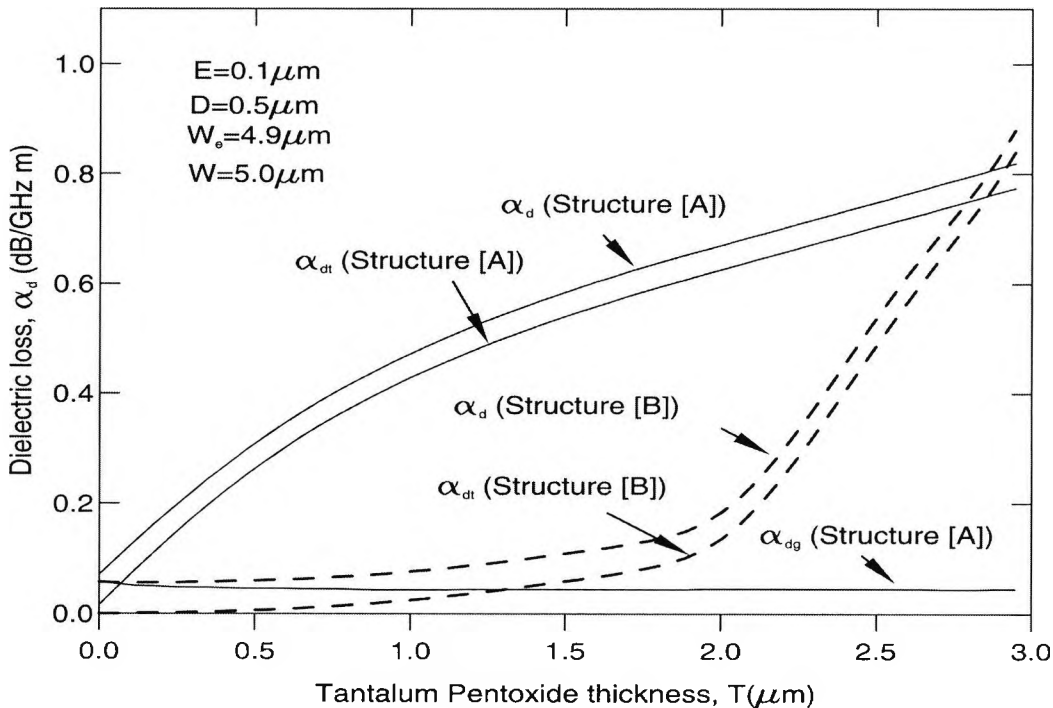


Fig. 8.13 Variation of the dielectric losses, α_d , α_{dg} , and α_{dt} , with the coating thickness, Ta_2O_5 for the structures, A and B .

Variations of the dielectric losses, with the Ta_2O_5 coating thickness, are shown in Fig. 8.13. Dielectric losses in the Ta_2O_5 , and $\text{GaAs}/\text{Al}_x\text{Ga}_{1-x}\text{As}$ layers and also the total dielectric losses are shown as α_{dg} , α_{dt} , and α_d , respectively. In this research, the loss tangent values for GaAs and Ta_2O_5 are taken as 0.0003 (Wu, 1991) and 0.053 (Khan, 1993), respectively. Dielectric losses are shown by solid lines and dashed lines for the structures *A* and *B* respectively. In this case the buffer layer thickness, D , and the electrode thickness, E , are set to $0.5 \mu\text{m}$, and $0.1 \mu\text{m}$ respectively. It can be observed that when the coating thickness is increased the dielectric loss in Ta_2O_5 , α_{dt} , is increased, whereas the dielectric loss, in $\text{GaAs}/\text{Al}_x\text{Ga}_{1-x}\text{As}$, α_{dg} , is slightly reduced. For both structures the total dielectric losses, α_d start to increase when the coating thickness of Ta_2O_5 is increased. It should be noted that most of the dielectric loss arises due to the higher loss tangent value used for Ta_2O_5 in this study.

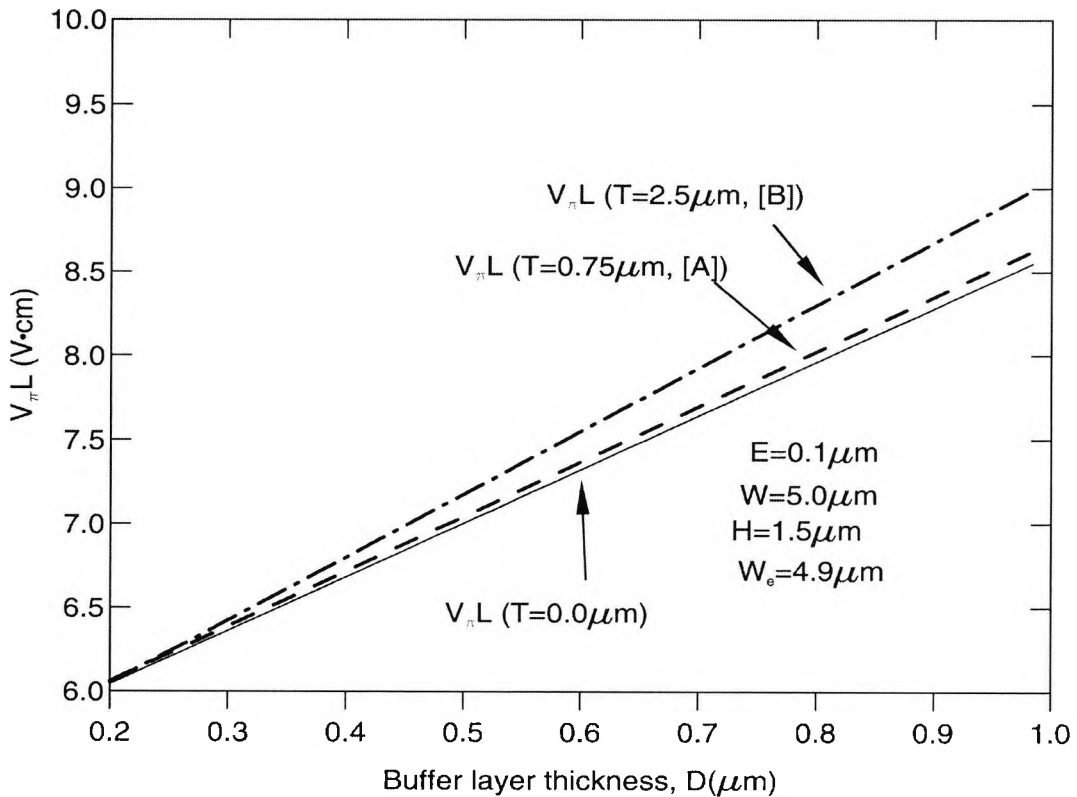


Fig. 8.14 Variation of the product $V_{\pi}L$ with buffer layer thickness, D , for coating thickness, $T=2.5 \mu\text{m}$, $T=0.75 \mu\text{m}$ and $T=0.0 \mu\text{m}$ for the structures, *A* and *B*.

The product, $V_{\pi}L$, of the length (L) and the half-wave voltage V_{π} is a key parameter in the design of an optical modulator. Fig. 8.14 shows the variation of the half-wave voltage length product, $V_{\pi}L$, with the buffer layer thickness, D , when the Ta_2O_5 coating thickness is adjusted to achieve velocity matching, at $0.75 \mu\text{m}$ and $2.5 \mu\text{m}$ for structures A and B respectively. In this case the core height, H , the electrode width, W_e , the waveguide width, W , and the electrode thickness, E , are set to $1.5 \mu\text{m}$, $4.9 \mu\text{m}$, $5.0 \mu\text{m}$ and $0.1 \mu\text{m}$, respectively. The effect of the Ta_2O_5 coating thickness on the half-wave voltage length product, $V_{\pi}L$ has been shown in this figure. It can be observed that when the buffer layer thickness, D , is increased the product, $V_{\pi}L$ is also increased, for both structures A and B . When the buffer layer thickness, D , is increased the overlap between the applied modulating field and the optical field is reduced as the optical field is pushed further down, away from the hot electrode. Hence as the buffer thickness, D , is increased, in order to maintain the 180° phase difference between the two waveguide branches of the MZ, the value of the applied voltage should be increased, leading to a linear increase of the half-wave voltage product, $V_{\pi}L$, as shown in Fig. 8.14. For the structure B , under velocity matching conditions, the product $V_{\pi}L$ is slightly increased compared with structure A as result of the thicker Ta_2O_5 coating needed to achieve phase matching and presented here with a dash-dotted line. The dashed line shown in this figure presents the variation of the product $V_{\pi}L$ with the buffer thickness, D , for the structure A . When the Ta_2O_5 coating thickness has been replaced with air, the product $V_{\pi}L$ has been slightly reduced, as shown here by the solid line. It is very important to note that the effect of the Ta_2O_5 coating thickness on the $V_{\pi}L$ product is very small, which makes it a promising material to achieve velocity matching without compromising its $V_{\pi}L$ values. The effect optical of Ta_2O_5 coating thickness is small due to its small optical refractive index of 2.03 compared to that of the $\text{GaAs}/\text{Al}_x\text{Ga}_{1-x}\text{As}$ layers used in the modulator. It is possible to conclude that by using the Ta_2O_5 coating, the optical properties of the semiconductor electrooptic modulator will remain similar. In practical terms, when the buffer thickness, D , is $0.2 \mu\text{m}$ the product $V_{\pi}L$ is $6.02 \text{ (V}\cdot\text{cm)}$, which is a very satisfactory value: however such a low buffer thickness could increase the optical loss of the modulator waveguides.

Variations of N_m and Z_c with the buffer layer thickness D for the coating thicknesses, of $0.75 \mu\text{m}$, and $2.5 \mu\text{m}$ are shown in Fig. 8.15 for structures A and B by dashed and dashed-dotted lines, respectively.

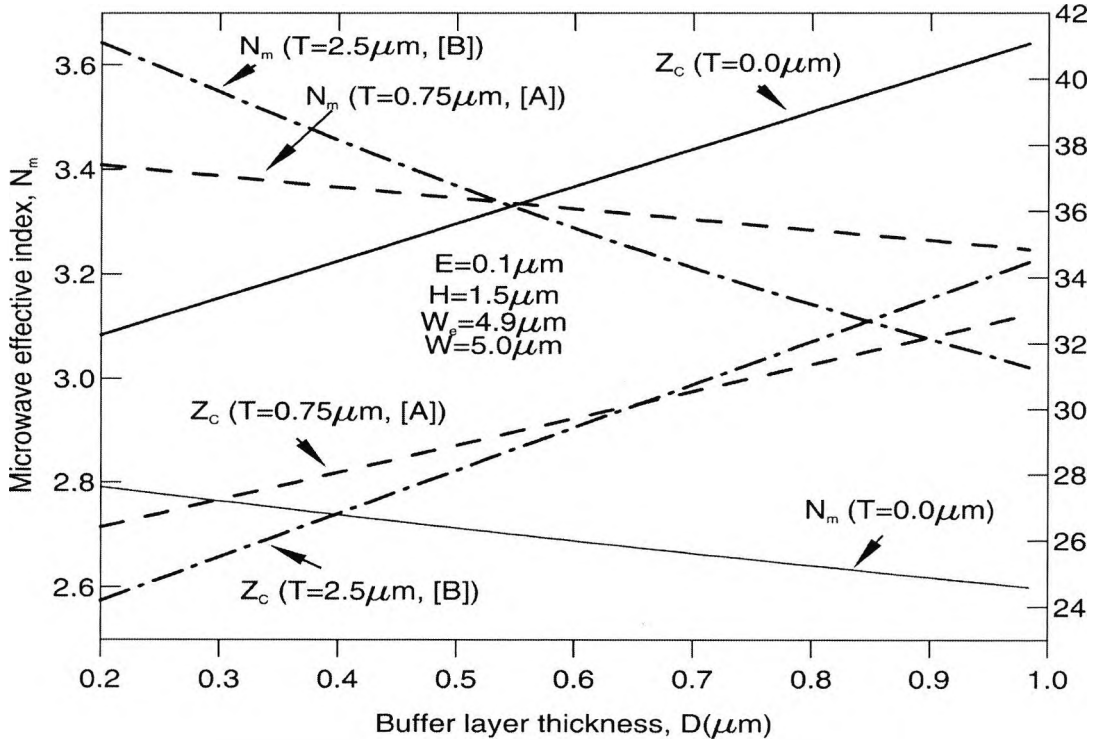


Fig. 8.15 Variation of the microwave effective index, N_m and characteristic impedance, Z_c with buffer layer thickness, D for the coating thickness, $T=2.5 \mu\text{m}$, $T=0.75 \mu\text{m}$ and $T=0.0 \mu\text{m}$ for both structures A and B .

In this case the electrode thickness, E , the core height, H , and the width of ground electrode, W_g , are set to $0.1 \mu\text{m}$, $1.5 \mu\text{m}$ and $5.0 \mu\text{m}$, respectively. It can be noted that N_m decreases when the buffer layer thickness, D , increases. It should be observed that the coating thicknesses were adjusted to obtain phase matching only for the buffer layer thickness D , equal $0.5 \mu\text{m}$. It is obvious that for a smaller value of the buffer layer thickness, D , the value of N_m can be higher than 3.35. For case A with the buffer layer thickness, D , equal to 0.2 the value of N_m is 3.41 whereas for the structure B this value is 3.62. It can be seen that in both cases N_m can be matched by adjusting the coating thickness for any given value of the buffer thickness, D . If the Ta_2O_5 coating is replaced

by air, the value of N_m would drop significantly as is shown here with a solid line. It is obvious that velocity matching *cannot* be achieved when the Ta_2O_5 coating is replaced by air. On the right hand side of this figure the variations of the characteristic impedance, Z_C with the buffer layer thickness, in both cases, A and B , with two different coating thicknesses, $0.75 \mu m$ and $2.5 \mu m$ respectively, are shown. The variation of the characteristic impedance, Z_C , for structure A at a coating thickness of $0.75 \mu m$ is presented here with a dashed line. The variation of the characteristic impedance, Z_C , for the structure B at a coating thickness of $2.5 \mu m$ is presented here with dashed-dotted line. It can be observed that when the buffer thickness, D , increases, the characteristic impedance, Z_C , also increases for both structures A and B . Impedance matching for these two structures cannot be achieved under these circumstances.

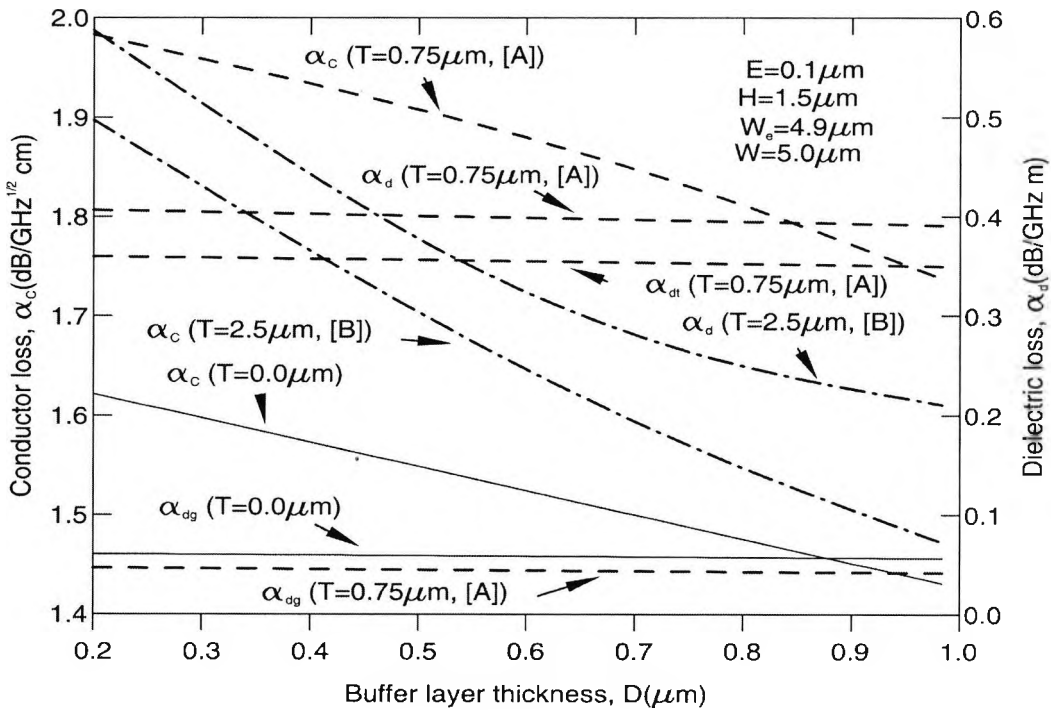


Fig. 8.16 Variation of the conductor loss, α_c , and dielectric losses, α_d , α_{dg} , and α_{dt} , with buffer layer thickness D for the coating thickness, $T=2.5 \mu m$, $T=0.75 \mu m$ and $T=0.0 \mu m$ for both structures A and B .

The variation of characteristic impedance Z_C , when the Ta_2O_5 coating is replaced by air is shown here with a solid line. In this case, it can be noted that when buffer layer thickness, D , is increased, the value of the characteristic impedance is increased significantly compared to that for the structures A and B .

The variations of the conductor loss, α_C , and dielectric loss, α_d , both normalized at 1 GHz, with the buffer layer thickness, D , are shown in Fig. 8.16. The variation of the losses for the structure A at a coating thickness of $0.75 \mu m$ is shown by a dashed line, whereas for the structure B at a coating thickness of $2.5 \mu m$ it is presented by a dashed-dotted line. The variations of the losses with the buffer layer thickness when the Ta_2O_5 coating is replaced by air are shown by solid lines. The dielectric loss in the GaAs and the Ta_2O_5 layers are shown separately to quantify the additional dielectric loss in the Ta_2O_5 coating. The dielectric losses in the Ta_2O_5 coating, in the GaAs substrate and the total loss are given by α_{dt} , α_{dg} , and α_d , respectively. It can be observed that the dominant loss factor α_C reduces as the buffer layer thickness is increased and this value is reduced significantly when the Ta_2O_5 coating is replaced by air. It can be seen that for structure A the total loss, α_d , increases slightly as the buffer layer thickness is increased. The dielectric loss in the GaAs region is almost constant as the buffer layer thickness is increased, and the dielectric loss is increased slightly when the coating thickness is replaced by air, as shown here with a solid line.

The variations of the microwave index, N_m , and the characteristic impedance, Z_C , with the electrode thickness, E , for different coating thicknesses, T , are shown in Fig. 8.17. It is obvious that when the electrode thickness, E , is increased, the microwave index, N_m , is reduced. It can be observed that when the coating thickness, T , is increased the microwave index is also increased. If the velocity matching condition is examined, it can be deduced easily, from Fig. 8.17, that for a higher coating thickness, T , a thicker electrode, E , is required to achieve the velocity matching. As an example, for the variable values of coating thicknesses, T , $0.75 \mu m$, $1.0 \mu m$, $1.5 \mu m$, $2.0 \mu m$ and $2.5 \mu m$, the corresponding required thicknesses of the electrode, E , to achieve the velocity matching are $0.05 \mu m$, $1.52 \mu m$, $4.51 \mu m$, $8.6 \mu m$ and $13.2 \mu m$, respectively. The variation of the characteristic impedance, Z_C , with the electrode thickness, E , for a coating thickness, T , of $1.0 \mu m$ and $2.0 \mu m$ are also presented in Fig.8.17, using the

dashed lines. It can be observed that this value also decreases when the electrode thickness is increased and the characteristic impedance decreases when the coating thickness is increased.

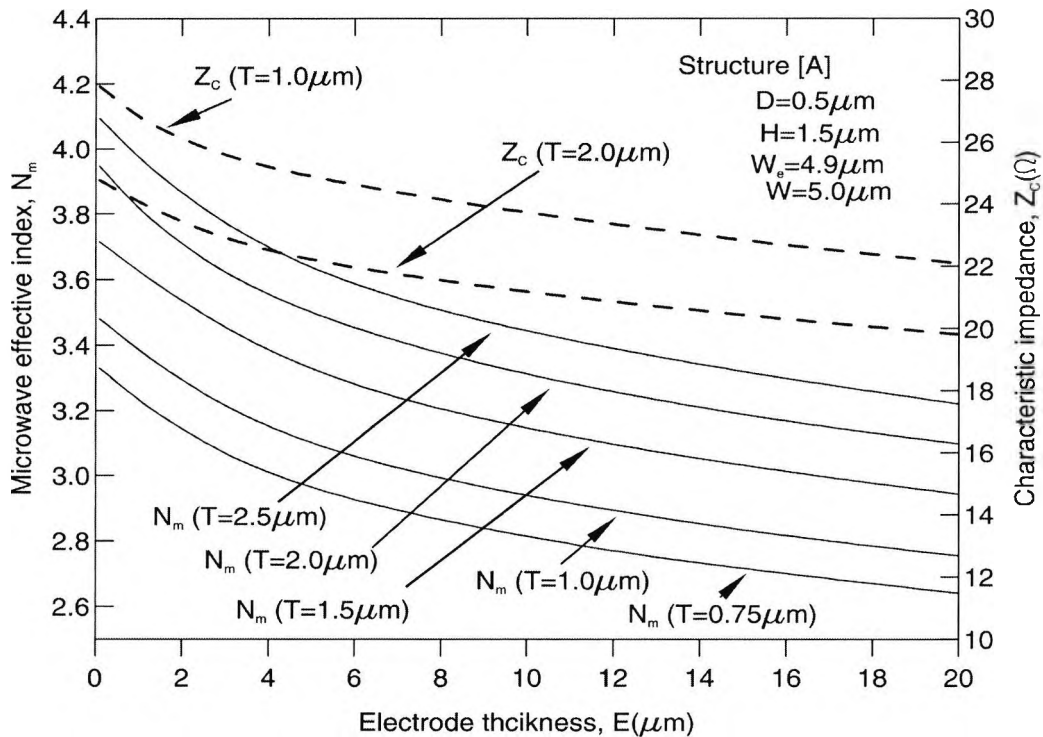


Fig. 8.17 Variation of the microwave effective index, N_m and characteristic impedance, Z_C with electrode thickness, E for the coating thickness, $T=2.5\ \mu\text{m}$, $T=2.0\ \mu\text{m}$, $T=1.5\ \mu\text{m}$, $T=1.0\ \mu\text{m}$ and $T=0.75\ \mu\text{m}$ for the structure A .

For the range considered here, N_m can easily be matched. From Figures 8.15 and 8.17 it can be seen that the simultaneous matching of both N_m and Z_C is mostly not possible by varying a *single* parameter such as the coating thickness, T , the electrode thickness, E , the core height, H , the buffer layer thickness, D , or the electrode width, W_e . On the other hand, the simultaneous matching of N_m and Z_C may be achieved by adjusting several optical parameters in tandem, but this has not been attempted in this study.

Fig. 8.18 shows the variation of the conductor loss, α_c , and the dielectric loss, α_d , both normalized at 1 GHz, with the electrode thickness, E , for different coating thicknesses, T , for the structure A . It can be observed that the conductor loss increases when the coating thickness, T , is increased. The conductor loss depends strongly on the electrode thickness, E , and reduces considerably when a thicker electrode is used.

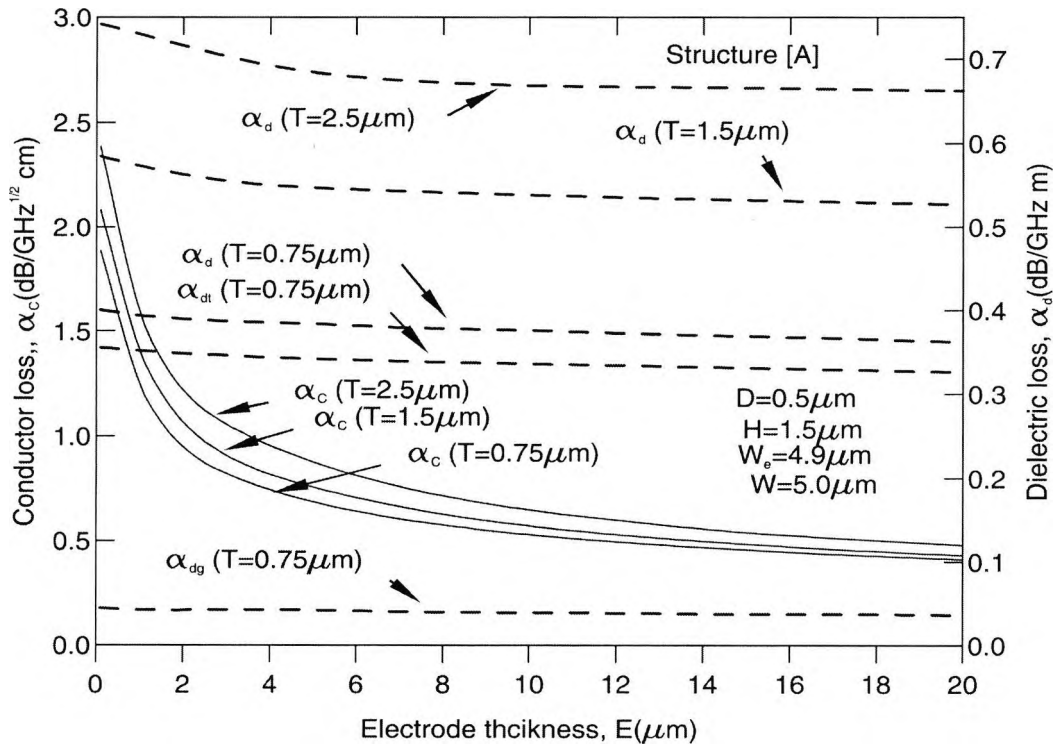


Fig. 8.18 Variation of the conductor loss, α_c and dielectric losses, α_d , α_{dg} , and α_{dt} , with electrode thickness, E for the coating thickness, $T=2.5 \mu\text{m}$, $T=1.5 \mu\text{m}$ and $T=0.75 \mu\text{m}$ for the structure A .

The conductor loss for the coating thickness $T=2.5 \mu\text{m}$ and the electrode thickness $E=0.1 \mu\text{m}$ is $2.435 \text{ dB} / \sqrt{\text{GHz}} \cdot \text{cm}$, whereas for an electrode thickness E , equal to $30 \mu\text{m}$, the conductor loss reduces to the value of $0.405 \text{ dB} / \sqrt{\text{GHz}} \cdot \text{cm}$, which is a significant reduction. In this case the other modulator parameters, such as the buffer layer thickness, D , the core height, H and the electrode width, W_e , are kept fixed, at $0.5 \mu\text{m}$, $1.5 \mu\text{m}$ and $4.9 \mu\text{m}$, respectively. In order to obtain a semiconductor electrooptic

modulator with a high bandwidth, it may be useful to use a thicker electrode to lower the conductor losses and use a higher coating thickness to achieve the velocity matching. On the other hand it can also be observed, from Fig. 8.18, that the dielectric loss, α_d , decreases slightly as the electrode thickness is increased. The dielectric loss increases as the coating thickness is increased, as a significant amount of the modulating field is confined in the Ta_2O_5 layer, which has a higher loss coefficient. The conductor loss is the dominant factor at the lower operating frequency, particularly at 1 GHz and its value is much higher compared to the dielectric loss. However, since the total dielectric loss is proportional to the operating frequency, f , compared to the conductor loss, which is proportional to \sqrt{f} , the dielectric loss, cannot be neglected for high-speed electrooptic modulators.

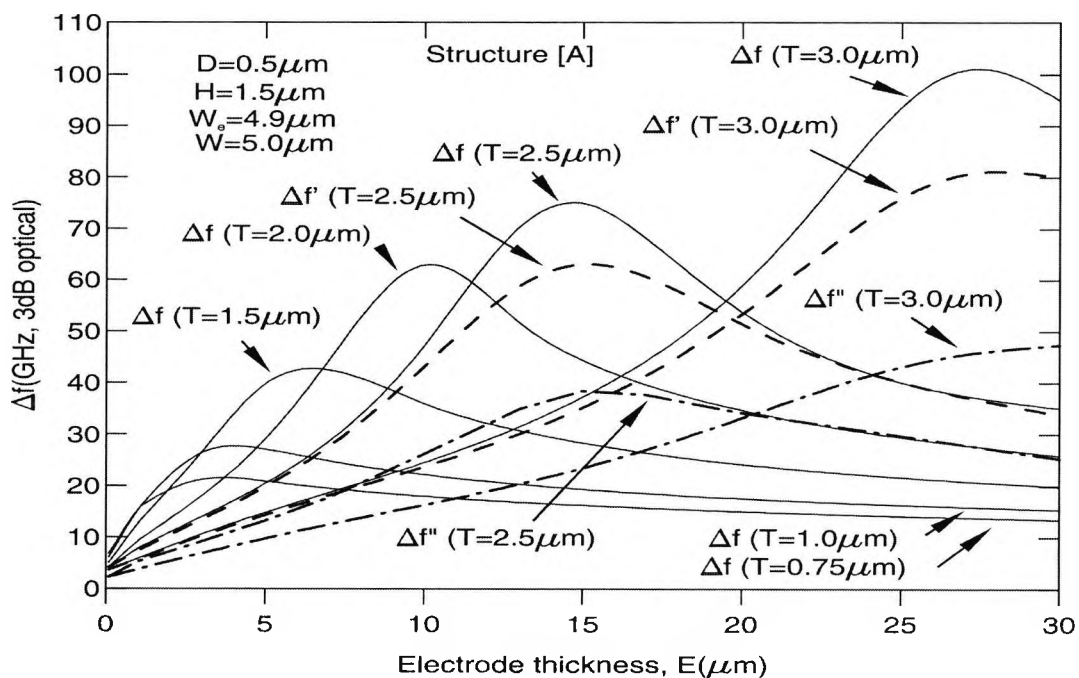


Fig. 8.19 Variation of the 3dB optical bandwidth for the structure A, with the electrode thickness, E , for coating thickness, $T=3.0 \mu\text{m}$, $T=2.5 \mu\text{m}$, $T=2.0 \mu\text{m}$, $T=1.5 \mu\text{m}$, $T=1.0 \mu\text{m}$ and $T=0.75 \mu\text{m}$.

The optical (3 dB) modulation bandwidth, Δf , is shown in Fig. 8.19 as a function of the electrode thickness, E , for different values of the coating thickness, T . In this case, the buffer layer thickness and the electrode length, L , are fixed at $0.5 \mu\text{m}$ and 1.4 cm

respectively. Variations of the optical bandwidth are shown by solid lines, when the effect of dielectric loss and impedance mismatch are ignored. It can be observed that for $T=3.0 \mu\text{m}$, when the effects of the dielectric losses, α_d , and the impedance mismatch are neglected, the bandwidth rises above 100 GHz. For a given coating thickness, the optical bandwidth reaches its maximum value when the velocity is matched for a particular electrode thickness. Besides the conductor loss, when the effect of α_d is included, the bandwidth is reduced to 80 GHz, as shown here by dashed lines, and labelled as $\Delta f'$. It can be observed that when the conductor loss, the dielectric loss and impedance mismatch are considered, the bandwidth is reduced significantly as shown here with a dashed-dotted line, and labelled as $\Delta f''$. For a coating thickness of $3.0 \mu\text{m}$, when all these parameters are considered, the maximum bandwidth is reduced to 47 GHz. In this case, the conductor loss was 3.3 (dB/cm) , the dielectric loss was 0.03 (dB/cm) at 47 GHz and the impedance $Z_c=17.3 \Omega$. It can be seen that the impedance mismatch plays a significant role in the bandwidth estimation. It is obvious that the peak value of the bandwidth occurs around the electrode thickness $E=27.5 \mu\text{m}$ for a coating thickness $T=3.0 \mu\text{m}$ where $N_m \cong 3.35$. A similar trend of the bandwidth can be explained for other coating thicknesses shown in this figure. It can be noted also that a thicker electrode is required to achieve velocity matching when a thicker Ta_2O_5 coating is used. Evidently, a thicker electrode, E , and a higher coating thickness, T , can be used to design higher performance modulators, due to the lower conductor loss when the velocities are matched. This study also confirms that the electrode thickness, E , has a significant impact on the bandwidth optimisation.

Fig. 8.20 shows the variation of the optical 3 dB modulation bandwidth Δf with the electrode thickness, E , for both structures A and B with the coating thicknesses, $3.0 \mu\text{m}$ and $4.0 \mu\text{m}$ only. It is obvious that the bandwidth increases as the electrode thickness, E is increased. For the coating thickness of $3.0 \mu\text{m}$ and the electrode thickness, $E=27.5 \mu\text{m}$ (for structure A) the bandwidth reaches a value of 100 GHz. By comparison the coating thickness of $4.0 \mu\text{m}$ and the electrode thickness $E=36.2 \mu\text{m}$ results in a structure A where the bandwidth reaches a maximum value of 99 GHz. From Fig. 8.19 it can be noted that, for a thicker Ta_2O_5 coating, a thicker electrode is required to achieve the velocity matching and the maximum bandwidth also has to be increased due to the lower

conductor loss for a thicker electrode. However, in Fig. 8.20, it can be noted that for $T=4.0 \mu\text{m}$ the maximum bandwidth is slightly lower than that of $T=3.0 \mu\text{m}$. This behaviour appears to be contradictory, but it can be explained as follows. It may be observed in Fig. 8.18 that initially the conductor loss reduces rapidly as E is increased; however, for a larger value of E this reduction is slower.

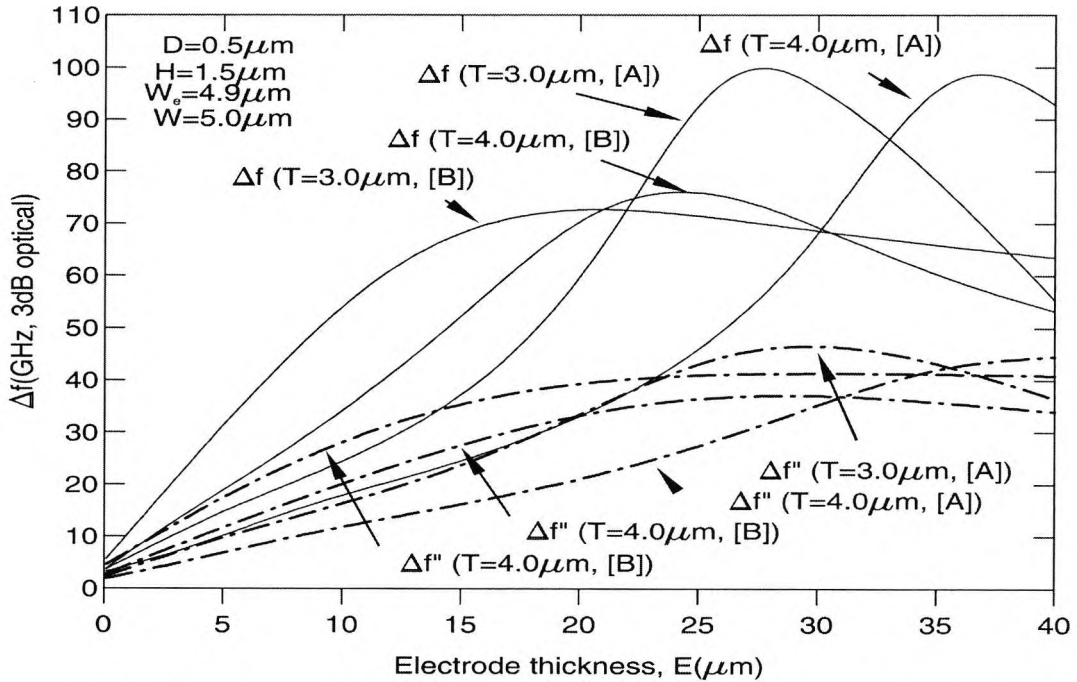


Fig. 8.20 Variation of the 3dB optical bandwidth for both structures *A* and *B*, with the electrode thickness, E , for coating thickness, $T=4.0 \mu\text{m}$, $T=3.0 \mu\text{m}$.

For $T=3.0 \mu\text{m}$, the required electrode thickness, $E=27.5 \mu\text{m}$, and the corresponding value of α_c , is $0.488 \text{ (dB}/\sqrt{\text{GHz}} \cdot \text{cm)}$ and when T is increased to $4.0 \mu\text{m}$, the required electrode thickness, $E=36.2 \mu\text{m}$, and the corresponding value of α_c , is $0.491 \text{ (dB}/\sqrt{\text{GHz}} \cdot \text{cm)}$, which is only slightly higher than in the previous case. This slight increase in α_c , despite using a thicker electrode, is due to the simultaneous use of a thicker Ta_2O_5 layer. This indicates that for a coating thickness higher than $3.0 \mu\text{m}$, the conductor loss will be higher and the bandwidth would reduce.

On the other hand, the 3dB optical bandwidth for structure *B* shows that, at the phase matching point, its value is slightly higher for a coating thickness of $4.0 \mu\text{m}$ compared to

3.0 μm . However it can be observed that when all the parameters (α_c , α_d , and Z_c) are considered, the overall bandwidth is reduced for a coating thickness of 4.0 μm compared to 3.0 μm . This is happening as a result of the conductor loss increase with coating thickness, T , which has been explained from the results shown in Fig. 8.18. The conductor loss value at the phase matching points for the corresponding electrode thicknesses for structure B , at values of 4.0 μm and 3.0 μm for the coating thickness are $0.570 (dB/\sqrt{\text{GHz}} \cdot \text{cm})$ and $0.635 (dB/\sqrt{\text{GHz}} \cdot \text{cm})$ respectively. The thickness of the electrode required to achieve phase matching is higher for the structure A compared to the structure B . Our observation shows that the maximum bandwidth of this type of electrooptic modulator can be achieved for the designed structure A , with a coating thickness of 3.0 μm and a electrode thickness of 27.5 μm .

8.5 Summary

In this chapter a numerical approach based on the efficient finite element method is developed and investigated to study some of the key semiconductor electrooptic modulator parameters. The effect of coating thickness of tantalum pentoxide to achieve velocity matching is presented. For optical modulators operating beyond 40 GHz, the total dielectric loss and the impedance mismatch will play a significant role in the determination of the overall speed of the modulator. It is shown that the coating thickness may play an important role in increasing the optical bandwidth. It is further shown that the electrode thickness also plays essential part in determining the bandwidth of a high-speed modulator. The effect of the impedance mismatch on the bandwidth is also presented. The numerical simulations presented here indicate that for GaAs modulators velocity matching is possible by using Ta_2O_5 coating instead of slow-wave structures with segmented electrodes, to increase the optical bandwidth. The $V_\pi L$ product and the bandwidth are investigated for a specific design requirement, by adjusting various device parameters such as the core height, width, electrode width, and the aluminium concentration of the AlGaAs buffer layer.

Polarization Conversion Phenomenon in Deeply-Etched Semiconductor Electrooptic Waveguide Modulators

9.1 Introduction

The design of ultra-high speed electrooptic (EO) modulators is of significant importance for the realization of future-trend optical communication systems to meet the increasing demand for ultra-fast transmission of huge data in multimedia and internet communication systems. Various research efforts have centred on the realization of novel broadband modulators with minimum driving voltages and losses. Much of this research work has been focused in the design of LiNbO₃ modulators (Haxha, 2002), (Mitomi, 1995) achieving much of the aforementioned modulator design goals. However, the difficulty in integration of LiNbO₃ modulators with other semiconductor optoelectronic devices makes them less useful than their EO semiconductor counterparts. On the other hand, with the recent development in semiconductor materials especially the AlGaAs/GaAs material system, semiconductor EO modulators have received increasing research attention with the purpose of optimizing their performance (Obayya, 2003) for better integration with other optoelectronic integrated circuits (OEIC) (Eldada, 2001).

Most of the reported work on semiconductor EO modulators has been on finding important parameters such as the half-wave voltage length product ($V_{\pi}L$), microwave properties or microwave analysis. It is usually assumed that the polarization state of the modulated lightwave remains the same as that of the input beam. However, this

assumption can really lead to totally misleading results if the waveguide structure in question has small fabrication imperfections.

9.2 Unexpected Polarization Conversion

Modes in optical waveguides, such as traveling waveguide electrooptic modulators with two-dimensional confinement are not strictly TE or TM, but hybrid in nature, which means that all the six components of the magnetic and electric fields are present. The H_y component is the dominant component for the quasi-TE (H_{11}^y) mode, and the H_x component is the nondominant field, which is usually very small. Similarly, for the fundamental quasi-TM (H_{11}^x) mode, the H_x is the dominant field component and the H_y component is the nondominant one. Pure TE or TM modes with only H_y or H_x components, without the other transverse component of the magnetic field, would not exchange power between themselves. The *polarization conversion* phenomenon can take place due to the interaction of the dominant and nondominant components of the quasi-TE and -TM modes (Obayya, 2003).

In this research work, an accurate numerical study of the polarization conversion phenomenon in deeply etched AlGaAs/GaAs EO modulator (Obayya, 2003) is presented, using the versatile finite element method. In particular, the effects of various waveguide parameters such as the slant angle of the waveguide sidewall, the aluminium (Al) concentration of the layer underneath the hot electrode, the modulating voltage on the polarization conversion ratio and the beat length is thoroughly investigated for the first time. If the waveguide sidewalls are slightly off-vertical or the hot electrode is shifted off-centre, the modulating electric field, especially the horizontal component, plays a crucial role in destroying the permittivity tensor giving a higher chances for polarization conversion to occur. Hence, it is very important to account quantitatively for such unwanted polarization conversion phenomenon to avoid this in the design process of EO semiconductor modulators. The modal hybridness is defined as the ratio of the nondominant to the dominant field components of the fundamental modes (Somasiri, 2003). It is an important parameter when considering *polarization crosstalk* studies for waveguide electrooptic modulators. Generally, the modal hybridness is quite

high in semiconductor waveguides, due to their higher refractive index contrast between the core and the substrate.

In order to calculate the power conversion between the two orthogonally polarized modes, when a pure TE or TM mode is incident from the input waveguide (with no modulating voltage), a rigorous and full vectorial approach is mandatory to obtain the scattering coefficients. In this regard, the simple overlap integral approach may be inadequate and in this paper a rigorously convergent fully vectorial least squares boundary residual (LSBR) method (given in Chapter 2) is employed to calculate the modal coefficients of the two hybrid modes at the junction interface. The idea of the LSBR method is to look for a stationary solution to satisfy the continuity conditions of the tangential electric and magnetic fields in the “least squares” sense by minimizing the functional, J , equation (2.5), where Z_o is the free space wave impedance, α is a dimensionless weighting factor, E_t^I and H_t^I are the transverse electric and magnetic fields, respectively in side I (the input waveguide section with no modulating voltage) and E_t^{II} and H_t^{II} are their counterparts in side II (the output waveguide section with nonzero modulating voltage). Once the optical modes of both sides I and II are generated using the VFEM, the functional J is minimized, in the least squares sense, to solve the modal expansion coefficients.

9.3 Simulated results for characterization of polarization conversion in semiconductor electrooptic modulators

The deeply-etched GaAs electrooptic modulator studied here in some details is investigated in Chapter 8. However with respect to polarization conversion the schematic diagram is illustrated in Fig. 9.1. As shown in this figure, an $0.2 \mu\text{m}$ 10%AlGaAs layer, a thick GaAs core with a height, $H(\mu\text{m})$, which is fixed to $2.5 \mu\text{m}$, and a buffer AlGaAs layer with an Al concentration of $x_1\%$ and a height, $B(\mu\text{m})$, are all deposited on a $2 \mu\text{m}$ thick 5% AlGaAs layer. The whole structure is deposited on very thick GaAs substrate, as shown in Fig. 9.1. The ground electrode, with $V=0$, is placed between the 10%AlGaAs layer and the substrate, while the hot electrode, $V \neq 0$, is deposited on top of the buffer AlGaAs layer.

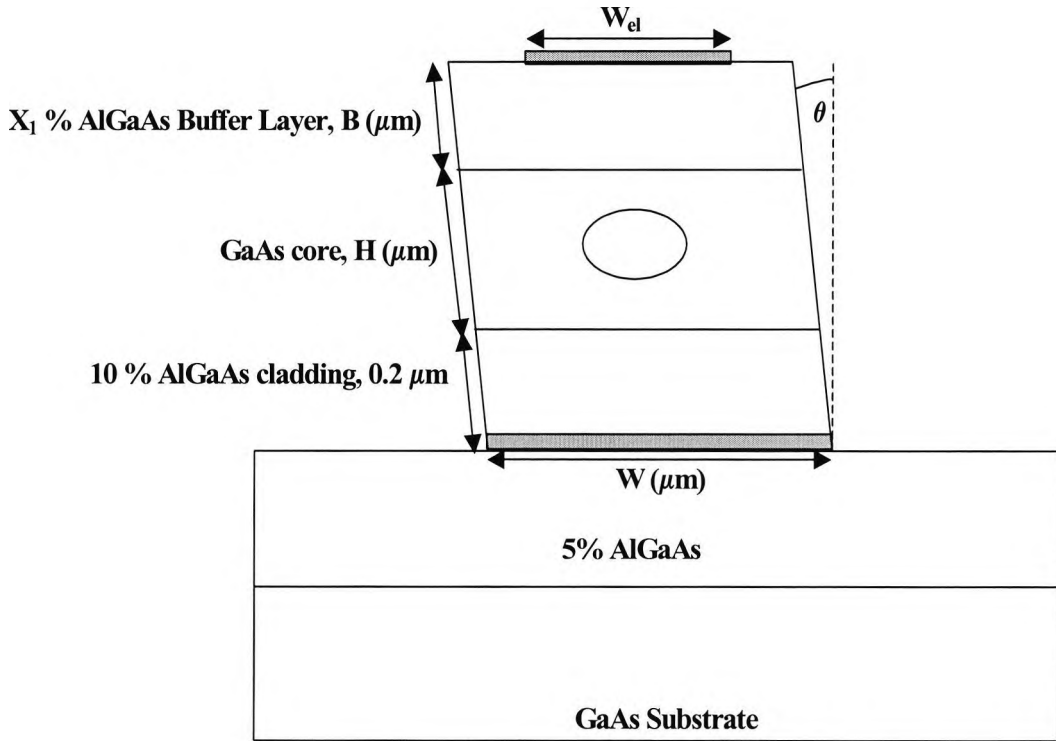


Fig. 9.1 Schematic diagram of a deeply-etched AlGaAs/GaAs semiconductor electrooptic modulator with slanted sidewalls.

It is assumed that such high speed GaAs electrooptic modulators have been developed using a highly doped layer underneath the lower cladding layer as a lower electrode, which is connected to a metal electrode on the side. The width of the waveguide is $W(\mu\text{m})$, while the electrode width is $W_{el}(\mu\text{m})$, and they are fixed to the values of $5.0 \mu\text{m}$ and $2.0 \mu\text{m}$ respectively, and the operating wavelength is $1.55 \mu\text{m}$. A similar structure has been thoroughly considered in Chapter 8 for the purpose of optimization of its optical properties as an EO modulator. However, in this chapter, the effect of the slant angle of the sidewalls and the Al concentration of the buffer layer, x_1 , on the polarization conversion phenomenon will be studied.

The variation of both the fundamental TE and TM propagation constants, β_{TE} and β_{TM} , with the modulating voltage for $x_1=30\%$ and for different slant angles, θ , of 0° , 5° and 10° is illustrated in the Fig. 9.2. For $\theta = 0^\circ$, and as may be seen from this figure, β_{TE} increases linearly as the voltage decreases negatively, while β_{TM} remains nearly constant

until the voltage reaches a value of -24.2 V, the difference between the two propagation constants, $\Delta\beta$, reaches a minimum and a crossover between the two modes occurs leading to polarization conversion.

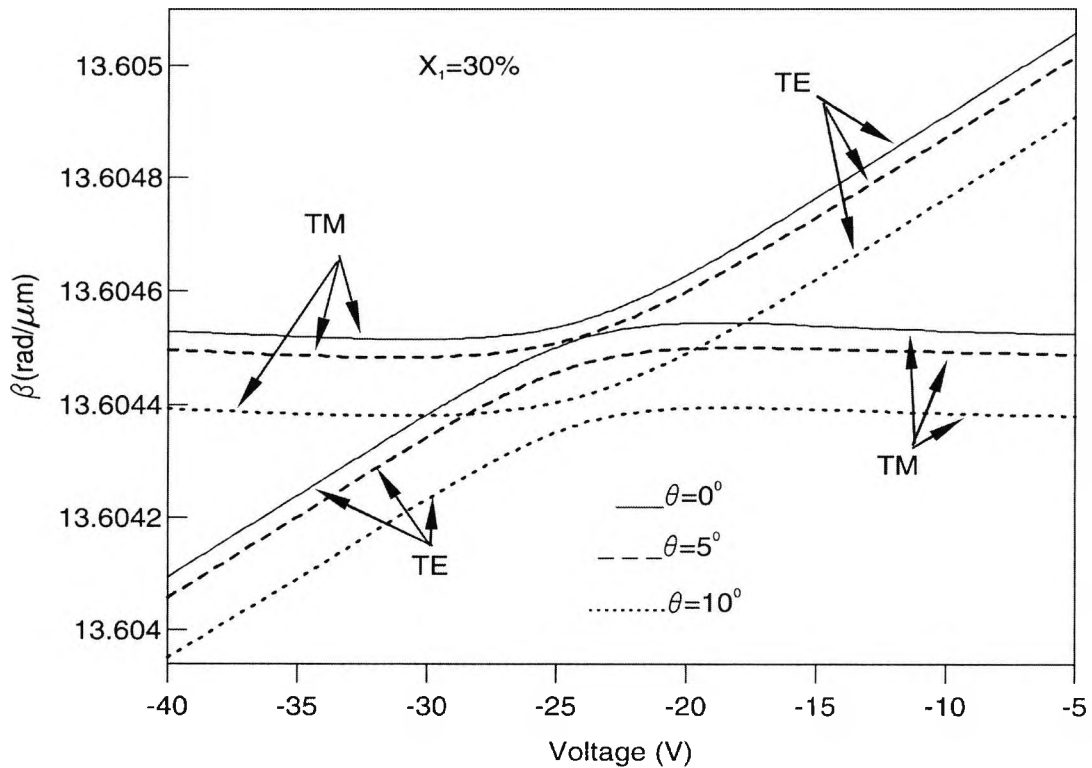


Fig. 9.2 Variation of the propagation constants of the fundamental TE and TM modes with the modulating voltage for different values of the slant angle.

However, for $\theta = 5^\circ$ and 10° , similar behaviour of both the TE and TM modes with the modulating voltage can be observed and a crossover between the two polarization modes has been found near -24.2 V, except that the minimum value of $\Delta\beta$ increases as θ increases. However, as may be noticed from Fig. 9.2, as θ increases the values of both β_{TE} and β_{TM} reduce. This may be justified if it has been noticed that the “equivalent” core area with vertical sidewalls decreases as the θ increases, giving rise to lower modal confinement to the core and lower β values.

Figure 9.3 shows the contour plot of the horizontal electric field profile, $E_x(x, y)$, under the applied voltage of -10 volt, when the $\theta=10^\circ$ and Al concentration is 30%.

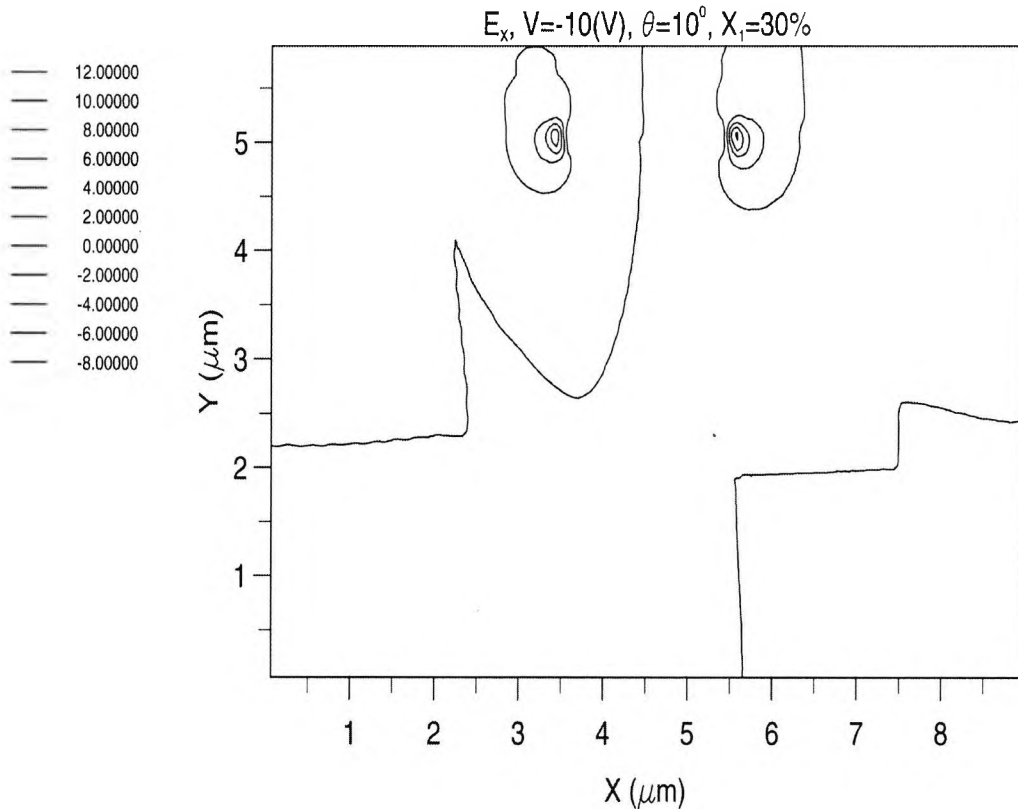


Fig. 9.3 Horizontal electric field or x component, $E_x(x, y)$ for slant sidewall.

It can be seen from Fig. 9.3 that the x component of the electric field $E_x(x, y)$ is asymmetric due to the breach of the sidewall symmetry of the waveguide. The asymmetry is very clear if this figure is compared to Fig. 8.5 in Chapter 8 of this thesis, with the only difference that there the voltage applied was 5 volt. Therefore its effect must be considered with respect to refractive change in horizontal direction.

Contour plot of the electric field y component under the applied voltage of -10 volt, when the angle $\theta=10^\circ$, and Al concentration is 30%, is illustrated in Fig. 9.4. It should be noted that the electric field $E_y(x, y)$ is heavily concentrated and asymmetric in the waveguide region. According to the equation (5.13), (4.42) and (4.43), H^y or E^x modes are mainly affected due to refractive index change in the x direction, but H^x or E^y modes are affected due to the refractive change in y direction, which must be taken into account due to the electromagnetic field asymmetry.

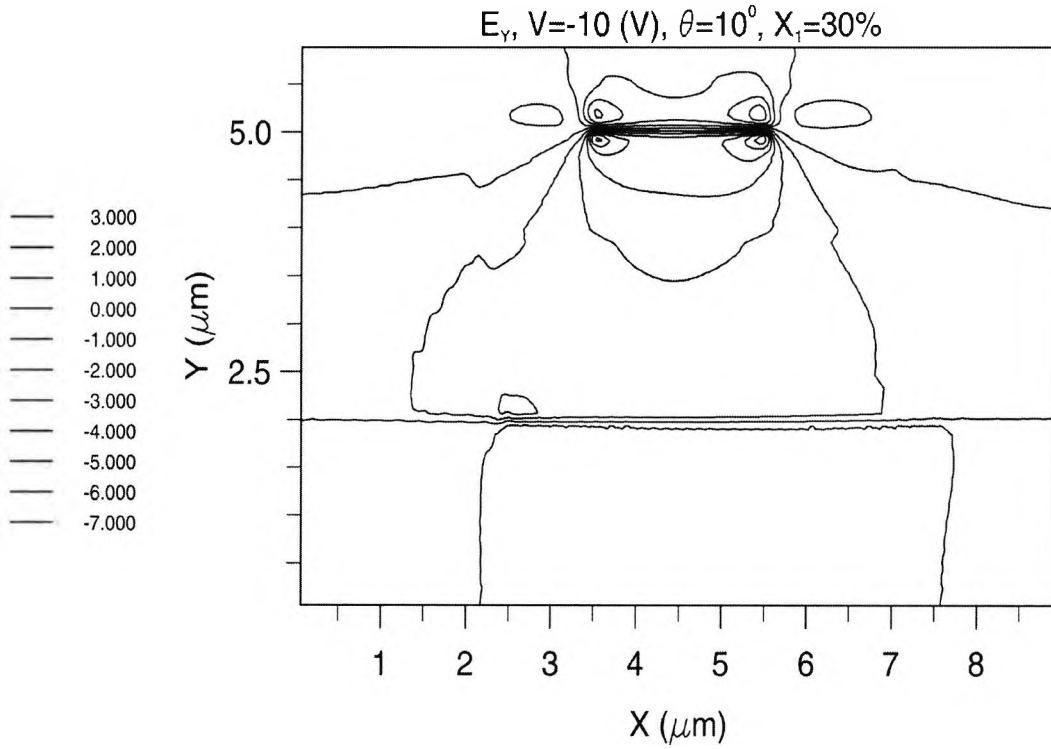


Fig. 9.4 Vertical or y component of the electric field $E_y(x, y)$ with slanted walls.

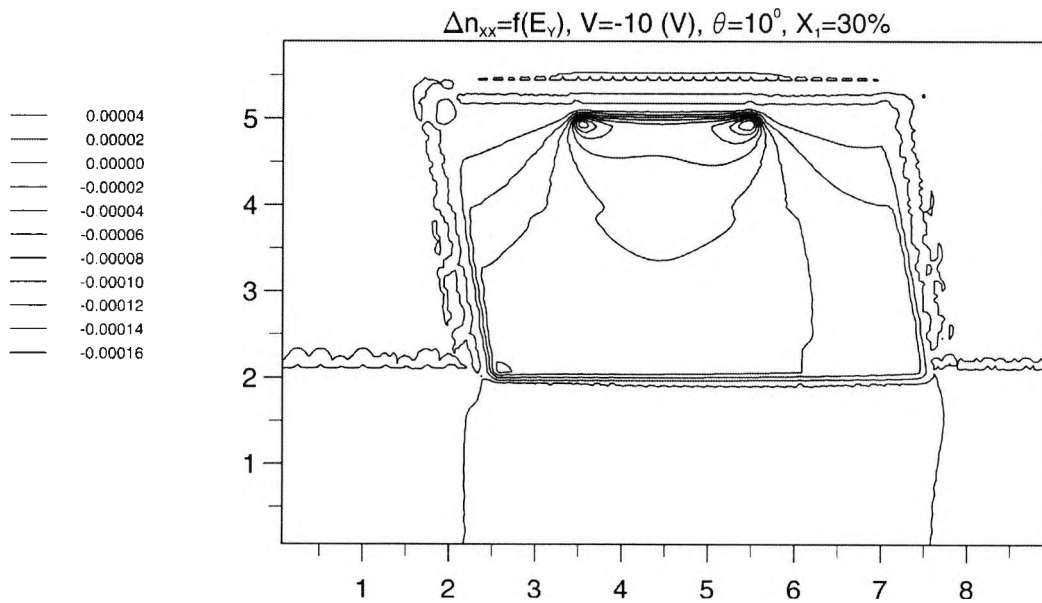


Fig. 9.5 Refractive change due to y component of electric field $E_y(x, y)$.

The refractive index change according to the equation (4.42) Δn_{xx} which is directly proportional to y component of the electric field $E_y(x, y)$ is illustrated in Fig. 9.5. It can be seen that the refractive change profile is asymmetric as a result of sidewall asymmetry. Refractive change due to y component of the electric field is heavily concentrated on the waveguide region; however its concentration is less compared with symmetric sidewall waveguide investigated in the Chapter 8.

On the other hand the refractive change according to the equation (4.43) Δn_{xy} which is directly proportional to x component of the electric field $E_x(x, y)$ is illustrated in Fig. 9.6.

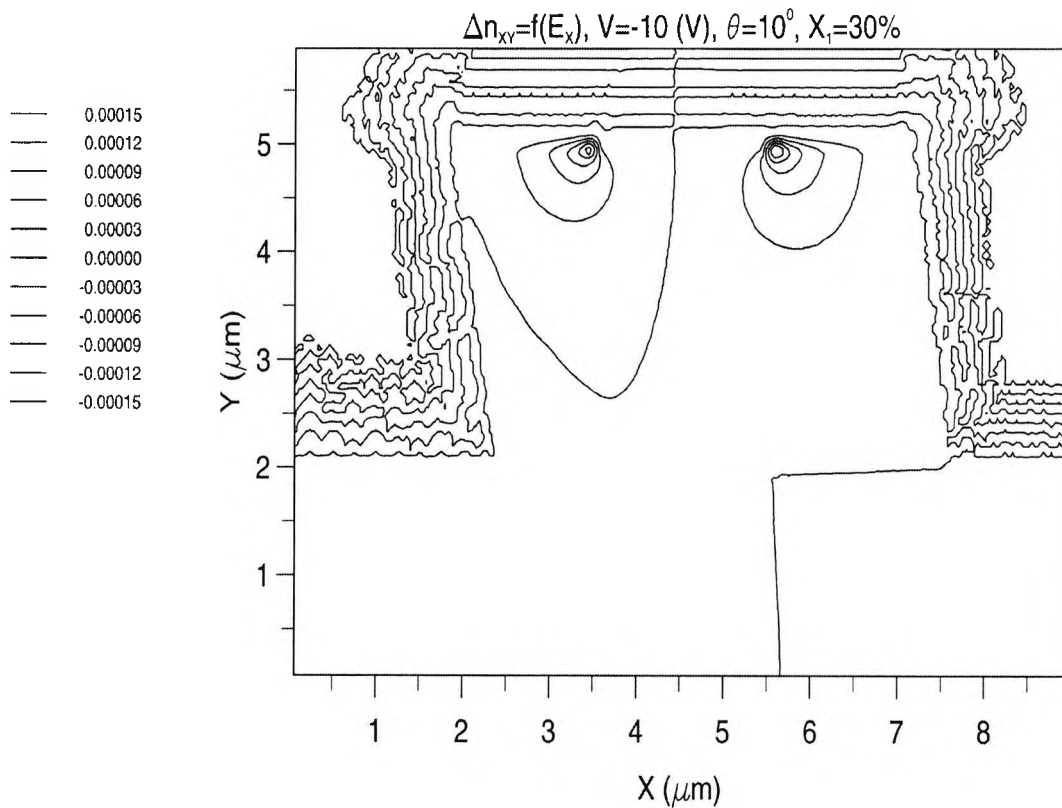
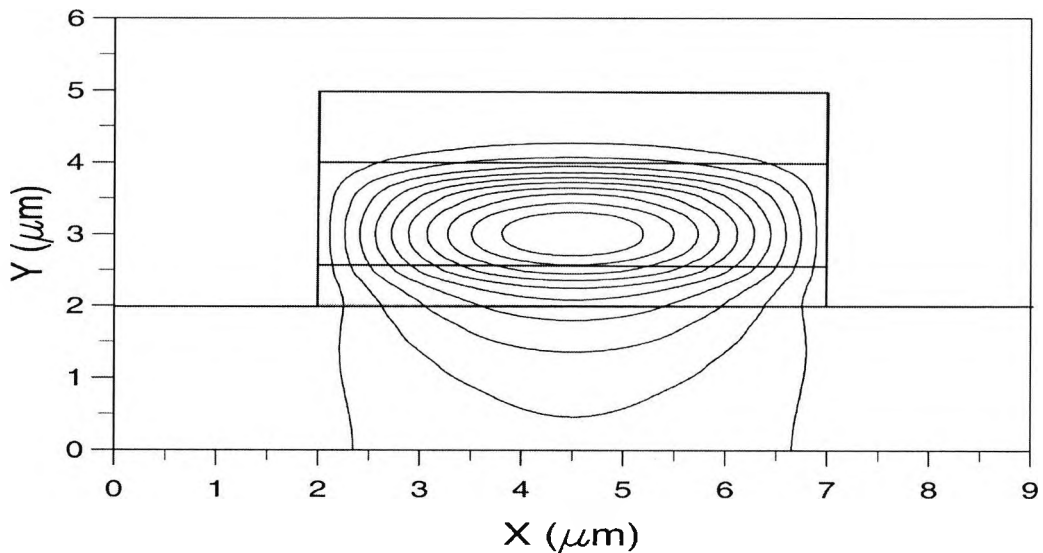


Fig. 9.6 Refractive change due to x component of electric field $E_x(x, y)$.

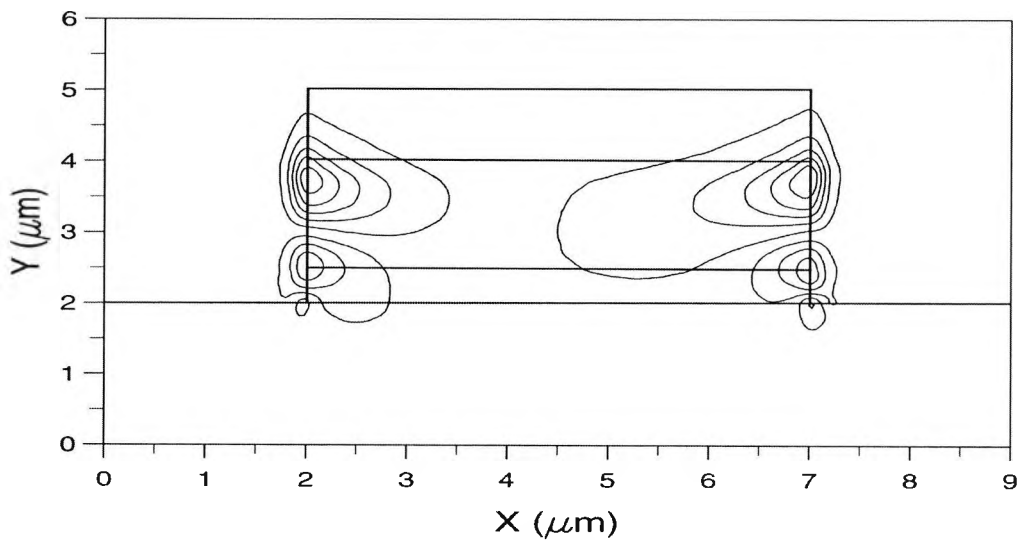
It can be seen that the refractive change profile corresponds to the x component of the electric field. Its is concentrated mainly on the edges of the hot electrode and is

asymmetric as a result of the sidewall asymmetry and the influence of the x component of the electric field.

Vertical sidewall waveguide with no modulating voltage and $x_1=30\%$, the major, H_x , and minor, H_y , field components of the fundamental TM mode are shown in Figs 9.7 (a) and Fig. 9.7 (b), respectively.



a)



b)

Fig. 9.7 Contour plot of the major (a) H_x and minor (b) H_y field components of the fundamental TM mode for zero modulating voltage.

As may be observed from these figures, the H_x profile is symmetrically distributed around the core region, while the H_y profile has the normal peaks at the waveguide corners in a noticeable mismatch to the H_x field distribution. Hence, it is well anticipated that the overlap between such orthogonal field components will be very small.

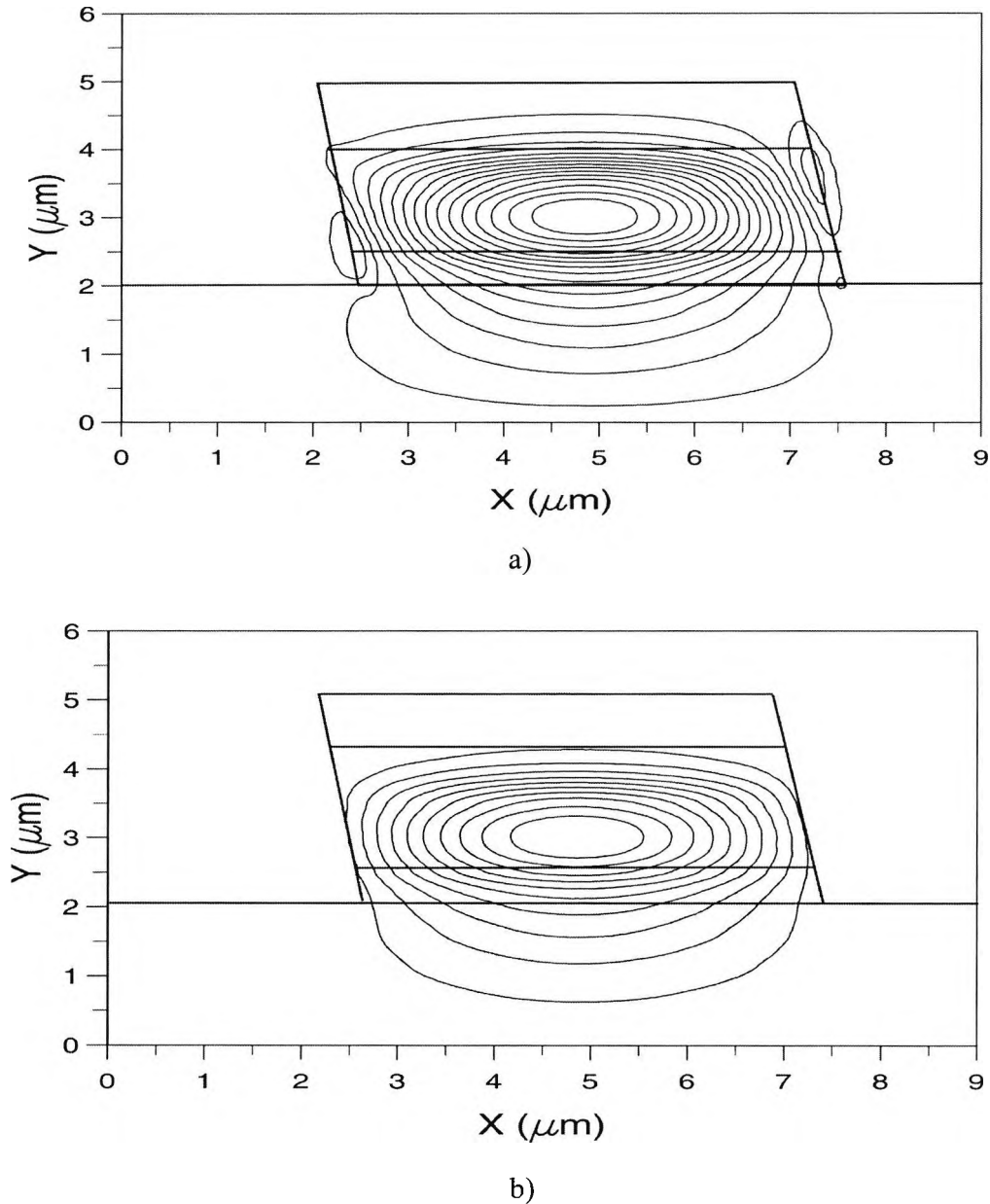
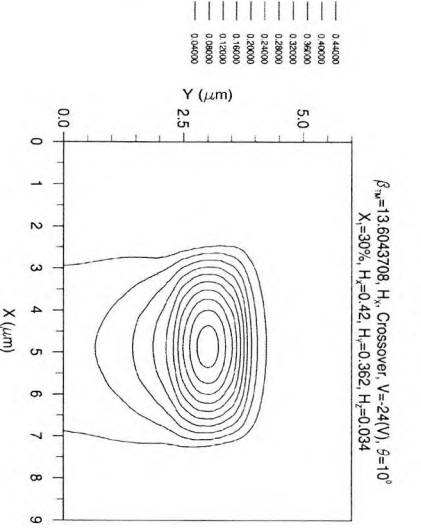
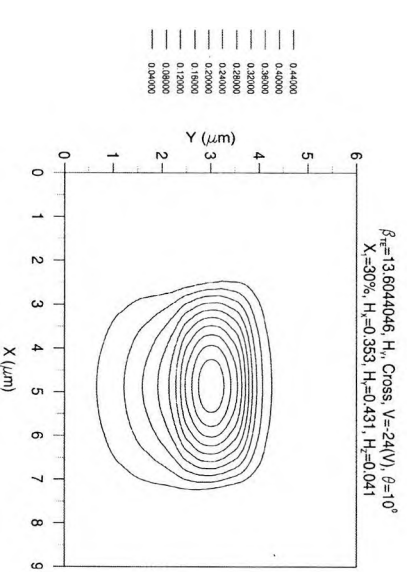
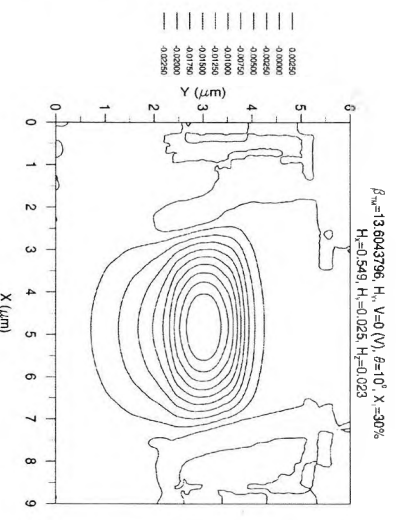
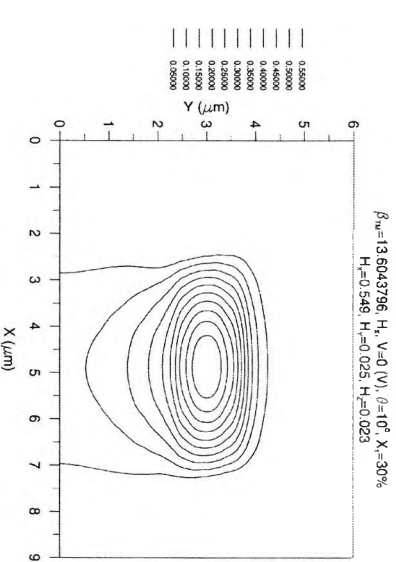
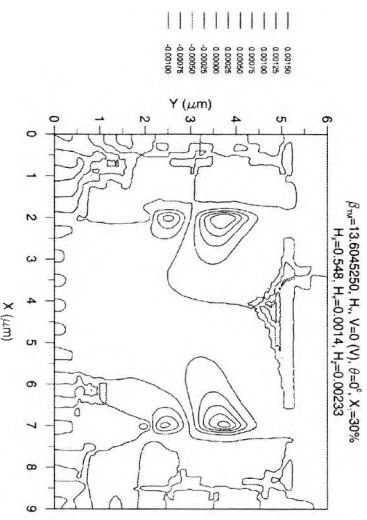
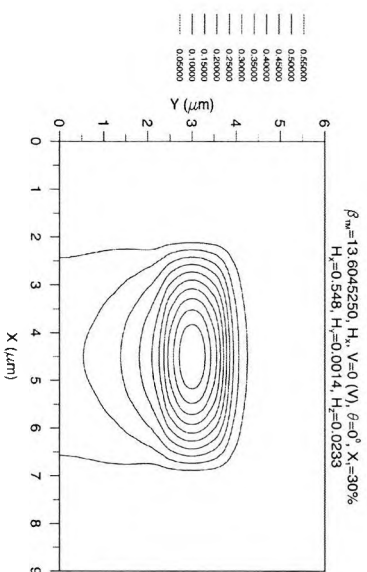
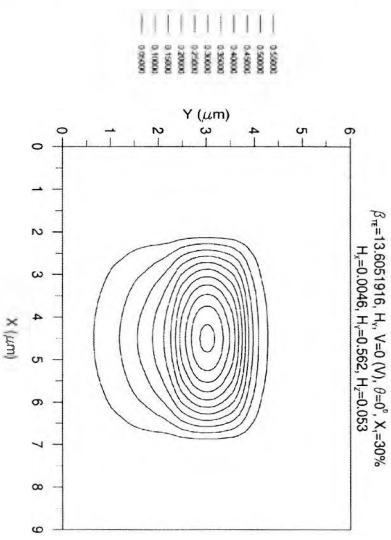
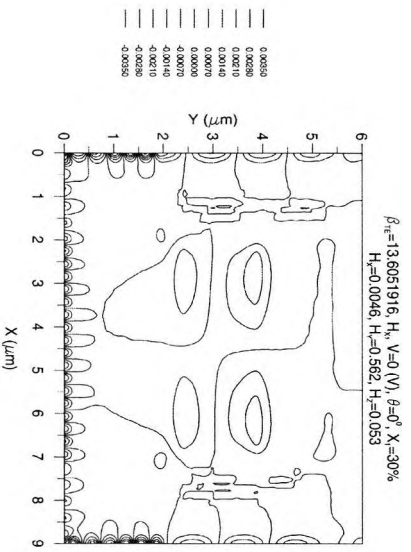


Fig. 9.8 Contour plot of the minor H_y field component of the fundamental TM mode when the modulating voltage is (a) -10 V and (b) -24.2 V.



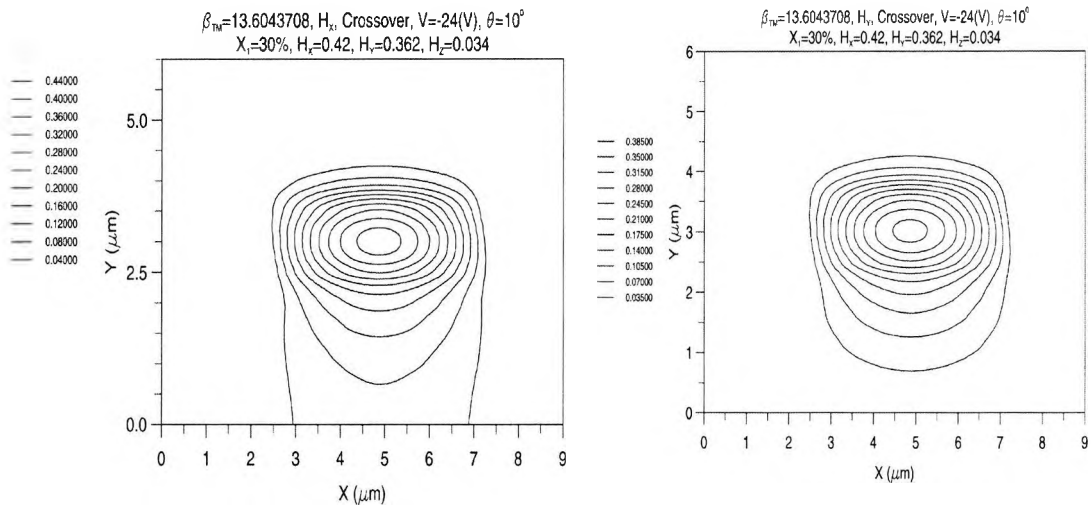


Fig. 9.9 Various field plots for $V=0$, $V=-24$, $\theta=0$, $\theta=10^\circ$ and $X_1=30\%$, for dominant and nondominant modes.

It should not be ignored that the maximum amplitude of the H_y component relative to that of the H_x component is less than 0.00001. Similarly for $\theta = 10^\circ$, and a modulating voltage of -10 V, the minor field component, H_y , of the fundamental TM mode is shown in Fig. 9.8 (a). As can be noticed from this figure, the H_y field distribution is beginning to transform to match that of the H_x component, shown earlier in Fig. 9.7 (a), which suggests a higher overlap integral between the two orthogonal components. However, as the maximum amplitude of H_y , relative to H_x , is still low, around 0.027, there is no appreciable polarization conversion level at this voltage. Negative increase of the voltage to nearly -24.2 V, the minor field component H_y , of the fundamental TM component, is shown in Fig. 9.8 (b). In this case, the H_y distribution is not only quite similar to the H_x distribution, shown in Fig. 9.7 (a), but also its relative maximum amplitude is nearly 0.93, which suggests that very high level of polarization conversion is expected at this voltage.

It is anticipated that the field values with mode crossover are equal for dominant and nondominant, as illustrated in the Fig. 9.9, where various field plots are shown. In this figure field plots are illustrated when there is no voltage applied for the angle $\theta=0$ and $\theta=10^\circ$; it is also shown when the voltage is applied for the same situation, when the modes crossover.

The effect of the modulating voltage with the slant angle on the different parameters of the polarization conversion phenomenon is thoroughly investigated. Figure 9.10 shows the variation of the beat length between the two fundamental polarization modes, L_π , with the modulating voltage for different values of the slant angle, θ . In the present analysis, L_π has been calculated using

$$L_\pi = \frac{\pi}{(\beta_{TE} - \beta_{TM})} \quad (9.1)$$

In terms of polarization conversion, L_π represents the minimum device length at which maximum possible polarization conversion occurs.

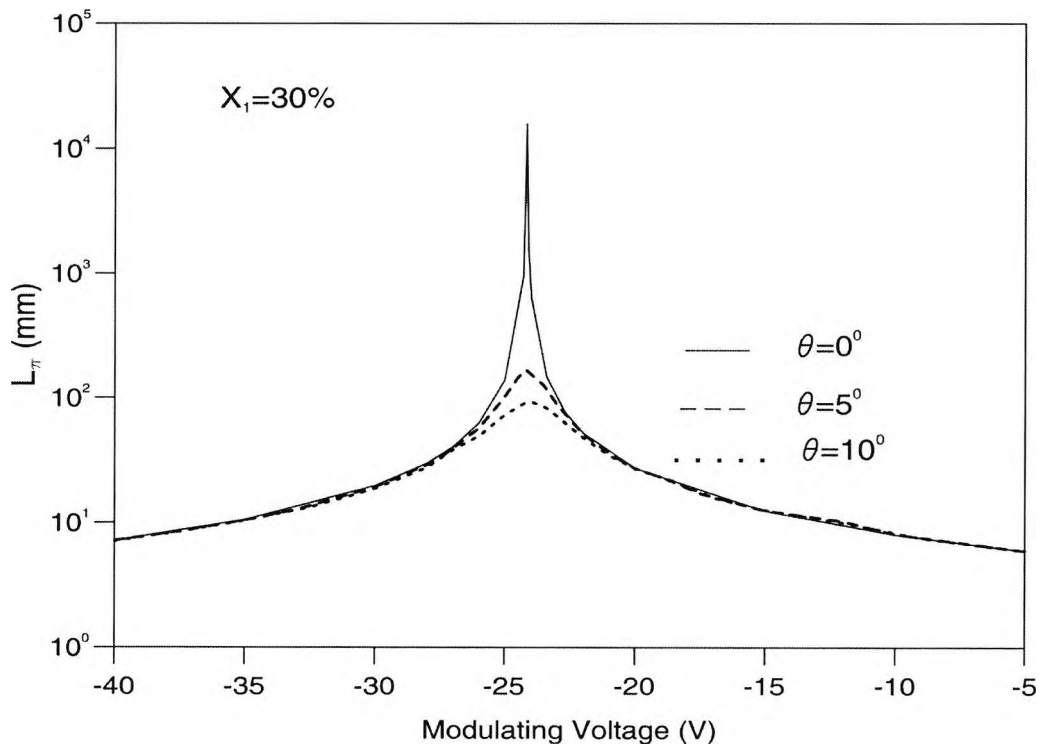


Fig. 9.10 Variation of the beat length with the modulating voltage for different values of the slant angle.

As can be observed from Fig. 9.10, the beat length curves, for all values of the slant angle, reach a peak, $L_{\pi, \max}$, exactly at the crossover voltage of nearly -24 V. However, as the slant angle increases, $L_{\pi, \max}$ is reduced, and for example it is nearly 15710 mm, 167 mm and 93 mm for slant angle values of 0° , 5° and 10° , respectively. Also, it can be observed from the same figure that as the slant angle increases, the “bandwidth” of the L_{π} is increasing giving rise to significant polarization conversion values at voltages slightly away from the crossover voltage. To quantify the amount of polarization conversion feasible, a full vectorial junction analysis, using the LSBR method, has been performed between side I, represented by a waveguide without modulating voltage, and side II, represented by the same waveguide but with variable modulating voltage.

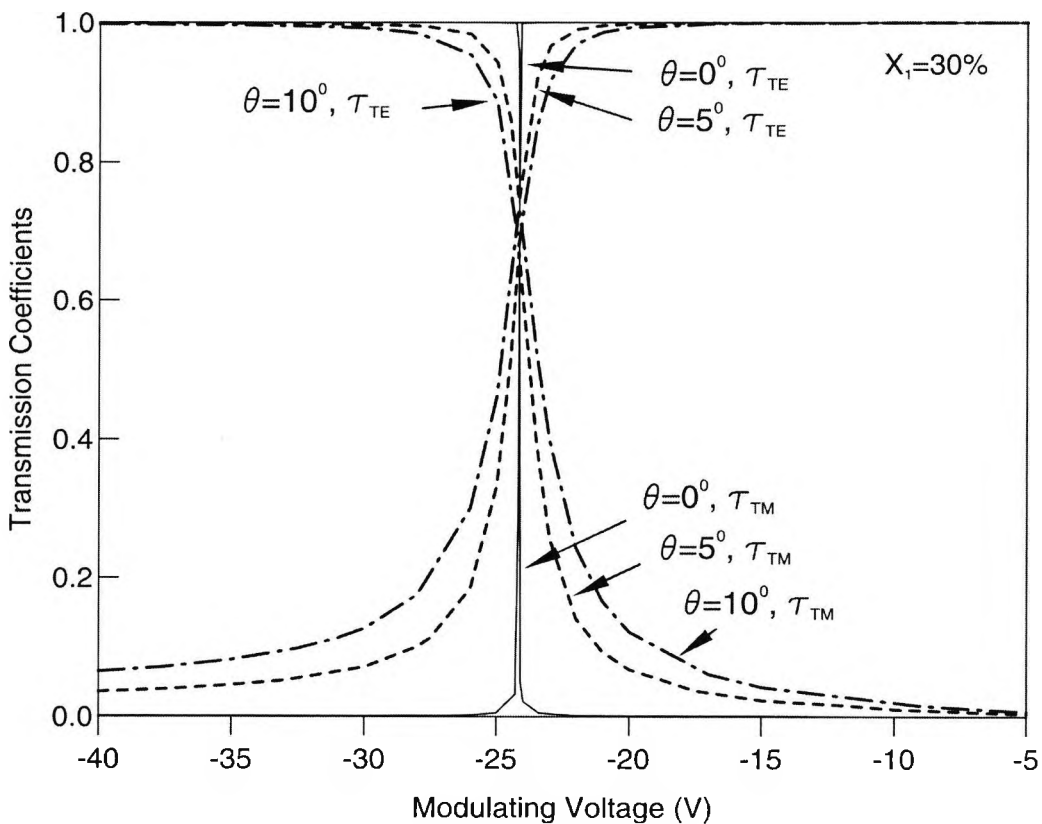


Fig. 9.11 Variation of modal transmission coefficients of both the fundamental TE and TM modes with the modulating voltage for different values of the slant angle.

The LSBR technique has been applied to find the modal transmission coefficients of the fundamental TE and TM modes, τ_{TE} and τ_{TM} , in side II, which variations with the modulating voltage are shown in Fig. 9.11. In all simulations it has been assumed that the incident wave from side I is the fundamental TE mode. Hence, as may be noticed from Fig. 9.11, for very highly negative voltage, τ_{TE} is nearly unity, while τ_{TM} is very small. However, as the voltage is decreased towards the crossover value, it can be noted that τ_{TE} is slowly reduced and τ_{TM} is slowly increased until both of them become equal to $1/\sqrt{2}$ at exactly the crossover voltage. At this particular voltage, both the TE and TM modes are at $\pm 45^\circ$ with respect to the propagation direction giving rise to possible 100% polarization conversion at propagation lengths equal to odd multiples of the beat length. Also, it may be noted that the “tolerance” of the modal transmission coefficients curve increases as the slant angle increases.

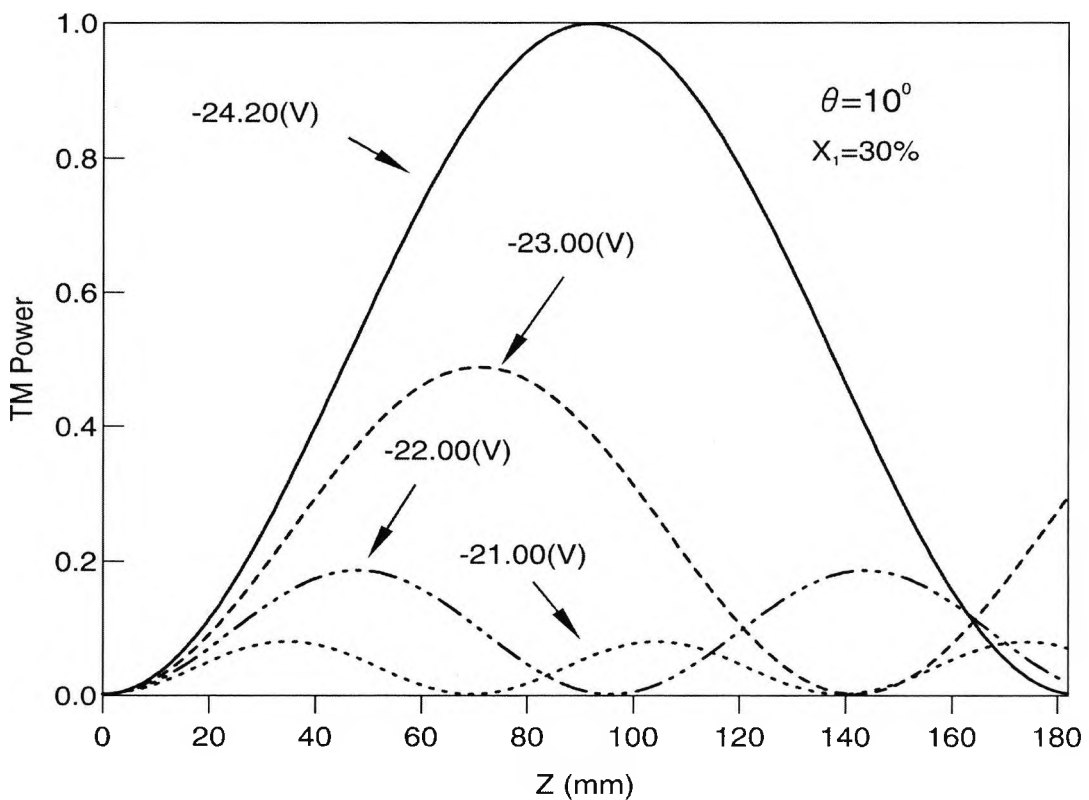


Fig. 9.12. Variation of the TM power with the propagation distance, Z , for different values of the modulating voltage.

In Fig. 9.12 is shown the variation of the TM power with the propagation distance, z , for different values of the modulating voltage when the incident wave is the fundamental TE mode of side I. For a voltage equals to the crossover value of -24.2 V, because of the proper phase matching and the high hybridism of the TE and TM modes, the TM power reaches nearly 100% at a length equal to 93 mm. However, as may be seen from the same figure, as the modulating voltage is slowly getting away from the crossover value, the maximum TM power is getting lower. For example, for a voltage of -23 V, the maximum TM power is nearly 48%, while if that voltage is decreased to -22 V, this maximum TM power is only 18%. Hence, this figure reveals that the amount of polarization conversion can be tuned by adjusting the value of the modulating voltage.

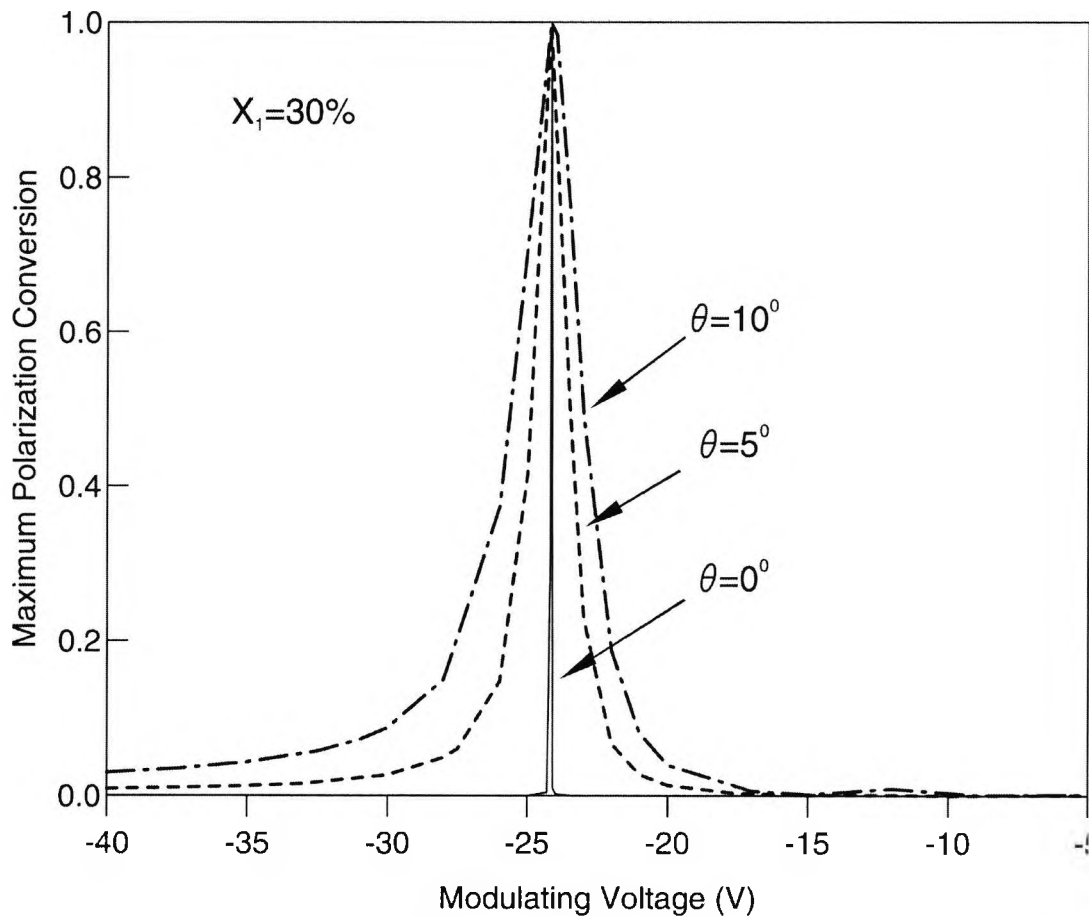


Fig. 9.13 Variation of the maximum polarization conversion ratio with the modulating voltage for different values of the slant angle.

Figure 9.13 shows the variation of the maximum polarization conversion with the modulating voltage for different values of the slant angle. The maximum polarization conversion is that calculated at a propagation distance exactly equal to the beat length. As may be seen from this figure, it is always possible to obtain 100% polarization conversion if the modulating voltage is equal to the crossover voltage, which is -24.2 V in this case. However, the “bandwidth” of the curve itself strongly depends on the verticality of the waveguide sidewalls in such a way that this bandwidth increases as the sidewall slant angle increases. As can be observed from this figure, for $\theta = 0^\circ$, the polarization conversion curve is so sharp that only ± 0.01 V deviation from the crossover voltage can get the maximum polarization conversion ratio from nearly 100% to zero. On the other hand, if the bandwidth, BW, is defined as the difference between the two 50% maximum polarization conversion points, it will be found that this BW is nearly 1.25 V and 1.50 V for slant angles, θ , of 5° and 10° , respectively.

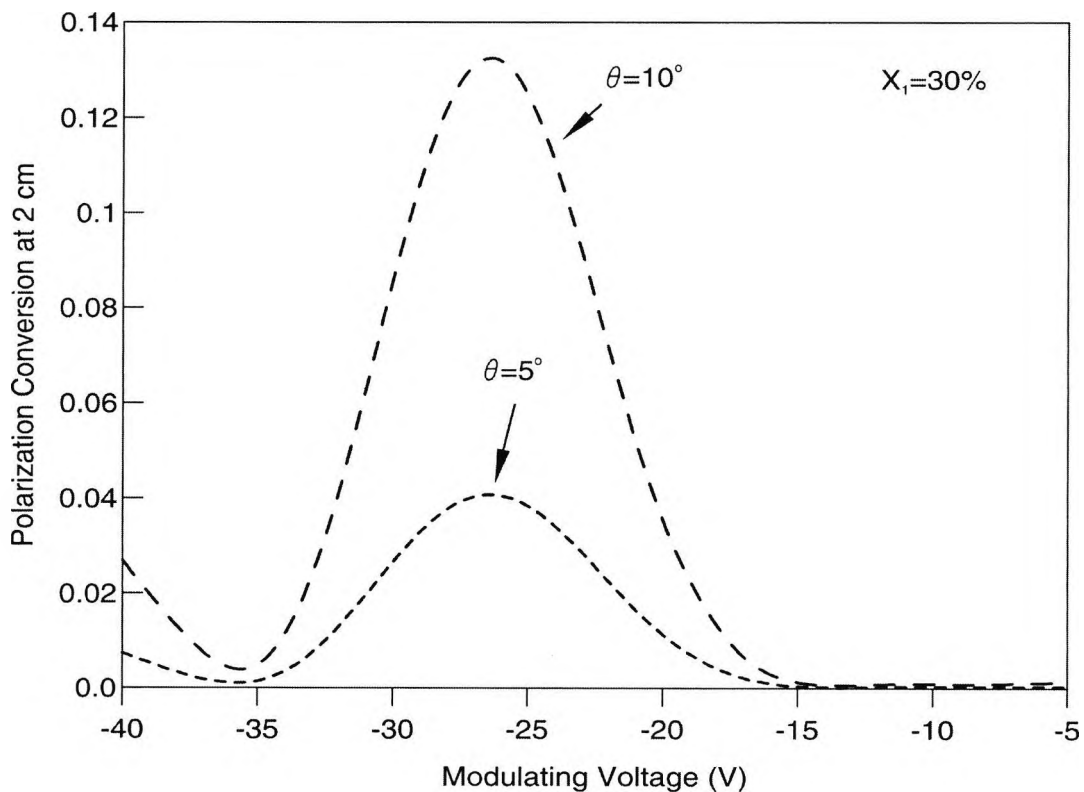


Fig. 9.14 Variation of the polarization conversion ratio with the modulating voltage for different values of the slant angle at 2 cm device length.

Variation of the polarization conversion ratio with the modulating voltage at 2 cm for two values of the slant angle, θ is illustrated in Fig. 9.14. As can be seen from this figure, the maximum polarization conversion ratios are obtained at the crossover voltage of -24.2 V. However, as the 2 cm device length is much shorter than the beat lengths, either for 5° or 10° cases, the maximum conversion ratios obtained are only 4% and 13% for 5° and 10° slant angles, respectively.

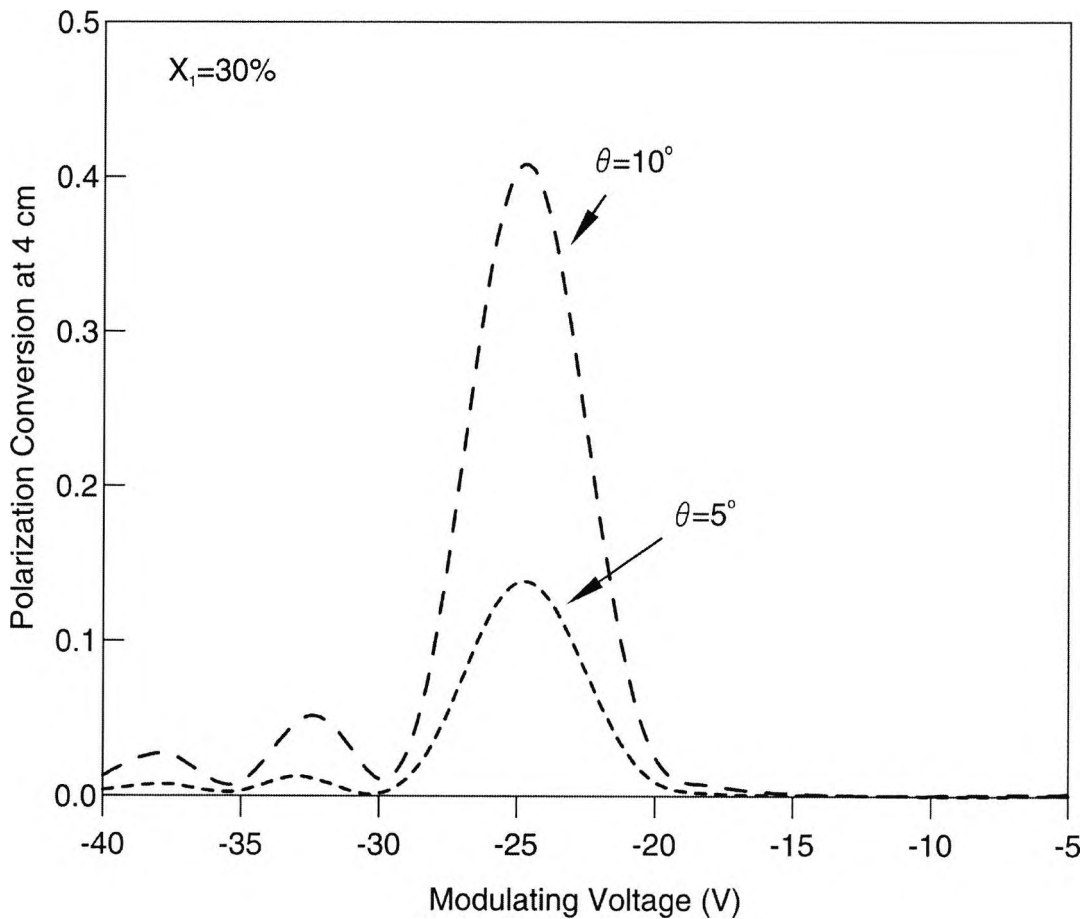


Fig. 9.15 Variation of the polarization conversion ratio with the modulating voltage for different values of the slant angle at 4 cm device length.

Fig. 9.15 shows the variation of the polarization conversion ratio with the modulating voltage at a specific device length of 4 cm for two values of the slant angle. Again, maximum values of the polarization conversion are obtained at exactly the crossover voltage; however here values are 11% and 40% for slant angles of 5° and 10° ,

respectively. These polarization conversion ratios are higher than their counterparts shown in Fig. 9.14 at 2 cm device length, because the 4 cm device length is more comparable to the beat lengths reported in Fig. 9.10. Also, it can be noted from the same figure that, at a voltage of -30 V, the polarization conversion ratios are nearly null. The justification for those null polarization conversion ratios can be seen if it is noted that the beat lengths at this particular voltage are nearly 2 cm. Hence, the polarization conversion ratios peak at this beat length and return to zero again at double this beat length, which is the current 4 cm device length. On the other hand, at a voltage of nearly -32.5 V, the polarization conversion ratios for both slant angle cases have minor peaks of 2% and 5% for 5° and 10° slant angles, respectively. Again, these minor peaks can be justified noting from Fig. 9.10 that the beat length at this voltage is nearly one-third of the 4 cm device length.

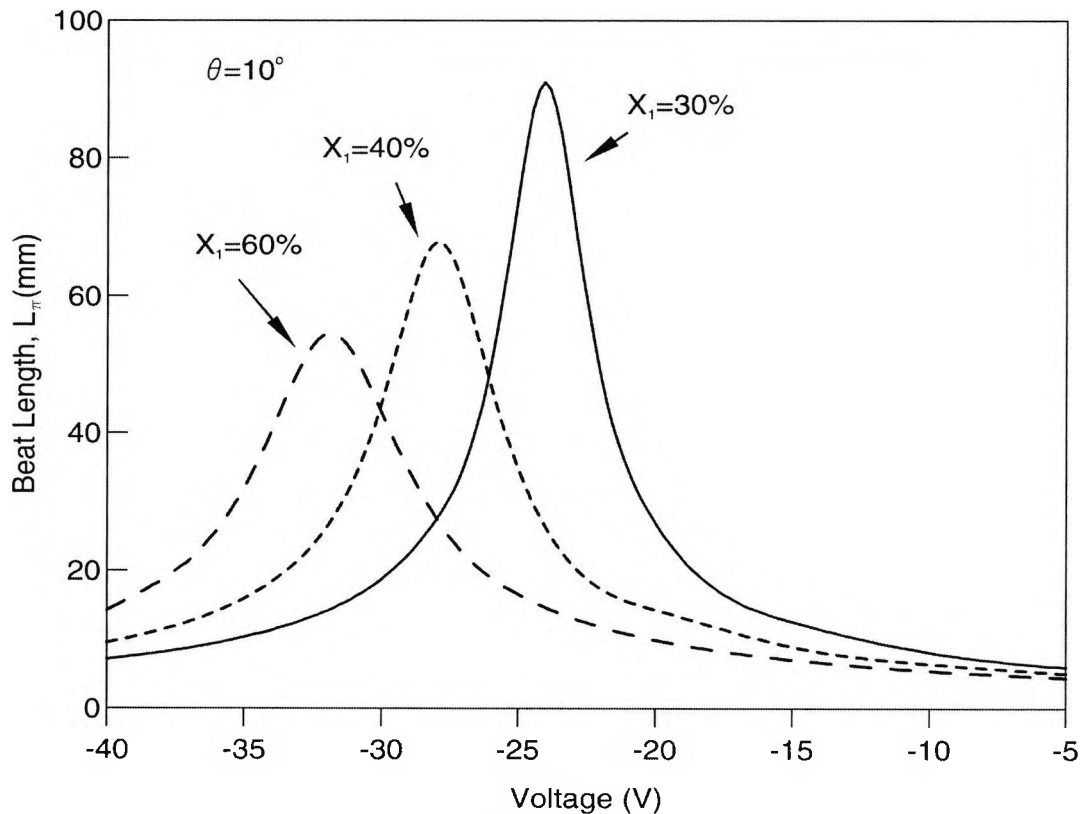


Fig. 9.16 Variation of the beat length with the modulating voltage for different values of the Al concentration of the buffer layer, x_1 .

The effect of varying the Al concentration of the buffer layer, x_1 , on the polarization conversion will be studied for a slant angle of 10° . Figure 9.16 shows the variation of the beat length, L_π , with the modulating voltage for x_1 values of 30%, 40% and 60%. As may be observed from this figure, as x_1 increases, the maximum beat length, $L_{\pi, \max}$ is reduced and the necessary crossover voltage is negatively increased. For example, when $x_1 = 30\%$, $L_{\pi, \max}$ is nearly 93 mm and the crossover voltage is -24.2 V, while if x_1 is increased to 60%, $L_{\pi, \max}$ is dramatically reduced to 55.2 mm at a crossover voltage of -32.0 V. As x_1 increases, there is a higher index contrast between the core and the buffer layers leading to an increasing difference between the two polarization mode propagation constants for zero modulation, that is why a higher negative modulating voltage is needed to bring them to phase matching.

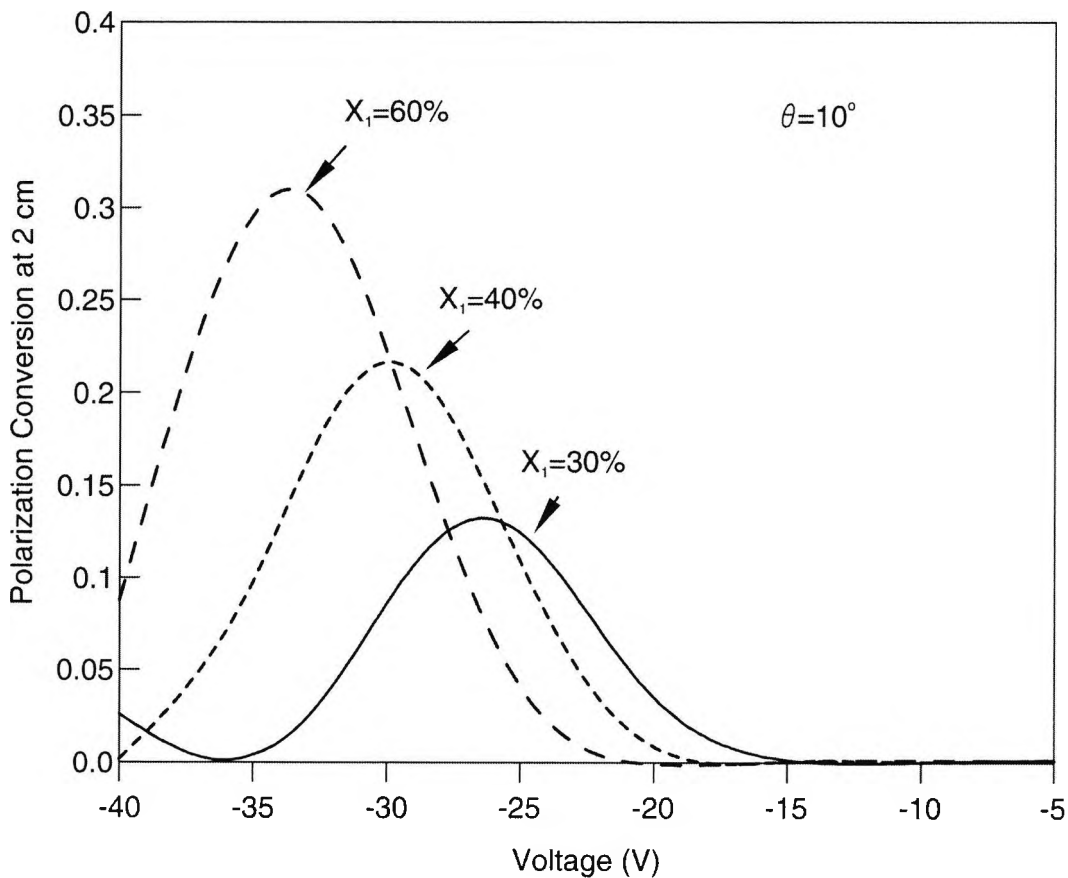


Fig. 9.17 Variation of the polarization conversion ratio with the modulating voltage for different values of the Al concentration of the buffer layer, x_1 , at 2 cm device length.

Variation of the polarization conversion ratio at a particular device length of 2 cm for different values of x_1 is illustrated in the Fig. 9.17. As may be seen from this figure, the polarization conversion ratios are reaching maxima only at the exact crossover voltage for each x_1 case. It may further be observed that as x_1 increases the maximum obtainable polarization conversion ratio increases.

Summary

In this chapter, a rigorous finite element analysis of the polarization conversion phenomenon in a deeply-etched GaAs/AlGaAs semiconductor electrooptic modulator has been investigated and physically justified. The effect of various imperfect fabrication parameters such as the slant angle, electrode offset, Al concentration of the buffer layer and the modulating voltage on the polarization conversion ratio, modal hybridism and beat length has been thoroughly investigated. It is confirmed that the use of full vectorial simulation techniques is mandatory in order to account for, and even beware of, such unexpected and also unwanted polarization conversion effects in electrooptic semiconductor modulators. For the new semiconductor electrooptic modulator design and fabrication it is essential to take into account these parameters in order to avoid unwanted polarization conversion, which can negatively impact on the performance of the device.

Conclusions and Suggestions for future work

10.1 General conclusions

A general evaluation of the research work carried out in the course of this study, in terms of the methodology used and the validity of the results presented, suggest that the objectives set out at the beginning of this research have essentially been achieved. The primary aims and objectives of this research were to an investigate and develop alternative design methodologies and devices configurations leading to improvement of the performance of LiNbO₃ (LN) and GaAs/AlGaAs electrooptic modulators, which has been achieved. Brief descriptions of some representative numerical techniques, useful for optical waveguide and millimeter-wave structures have been explained, with their advantages and disadvantages one over the other. In particular the finite element method and its application has been fully presented. Variational principles in the modal solution of microwave and optical waveguides have been studied. Various aspects of the finite element method have been examined, including different scalar and vector formulations, boundary conditions, natural boundary conditions, shape functions, global matrices and infinite elements.

The full vectorial FEM has been applied to study various aspects of LN and semiconductor waveguide electrooptic modulators. In particular FEM and LSBR technique have been employed throughout this research work. Microwave properties of the LiNbO₃ and semiconductor electro-optic modulators have been thoroughly investigated by applying FEM with quasi static-TEM analysis. Numerical technique has been introduced to calculate the scalar potential functions, the horizontal and vertical components of the electric field for etched (LiNbO₃), unetched (LiNbO₃) and semiconductor electrooptic modulators. Next the line integral based on divergence

theorem has been established to calculate the capacitance C , the free medium capacitance, C_0 , microwave index, N_m , and characteristic impedance, Z_C , for etched and unetched LNs, and semiconductor electrooptic modulators. Conductor losses due to imperfect conductors (metal electrode), α_C , have been calculated by using the “incremental inductance rule” for different electrode designs for both LN and GaAs modulator structures. Dielectric losses of the different dielectric layers, α_d , for coplanar waveguide structures with an anisotropic LiNbO₃ substrate and a SiO₂ buffer layer thickness for unetched and etched Z-cut LN structures and GaAs/AlGaAs electrooptic modulators have been calculated by applying perturbation theory. The 3dB optical bandwidth of the LiNbO₃ and GaAs modulator has been calculated. The effect of the conductor loss on the reduction of the overall bandwidth of the device and for the first time the dielectric loss have been investigated and in particular a significant increase of the bandwidth of the device has been achieved, which was an objective of this research work.

For the first time it has been shown that at high frequency, for both LN and GaAs, the 3dB optical bandwidth can be overestimated if the dielectric losses are neglected. The effect of the different parameters in the design optimization of the modulator for both LN and GaAs structures has been studied. The effects of each parameter for LN etched and unetched structures and such as the buffer thickness, the electrode thickness, the electrode width, the gap between the electrodes and the ridge depth have been thoroughly investigated too, and their impact on the device performance has been analyzed. New design optimization of these parameters has been achieved leading to an improvement of the modulator performance.

Velocity and impedance matching between optical and microwave signals has been investigated for both LN (etched and unetched) and different types of GaAs structures. Simultaneous matching of velocity and impedance between optical and microwave signals has been achieved and its effect on the determination of the overall bandwidth of the modulators has been investigated. The advantage of the Z-cut crystal orientation over the X-cut and Y-cut, by comparing data with experimental results from the different research groups around the world, has been considered. With respect to LN electrooptic

modulators, the new design has been studied in terms of the advantages of etched over unetched structures.

The effect of an external E -Field to a length of Pockels material while an optical signal is passed through it, which resulted in an optical phase shift, has been investigated. The electro-optic effect and the change in the refractive index caused by an external applied electric field has also been established and investigated for both LN and GaAs modulators, respectively. In particular the key parameter for the optical modulator $V_{\pi}L$ half-voltage product has been calculated by using the full vectorial FEM-based modal solution approach. The product of half-wave voltage length has been investigated in order to improve the modulator performance, and details of different modulator parameters have been widely investigated, resulting in a good design of a LN modulator with low $V_{\pi}L$.

New designs for the velocity and impedance matching of a deep-etched semiconductor electrooptic modulators has been presented here for the first time. Tantalum pentoxide (Ta_2O_5) coating is considered to achieve velocity matching between microwave and optical signals. The effects of the velocity mismatch, the conductor loss, the dielectric loss and the impedance mismatch have been studied on the optical bandwidth of a high-speed semiconductor modulator. Determination of the 3dB optical bandwidth of the GaAs modulator for different Ta_2O_5 coating thickness structures have been carried out in this research work.

The least squares boundary residual (LSBR) method, with the exploitation of the accurate modal solution obtained from the finite element method, has been established for the studying of unexpected polarization conversion in the deeply-etched GaAs modulator. The power conversion between the two orthogonally polarized modes, when a pure TE or TM mode is incident from the input waveguide (with no modulating voltage), has been thoroughly investigated. Such a study has been carried out for the first time with respect to avoiding various imperfect fabrication conditions on the unwanted and unexpected polarization conversions in electrooptic semiconductor modulators.

Based on the conclusion of this research work, and previous, published work, advantages and disadvantages of LN and GaAs can be identified and compared as follows:

Advantages of LiNbO₃ electrooptic modulators:

- LiNbO₃, among all external modulators, has the most mature technology
- The large market for such components is the driving force that makes them readily available.
- LiNbO₃ can operate at constant bias for thousands of hours under the control of appropriate biasing circuitry
- Electrical bandwidths higher than 75 GHz and driving voltages around 3 V, so far, have been reported.
- They can handle large optical powers
- The device is promising for high-speed and long-haul optical fibre transmission
- There is low frequency chirp
- They have wide bandwidth
- They have low switching voltage

Advantages of GaAs electrooptic modulators:

- GaAs/AlGaAs is material of choice in many optoelectronic components
- They offer very stable operation
- The electrical bandwidth is higher than 50 GHz and driving voltage is around 15 V, as so far reported.
- They can handle a very large amount of optical powers
- They can easily be integrated with other optoelectronic devices
- Fibre-to-fibre insertion loss is in 10-15 dB range
- The effects of reducing the driving voltage, insertion loss and increasing bandwidth are under consideration.

Details of FEM, LSBR and Quasi-TEM software implementation and their interaction are illustrated in the Appendix 3 of this thesis.

10.2 Future work

The future direction of recommended work on LN and GaAs electrooptic modulators can be summarized as aiming to improve their performance, studying new applications,

(in particular integration with other optoelectronic devices), and establishing full-wave analysis using finite element method. Future improvement of performance can be considered along these major lines of research.

This research has shown the effect of different parameters on the overall bandwidth of electrooptic modulators. Future work for LN electrooptic modulators can be carried out with new electrode designs such as thicker electrodes, slanted-wall electrodes, overhanging electrodes, backslot electrodes and floating electrodes, in order to reduce the insertion losses and the driving power.

With respect to GaAs electrooptic modulators, new electrode designs can be investigated, such as the position of the hot and ground electrodes, using thicker “hot” electrodes which also will lead to the reduction of conductor losses. The conductivity of the ground electrode, which, in this study, is considered a *highly doped* (with doping concentration $1 \times 10^{18} / \text{cm}^3$), could be taken into account as semi-insulating substrate with its conductivity. All the characterizations of AlGaAs layers, with their conductivity, can be objects of further investigation.

Full-wave analysis of hybrid edge/nodal elements is required in order to investigate the frequency dispersion for both LN and GaAs electrooptic modulators. The inclusion of the time domain in the present finite element method could be a step forward in the investigation of the electrooptic modulators.

Different material compositions for the buffer layer can be considered in order to reduce the driving power, the optical losses, and the dielectric losses, leading to an increase of the bandwidth and simplify fabrication.

For the complete modulator design other parameters such as spot-size estimation, butt-coupling loss at the input/output sections, bending loss of the curved waveguide sections, Y-junction, and the power splitters could usefully be investigated.

A further application of the present work could be the development of the approach to the characterization of some more recent advances in integrated optics technology, such as semiconductor polarization converters, optical switches and polarization controllers. Also several, other modern developed CAD-type user friendly packages would be beneficial to assist research workers in this area of optoelectronics.

Electro-optic Effect

In this part of the thesis we consider the problem of propagation of optical radiation in crystals in the presence of an applied the external electric field. In certain types of crystals, the application of an electric field results in a change in both the dimensions and orientation of the index ellipsoid. This is referred to as *electro-optic effect*.

The ellipsoid equation is given as:

$$\frac{x^2}{n_x^2} + \frac{y^2}{n_y^2} + \frac{z^2}{n_z^2} = 1 \quad (\text{A1.1})$$

After electric field is applied, the orientation of \mathbf{D} and \mathbf{E} are parallel.

$$\left(\frac{1}{n^2}\right)_1 x^2 + \left(\frac{1}{n^2}\right)_2 y^2 + \left(\frac{1}{n^2}\right)_3 z^2 + 2\left(\frac{1}{n^2}\right)_4 yz + 2\left(\frac{1}{n^2}\right)_5 xz + 2\left(\frac{1}{n^2}\right)_6 xy = 1 \quad (\text{A1.2})$$

$$\Delta\left(\frac{1}{n^2}\right)_i = \sum_{j=1}^3 r_{ij} \mathbf{E}_j \quad (\text{A1.3})$$

where, 1 = x, 2 = y, and 3 = z.

In matrix form

$$\begin{bmatrix} \Delta\left(\frac{1}{n^2}\right)_1 \\ \Delta\left(\frac{1}{n^2}\right)_2 \\ \Delta\left(\frac{1}{n^2}\right)_3 \\ \Delta\left(\frac{1}{n^2}\right)_4 \\ \Delta\left(\frac{1}{n^2}\right)_5 \\ \Delta\left(\frac{1}{n^2}\right)_6 \end{bmatrix} = \begin{bmatrix} r_{11} & r_{12} & r_{13} \\ r_{21} & r_{22} & r_{23} \\ r_{31} & r_{32} & r_{33} \\ r_{41} & r_{42} & r_{43} \\ r_{51} & r_{52} & r_{53} \\ r_{61} & r_{62} & r_{63} \end{bmatrix} \begin{bmatrix} \mathbf{E}_1 \\ \mathbf{E}_2 \\ \mathbf{E}_3 \end{bmatrix} \quad (\text{A1.4})$$

In general form the equation (A1.14) can be written:

$$S_{ij}x_i x_j = 1 \quad (\text{A1.5})$$

where

$$S_{11} = \frac{1}{n_o^2}; \quad S_{22} = \frac{1}{n_o^2}; \quad S_{33} = \frac{1}{n_e^2}; \quad S_{23} = S_{32} = \frac{1}{r} E_x \quad (\text{A1.6})$$

The problem is to find the magnitudes and directions of the principal dielectric axes of the ellipsoid given in (A1.15). If a vector from the origin to a point (x_1, x_2, x_3) on the ellipsoid (A1.5) is denoted by $\bar{R}(x_1, x_2, x_3)$, then the vector \bar{N} with components is:

$$N_i = S_{ij}x_j \quad (\text{A1.7})$$

Is normal to the ellipsoid at R .

We applied the above rule in order to find the principal dielectric axes by imposing being parallel to normal.

$$S_{ij}x_j = Sx_i \quad (\text{A1.8})$$

where S is an independent constant, for $i = 1, 2,$ and 3 results in:

$$\begin{aligned} (S_{11} - S)x_1 + S_{12}x_2 + S_{13}x_3 &= 0 \\ S_{21}x_1 + (S_{22} - S)x_2 + S_{23}x_3 &= 0 \\ S_{31}x_1 + S_{32}x_2 + (S_{33} - S)x_3 &= 0 \end{aligned} \quad (\text{A1.9})$$

The condition for a nontrivial solution of (A1.9) is:

$$\det[S_{ij} - S\delta_{ij}] = 0 \quad \delta_{ij} = \begin{cases} 1 & i = j \\ 0 & i \neq j \end{cases} \quad (\text{A1.10})$$

1). Find the eigenvalues and eigenvectors of the S matrix.

$$\begin{bmatrix} S_{11} & S_{12} & S_{13} \\ S_{21} & S_{22} & S_{23} \\ S_{31} & S_{32} & S_{33} \end{bmatrix} \quad (\text{A1.11})$$

where S' , S'' , and S''' are three eigenvalues

2). The length of the principal axes along X' , X'' and X''' are $2/\sqrt{S'}$, $2/\sqrt{S''}$ and $2/\sqrt{S'''}$

3). The index ellipsoid equation in terms of a Cartesian system whose axes are parallel to X' , X'' and X''' becomes:

$$S'x'^2 + S''y'^2 + S'''z'^2 = 1 \quad (\text{A1.12})$$

with the unit vectors x' , y' , and z' are taken as parallel to X' , X'' and X''' , respectively.

Example. Find the refractive change for GaAs under an applied electric field?.

In general form the when \bar{E} field is applied to GaAs crystal is the matrix form of the coefficients is given as:

$$[r_{ij}] = \begin{bmatrix} 0 & 0 & 0 \\ 0 & 0 & 0 \\ 0 & 0 & 0 \\ r & 0 & 0 \\ 0 & r & 0 \\ 0 & 0 & r \end{bmatrix} \quad (\text{A1.13})$$

$$\frac{x^2}{n_o^2} + \frac{y^2}{n_o^2} + \frac{z^2}{n_e^2} + 2r_{41}E_x yz + 2r_{41}E_y xz + 2r_{63}E_z xy = 1 \quad (\text{A1.14})$$

$$r = r_{41} = r_{52} = r_{63} \quad (\text{A1.15})$$

$$S = \begin{bmatrix} S_{xx}^{11} & S_{xy}^{12} & S_{xz}^{13} \\ S_{yx}^{21} & S_{yy}^{22} & S_{yz}^{23} \\ S_{zx}^{31} & S_{zy}^{32} & S_{zz}^{33} \end{bmatrix} = \begin{bmatrix} \frac{1}{n_o^2} & rE_z & rE_y \\ rE_z & \frac{1}{n_o^2} & rE_x \\ rE_y & rE_x & \frac{1}{n_e^2} \end{bmatrix} \quad (\text{A1.16})$$

The eigenvectors are given as the solutions of the equation:

$$\det \begin{bmatrix} \frac{1}{n_o^2} - S & rE_z & rE_y \\ rE_z & \frac{1}{n_o^2} - S & rE_x \\ rE_y & rE_x & \frac{1}{n_e^2} - S \end{bmatrix} = 0 \quad (\text{A1.17})$$

$$\left(\frac{1}{n_o^2} - S \right) \left[\left(\frac{1}{n_o^2} - S \right) \left(\frac{1}{n_e^2} - S \right) - r^2 E_x^2 \right] - rE_z \left[rE_z \left(\frac{1}{n_e^2} - S \right) - r^2 E_x E_y \right] + \quad (\text{A1.18})$$

$$rE_y \left[r^2 E_z E_x - rE_y \left(\frac{1}{n_o^2} - S \right) \right] = 0$$

However, for $E = 0$, GaAs becomes isotropic, i.e., $n_o^2 = n_e^2 = n^2$ therefore

$$\left(\frac{1}{n^2} - S \right)^3 - r^2 E_x^2 \left(\frac{1}{n^2} - S \right) - r^2 E_z^2 \left(\frac{1}{n^2} - S \right) - r^3 E_x E_y E_z + r^3 E_x E_y E_z - r^2 E_y^2 \left(\frac{1}{n^2} - S \right) = 0$$

(A1.19)

then

$$\left(\frac{1}{n^2} - S\right)^3 - \left(\frac{1}{n^2} - S\right) \left[r^2 |\mathbf{E}|^2 \right] = 0 \quad (\text{A1.20})$$

where

$$|\mathbf{E}|^2 = E_x^2 + E_y^2 + E_z^2 \quad (\text{A1.21})$$

from the equation (A1.20) hence:

$$\left(\frac{1}{n^2} - S\right) = 0 \quad \Rightarrow \quad S' \sim x' \quad (\text{A1.22})$$

$$\left(\frac{1}{n^2} - S\right)^2 - (r|\mathbf{E}|)^2 = 0 \quad (\text{A1.23})$$

from equation (A1.22) hence:

$$S' = \frac{1}{n^2} \quad (\text{A1.24})$$

equation (A1.20) can be written as:

$$\left[\left(\frac{1}{n^2} - S'' \right) - r|\mathbf{E}| \right] \left[\left(\frac{1}{n^2} - S''' \right) + r|\mathbf{E}| \right] = 0 \quad (\text{A1.25})$$

from equation (A1.25) hence $S'' \sim x''$ and $S''' \sim x'''$ are:

$$S'' = \frac{1}{n^2} + r|\mathbf{E}| \quad (\text{A1.26})$$

$$S''' = \frac{1}{n^2} - r|\mathbf{E}| \quad (\text{A1.27})$$

A). For $S = S' = 1/n^2$ is assumed Z-cut crystal orientation where, $\mathbf{E}_z \neq 0$, $\mathbf{E}_x = \mathbf{E}_y = 0$

from the equation (A1.8) the system of equations is:

$$\left. \begin{aligned} \left(\frac{1}{n^2} - \frac{1}{n^2}\right)x'_1 + r\mathbf{E}_z x'_2 + \mathbf{E}_y x'_3 &= 0 \\ r\mathbf{E}_z x'_1 + \left(\frac{1}{n^2} - \frac{1}{n^2}\right)x'_2 + r\mathbf{E}_x x'_3 &= 0 \\ r\mathbf{E}_y x'_1 + r\mathbf{E}_x x'_2 + \left(\frac{1}{n^2} - \frac{1}{n^2}\right)x'_3 &= 0 \end{aligned} \right\} \quad (\text{A1.28})$$

or

$$\left. \begin{aligned} r\mathbf{E}_z x'_2 + r\mathbf{E}_y x'_3 &= 0 \\ r\mathbf{E}_z x'_1 + r\mathbf{E}_x x'_3 &= 0 \\ r\mathbf{E}_y x'_1 + r\mathbf{E}_x x'_2 &= 0 \end{aligned} \right\} \quad (\text{A1.29})$$

The above equations can be satisfied by choosing, equation, $x'_1 = x'_2 = 0$, and x'_3 can be any value that will satisfy the 1st couple equations. The eigenvector X' corresponding to $S' (=1/n^2)$ is thus parallel to the Z-axis.

B). For the case when, $S = S'' = \frac{1}{n^2} + r|\mathbf{E}|$ then;

$$\left. \begin{aligned} \left(\frac{1}{n^2} - \frac{1}{n^2} - r|\mathbf{E}| \right) x'_1 + rE_z x'_2 + rE_y x'_3 &= 0 \\ rE_z x'_1 + \left(\frac{1}{n^2} - \frac{1}{n^2} - r|\mathbf{E}| x'_2 \right) + rE_x x'_3 &= 0 \\ rE_y x'_1 + rE_x x'_2 + \left(\frac{1}{n^2} - \frac{1}{n^2} r|\mathbf{E}| \right) x'_3 &= 0 \end{aligned} \right\} \quad (\text{A1.30})$$

$$\left. \begin{aligned} -r|\mathbf{E}|x'_1 + rE_z x'_2 + rE_y x'_3 &= 0 \\ rE_z x'_1 - r|\mathbf{E}|x'_2 - rE_x x'_2 - r|\mathbf{E}|x'_3 &= 0 \\ rE_y x'_1 + rE_x x'_2 - r|\mathbf{E}|x'_3 &= 0 \end{aligned} \right\} \quad (\text{A1.31})$$

for Z-cut crystal orientation $E_z \neq 0$ and $E_x = E_y = 0$ therefore;

$$\left. \begin{aligned} -rE_z x'_1 + rE_z x'_2 &= 0 \\ rE_z x'_1 - rE_z x'_2 &= 0 \\ rE_z x'_3 &= 0 \end{aligned} \right\} \quad (\text{A1.32})$$

The solution $(x'_1 - x'_2) = 0$ and $x'_3 = 0$ satisfy the above conditions, i.e., the eigenvector X'' is parallel to $(\hat{x} - \hat{y})$.

Similarly, we can show that the third eigenvector X''' is parallel to $(\hat{x} + \hat{y})$. The equation of the ellipsoid in the transformed coordinates is given by:

$$\left(\frac{1}{n^2} - rE_z \right) x'^2 + \left(\frac{1}{n^2} + rE_z \right) y'^2 + \frac{z'^2}{n^2} = 1 \quad (\text{A1.33})$$

where x'^2 is related to $(\hat{x} - \hat{y})$, y'^2 is related to $(\hat{x} + \hat{y})$ and z'^2 is related to Z-cut crystal orientation.

The last equation can be put in the form:

$$\frac{x'^2}{n_x'^2} + \frac{y'^2}{n_y'^2} + \frac{z'^2}{n_z'^2} = 1 \quad (\text{A1.34})$$

$$\frac{1}{n'^2_x} = \frac{1}{n^2} - rE_z \quad (\text{A1.35})$$

$$d\left(\frac{1}{n'^2_x}\right) = \frac{-2}{n'^3_x} dn'_x \approx \frac{-2}{n^3} dn'_x \quad \text{as} \quad (rE_z \ll \frac{1}{n^2}) \quad (\text{A1.36})$$

$$d(n'_x) \approx \frac{-n^3}{2} d\left(\frac{1}{n'^2_x}\right) = \frac{n^3}{2} rE_z \quad (\text{A1.37})$$

Similarly

$$d(n'_y) = \frac{-n^3}{2} rE_z \quad (\text{A1.38})$$

$$n'_{x,y} = n + d(n'_{x,y}) \quad (\text{A1.39})$$

$$n'_x = n + \frac{n^3}{2} rE_z \quad (\text{A1.40})$$

$$n'_y = n - \frac{n^3}{2} rE_z \quad (\text{A1.41})$$

$$n'_z = n_z = n \quad (\text{A1.42})$$

In this case E_z plays the role of E_y from Laplace and x' is z is the direction of the propagation and z is x direction of propagation.

Appendix 2

Divergence theorem

Let us consider the infinitesimal volume dx, dy, dz , and the vector A with its components as illustrated in the Fig. A2.1 where A_x, A_y, A_z are functions of the coordinates x, y, z . The value of A_x at the center of the right-hand face can be taken to be the average value over that face. The right-hand and left-hand face of the volume element, the outgoing flux are (Paul, 1978):

$$d\Phi_R = \left(A_x + \frac{\partial A_x}{\partial x} \frac{dx}{2} \right) dydz \quad (\text{A2.1})$$

$$d\Phi_L = - \left(A_x - \frac{\partial A_x}{\partial x} \frac{dx}{2} \right) dydz \quad \text{A2.2}$$

The net outward flux through two faces is:

$$d\Phi_R + d\Phi_L = \frac{\partial A_x}{\partial x} dx dy dz = \frac{\partial A_x}{\partial x} d\tau \quad (\text{A2.3})$$

To extend this calculation to a finite volume, we sum the individual fluxes for each of the infinitesimal volume elements in the finite volume, and the total outward flux is:

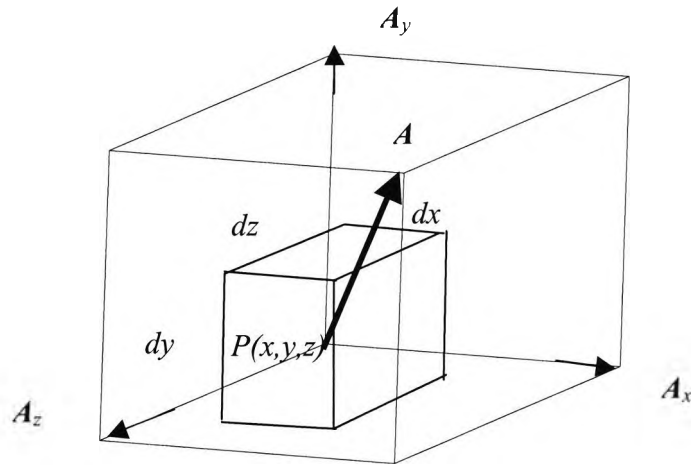


Fig. A2.1 Element of the volume dx, dy, dz around the point P , with the vector A

$$\Phi_{tot} = \int_{\tau} \left(\frac{\partial A_x}{\partial x} + \frac{\partial A_y}{\partial y} + \frac{\partial A_z}{\partial z} \right) d\tau \quad (\text{A2.4})$$

At any given point the volume, the quantity is thus the outgoing flux per unit volume defined as *divergence* of the vector A at that point and can be expressed as:

$$\nabla \cdot A = \frac{\partial A_x}{\partial x} + \frac{\partial A_y}{\partial y} + \frac{\partial A_z}{\partial z} \quad (\text{A2.5})$$

The total outward flux given in equation (A2.4) is also equal to the surface integral of the normal outward component of A . Thus

$$\int_S A \cdot da = \int_{\tau} \left(\frac{\partial A_x}{\partial x} + \frac{\partial A_y}{\partial y} + \frac{\partial A_z}{\partial z} \right) d\tau = \int_{\tau} \nabla \cdot A d\tau \quad (\text{A2.6})$$

This is the divergence theorem. For the close path in the xy -plane and for any A the integration around the path illustrated in the Fig. A2.2.

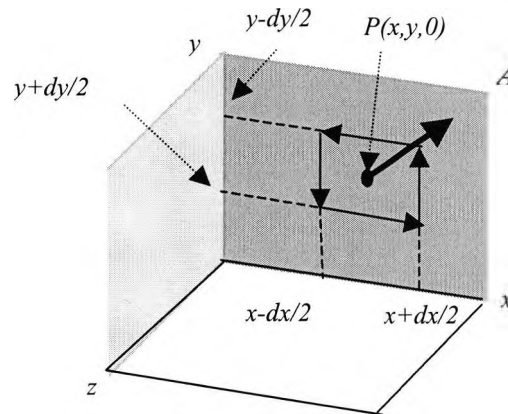


Fig. A2.2 Closed, rectangular path in the xy -plane, the integration path, S is performed in the direction of the arrows.

$$\oint \mathbf{A} \cdot d\mathbf{l} = \oint A_x dx + \oint A_y dy = \left(\frac{\partial A_y}{\partial x} - \frac{\partial A_x}{\partial y} \right) dx dy \quad (\text{A2.7})$$

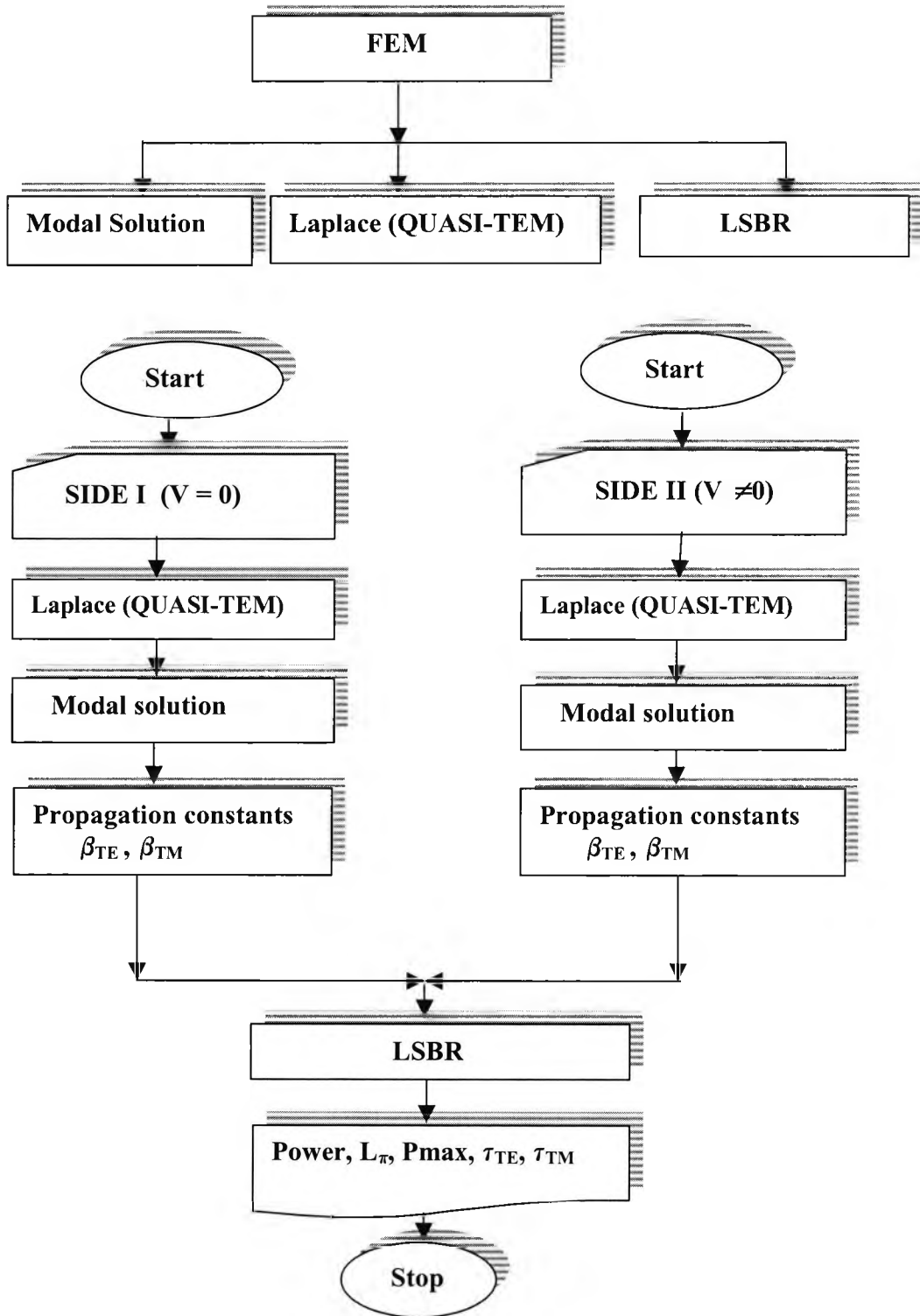
where

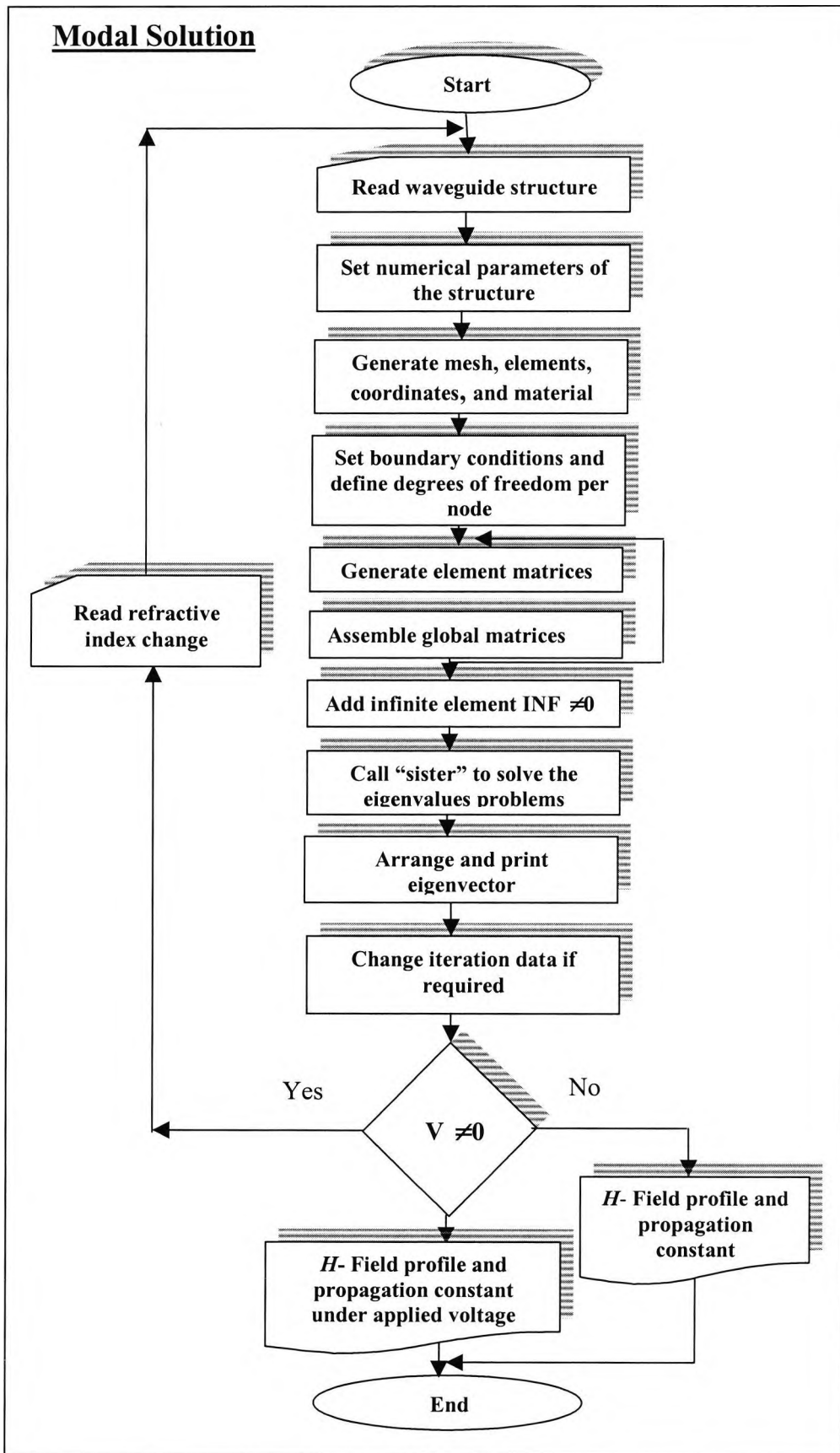
$$\oint A_x dx = \left(A_x - \frac{\partial A_x}{\partial y} \frac{dy}{2} \right) dx - \left(A_x + \frac{\partial A_x}{\partial y} \frac{dy}{2} \right) dx = -\frac{\partial A_x}{\partial y} dy dx \quad (\text{A2.8})$$

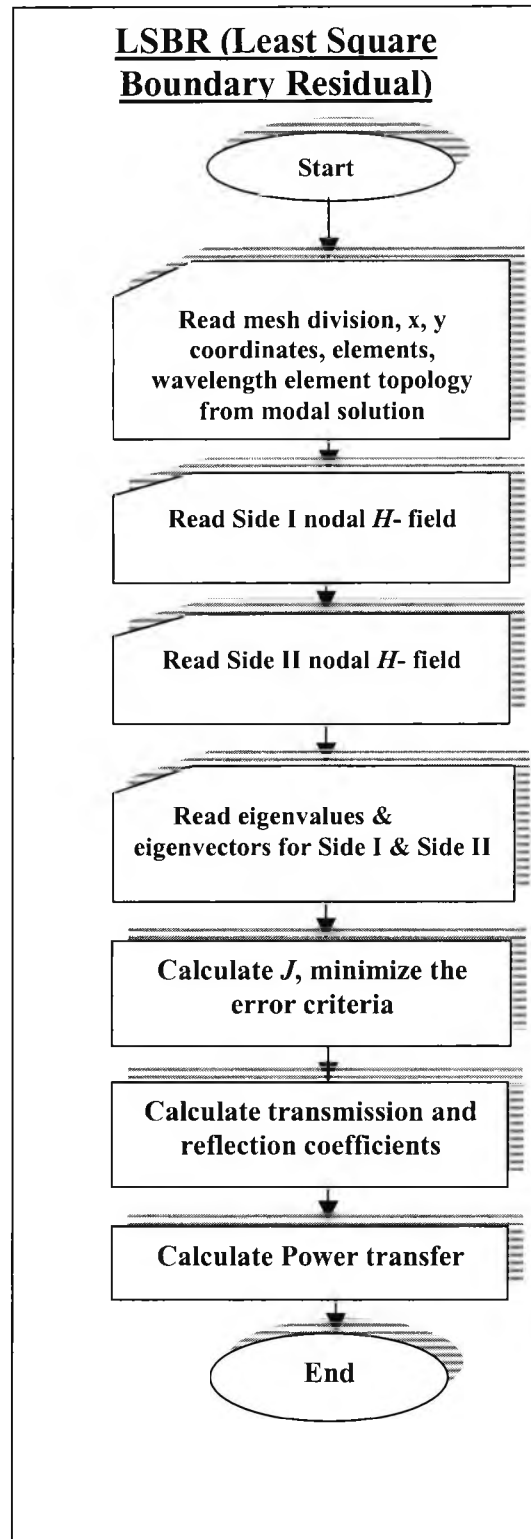
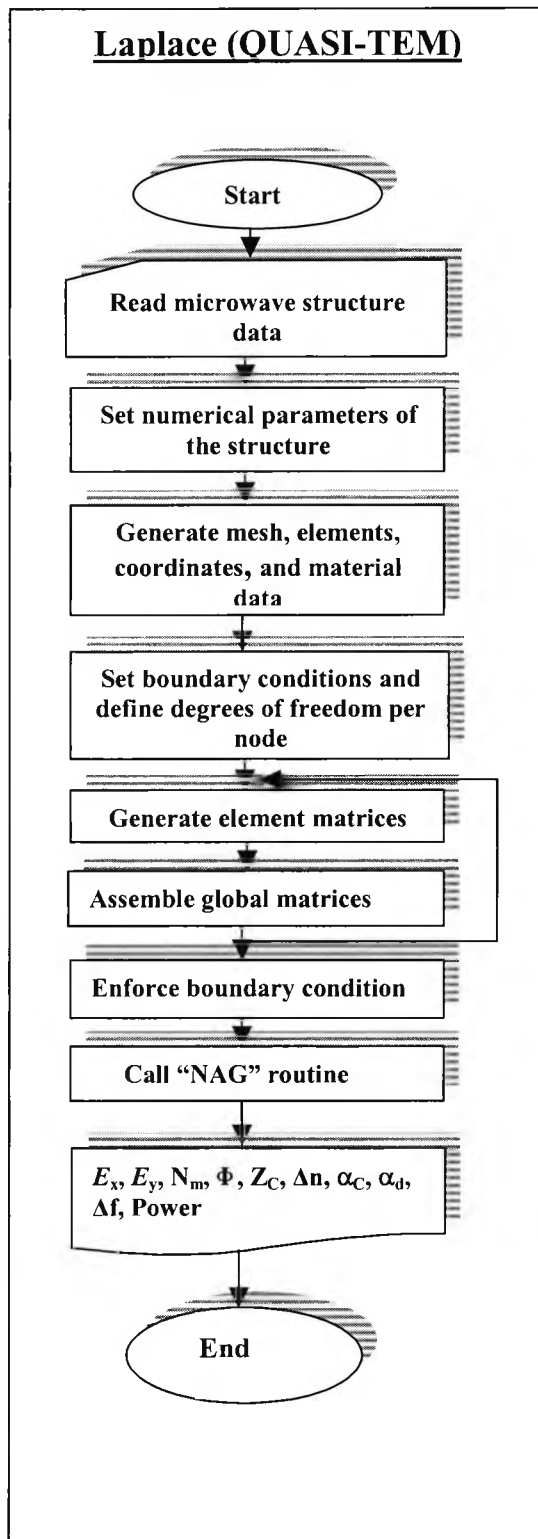
similarly,

$$\oint A_y dy = \frac{\partial A_y}{\partial x} dx dy \quad (\text{A2.9})$$

Flow Chart of FEM Implementation







List of Publications by the author relevant to the thesis

1. Anwar N S. S. A. Obayya S. S. A, Haxha S, Themistos C, Rahman B. M. A, and Grattan K. T. V. (2002). The Effect of Fabrication Parameters on a Ridge Mach-Zender Interferometric (MZI) Modulator. Journal of Lightwave Technology LT-20 (5): 826-833.
2. Rahman B. M. A. and Haxha S. (2002). Optimization of microwave properties for ultrahigh-speed etched and unetched lithium niobate electrooptic modulators. Journal of Lightwave Technology LT-20 (10): 1856-1863.
3. Haxha S and Rahman B. M. A (2002). Bandwidth calculation of high-speed optical modulators. 7th IEEE High Frequency Postgrad. Student's Colloquium London: 145-152.
4. Rahman B. M. A, Wongcharoen T, Haxha S, Themistos C, Rajarajan M, and Grattan K. T. V. (2002). Design and optimization of photonic devices by use of the finite element method. International Conference on Optical Communications and Networks (ICCON), Singapore.
5. Rahman B. M. A, Wongcharoen T, Haxha S, Themistos C, Rajarajan M, and Grattan K. T. V. (2002). Rigorous design optimization of photonic devices," Photonics India 2002, Bombay.

6. Haxha S, Rahman B. M. A and Grattan K. T. V. (2003). Bandwidth estimation for ultra-high-speed lithium niobate modulators. Journal of Applied Optics-LP-42 (15): 2674-2682.
7. Obayya S S A, Haxha S, Rahman B. M. A and Grattan K. T. V. (2003) Optimization of the optical properties of a deeply-etched semiconductor electrooptic modulator Journal of Lightwave Technology LT-21 (8): 1813-1819.
8. Rajarajan M, Rahman B M A, Wongcharoen T, Themistos C, Somasiri N, Haxha S, and K T V Grattan. (2003). Review of finite element characterization of photonic devices. Journal of Modern Optics 50 (12): 1835-1848.
9. Haxha S, Rahman B. M. A, Obayya S. S, Grattan K. T. V. Velocity matching of a GaAs Electrooptic Modulator (2003). Journal of Applied Optics-LP :7179-7187.
10. Obayya S. S, Haxha S, Rahman B. M. A and Grattan K. T. V. (2003). Accurate Characterization of Polarization Conversion in Semiconductor Electrooptic Modulators. Accepted for publication in Journal of Lightwave Technology.
11. Rahman B. M. A and Haxha S (2003). Effect of device parameters on the bandwidth calculations of high-speed optical modulators. Photonics West Conference: 4986-68 SPIE, San Jose California (USA).
12. S Haxha, Rahman B. M. A and Grattan K. T. V. (2003). Phase matching of GaAs electrooptic modulators by using a highly dispersive tantalium pentoxide overlayer. Integrated Photonics Research, IPR03, Washington, (USA).
13. Rahman B. M. A, Haxha S, Obayya S. S, and Grattan K. T. V. (2003). Design issues for high-speed electrooptic modulators. Information Technologies and Communications (ITCom) conference, SPIE, Orlando, Florida, USA.

14. Rahman B. M. A, Wongcharoen T, Obayya S. S, Haxha S, Somasiri N, Themistos C, Rajarajan M, and Grattan K. T. V. (2003). Characterization of photonic devices by finite element method. 2nd Symp. on Photonics, Networking & Computing, Cary, North Carolina, (USA).

15. Rahman B. M. A, Somasiri N, Wongcharoen T, Haxha S, Obayya S. S, Themistos C, Rajarajan M, and K T V Grattan (2004). Finite element characterization of photonic devices for optical communications. Invented paper, International Conf. on Computer & Devices for Communication, India, Calcutta.

References

- ◆ Agrawal N, Weinert C. M, Ehrke H. J, Mekonnen G. G, Franke D, Bornholdt C, and Langenhorst R. (1995). Fast 2*2 Mach-Zehnder optical space switches using InGaAsP-InP multiquantum-well structures. IEEE Photonics Technology Letters 7 (6): 644-645.
- ◆ Alferness R. C. (1988). Titanium-diffused lithium niobate waveguide devices. In Guided Wave Optoelectronics Edited by Tamir T. (Berlin, Germany: Springer-Verlag) 155-157.
- ◆ Alferness R. C, Korotky K. S, and Marcatili J. A. E. (1984). Velocity-matching techniques for integrated optic traveling wave switch/modulators. IEEE Journal of Quantum Electronics QE-20 (3): 301-309.
- ◆ Alferness, R. C, Economou N. P and Buhl L. L. (1981). Fast compact optical waveguide switch modulator. Applied Physics Letters 38 (11): 214-217.
- ◆ Anderson B. D. (1965). Optical and Electro-optic information Processing. MIT Press (Cambridge): 221.
- ◆ Anwar N S. S. A. Obayya S. S. A, Haxha S, Themistos C, Rahman B. M. A, and Grattan K. T. V. (2002). The Effect of Fabrication Parameters on a Ridge Mach-Zehnder Interferometric (MZI) Modulator. Journal of Lightwave Technology LT-20 (5): 826-833.
- ◆ Anwar N, Themistos C, Rahman B. M. A, and Grattan K. T. V. (1999). Design considerations for an electrooptic directional coupler modulator. Journal of Lightwave Technology LT-17 (4): 598-605.
- ◆ Bathe K. J., and Wilson, E. L. (1976). Numerical methods in finite element analysis. (New Jersey: Prentice Hall).
- ◆ Berini P. and Wu K. (1996). Modeling lossy anisotropic dielectric waveguides with the method of lines. IEEE Transactions on Microwave Theory and Techniques MTT-44 (5): 749-759.

References

- ◆ Berk A. D. (1956). Variational principles for electromagnetic resonators and waveguides. IRE Transactions on the Antennas and Propagation AP-4: 104-111.
- ◆ Born M. and Wolf E. (1980). Principles of Optics. The 6th edition (Pergamon Press).
- ◆ Burke S. V. (1990). Spectral index method applied to rib and strip-loaded directional couplers. IEE Proceedings J-137 (1): 7-10.
- ◆ Charczenko W, Januar I and Mickelson A. R. (1993). Modeling of proton-exchanged and annealed channel waveguides and directional couplers. Journal of Applied Physics 73 (7): 3139-3148.
- ◆ Chen D, Bhattacharya D, Udupa A, Tsap B, Fetterman H. R, Antao C, Sang-Shin L, Jinghong C, Steier W. H, and Dalton L. R. (1999). High-frequency polymer modulators with integrated finline transitions and low V_{pi}. IEEE Photonics Technology Letters 11 (1): 54-56.
- ◆ Chen D, Fetterman H. R, Antao C, Steier W. H, Dalton L. R, Wenshen W, and Yongqiang S. (1997). Demonstration of 110 GHz electro-optic polymer modulators. Applied Physics Letters 70 (25): 3335-3337.
- ◆ Chiang K. S. (1994). Review of numerical and approximate methods for the modal analysis of general optical dielectric waveguides. The Bell System Technical Journal 26: S113-S314.
- ◆ Chung Y. and Dagli N. (1990). An Assessment of finite difference beam propagation method. IEEE Journal of Quantum Electronics QE-26 (8): 1335-1339.
- ◆ Corr D. G. and Davies J. B. (1972). Computer analysis of the fundamental and higher order modes in single and couple microstrips. IEEE Transactions on Microwave Theory and Techniques MTT-20 (10): 669-678.
- ◆ Courant R. (1943). Variational methods for the solution of problems of equilibrium and vibrations. Bulletin of the American Mathematical Society 49: 1-23.
- ◆ Craig D. L, Whitaker J. F, and Mourou G. (1997). Travelling-wave electro-optic modulator with a novel broadband velocity-matching structure. Laser & Electrooptic Soc-10th Annual meeting, IEEE Conference Proceedings 2: 314-315.
- ◆ Csendes, Z. J. and Silvester, P. (1970). Numerical solution of the dielectric loaded waveguides: I-finite-element analysis. IEEE Transactions on Microwave Theory and Techniques MTT-18 (12): 1124-1131.

References

- ◆ Dagli N. (1999). Wide-bandwidth laser and modulators for RF Photonics. IEEE Transactions on Microwave Theory and Techniques MTT-47 (7): 1151-1171.
- ◆ Daniels P. (1984). Two-dimensional propagating beam analysis of an electrooptic waveguide modulator. IEEE Journal of Quantum Electronics QE-20 (9): 1093-1097.
- ◆ Davies J. B. (1972). Review of method for numerical solution of the hollow-waveguide problem. IEEE Conference Proceedings 119 (1): 33-37.
- ◆ Davies J. B. (1973). A least-square boundary residual method for the numerical solution of scattered problems. IEEE Transactions on Microwave Theory and Techniques MTT-21 (2): 99-104.
- ◆ Davies, J. B. (1989). The finite element method, in numerical techniques from microwave and millimeter-wave passive structures. Edited by Itoh. T. (New York: Wiley) 33-132.
- ◆ Davies, J. B. (1993). Finite element analysis of waveguides and cavities-A review. IEEE Transactions on Magnetism 29 (2): 1578-1583.
- ◆ Dean P. J. (1985). Optical fiber communications. (London: Prentice-Hall).
- ◆ Dolfi D. W. and Ranganath T. R. (1992). 50 GHz velocity-matched broad wavelength LiNbO₃ modulator with multimode active section. Electronics Letters 28 (13): 1197-1198.
- ◆ Eldada L. (2001). Advances in telecom and datacom optical components. Optical Engineering 40 (7): 1165-1178.
- ◆ Ermer S, Anderson W. W, Van Eck T. E, Girton D. G, Lovejoy S. M, Leung D. S, Marley J. A. and Harwit A. (1997). Progress in optoelectronic polymers and devices. San Jose, CA 1997. Proceedings SPIE'97: 397-404.
- ◆ Fernandez A. F. and Lu Y. (1996). Microwave and Optical Waveguide Analysis by the Finite Element Method. (London: John Wiley & Sons Inc.).
- ◆ Feit M. D. and Fleck J. A. (1980). Computer of modes properties in optical fiber waveguides by a propagating beam method. Applied Optics 19 (7): 1154-1164.
- ◆ Fetterman M, Chao C. P, and Forrest S. R. (1996). Fabrication and analysis of high-contrast InGaAsP-InP Mach-Zehnder modulators for use at 1.55- μm wavelength. IEEE Photonics Technology Letters 8 (1): 69-71.

References

- ◆ Fouchet S, Carenco A, Daguet C, Guglielmi R, and Riviere L. (1987). Wavelength dispersion of Ti induced refractive index change in LiNbO₃ as a function of diffusion parameters. Journal of Lightwave Technology LT-5 (5): 700-708.
- ◆ Fukuma M and Noda J. (1980). Optical properties of titanium-diffused LiNbO₃ strip waveguide and their coupling-to-a-fiber characteristics. Applied Optics 19 (4): 591-597.
- ◆ Gee C. M, Thurmond G. D and Yen H. W. (1983). 17-GHz bandwidth electrooptic modulator. Applied Physics Letters 43 (11): 998-1000.
- ◆ Girton D. G, Kwiatkowski S. L, Lipscomb G. F and Lytel R. S. (1991). 20 GHz electro-optic polymer Mach-Zehnder modulator. Applied Physics Letters 58 (16): 1730-1732.
- ◆ Goell J. E. (1969). A circular-harmonic computer analysis of rectangular dielectric waveguides. The Bell System Technical Journal 48: 2133-2160.
- ◆ Gopalakrishnan G. K, Bulmer C. H, Burns W. K, McElhanon R. W, and Greenblatt A. S. (1992). 40 GHz, low half-wave voltage Ti: LiNbO₃ intensity modulator. Electronics Letters 28: 826-827.
- ◆ Gopalakrishnan G K, William K. B, and Catherine B. H. (1993). Microwave-Optical Mixing in LiNbO₃. IEEE Transactions on Microwave Theory and Techniques MTT-41 (12): 2383-2391.
- ◆ Gupta K. C., Garg R., Bahl I. J. (1979). Microstrip lines and slotlines. First edition (Boston, London: Artech House).
- ◆ Harrington, R. F. (1968). Field computation by moment methods. (Florida: R. E. Krieger Publishing Company).
- ◆ Hatsuda T. (1975). Computation of coplanar-type strip-line characteristics by relaxation method and its application to microwave circuits. IEEE Transactions on Microwave Theory and Techniques MTT-23 (10): 795-802.
- ◆ Hayata, K., Koshiba, M., Eguchi, M. and Suzuki, M. (1986). Vectorial finite element method without any spurious solutions for dielectric waveguiding problems using transverse magnetic-field component. IEEE Transactions on Microwave Theory and Techniques MTT-34 (11): 1120-1124.

References

- ◆ Hayata K., Misawa A. and Koshiba M. (1990). Split-step finite-element method applied to nonlinear integrated optics. Journal of the Optical Society of America B 7 (9): 1772-1784.
- ◆ Heaton J. M, Bourke M. M, Jones S. B, Smith B. H, Hilton K. P, Smith G. W, Birbesk J. C. H, Berry G, Dewar S. V, and Wight D. R. (1999). Optimization of deep-etched, single-mode GaAs/AlGaAs optical waveguides using controlled leakage into the substrate. Journal of Lightwave Technology LT-17 (2): 267-281.
- ◆ Heismann Fred. (1994). Analysis of a reset-free polarization controllers for fast automatic polarization stabilization in fiber-optics transmission systems. Journal of Lightwave Technology LT-12 (4): 690-699.
- ◆ Henry C. H. (1982). Theory of the linewidth of semiconductor lasers. IEEE Journal of Quantum Electronics QE-18 (2): 259-264.
- ◆ Hondros D. and Debye P. (1910). Electromagnetic waves along long cylinders of dielectric. Annal Physik 32 (3): 465-476.
- ◆ Hung P. W., Xu C. L. and Chaudhuri S. K. (1992). A wide angle vector beam propagation method. IEEE Photonics Technology Letters 4 (1): 1118-1120.
- ◆ Hui W. K, Chiang S. K., Wu B. and Zhang H. Z. (1998). Electrode optimization for high-speed traveling-wave integrated optic modulators. Journal of Lightwave Technology LT-16 (2): 232-238.
- ◆ Hutchings D. C, Sheik-Bahae M, Hagan D. J, and van Stryland E. W. (1992). Kramers-Kronig relations in nonlinear optics. Optical Quantum Electronics 24: 1-30.
- ◆ Ido T, Tanaka S, Suzuki M, Koizumi M, Sano H, and Inoue H. (1996). Ultra-high-speed multiple-quantum-well electro-absorption optical modulators with integrated waveguides. Journal of Lightwave Technology LT-14 (9): 2026-2034.
- ◆ Ishii K. T. (1989). Microwave Engineering. (Orlando, Florida, USA: Harcourt Brace Jovanovich, Publisher).
- ◆ Januar I, Fuerstain R. J, Mickelson A. R, and Sauer J. R. (1992). Wavelength sensitivity in directional couplers. Journal of Lightwave Technology LT-10 (9): 1202-1209.
- ◆ Jungerman R. L, Johnson C, McQuate D. J, Salomaa K, Zurakowski M. P, Bray R. C, Conrad G, Cropper D and Hernday P. (1990). High Speed Modulator for

References

- Applications in Instrumentation. Journal of Lightwave Technology LT-8 (9): 1363-1370.
- ◆ Kao K. C. and Hockham G. A. (1966). Dielectric-fiber surface waveguides for optical frequencies. Proceedings of IEE 113: 1151-1158.
 - ◆ Kawano K, Kitoh T, Jumonji H, Nozawa T and Yanagibashi M. (1989). New travelling-wave electrode Mach-Zehnder optical modulator with 20 GHz bandwidth and 4.7 V driving voltage at 1.52 μm wavelength. Electronics Letters 25 (20): 1382-1383.
 - ◆ Kawano K. K, Noguchi K, Kitoh T, and Miyazawa H. (1991). A finite element method (FEM) analysis of a shielded velocity-matched Ti: LiNbO₃ optical modulator. IEEE Photonics Technology Letters 3 (10): 919-921.
 - ◆ Keen A. G, Wale M. J, Sobhy M. I, and Holden A. J. (1990). Quasi-static analysis of electrooptic modulators by the method of lines. Journal of Lightwave Technology LT-8 (1): 42-50.
 - ◆ Kendall P. C., Mclroy P. W. A. and Stern M. S. (1989). Spectral index method for rib waveguide analysis. Electronics Letters 25 (2): 107-108.
 - ◆ Khan M. N, A. Gopinath A, Bristow J. P. G, and Donnelly J. P. (1993). Technique for velocity-matched travelling-wave electrooptic modulator in AlGaAs/GaAs. IEEE Transactions on Microwave Theory and Techniques MTT-41 (2): 244-249.
 - ◆ Khazaei H. R, Berolo E, and Ghannouchi F. (1998). High-speed slow-wave coplanar strip GaAs/AlGaAs electro-optic laser modulator. Microwave and Optical Technology Letters 19: 184-186.
 - ◆ Kitazawa T, Polifko D, and Ogawa H. (1992). Analysis of CPW for LiNbO₃ optical modulator by extended spectral-domain approach. Microwave and Guided Wave Letters 2 (8): 313-315.
 - ◆ Knox R. M. and Toullos P. P. (1979). In: Proceedings of MRI Symposium on submillimeter waves, edited by Fox. J. (Brooklyn: Polytechnic Press): 497-516.
 - ◆ Koch T. L and Bowers J. E. (1984). Nature of wavelength chirping in directly modulated semiconductor lasers. Electronics Letters 20: 1038-1040.
 - ◆ Koch T. L and Linke R. A. (1986). Effect of nonlinear gain reduction on semiconductor laser wavelength chirping. Applied Physics Letters 48 (10): 613-615.

References

- ◆ Konrad A. (1976). Vector variational formulation of electromagnetic field in anisotropic media. IEEE Transactions on Microwave Theory and Techniques MTT - 24 (9): 553-559.
- ◆ Korotky S. K, and Alferness R. C. (1987). Ti: LiNbO₃ integrated optic technology,” in Integrated Optical Circuits and Components: Design and Applications, L. D. Hutchenson, Edited (New York: Marcel Dekker).
- ◆ Koshiha M. Hayata and Suzuki .M. (1982). Approximation scalar finite-element analysis of anisotropic optical waveguides. Electronics Letters 18 (10): 411-413.
- ◆ Koshiha M. and Suzuki M. (1985). Vectorial wave analysis of optical waveguides with rectangular cross-section using equivalent network approach. Electronics Letters 21 (22): 1026-1027.
- ◆ Koshiha M. and Kumagani H. (1987). Theoretical study of silicon-clad planar diffused optical waveguide”, IEE Proceedings 134 (6): 333-338.
- ◆ Koshiha, M. (1992). Optical waveguide theory by the finite element method. (London: Kulwer Academic Publisher).
- ◆ Koshiha, M. and Inoue, K. (1992). Simple and efficient finite element analysis of microwave and optical waveguides. IEEE Transactions on Microwave Theory and Techniques MTT-40 (2): 371-377.
- ◆ Koshiha M, Tsuji Y, and Nishio M. (1999). Finite-element modelling of broad-band traveling-wave optical modulators. IEEE Transactions on Microwave Theory and Techniques MTT-47 (9): 1627-1633.
- ◆ Koyama F and Iga K. (1988). Frequency chirping in external modulators. Journal of Lightwave Technology LT-6 (1): 87-93.
- ◆ Kubota K, Noda J and Mikami O. (1980). Travelling wave optical modulator using a directional coupler LiNbO₃ waveguide. IEEE Journal of Quantum Electronics QE-16 (7): 754-760.
- ◆ Lee H. M, Wol-Yon H, Min-Cheol O, Heuk P, Taehyoung Z, and Jang-Joo K. (1997). High performance electro-optic polymer waveguide device. Applied Physics Letters 71 (26): 3779-3781.
- ◆ Livescu G. (2002). Optical Technology. (New Jersey: Holmdel)

References

- ◆ Maack, D.R. (1999). Reliability of Lithium Niobate Mach Zehnder modulators for digital optical fiber telecommunication systems. (1999). In: Reliability of Optical Fibers and Optical Fiber Systems Bellingham, WA, 73 SPIE: 197 – 230.
- ◆ Mayaba N. Lagasse P. A. and Vandenbulcke P. (1981). Finite element analysis of optical waveguides. IEEE Transactions on Microwave Theory and Techniques MTT-29 (6): 600-604.
- ◆ Marcatili, E. A. J. (1969). Dielectric rectangular waveguide and directional coupler for integrated optics. The Bell System Technical Journal 48: 2071-2102.
- ◆ Marcuse D. (1989). Electrostatic fields of coplanar lines computed with point matching method. IEEE Journal of Quantum Electronics QE-25 (5): 939-947.
- ◆ Matsui Y, Murai H, Arahira S, Kutsuzawa S, and Ogawa Y. (1997). 0-GHz bandwidth 1.55- μm strain-compensated InGaAlAs-InGaAsP MQW laser. IEEE Photonics Technology Letters 9 (1): 25-27.
- ◆ Mitomi O, Noguchi K, and Miyazawa H. (1995). Design of ultra-broad-band LiNbO₃ optical modulator with ridge structure. IEEE Transactions on Microwave Theory and Techniques MTT-43 (9): 2203-2207.
- ◆ Minakata M. (2001). Recent progress of 40 GHz high-speed LiNbO₃ optical modulator. Active and Passive Optical components for WDM communication. In: Denver 2001. Proceedings SPIE 4532. Edited by: Dutta A. K, Awwal A. A. S, Dutta N. K and Okamoto K. pp.16-27.
- ◆ Mollenauer L. F, Gordon J. P and Evangelides S. G. (1991). Multigigabit Soliton Transmission Traverse Ultralong Distances. Laser Focus World 27 (11): 159-170.
- ◆ Montanari E., Selleri S., Vincetti L. and Zoboli M. (1998). Finite-element full-vectorial propagation analysis for three-dimensional z-varying optical waveguides. Journal of Lightwave Technology LT- 16 (4): 703-714.
- ◆ Morita N. (1990). The boundary element method. In: Analysis methods for electromagnetic wave problems. Edited by Yamashi E. (London: Artech House). pp. 33-77.
- ◆ Mur. G. (1974). Finite difference method for the solution of electromagnetic waveguide discontinuity problem. IEEE Transactions on Microwave Theory and Techniques MTT-22 (1): 54-57.

References

- ◆ Nagata, H. (2000). Activation energy of DC-drift of x-cut LiNbO₃/optical intensity modulators. IEEE Photonics Technology Letters 12 (4): 386 – 388.
- ◆ Nees J, Williamson S and Mourou G. (1989). 100 GHz travelling-wave electro-optic phase modulator. Applied Physics Letters 54 (20): 1962-1964.
- ◆ Noguchi K, Miyazawa H, and Mitomi O. (1994). 75 GHz broadband Ti:LiNbO₃ optical modulator with ridge structure. Electronics Letters 30 (12): 949-950.
- ◆ Noguchi K, Mitomi O, Miyazawa H, and Seki S. (1995). A Broadband Ti-LiNbO₃ Optical Modulator with a ridged Structure. Journal of Lightwave Technology LT-13 (6): 1164-1169.
- ◆ Noguchi K, Miyazawa H. and Mitomi O. (1998). Frequency-dependent propagation characteristics of coplanar waveguide electrode on 100 GHz Ti:LiNbO₃ optical modulator. Electronics Letters 34: 661-663.
- ◆ Noguchi K, Miyazawa H, and Mitomi O. (1998). 40-Gbit/s Ti:LiNbO₃ optical modulator with a two-stage electrode. IEICE Transactions on Electronics (Japan)-E81-C: 1316-1320.
- ◆ Obayya S. S. A, Haxha S, Rahman B. M. A, Themistos C and Grattan K. T. V. (2003). Optimization of the optical properties of a deeply-etched semiconductor electrooptic modulator. Journal of Lightwave Technology LT-21 (8): 1813-1819.
- ◆ Obayya S. S. A, Rahman B. M. A, Grattan K. T. V, and El-Mikati H. A. (2001). Beam propagation modeling of polarization rotation in deeply etched semiconductor bent waveguides. IEEE Photonics Technology Letters 13 (7): 681–683.
- ◆ Obayya S. S. A, Rahman B. M. A, and El-Mikati H. A. (2000). New full-vectorial numerical efficient propagation algorithm based on the finite element method. Journal of Lightwave Technology LT-18 (3): 409-415.
- ◆ Okamoto K. (2000). Fundamentals of optical waveguides. (London: Academic Press)
- ◆ Osinski M and Buus J. (1987). Linewidth broadening factor in semiconductor lasers—an overview. IEEE Journal of Quantum Electronics QE-23 (1): 9-29.
- ◆ Pantic Z and Mittra R. (1986). Quasi-TEM analysis of microwave transmission lines by the finite-element method. IEEE Transactions on Microwave Theory and Techniques MTT-34 (11): 1096-1103.

References

- ◆ Paul L. and Dale R. C. (1978). Electromagnetism: Principles and Applications. (San Francisco: W. H. Freeman and Company) pp. 19-25.
- ◆ Pen S. T. and Oliner A. A. (1981). Guidance and leakage properties of a class of open dielectric waveguides: Part I-Mathematical formulations. IEEE Transactions on Microwave Theory and techniques MTT-29 (9): 843-855.
- ◆ Pohlmann Thomas. (1991). Polarization independent Ti:LiNbO₃ switches and filters. IEEE Journal of Quantum Electronics QE-27 (3): 602-607.
- ◆ Rahman B. M. A, and Davies J. B. (1984a). Finite –element analysis of optical and microwave problems. IEEE Transactions on Microwave Theory and Techniques MTT-32 (1): 20-28.
- ◆ Rahman B. M. A, and Davies, J. B. (1984b). Penalty function improvement of waveguide solution by finite elements. IEEE Transactions on Microwave Theory and Techniques MTT-32 (8): 922-928.
- ◆ Rahman B. M. A, and Davies J. B. (1984c). Finite-element solution of integrated optical waveguides. Journal of Lightwave Technology LT-2 (5): 682-688.
- ◆ Rahman B. M. A and Davies J. B. (1988). Analysis of optical waveguide discontinuities. Journal of Lightwave Technology LT-6 (1): 52-57.
- ◆ Rahman B. M. A. and Haxha S. (2002). Optimization of microwave properties for ultrahigh-speed etched and unetched lithium niobate electrooptic modulators. Journal of Lightwave Technology LT-20 (10): 1856-1863.
- ◆ Ramer O. G. (1982). Integrated optic electrooptic modulator electrode analysis. IEEE Journal of Quantum Electronics QE-18 (3): 386-392.
- ◆ Rangaraj M, Hosoi T, and Kondo M. (1992). A wide-band Ti:LiNbO₃ optical modulator with a conventional coplanar waveguide type electrode. IEEE Photonics Technology Letters 4 (9): 1020-1022.
- ◆ Rolland C. (1998). InGaAsP-based Mach-Zehnder modulators for high-speed transmission systems. Optical Society of America (OSA) OFC'98 San Jose CA pp. 283-284.
- ◆ Sadiku M. N. O. (1989). A simple introduction to finite element analysis of electromagnetic problems. IEEE Transactions on Education 32 (2): 85-93.

References

- ◆ Schultz U. and Pregla R. (1981). A new technique for the analysis of the dispersion characteristics of planar waveguides and its application to microstrips with tuning septums. Radio Science 16 (6): 1173-1178.
- ◆ Shin C. Y. and Gray G. K. (1983). Convergence of numerical solutions of step-type waveguide discontinuity problems by modal analysis. IEEE MTT-S Inc. Microwave Symposium Digest pp. 233-235.
- ◆ Simes R. J, Yan R. H, Barron C. C, Derrickson D, Lishan D. G, Karin J, Coldren L. A, Rodwell M, Elliott S and Huges B. (1991). High-Frequency Electro-optic Fabry-Perot Modulators. IEEE Photonics Technology Letters 3 (6): 513-515.
- ◆ Spickermann R, Peters M. G, and Dagli N. (1996a). A polarization independent GaAs-AlGaAs electrooptic modulator. IEEE Journal of Quantum Electronics QE-32 (5): 764-769.
- ◆ Spickermann R, Sakamoto S. R, Peters M. G, and Dagli N. (1996b). GaAs/AlGaAs travelling wave electro-optic modulator with an electrical bandwidth >40 GHz. Electronics Letters 32 (11): 1095-1096.
- ◆ Somasiri N and Rahman B. M. A. (2003). Polarization crosstalk in high index contrast planar silica waveguides with slanted sidewalls. Journal of Lightwave Technology LT-21 (1): 54-60.
- ◆ Tan M. R. T, Kim I, Chang J, and Wang S. Y. (1990). Velocity matching of III-V travelling-wave electro-optic modulator structures. Electronics Letters 26 (1): 32-33.
- ◆ Themistos C, Rahman B. M. A, Hadjucharalambous A, and Grattan K. T. V. (1995). Loss/gain characterization of optical waveguides. Journal of Lightwave Technology LT-13 (8): 1760-1765.
- ◆ Van Schooti P, Lambecki V, Gilde M. J, Chan Y. P, Lecomte J. P, Tapolsky G, Meyrueix R, Kershaw S. V, and Collins J. V. (1996). Design and realisation of a MZI type polymer based high speed EO-modulator. ECOC'96. 3. 1996 Oslo, Norway pp. 281-284.
- ◆ Vassalo C. "1993-1995 optical mode solvers. (1997). Optical and Quantum Electronics 29 (2): 95-114.

References

- ◆ Wakita K, Kotaka I, Mitomi O and Asai H. (1990). High Speed InGaAs/InAlAs multiple quantum well optical modulators with bandwidth in excess of 40 GHz at 1.55 μm . In: Technical Digest CLEO'90, Anaheim, California, 1990, paper CTUC6.
- ◆ Wakita K, Kotaka I, and Asai H. (1992). High-speed InGaAlAs/InAlAs multiple quantum well electrooptic phase modulators with bandwidth in excess of 20 GHz. IEEE Photonics Technology Letters 4: 29-31.
- ◆ Walker R. G. (1991). High-speed III-V semiconductor intensity modulators. IEEE Journal of Quantum Electronics QE-27 (3): 654-667.
- ◆ Walker R. G. (1994). High speed semiconductor guided-wave optic modulators. IEE Colloquium, No. 22: pp.1/1-1/6.
- ◆ Wang S. Y and Lin S. H. (1988). High speed III-V electrooptic waveguide modulators at $\lambda=1.3 \mu\text{m}$. Journal of Lightwave Technology LT-6 (6): 758-771.
- ◆ Wexler A. (1969). Computation of electromagnetic fields. IEEE Transactions on Microwave Theory and Techniques MTT-17 (8): 416-439.
- ◆ Wooten, E. L, Kissa K. M, Yi-Yan, A. (2000). A Review of Lithium Niobate Modulators for Fiber-Optic Communications Systems. IEEE Journal of Selected Topics in Quantum Electronics 6 (1): 69-82.
- ◆ Wu R. B, and Chen C. H. (1986). A scalar variational conformal mapping technique for weakly guiding dielectric waveguides. IEEE Journal of Quantum Electronics QE-22 (5): 603-609.
- ◆ Wu K, Tong C. E, and Vahldieck R. (1991). Microwave characteristics of high-speed travelling-wave electrooptic modulators on III-V semiconductors. Journal of Lightwave Technology LT-9 (10): 1295-1304.
- ◆ Yamashita. (1968). Variational method for the analysis of microstrip-like transmission lines. IEEE Transactions on Microwave Theory and Techniques MTT-16 (9): 529-535.
- ◆ Yariv A and Yeh P. (1984). Optical Waves in Crystals. (New York: Wiley Interscience).
- ◆ Yariv, A. (1985). Introduction to Optical Electronics. (3rd edition by Holt, Rinehart and Winston, New York)

References

- ◆ Yi J. C, Kim S. H, and Choi S. S. (1990). Finite-element method for the impedance analysis of travelling-wave modulators. Journal of Lightwave Technology LT-8 (6): 817-822.
- ◆ Yoshida Keiji, Kanda Yutaka, and Kohjiro Satoshi. (1999). A travelling-wave-type LiNbO₃ optical modulator with superconducting electrode. IEEE Transactions on Microwave Theory and Techniques MTT-47 (7): 1201-1205.
- ◆ Young T. P. (1988). Design of integrated optical circuits using finite elements. Science, Measurement and Technology, IEE Proceedings-135 (3): Pt. A, pp. 135-144.
- ◆ Zhang X and Miyoshi T. (1995). Optimum design of coplanar waveguide for LiNbO₃ optical modulator. IEEE Transactions on Microwave Theory and Techniques MTT-43 (3): 523-528.
- ◆ Zhang X, Gutierrez-Aitken A, Klotzkin D, Bhattacharya P, Caneau C, and Bhat R. (1997). 0.98- μm multiple-quantum-well tunneling injection laser with 98-GHz intrinsic modulation bandwidth. IEEE Journal of Selected Topics in Quantum Electronics 3 (2): 309-314.
- ◆ Zhou W. B. and Itoh T. (1982). Analysis of trapped image guides using effective dielectric constant and surface impedances. IEEE Transaction on Microwave theory and Techniques MTT-30 (12): 2163-2166.
- ◆ Zienkiewicz, O. C. (1977). The finite element method in engineering science. 3rd edition (London: McGraw-Hill).